Transfer of X-ray phase contrast imaging from the synchrotron to the hospital : development and optimization of modulations-based imaging

Laurène Quenot

THÈSE

Pour obtenir le grade de

DOCTEUR DE L'UNIVERSITÉ GRENOBLE ALPES

École doctorale : ISCE - Ingénierie pour la Santé la Cognition et l'Environnement
Spécialité : BIS - Biotechnologie, instrumentation, signal et imagerie pour la biologie, la médecine et l'environnement
Unité de recherche : STROBE - Rayonnement Synchrotron pour la Recherche Biomédicale

Transfert de l'imagerie X en contraste de phase du synchrotron à l'hôpital : développement et optimisation de l'imagerie par modulations

Transfer of X-ray phase contrast imaging from the synchrotron to the hospital: development and optimization of modulations-based imaging

Présentée par :

Laurène QUENOT

Direction de thèse :

Sylvain BOHIC CHARGE DE RECHERCHE, Université Grenoble Alpes	Directeur de thèse
Emmanuel BRUN INSERM	Co-directeur de thèse

Rapporteurs :

PAOLA COAN
Professeur, Ludwig-Maximilians- Universität München
SIMON ZABLER
Professeur, Deggendorf Institute of Technology

Thèse soutenue publiquement le **30 septembre 2022**, devant le jury composé de :

SYLVAIN BOHIC Chargé de recherche HDR, INSERM DELEGATION AUVERGNE-RHONE-ALPES	Directeur de thèse
PAOLA COAN Professeur, Ludwig-Maximilians- Universität München	Rapporteure
SIMON ZABLER Professeur, Deggendorf Institute of Technology	Rapporteur
CLARISSE FOURNIER Ingénieur docteur, CEA CENTRE DE GRENOBLE	Examinatrice
PHILIPPE ZEITOUN Directeur de recherche, CNRS DELEGATION ILE-DE-FRANCE SUD	Examinateur
ANNE BONNIN Docteur en sciences, Paul Scherrer Institut	Examinatrice
SAM BAYAT Professeur des Univ. - Praticien hosp., UNIVERSITE GRENOBLE ALPES	Président
EMMANUEL BRUN Chargé de recherche HDR, INSERM DELEGATION AUVERGNE-RHONE-ALPES	Co-directeur de thèse

PhD Manuscript

Transfer of X-ray phase contrast imaging from the synchrotron to the hospital: development and optimization of modulations-based imaging

Laurène Quénot

Thèse soutenue le 30 septembre 2022

Key words:
x-ray phase contrast imaging, x-ray dark-field imaging, numerical simulations, image processing, tomography.

Mots clés:
imagerie x en contraste de phase, imagerie x en champ sombre, simulations numériques, traitement d'images, tomographie.

Alice laughed. “There’s no use trying,” she said: “one can’t believe impossible things.”
“I daresay you haven’t had much practice,” said the Queen. “When I was your age, I always did it for half-an-hour a day. Why, sometimes I’ve believed as many as six impossible things before breakfast.

– *Alice through the Looking-Glass*
– Lewis Carroll

Contents

Contents v

Acknowledgements 1

Introduction 5

1 Context, physics and principles of x-ray imaging 7
1.1 Medical imaging . . . 7
1.1.1 Clinical routine imaging modalities . . . 7
1.1.2 Medical interest of phase and dark-field imaging . . . 9
1.2 Physics and technologies of x-ray imaging . . . 11
1.2.1 X-ray physics . . . 12
1.2.2 X-ray imaging set-ups . . . 14
1.2.3 Computed tomography . . . 25
1.3 Phase contrast imaging . . . 26
1.3.1 From interactions to contrast . . . 27
1.3.2 Phase contrast and dark-field imaging techniques . . . 30
1.3.3 Summary of the pros and cons . . . 39
Résumé du Chapitre 1 en Français . . . 41

2 Simulation of modulations-based imaging 45
2.1 State of the art . . . 46
2.1.1 Existing software programs . . . 46
2.1.2 Previous similar works . . . 47
2.1.3 Useful resources . . . 48
2.2 The PARESIS software . . . 50
2.2.1 Physical models and principles . . . 50
2.2.2 Membrane geometry . . . 55
2.2.3 Implementation and features . . . 58
2.3 Validations and limitations . . . 65
2.3.1 Phase effects validation on a monochromatic synchrotron set-up . 65
2.3.2 Phase effects validation on a polychromatic laboratory set-up . . . 68
2.3.3 Comparison of the dark-field simulation to a synchrotron experiment 70
2.3.4 Limitations . . . 70
2.4 Optimization of MoBI based on simulations . . . 72
2.4.1 Influence of the number of membrane positions . . . 72
2.4.2 Influence of the number of photons per acquisition . . . 73
2.4.3 Influence of low energy filtering . . . 74

2.4.4 Conclusion . . . 76
Résumé du Chapitre 2 en Français . . . 78

3 Phase retrieval **81**
3.1 State of the art . . . 81
3.1.1 Explicit tracking . . . 83
3.1.2 Implicit tracking . . . 85
3.1.3 Integration methods . . . 87
3.2 Fourier transform analysis of Fresnel interference patterns applied to MoBI 89
3.2.1 Ambiguity function to TIE . . . 89
3.2.2 Contrast transfer function multi-energy method . . . 90
3.3 Development of a new algorithm optimized for low coherence systems . . 94
3.3.1 Theoretical development . . . 94
3.3.2 First validations on a synchrotron experiment . . . 95
3.3.3 Studies on conventional laboratory set-ups . . . 98
3.4 Comparison of algorithms . . . 107
3.4.1 Synchrotron biomedical case . . . 107
3.4.2 Synchrotron quantitative measurements . . . 110
3.4.3 Conventional source imaging . . . 114
3.4.4 Summary of the comparison of the algorithms . . . 116
3.4.5 Note on integration algorithms . . . 117
3.5 Conclusion . . . 118
Résumé du Chapitre 3 en Français . . . 119

4 Dark-field retrieval developments **121**
4.1 Dark-field inverse problem algorithms . . . 123
4.1.1 State of the art . . . 123
4.1.2 Completing the LCS with a dark-field term . . . 125
4.2 Directional dark-field . . . 128
4.2.1 Theoretical developments and implementations . . . 129
4.2.2 From tensors to ellipses . . . 132
4.3 Applications to biological samples . . . 137
4.3.1 Directional dark-field on a Mouse knee . . . 137
4.3.2 Directional dark-field tomography of a tooth . . . 138
4.3.3 *In-vivo* dark field radiography and tomography for the study of lung injuries . . . 140
4.4 Dark-field on conventional laboratory sources . . . 144
4.4.1 Directional dark-field with a low energy conventional source . . . 144
4.4.2 High energy laboratory set-up . . . 146
4.5 Conclusion . . . 148
Résumé du Chapitre 4 en Français . . . 150

Conclusion **153**

Scientific communications **155**

Bibliography **157**

List of figures **166**

List of tables **171**

Summary **173**

Acknowledgements

Une thèse c'est comme une aventure. On se lance sans être sûr d'arriver au bout et sans vraiment savoir comment. Avant de se lancer, on a plein de gens autour de nous qui nous demandent si on est sûr de vouloir y aller, si on est bien préparés, si on est bien conscient que cela va être difficile. Je ne dirai pas que mon aventure à été simple. Je dirai qu'elle a été pleine d'épreuves mais que grâce aux nombreuses personnes qui m'ont accompagnées, elle a aussi été pleine d'expériences merveilleuses. On atteint un premier sommet, on découvre un paysage fantastique pour se rendre compte que le véritable sommet est encore beaucoup plus loin. Alors on redescend un petit peu avant de remonter. Mais dans toute cette aventure j'ai eu beaucoup de chance, et j'ai eu beaucoup de mains tendues qui m'ont permis de grimper un peu plus haut et pour lesquelles j'éprouve une profonde gratitude.

La première main tendue que je veux remercier, c'est celle d'Emmanuel Brun qui m'a acceptée en tant que stagiaire il y a de cela déjà presque quatre ans. Puis il m'a accompagnée sur tout le chemin en me tendant des branches auxquelles me raccrocher et en me donnant du courage quand il y en avait besoin. Au début du voyage, je remercie également Hélène Rougé-Labriet qui m'a fait embarquer sur leur projet, m'a appris à le naviguer avant de me laisser au commandement. Je remercie également Sam Bayat qui m'a accueillie au sein du Laboratoire Strobe, cette terre où l'échange de savoir se confronte aux problèmes politiques du monde du travail. À la fin du stage, Emmanuel et moi avons décidé de continuer ensemble pour trois années de plus. Je suis reconnaissante envers Sylvain Bohic d'avoir accepté de se porter garant pour moi et me permettre d'entamer une thèse sous sa direction. Je te remercie pour avoir vérifié régulièrement ma feuille de route et que ma boussole fonctionnait correctement.

La véritable aventure a alors pu commencer. Avec la bienveillance de mon encadrant Emmanuel, j'ai pu progresser doucement sur le sentier de la recherche. J'ai exploré des idées, trouvé des petits trésors en chemin que j'ai pu partager avec le monde lors de conférences internationales au Japon ou en Grèce. Dans mon entreprise, j'ai également eu la chance d'être présentée à de nombreux scientifiques avec qui j'ai partagé une partie du chemin. Je remercie notamment Jean-Michel Letang et Max Langer qui m'ont aidée à mieux comprendre les pavés de la physique des rayons x pour la simulation de l'imagerie en contraste de phase. Au détour d'un sentier, j'ai rencontré au travers d'un écran des scientifiques de l'autre bout du monde : les professeurs Pavlov, Paganin et Morgan qui m'ont ouvert de nouveaux horizons en me faisant découvrir et participer au développement du dark-field orienté et que je remercie grandement. Quelques mois après le début de ma thèse, Emmanuel m'a proposé de me rendre dans un lieu de savoir où je pourrai acquérir de nouvelles compétences qui me serviraient pour la suite de l'aventure. C'est ainsi que j'ai pu participer à Hercules, cette école sur l'utilisation des Grands Instruments où j'ai rencontré de nombreux autres petits aventuriers en herbes et différents instructeurs qui nous ont donnés des outils pour nous aider dans nos quêtes. Cette expérience à cependant pris fin assez

abruptement et j'ai dû emprunter un tunnel un peu plus solitaire où j'ai été menée par un arrivant inattendu : le coronavirus. Mais je n'ai pas perdu espoir, j'ai trouvé d'autres itinéraires pour progresser de mon côté. Et j'avais toujours l'oreille attentive de mon encadrant Emmanuel qui me parvenait à travers ce petit rectangle lumineux. J'ai progressé peu à peu jusqu'à un plateau, puis un suivant, traversant des rivières et empruntant des passages escarpés. Je remercie Jean-Pierre Guigay, qui m'a vue avancer au loin et a proposé de me guider vers un sentier nouveau qu'il avait découvert de nombreuses années auparavant et corrigeant ma trajectoire lorsque je m'égarais. Sur le chemin, Emmanuel m'a également emmené dans divers laboratoires qui nous ont ouverts leurs portes et prêtés leurs instruments le temps de quelques journées et nous ont permis de valider (ou non) nos théories sur de vraies expériences. Je remercie notamment Luc Salvo et Pierre Lhuissier du Simap, Sabine Rolland du Roscoat du 3SR, Renaud Boistel du Museum d'Histoire Naturelle de Paris et Clarisse Fournier du LASP au CEA de Grenoble. Ces expériences nous ont permis de faire des bons de plusieurs kilomètres en direction du sommet car même les échecs nous ont permis de mieux comprendre notre environnement et d'optimiser le reste de l'itinéraire. En plus des laboratoires, j'ai pu visiter des entreprises qui nous ont aidé à construire des ponts pour avancer plus loin et atteindre de nouveaux sommets. Je remercie Laurent Bernard et Rémi Abbal de ReactivIp, pour le travail en traitement d'image qui a permis de rendre mes algorithmes beaucoup plus rapides, ainsi que Dan Cenda, Bertrand Faure et Blandine Lantz de Xenocs qui ont travaillé avec nous sur l'implémentation du contraste de phase sur leur dispositif de laboratoire. Au fil de ma progression, j'ai aussi croisé d'autres explorateurs qui avaient un sac à dos remplis d'outils différents des miens et m'ont aidé dans ma progression. Je remercie pour cela Ludovic Broche, Luca Fardin, Rafael Celestre, Jayde Livingstone, Alberto Bravin et Sebastien Berujon. Enfin, sur certaines pentes un peu raides, Emmanuel m'a aidée à trouver des partenaires de cordées, des stagiaires auxquels j'ai enseigné les bases pour qu'ils puissent m'accompagner et ouvrir de nouvelles voies. Je remercie Robin Gallix et Clara Magnin pour leur motivation, leur travail rigoureux et l'enthousiasme qu'ils ont pu montrer dans cette aventure pas toujours facile.

Je remercie donc toutes ces personnes d'avoir participé à mon ascension jusqu'au sommet du Mont Blanc. Mais en plus de ces personnes qui m'ont tirée vers le haut, je souhaite remercier tous ceux qui m'ont empêchée de tomber en arrière, de faire demi-tour et qui m'ont motivée à continuer d'avancer. La première personne que j'ai rencontrée dans cette aventure, c'est Ines Zaouac. Je te remercie pour avoir fait de mes six mois de stage une randonnée pleine de découvertes, de rigolade, de détente lorsque cela était nécessaire et lorsque ça ne l'était pas. Merci pour ton amitié que j'ai eu la chance de garder après ton départ du laboratoire. Je remercie aussi Marion Carribon pour ses récits d'aventures plus fous les uns que les autres qui nous changeaient les idées et nous faisaient rire. Merci à Sarvi Keshmiri qui, malgré que nous ne gravissions pas la même montagne, a été présente du début à la fin de mon périple. Merci pour m'avoir montré que, même si ma montagne était difficile à gravir, au moins la mienne n'abritait pas de chats sauvages aux griffes acérées. Mille merci à Clément Tavakoli qui m'a fait rire chaque jour où nous nous croisions au bureau. Merci d'avoir écouté mes problèmes même quand il n'y avait rien

que tu puisses faire pour m'aider. Merci d'avoir résolu tous ceux que tu pouvais résoudre. Merci d'avoir eu des problèmes toujours plus gros que les miens. Merci d'avoir eu des craquages de fin de journée avec moi à l'ESRF. Merci pour toutes les news Twitter dont je n'aurai jamais entendu parler. Merci pour m'avoir supportée aussi longtemps. Merci à tous mes autres collègues qui ont été présents lors des pauses pour reprendre des forces avec un morceau à manger ou un café avant de repartir : Victor, Shifali, Nico, Alex, Chris, Pierre-Louis, Florian, Théo, Laura, Noémie et j'en oublie peut-être. Et en dehors de cette aventure, je remercie ma famille et mes amis qui m'ont encouragée, conseillée, entourée. Merci à ma grande sœur Delphine dont l'admiration pour mon travail m'a toujours donné plus de force pour avancer. Merci à mes parents qui m'ont encouragée dans la direction de la thèse sans jamais douter de moi. Merci à mes amis qui m'ont écoutée me plaindre et m'ont fait oublier les petites embuches du chemin. Merci surtout à Pauline et Loïcia pour votre façon de me comprendre et de partager mes plus gros défauts. Évidemment je veux remercier une personne en particulier qui a rejoint mon aventure au cours de la première année, qui m'a accompagnée d'une façon très particulière jusqu'en haut. Qui a passé des journées à travailler à mes côtés quand nous ne pouvions plus sortir et dont le dévouement pour son travail m'a inspiré. Merci à toi, Jérémy, Jim, mon partenaire, qui arrive à trouver les mots pour me rassurer quand je suis inquiète et me calmer quand je panique. Tu as rendu cette aventure tellement plus belle.

Et avant même le début de cette aventure, je souhaite remercier particulièrement Sabine Bailly, ma belle-mère, qui a grandement contribué à mon envie de faire la recherche. Merci pour les conseils que tu m'as donné sur la façon d'appréhender la thèse même si tu en dépeins un tableau plus effrayant que cela l'a été en réalité. Au moins j'étais préparée.

Pour finir encore une fois merci à toi, Manu, pour ton encadrement mais aussi pour plein d'autres choses : pour les voyages, les formations, les recrutements de mes collègues, pour avoir toujours eu le réflexe de me dire que c'était très bien avant de faire des remarques, pour le laser-game et le karting, les pains au chocolat du petit dej, les pauses café parfois beaucoup trop longues, les idées d'échantillons toujours plus farfelus, les bonbons Haribo et surtout les Maltesers, les petits bacs et les blind-test de manips à 2h du mat', pour David Castello-Lopes, pour les discussions cinéma, la télévision 45k de la salle de réu, et tout plein d'autres choses.

General Introduction

Current clinical and preclinical imaging modalities have strong limitations for osteoarticular diseases and lung injuries diagnosis. Conventional x-ray absorption-based Computed Tomography (CT) allows a clear 3D visualization of bone tissues but provides reduced sensitivity in the soft tissues. Changes in the composition of joint cartilage or soft tissues are usually evaluated using Magnetic Resonance Imaging (MRI). Yet, the images acquired by MRI struggle to render properly the bony changes and the micro-calcifications that are first signs of osteoarticular troubles. Additionally, MRI of the lung is technically challenging due to the low proton density of the lung tissue. CT is the gold standard for evaluating lung injuries thanks to the good contrast it provides between the lung tissues and air. Nevertheless, the resolution obtained with clinical CTs limits the diagnosis to a macroscopic evaluation. In parallel, UltraSonography (US) is still confined to a minor role in the clinical routine because it remains a non-reproducible method for osteaoarticular evaluation. Moreover, US penetration depth does not allow to image the lungs.

Recently, at synchrotrons, x-ray Phase Contrast and Dark-field Imaging (PCDI) has been proposed to overcome those limitations. Since the seminal work of Roentgen, x-ray imaging is based on the same physical phenomenon: the absorption of light by the tissues. But phase shift, associated to refraction, the fact that light is deviated when passing through matter, can be even more interesting. Indeed, the refraction index of the material can be a thousand times greater than its counterpart absorption factor for light elements. This translates into a greater contrast for all the different human tissues with x-ray imaging methods based on phase sensing. A third type of contrast, named "dark-field", is sensitive to small angle scattering related multiple refraction in micro-structures and gives access to a sub-pixel information, very valuable for lung imaging.

Over the past few decades, an increasing number of studies have demonstrated the high diagnostic potential of PCDI, as compared to conventional radiology, in a wide range of pathologies including osteoarticular and pulmonary diseases. With the emergence of partially coherent x-ray sources twenty years ago, expectations regarding PCDI became feasible and several PCDI methods have been developed at synchrotrons. Unfortunately, due to the dimensions and cost of such infrastructures, synchrotrons cannot be used for clinical routine for widespread pathologies. Therefore, several teams in the world are working on the transfer of x-ray PCDI to conventional laboratory systems more adapted to the clinical constraints.

The two main current available approaches capable of rendering such contrasts on conventional laboratory systems are Grating Interfermetry, and Edge Illumination. Albeit presenting a good sensitivity, these techniques require complex experimental set-ups that limits their use for 3D imaging. Although significant developments have been made to extend these techniques to practical imaging applications, many key issues still have to be addressed. Recent advances have shown impressive results

on human patients using grating interferometry dark-field imaging, but they remain in 2D or with a too long acquisition for patient imaging.

The goal of this thesis is to examine the possibility of transfering x-ray phase contrast and dark field imaging, in 3D, to the clinics, with a simple set-up. During this PhD, I investigated a recent technique that has the ambition to fully respect the clinical routine constraints.

Modulations-Based Imaging (MoBI) was introduced in 2012 by Berujon, Wang, and Sawhney, Morgan, Paganin, and Siu at synchrotrons, using the "speckle phenomenon" to create a random phase pattern. Introduction of the sample in the beam induces modifications of the pattern carrying its phase and dark-field information. The experimental set-up involves only the sample, an x-ray imaging detector and a randomly structured membrane containing small granular structures of a few pixels in size creating a high spatial frequency pattern. This set-up, besides its simplicity of implementation, has the main advantages of having no field of view limitation other than the detector (the membrane is easy to manufacture), no resolution limitation other than the optical system (modulations of a few pixels can be generated down to tens of nm) and finally the requirements on the beam coherence are expected to be low. This technique has been demonstrated to be very efficient at high resolution at synchrotrons. The goal of this PhD was to adapt this method to low resolution and low coherence systems.

The first chapter of this manuscript is devoted to fully describing the context of this study. Firstly, the medical needs in terms of imaging for osteoarticular and lung diseases are introduced. Then, the physical concepts associated to x-ray imaging in general and later some phase contrast and dark-field imaging notions are presented. Chapter two concerns the simulation of modulations-based imaging. After introducing the existing software and resources, the tool named PARESIS that I developed during this Ph.D is presented. Then this tool validations on actual experiments are reported before some experimental configurations optimization studies. The third chapter focuses on the numerical aspect of phase retrieval. The different (already existing) algorithms are introduced before the new theoretical development I have done and implemented for low coherence systems and that is validated on experiments. The last section of this chapter, contains an extensive review on the performance of seven different algorithms on different imaging cases. The final chapter is devoted to the dark-field retrieval developments using MoBI. After introducing the concepts of the dark-field inverse problem, my two main theoretical contributions are described. Their applications to different biological samples cases are reported, including *in-vivo* tomography. Finally, those algorithms are applied to low coherence systems.

Context, physics and principles of x-ray imaging

1

The goal of this chapter is to expose the context of x-ray phase contrast imaging for medical diagnosis. First, x-ray imaging is placed in its historical and current medical context to better explain the interest of phase contrast imaging. Then the physical aspect and technicalities of x-ray imaging are developed. Finally, the origin of the phase and dark-field contrasts are explained, and the various techniques that exists associated to those contrast modalities are listed. This chapter should give an idea of the appeal of phase contrast for medical imaging and the main challenges underlying its implementation on clinical devices.

1.1 Medical imaging 7
Clinical routine imaging modalities 7
Medical interest of phase and dark-field imaging 9
1.2 Physics and technologies of x-ray imaging 11
X-ray physics 12
X-ray imaging set-ups 14
Computed tomography 25
1.3 Phase contrast imaging 26
From interactions to contrast 27
Phase contrast and dark-field imaging techniques 30
Summary of the pros and cons39
Résumé du Chapitre 1 en Français 41

1.1 Medical imaging

Medical imaging refers to techniques and processes used to create images of the human body and observe internal structures without having to cut the body. In clinical routine, those techniques are used to establish a diagnosis, determine the severity of injuries and assist the treatment decision. In the clinical research field, medical imaging is used to better understand pathologies, follow their evolution and the effects of some new therapies. In clinical routine, there are four major 'families' of imaging techniques that will be briefly introduced below: x-rays, ultrasound, magnetic resonance imaging (MRI) and nuclear medicine. All are related to different physical phenomena and give different contrasts with their advantages and limitations.

1.1.1 Clinical routine imaging modalities

X-rays were discovered at the very end of the 19th century by a German physicist, W. C. Roentgen [3]. Only a few months later, they were used in medicine to image the body and diagnose skeletal traumas. About a century later, the British engineer Godfrey Hounsfield of Electronical Musical Instrumental company and the South Africa-born physicist Allan Cormack of Tufts University[4], came up with Computed Tomography. The principle is to reconstruct a 3D image of the body using x-ray images taken at different angles around a rotation angle virtually placed in the middle of the part to image. By then, the acquisition and reconstruction required a large deposited dose and a lot of time. Those parameters have been greatly improved since but are still a very challenging topic for researchers.
The main restrictions of today's x-ray imaging are the cancer risk associated with the deposited dose and the low absorption factor variations in soft tissues. Gonzalez and Darby [5] showed that "in the UK about 0.6% of the cumulative risk of cancer to age 75 years could be attributable to diagnostic x-rays".

Ultrasound's history starts at the beginning of the 20th century, first developed to image the depths of oceans to detect icebergs and submarines. It kept evolving and improving during the century and medical applications started in the 1950s.
The principle is to send high frequency sound waves and measure the echos when the waves are reflected by internal structures.
One of its first application in clinical routine was for unborn foetus imaging and it is still today one of its major use. Apart from that, ultrasound imaging can be used to observe superficial lesions but it is still confined to a minor role in clinical routine in the context of joint or lung diseases. It is explained by the fact that, albeit being fast, efficient and harmless, it remains a non-reproducible method with a limited penetration depth, limited spatial resolution and that it is not capable of imaging bony tissues.

Magnetic Resonance Imaging was developed following the discovery of nuclear magnetic resonance (NMR) by Isidor Rabi in 1937. The first MRI images were acquired in the 1970s by the team of the doctor Paul Lauterbur.
MRI is based on the introduction of a strong magnetic field gradient that allows to differentiate protons local magnetization when excited by a radio-frequency pulse. When going back to their rest state, the protons emit a signal that depend on their electronic environment (i.e. the material they are in).
Today, MRI allows the acquisition of 3D images with very low risks for the patient, but it struggles to correctly render structures containing a low concentration of hydrogen atoms such as bones and cartilage. MRI presents a very good contrast in soft tissues but its spatial resolution is very limited compared to what is achievable with x-rays and it is a very costly exam.

Positron Emission Tomography (PET) and Single Photon Emission Computed Tomography (SPECT) are nuclear medicine functional imaging techniques. They reconstruct 3D images by detecting very high energy photons produced as a result of the decay of radioactive elements bound to molecules of interest to follow certain metabolisms. The first PET camera was built for human studies by Edward Hoffman, Michael M. Ter-Pogossian, and Michael E. Phelps in 1973 at Washington University and the first PET scanner was built in 1977. These modalities are called functional imaging as they allow to follow certain metabolisms, showing where those take place, but they do not give anatomical images of the structures. Actually, they are often associated to CT to locate the source of the PET or SPECT signal in the body.

All those modalities present their own advantages but also limitations and, in the search of a method ever more efficient to differentiate various structures with the best possible spatial resolution and the minimum risks for the patient, many more techniques not yet available in clinical routines are being investigated.

This project focuses on x-ray imaging. The evolution of x-ray imaging is following various paths with the development of contrasts agents, photon counting detectors and spectral detectors that allows to differentiate particles energies but the contrasts at the heart of this project are x-ray Phase Contrast Imaging (PCI) and Dark-Field imaging (DF).

The principle of phase contrast was discovered for visible light in the 1930s [6] and the idea was adapted to x-rays in 1965. The actual use of phase contrast for x-ray imaging started in 1995 with the emergence of 3rd generation synchrotrons [7]. In PCI, the signal extracted corresponds to the phase difference induced in the radiation wave due to traversing the sample.
Recently, X-ray dark-field imaging emerged as a new complementary imaging modality [8]. It is essentially a phase effect that can be defined as multiple refraction phenomena at the micrometer scale [9]. The method is sensitive to the micro-structure changes of density that generate a specific image contrast complementary to phase or absorption contrast-based methods.
It becomes clear that advanced phase-contrast and dark-field imaging modalities are now in reach for medical imaging routines. In the sections below, the interest of phase contrast and dark-field imaging for clinical applications will be outlined and the various techniques that are investigated in this endeavor will be introduced.

1.1.2 Medical interest of phase and dark-field imaging

Phase contrast imaging has a proven ability to make visible details that are usually invisible with conventional attenuation based x-ray. Today, the number of scientific articles demonstrating the potential of PCI are numerous especially demonstrating the enhanced image contrast that can be obtained in soft tissues. In 2013, Bravin, Coan, and Suortti [7], published a very complete review article on the phase contrast imaging techniques existing at that time and the clinical applications of PCI.
Because the techniques are not yet completely available for clinical routines, most studies use ex-vivo human explants or animals.

As it will be extensively detailed in the next section, the interaction of x-rays with matter are quantified by their complex refractive index: $n = 1 - \delta + i\beta$ where the real coefficient δ accounts for phase effects and the imaginary part β accounts for attenuation phenomena. They both depend on the energy of the incident photons and the atomic structure of the material. In the range of energies used in x-ray medical imaging, the refraction coefficient is several orders of magnitudes higher than the absorption coefficient and this difference increases with the energy (see Figure 1.1). It means that, when increasing the energy, and consequently reducing the dose, phase images render a higher contrast between those tissues than attenuation [7, 10, 11].

One of the main demonstrated application of PCI is osteo-articular imaging. Osteoarthritis (OA) is a chronic degenerative disease affecting millions of people around the world. It is one of the most co-occurring diseases among patients aged 55 years and beyond [12, 13]. Because osteoarticular diseases have multi-factorial causes, having a high contrast between the different tissues of a joint has always been the holy grail of musculoskeletal imaging. Joint imaging is a real challenge for conventional clinical imaging methods as ultrasound has difficulty penetrating bone and other dense material and consequently commonly depict the outer surface of bony structures, MRI has a very limited sensitivity to bones and conventional radiography renders well bones but has a very low contrast in soft tissues. Figure 1.2 displays MRI, conventional CT and

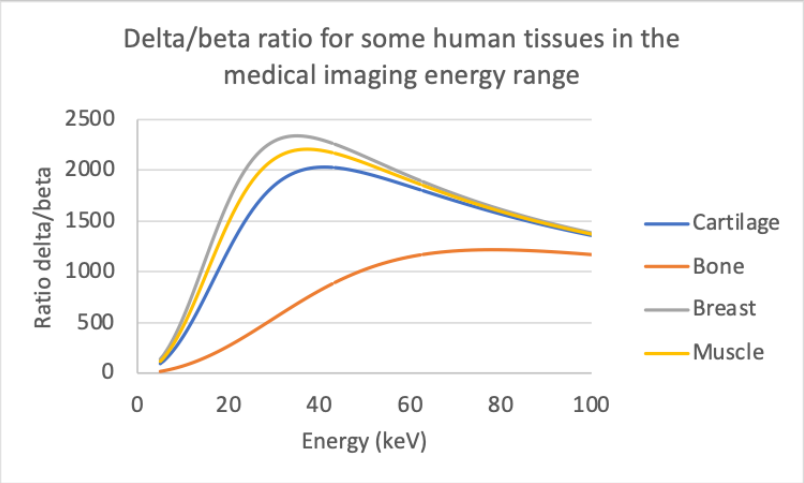

Figure 1.1: Ratio δ/β for some human tissues at clinical x-ray energies.

PCI images of a human wrist and where the visibility of different types of tissues have been graded (from 0 to 3) by radiologists and rheumatologists (from [11]). It shows that they judged that the phase contrast was the best technique to observe all different types of tissues in a single image. If phase contrast imaging was available in hospitals, it would therefore be a great tool to study osteo-articular diseases, allowing a better visualisation of all the tissues of the articulation at once. On human anatomical pieces PCI-CT has demonstrated to outperform the other conventional imaging modalities [14]. This technique is able to detect and improve contrast in both hard and soft tissues and shows micro-calcifications that are not perceptible on conventional imaging [14]. PCI-CT has a strong correlation with MRI in measuring cartilage thickness and with conventional CT in detecting subchondral bony changes [15].

Due to its ability to render a high contrast in soft tissues, one of the other demonstrated clinical application to PCI in literature is mammography [16, 17] mainly because it was thought to be possible to image at a lower dose than conventional imaging. Moreover, mammography, despite being the primary imaging tool for screening and diagnosis of human breast cancers, has serious limitations. Approximately 10 to 20% of palpable tumors are not detectable on mammograms and only about 40% of biopsied lesions are malignant [18]. Finally repeated mammography examinations have the potential of causing cancers [18]. Dedicated breast computed tomography (CT) can reduce some of these risks, but its spatial resolution ($\approx 400\ \mu m$) is mainly limited by the x-ray dose deliverable to the radiation sensitive human breast and its detection of microcalcifications is inferior to mammography [19]. Moreover, some tumors are not visible in CT because its image contrast based on the x-ray absorption coefficient is intrinsically low between tumors and normal tissues. Phase contrast imaging appears as a very promising approach to significantly improve the image contrast and therefore detectability and the diagnosis of breast tumors.
No mammography examples will be shown in this thesis but it is one of the possible future application of the technique.

As already mentioned, complementary to phase contrast imaging, dark-field imaging gives a contrast that is created by the presence of micro-structures in the sample. The lungs being composed of numerous mi-

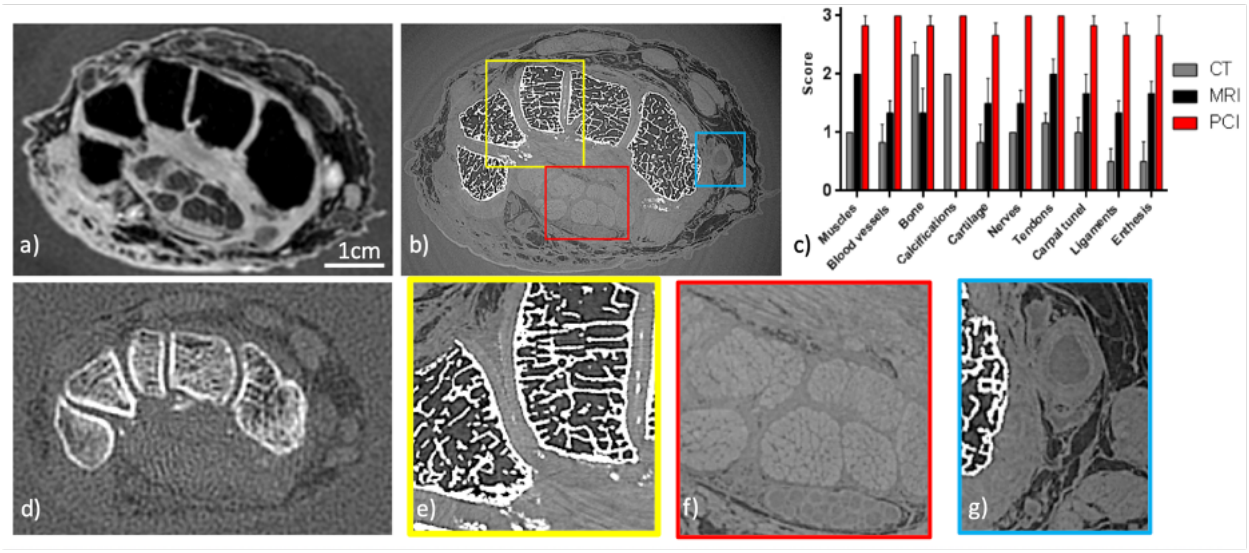

Figure 1.2: Images of a human wrist: a) MRI, b) synchrotron phase contrast tomography, d) conventional tomography. c) displays the visibility of numerous structures rated by radiologists for the different modalities. Results from Rougé-Labriet et al. [11].

croscopic alveoli, they are the perfect candidate for dark-field clinical applications to study for example Chronic Obstructive Pulmonary Disease (COPD) or Ventilator-Induced Lung Injury (VILI)[20].
COPD is one of the most common cause of death in the world according to the World Health Organization (ranking third with 3.23 million deaths in 2019 [1]). COPD is characterized by abnormalities of the small airways, obstructing the airflow to the alveoli.
Mechanical ventilation exposes the lung to mechanical stress and strain that can exacerbate or induce injury in patients with Acute Respiratory Distress Syndrome (ARDS) a complication of SARS-Cov-2 infection among other causes. This leads to a condition known as VILI[21], which is particularly urgent to address in the context of the current COVID-19 pandemic where adverse effects of mechanical ventilation strongly contribute to ICU mortality.
The clinical imaging tools to study and diagnose those pathologies amongst many other lung pathologies are still very limited. Dark-field imaging emerged only a few years ago and already, its interest in these domains has been extensively demonstrated with small animal studies for lung cancer diagnosis [22], lung inflammation [23] or neonatal VILI [24] and many others. The very first clinical trials on human lungs COPD observed with dark-field imaging have also been very recently published [25].

1: https://www.who.int/news-room/fact-sheets/detail/the-top-10-causes-of-death

This first part aimed at placing phase contrast and dark-field imaging in the medical imaging context, presenting its interest compared to other existing imaging modalities especially in the cases of osteoarticular imaging, mammography and pulmonary imaging. In the next section, the physical and technological context of x-ray imaging will be detailed.

1.2 Physics and technologies of x-ray imaging

X-ray phase contrast and dark-field imaging techniques are complementary to the common attenuation contrast and require similar instruments.

In this part, the context and prerequisites concerning x-ray physics and x-ray imaging will be introduced. After briefly introducing x-ray particles/waves and their interaction with matter, we will present the instruments used in x-ray imaging and their features depending on the type of set-up. Finally, the principle of computed tomography will be explained as it is used in conventional radiography and can be used in multi-contrast x-ray imaging.

1.2.1 X-ray physics

The physics of light particles are a mix between classical optics and wave physics. The dual particle/wave nature of the radiation must be considered in order to fully understand how it interacts with matter. This section aims at defining x-rays, their interactions with matter, the various ways they can be produced and detected in different configurations. As x-rays can be used for imaging different types of samples with various objective and constraints, the imaging set-up must be adapted and different configurations are required for different applications.

What are x-rays?
X-rays are the very energetic version of what we call "light" in everyday life. This light has this very particular characteristic that it is both described as a wave and as particles that we call electromagnetic waves and photons. When talking about its wave characteristic, we will often describe it with its wavelength, λ or its frequency $\nu = c/\lambda$ (c the velocity of light) and its wave number $k = 2\pi/\lambda$. When considering the particle, we will more often talk about its energy $E = hc/\lambda$ with h the Plank constant. Because the energy of a photons in Joules is extremely low, we usually use the electron volt as a unit.

Definition: Electronvolt

An electronvolt corresponds to the energy gained by a resting electron of charge $e = 1.6 \times 10^{-19} C$ when an electric potential of 1 V is applied in vacuum.
$1eV = 1.6 \times 10^{-19} J$.

The photon energy will determine how it interacts with matter. Figure 1.3 outlines the wavelength and energies of electromagnetic waves and some examples of the everyday life objects emitting them. X-rays are amongst the most energetic particles known, far more energetic than the visible light and radio waves. It is thanks to this very high energy that they are able to go through matter, without being stopped. X-ray energies vary approximately from 0.1 keV to a few MeV but is limited to about 120 keV in medical imaging. They can be divided into two categories: soft x-rays from 0.1 to 10 keV that are used for diffraction studies of very thin samples and hard x-rays from 10 to 120 keV that are used for imaging thick samples.

Now that we have defined our radiation, lets see how they interact with matter and how we can use them to retrieve information about a complex sample.

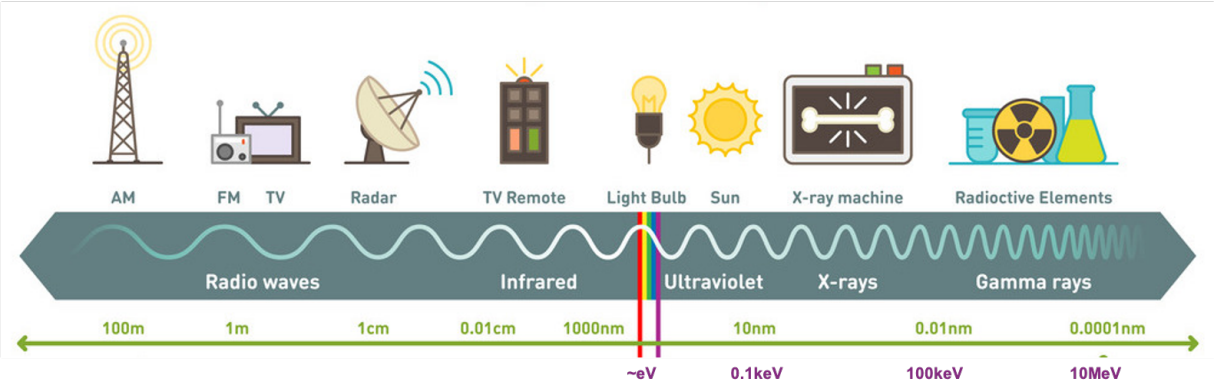

Figure 1.3: Schematic of radiations wavelength and energy associated to technological applications. (From https://www.embibe.com/exams/x-rays/)

X-ray interactions with matter

When an x-ray photon enters a material, it will come across a very large number of atoms constituting that material. Then, as represented in Figure 1.4, five main interactions can occur.

A. The photon does not interact with the atom nucleus or electronic cloud and is transmitted unaffected through the atom.
B. There is a photoelectric absorption of the photon upon collision with an electron from the atom inner-shell. It can only happen if the photon energy is higher than the binding energy of the electron. This electron is then ejected from the atom with a kinetic energy corresponding to the difference between the photon energy and the binding energy. This event induces the descent of one of the electrons from an upper shell to the vacant place with the emission of a photon with a characteristic energy corresponding to the difference in binding energy between the shells. This energy is a characteristic of the atom.
C. Rayleigh scattering: the photon collides with an outer shell electron and is scattered elastically without any loss of energy.
D. The photon collides with an outer shell electron and is also scattered but inelastically with a loss of energy transmitted to the electron as it recoils. This is called Compton scattering.
E. The final phenomenon is pair production. This happens when the photons gets close enough to the nucleus and interacts with its very strong electric field. It then changes state and creates an electron-positron pair. For this to happen, the incident photon must have been at least 1022 keV as creating the mass of the electron and positron requires 511 keV each. This phenomenon induces a cascading second one which is the rapid annihilation of the positron with another electron in the medium producing in turn two photons of 511 keV emitted in opposite directions.

All those events can be quantified by their probability of interaction referred to as cross sections. They contribute to the linear attenuation coefficient μ depending on the energy of the radiation E and the atomic number Z of the material as described in Table 1.1 [27]. m_e is the electron mass.

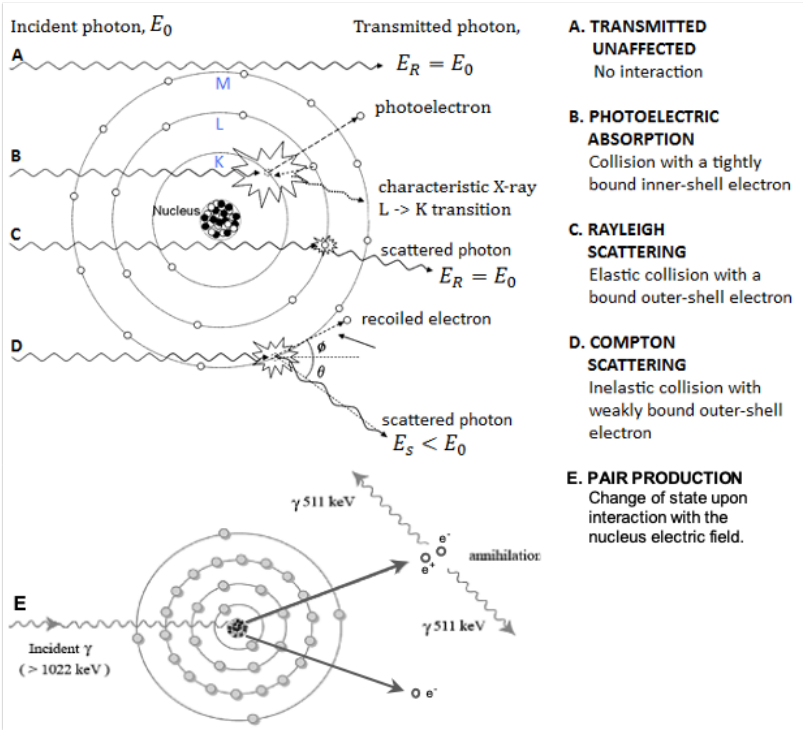

Figure 1.4: Interactions of x-rays with matter, schematic. (Figure adapted from O'Hea [26]).

Table 1.1: Interactions cross sections [27]

Interactions	Dependencies
Photoelec	$\sigma_{ph} \propto \frac{Z^5}{E^{3.5}}$
Compton	$\sigma_c \propto \frac{Zm_e.c^2}{E+m_e.c^2}$
Rayleigh	$\sigma_r \propto \frac{Z^2}{E^2}$

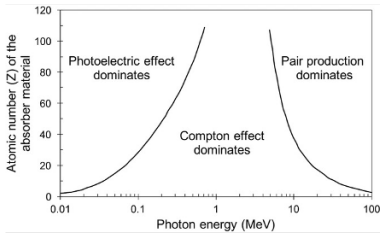

Figure 1.5: Interactions predominance depending on material atomic number and photons energy.

Figure 1.5 shows the predominance of the different interactions for a range of energies and varying atomic numbers. At the energies used in x-ray medical imaging (<120 keV) the pair production is extremely rare and the photoelectric effect and Compton scattering are the major reasons for attenuation of the x-ray beam.
The linear attenuation coefficient is used to describe the decrease of intensity of an x-ray beam after a sample by the Beer-Lambert law:

$$I = I_0 e^{-\int_z \mu(z)dz} \tag{1.1}$$

where I_0 is the incident beam intensity and μ is the linear attenuation coefficient. The attenuation is integrated over the thickness of the material penetrated in the direction of propagation z.

1.2.2 X-ray imaging set-ups

In the case of an x-ray imaging experiment an x-ray source illuminates a sample and a detector captures the remaining intensity after interactions within the sample and propagation to the detector. In this section, those elements will be described considering different experimental conditions from the synchrotron to the clinical device and how their characteristics differ. Those differences will constitute the main challenges in transferring the technique from the synchrotron to the hospital.

X-ray sources

Since the discovery of x-rays in the late 19th century, several types of x-ray sources have been created with various characteristics. This introduction to x-ray sources will focus mainly on conventional x-ray tubes and

synchrotron sources but other types of sources will be discussed at the end of this subsection.

Synchrotron sources

In 1947, synchrotron radiation was first discovered in a particle accelerator at General Electric in the US. It caused a loss of energy of the particles which was in their case an annoying phenomenon. It is only during the 60s that it was realized that this loss of energy was actually producing x-ray with astonishing properties compared to standard x-ray tubes.

Figure 1.6: Photography of the scientists from General Electric synchrotron around the vacuum chamber in 1947 (photo courtesy of NSLS, Brookhaven).

There exists synchrotrons with various characteristics and specifications in the world but their main principle remains the same. First, electrons are accelerated as close as possible to the speed of light in vacuum. The trajectory of each relativistic electron of very high energy is bent by magnetic fields (Lorentz force) resulting in the emission of light, tangential to the electron trajectory, in an extremely fine beam. This emitted light usually ranging from infrared to hard x-rays are then used in beamline experimental hutches to study material structure, arrangements, state and image samples down to the nanoscopic scale. Their range of applications is extremely wide: from material sciences to structural biology, through electro-chemistry and archaeology, and, of course, medicine and health.

The principal components of a synchrotron are displayed in Figure 1.7. First, electrons are emitted from an electron gun and accelerated by magnets in the linear accelerator. Then they are introduced in the booster ring which keeps accelerating them (up to 6 GeV at the European Synchrotron Radiation Facility (ESRF)). Finally, they are injected into the storage ring where they will encounter different types of devices that will very slightly deflect the bunches of electrons, decreasing slightly their energy resulting in the emission of light at different wavelength.
Among the devices the electrons encounter, the simple bending magnets deflect slightly their trajectory only in one direction leading them in the circular pattern instead of letting them go in straight line. This deviation produces a first kind of light beam with a large frequency bandwidth and a wide opening angle.
Another device that they can encounter is an undulator. This one, composed of magnets with an alternating polarization will make the electrons oscillate slightly at a certain frequency which will produce a radiation with a narrow bandwidth.
The light produced then usually enters a room with various optics: monochromator crystals to narrow further the bandwidth, focusing optics or various kinds of filters. Finally, the beam reaches the experimental hutch where it will encounter the sample to characterize.

The synchrotron experiment results presented in this thesis were done at the ESRF, the European Synchrotron in Grenoble and mainly at the ID17 medical beamline.
The ESRF project that was born in the 80s and is today the most brilliant x-ray source in the world as it has been recently upgraded to an extremely brilliant source (EBS) being the first high-energy fourth-generation synchrotron, with x-ray production performances increased by a factor 100. Its storage ring has a circumference of 844 m and it has 44 experimental beamlines.

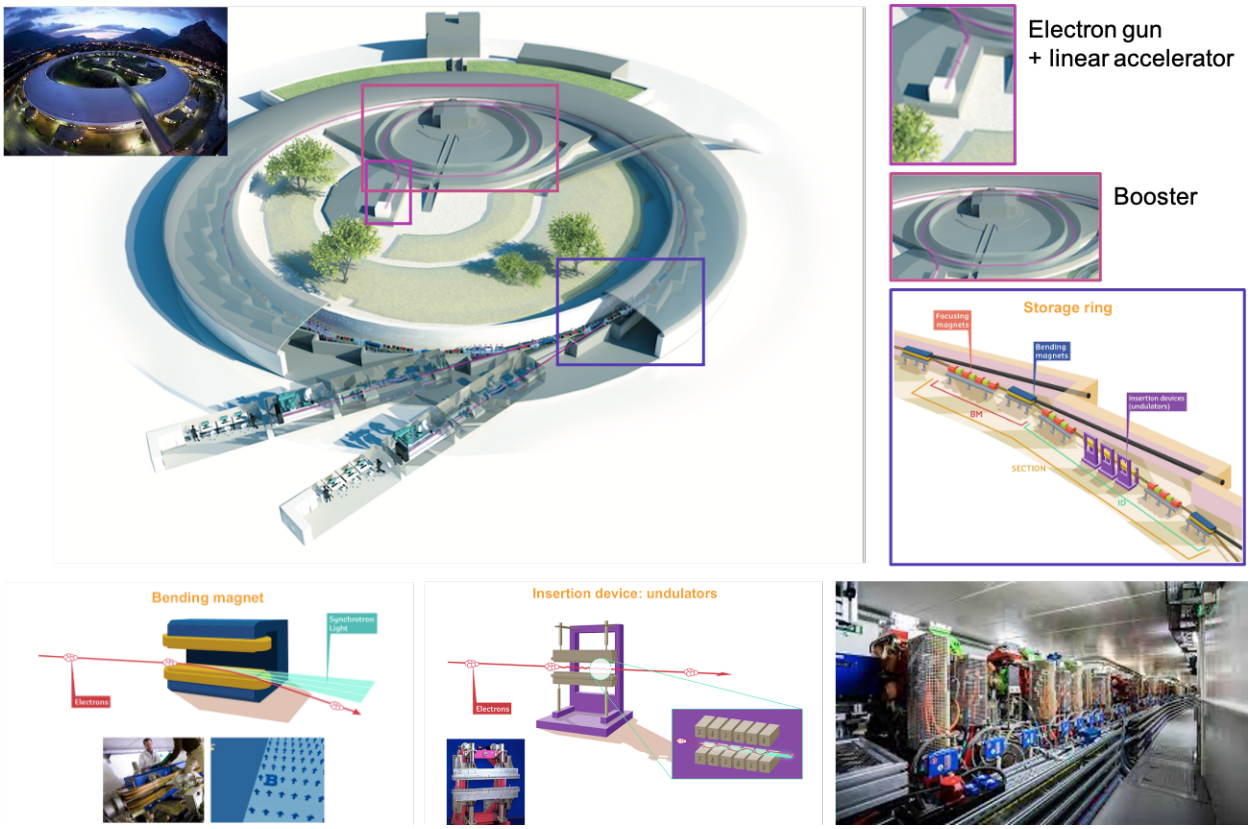

Figure 1.7: Synchrotron source and its different parts. (Adapted from https://www.esrf.fr/)

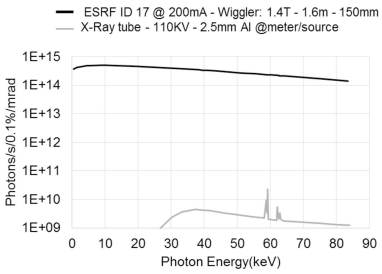

Figure 1.8: ID17 beamline x-ray available spectrum in comparison to a conventional x-ray tube spectrum 110 kVp. From [28].

One of the most interesting properties of the synchrotron beam on a beamline as ID17 is its very high photon flux up to 5 orders of magnitude greater than a x-ray tube as shown Figure 1.11. This great flux allows to use a monochromator to get a temporally coherent beam (i.e. a very narrow energy bandwidth) whilst still having a flux high enough for fast imaging.

Definition: Longitudinal temporal coherence length

The longitudinal temporal coherence length defines the distance at which a polychromatic wavefield no longer presents interference fringes due to the desynchronization of the phase of waves at different energies. It can be written:

$$l_t = \frac{\langle \lambda \rangle^2}{\Delta \lambda} \tag{1.2}$$

where $\langle \lambda \rangle$ is the average wavelength and $\Delta \lambda$ is the wavelength bandwidth[29].

The second major advantage of the synchrotron beam is that the x-ray emission spot is very focused (about 60 μm) and so very distant from the sample (140 m from emitting point to imaging hutch for ID17) that it appears almost point-like. Thanks to this configuration, it provides a beam with a very high spatial coherence.

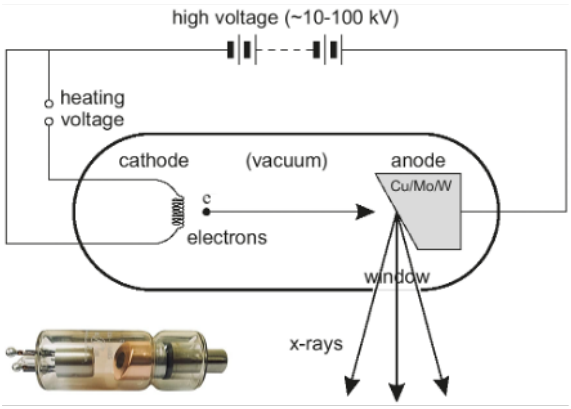

Figure 1.9: X-ray tube schematic.

Definition: Transverse spatial coherence length

The transverse spatial coherence length defines the maximum distance between two transverse points where the wavefield is still strongly correlated. In other words, if there is a sample in the path of the beam, it is the maximum distance between two points of this sample that can induce a coherent interference. It can be written:

$$l_{\perp} = \lambda \frac{z_0}{s} \tag{1.3}$$

where λ is the wavelength, z_0 is the distance from the source to the plane where the coherence is considered (sample plane) and s is the source size [29]. This definition is often used to describe the degree of spatial coherence of an imaging system and sometimes used as a criterion to determine the possible visibility of the edge enhancement phase effect [30–32]. This coherence length can also be related to the system resolution to discuss the visibility of phase effect [33].

Remark: in the manuscript, when not specified otherwise, the term 'resolution' refers to the *spatial* resolution.

Despite those extremely interesting features, medical imaging (which is the final goal of the project) at a synchrotron facility presents some major drawbacks:

- The instrument cannot be accessible in a clinical routine. If we did not mention the tremendous space required to install a synchrotron, the cost is more than enough to make it inaccessible to clinics.
- Performing tomography of a patient is extremely difficult because the source can obviously not turn around the patient as it is the case in clinical CT.

Conventional x-ray tube

X-ray tubes are constituted of an anode and a cathode in a vacuum chamber as represented in Figure 1.9. When a potential is applied between the two electrodes, electrons are going to escape the heated cathode and, after a brief acceleration in the electric field in vacuum, hit the anode. When accelerated by an electric potential, the kinetic energy gained by the electron is $E = e.V$ with e the elementary charge and V the potential applied between the electrodes. It means that if we apply a potential of 100 kV (or kVp for kilovolt peak) the kinetic energy of the electrons accumulated when it hits the anode is 100 keV. It also means that when

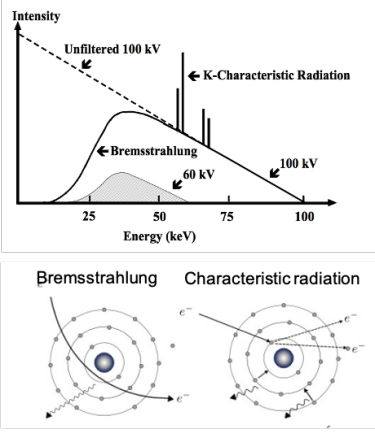

Figure 1.10: X-ray tube spectrum and schematic of the involved physical interactions.

being stopped in the anode, it will deposit 100 keV. The cooling of the system is then of a particular importance.

This energy deposition can happen in two ways that are sketched in Figure 1.10. The electron can collide with an electron of one of the inner shells of the atom and knock it away, giving it part of its energy. This will leave a vacancy in the shell that will be filled by an electron of lower binding energy (situated in an upper shell). When doing so, the electron will lose the energy corresponding to the difference in binding energy between the two shells and it will emit a photon at a specific energy. This is called X-ray fluorescence and the emission is called the characteristic radiation. It can happen between different shells of the atom with certain different energies. They appear on the source emission spectrum as high peaks at those specific energies.
The second interaction is a deviation of the electron by the magnetic field of the nucleus. This deflection is associated with a loss of kinetic energy which is released as Bremsstrahlung radiation. The photons emitted this way can have various energies depending on the strength of the interaction with the nucleus and can range up to the maximum of the electron kinetic energy. Therefore when the voltage is 100 kVp, the electrons have a kinetic energy of 100 keV and the emitted spectrum ranges up to 100 keV. Obviously, the electron can interact with several atoms of the anode and lose its energy through multiple emissions before being completely stopped. In the end, the emitted spectrum does not comprise very low energies as they are reabsorbed in the anode before having a chance to leave it.

The vacuum chamber is contained in a lead shielded casing with just an opening window in the main emission direction to avoid radiation escaping in every directions.

The flux of electrons emitted from the cathode is regulated by the current going through the device. The greater the electron flux, the greater the flux of photons emitted. However, the collisions of the electrons in the anode also produce a lot of heat which will limit the flux that can be generated by the tube without deteriorating the anode. In order to increase that flux limit, rotating anodes were invented, letting the electrons focal spot move along the anode and limiting the heat accumulation in one spot.

This kind of source is polychromatic because it emits overs a wide range of energies. The focal spot size can vary from a few micrometers in micro-focus sources to several hundreds of microns in clinical devices. Their main advantage is that they are very compact and very cheap compared to other kinds of sources.

Other recent sources

Recently, to overcome the lack of spatial coherence of x-ray tubes and the drawbacks of synchrotron sources, other alternatives have been developed (see Figure 1.11).

First to overcome the limitation of flux due to overheating of the anode, a new type x-ray tube was invented using liquid metal jet as the anode [34]. This reduces a lot the heat overload in a very small device with a very focused emitting spot. This source remains a lot more expensive than the simple x-ray tube and requires to be kept in a vertical position

for the flow to work correctly making it difficult to use for tomography of patients.

Other projects such as the Cala project in Munich or ThomX in Paris tend to recreate synchrotron radiation but in smaller devices to fit them in big rooms, similar to the size of radiotherapy facility found at hospitals, and make them more accessible. Those project are still too expensive for clinical routine and not accessible for rotational gantries.

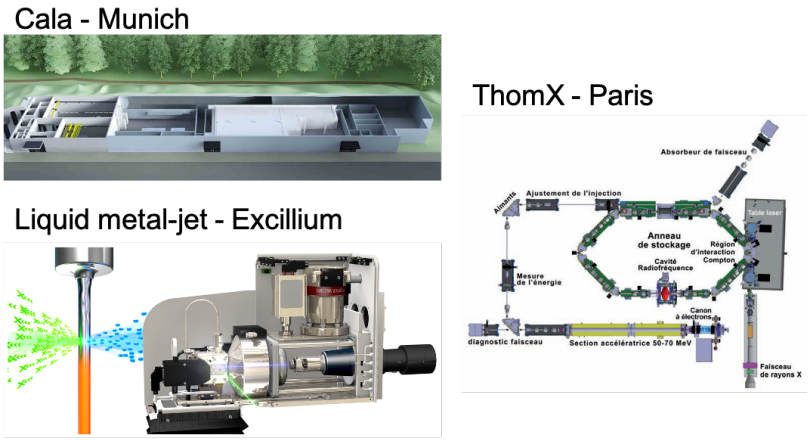

Figure 1.11: Examples of recent x-ray sources and projects.

The two types of source that are considered in this work are synchrotrons and x-ray tubes as the other ones are still too expensive and impractical for patient tomography. As mentioned, x-ray tubes are the ones used in clinical devices while phase contrast imaging was developed with high performance synchrotron sources. Adapting the method to x-ray tube means working with a lower flux, a polychromatic beam and a bigger source size which will introduce many difficulties as will be shown in later sections.

Detectors and image formation

Once the beam has been emitted and has travelled all the way through various optical elements and the sample of interest, its intensity is collected by a detector. Today, a detector is composed of a 2D array of microscopic pixels that translate the local radiation intensity into an electrical signal which will in turn be reconstituted into an image on our computer screen.

Figure 1.12: Example of old radiograph films.

The first type of x-ray detector ever invented, long before the invention of computers, was a detector film [3] (see Figure 1.12). It has the advantage of having high sensitivity, high resolution, low cost and can both record and store information. The drawbacks of such detectors are that their response is not linear with the energy deposited, their need to be digitized for further processing, the degradation of the films with time and their inability to differentiate energies.

Later, digital pixelated detectors were invented. Today, there are two main types of digital detectors as displayed in Figure 1.13: direct counting detectors that count photons individually, and integrating detectors that accumulate a signal as a function of the energy deposited in a scintillator screen during an integration period.

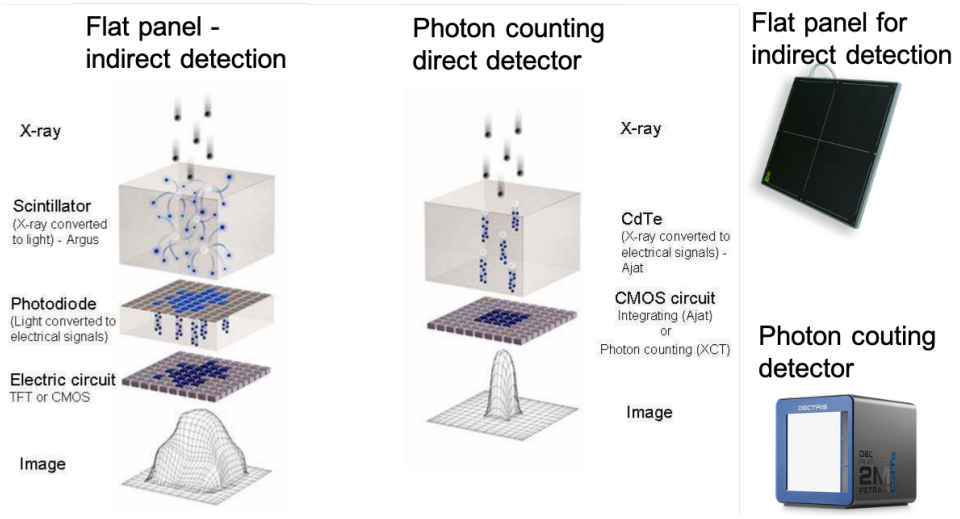

Figure 1.13: X-ray direct vs indirect detector.

The latter ones, indirect detectors, are composed of a scintillator screen that converts the received x-rays into photons of energy in the visible light spectrum through a luminescence mechanism. Those visible photons are in turn captured by other elements that will translate the signal to an electrical one.
Some very popular devices to do so are charge coupled devices (CCDs). They are two dimensional arrays in which pixels accumulate electric charge linearly with the amount of photon energy received. The advantages of such detectors are that they have a small pixel size, they give direct digital data, and they have an excellent linearity.
A more recent type that is a little similar to the previous one is CMOS detector. The charge accumulation principle is similar to that of CCD detectors but a semi-conductor is added in each pixel to translate the charge accumulation into a voltage [35]. The advantage of indirect detectors is that they can have very small pixels (down to a few microns) but the conversion process in the scintillator induces a loss of precision of the position where the incident photon arrived as the re-emitted photons are spreading in the material before reaching the conversion part of the chip (see sketch in Figure 1.13). This loss of precision is defined by the point spread function which is defined as the full width half maximum of the measured signal in response to a punctual received signal. It is usually associated to a Gaussian shape. In practice, this point spread function (PSF) induces a slight blur of the detected image.

Photon counting detectors are based on the conversion of each received photon into an individual electric signal. This conversion happens in a pixelated sensor layer usually made of CdTe, GaAs or Si, doped semiconductor, in which the received photons create electron-holes pairs. The electrons are then accumulated before being translated into a current, directly proportional to the number of photons integrated, at the end of the exposure time. These detectors have almost no loss in position precision of the detected photon, we consider that their PSF is 1.

X-ray detectors are usually made for a certain range of energy partly defined by the layer receiving x-rays. Indeed, in order to stop high energies, this layer needs to be thick enough but, the thicker it, is the

more the converted signal drifts before being converted into electric signal and the more it degrades the spatial precision.

In this part, the source and detector features were introduced, mentioning the source flux and the detector integration of photons. What role will those parameters play in image formation? And what are the sources of noise that can degrade our image?

Sources of noise

There are two main sources of noise in x-ray images:

1. One is the electric noise inherent to the detector. This electric noise can be seen and partially corrected by taking an image "in the dark" without any beam which gives an image containing only the electric noise. This noise is usually small and will not be the prevailing source of degradation of the image.

2. The second main source of noise is the shot noise due to the statistical nature of the event "the pixel receives N photons". What does this mean? The intensity received in a pixel is a random phenomenon. Let's assume a homogeneous illumination. On average, each pixel of the detector receives N photons in t seconds. However it is like counting drops falling in a bucket under the rain. Some pixels will actually get N+1 photons others N-2, others N+5 as illustrated in Figure 1.14.
   This number N is not an absolute truth. It is common to associate this phenomenon to a Poisson distribution (see Figure 1.15). In this distribution the standard deviation is equal to the square root of the mean value. This standard deviation (the amount of variation from the average value) corresponds to noise in the image. In Figure 1.15, there is an example of an imaging formation with an increasing number of photons. With very few photons, the image looks very noisy because the local distribution is very dispersed. A common way to quantify the image quality is to use the signal to noise ratio (SNR). The higher the SNR, the better the image quality. In the poisson distribution this SNR can be easily estimated as: $SNR = N/\sqrt{N} = \sqrt{N}$. In the end, this means that the image quality increases with the number of photons. Hence the importance of the photons flux and the capacity of the detector to integrate a large number of them.

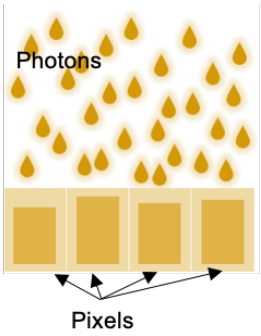

Figure 1.14: Schematic of photons as rain being collected into pixels 'buckets'.

Different kinds of sources and detectors are used for different kinds of imaging techniques depending on the sample to analyze, the scale that we seek and the constraints associated with the sample.

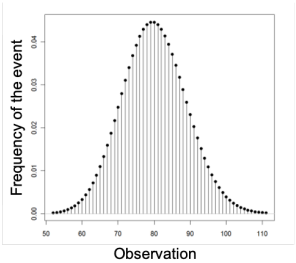

Figure 1.15: Poisson distribution and shot noise.

Different kinds of set ups for various applications

In this section, we will discuss three different kinds of imaging set ups: a synchrotron set-up, laboratory set-ups and clinical devices and the characteristics of the images they produce.

Synchrotron set-up

The main characteristics of a synchrotron have already been described in the previous section. We know that it has the advantage of being a highly coherent source producing a very high flux. The imaging applications of synchrotrons are mainly focused on obtaining very high resolution images. Due to that very high flux, it is possible to use very small pixels while still having enough statistics. This very high resolution however comes at the price of a limited field of view. The smaller the pixels the larger their number needs to be to expand the field of view. However, there are two main drawbacks to that expansion, the more pixels the detector has, the more expensive it gets and the larger the data volume collected will be.
It is worth mentioning here that working with high resolution images comes with the issues of storing them and manipulating them. The ESRF has a huge storing center and yet the amount of data produced each year reaches the limits of available storing volume. The ESRF is also equipped with a very powerful computational center that is necessary to treat the amount of data generated that would overload common computers.

Regarding medical imaging at the ESRF, two main kinds of experiment are conducted: very high resolution virtual histology and anatomical *in-vivo* or *post-mortem* imaging.
For virtual histology we can reach a resolution of a few tens of nanometers. In that case, low energy x-rays are used to obtain a contrast in very thin samples. *Post-mortem* and *in-vivo* experiment can be performed on animals or human anatomic pieces at various resolutions ranging from a few microns to several tens of microns to study the evolution or visible features of pathologies.
Often, those experiments are performed in tomography, which means acquiring series of images while rotating the sample which allows to obtain information in a 3D volume.
One last particularity of the synchrotron is that, because the source is placed so far away from the sample and detector, we can consider that the beam traversing the sample is parallel and that there is no magnification as represented on the top scheme of Figure 1.16.

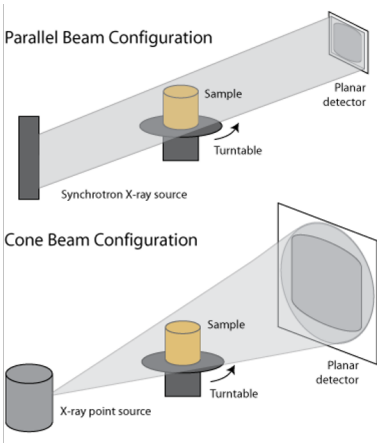

Figure 1.16: Representation of a parallel beam and a cone beam (adapted from https://serc.carleton.edu/18399)

Laboratory micro-CT

Micro-CT are laboratory x-ray imaging equipment usually used to obtain high resolution images of small samples. This high resolution being of several microns to several tens of microns: lower than what can be achieved at the synchrotron but higher than what is used in clinical set-ups. Those set-ups usually use x-ray tubes (micro/nano-focus or not) and therefore are polychromatic and have a lower spatial coherence and a flux three to five orders of magnitude smaller than a synchrotron. They use detectors with a pixel size of 50 to 100 microns but make use of the magnification to obtain a high resolution in the sample (Figure 1.16), contrary to synchrotrons where the parallel beam implies that the final resolution of the image is the one of the detector.
These set-ups are used for material science or medical studies on small animals. Their mean energy and voltage depend on the studied material but it usually ranges between 30 kVp for low absorbing materials and 100 kVp for heavy materials and can even go up to 300 kVp for some materials.

Definition: Magnification

Image enlargement upon propagation of a cone beam defined as the ratio of the distance source to detector over the distance source to sample.

$$M = \frac{distance\_source\_to\_detector}{distance\_source\_to\_sample}. \tag{1.4}$$

Clinical set-ups

Clinical x-ray devices are also diverse depending on the body part to image and the contrast to obtain. For simple 2D projection imaging the source simply illuminates the body part that is placed in front of the detector as shown in Figure 1.17. For a CT scanner, the source and the detector are placed in a rotational gantry that will turn around the patient during the acquisition (contrary to the previous cases where the sources were fixed and the sample was rotated).

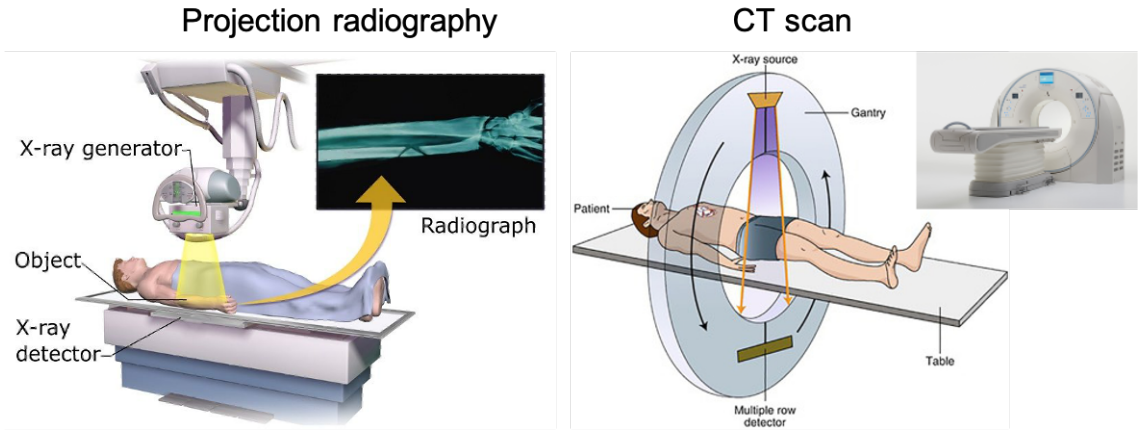

Figure 1.17: Two types of clinical devices: a simple radiography machine (2D imaging) and a CT scan with a rotational gantry (3D imaging). (Images from https://en.wikipedia.org/wiki/X-ray_machine and Garnett [36])

The source voltage for a CT and radiographs of bone structure is usually about 100 kVp (average:50 keV). For imaging soft tissue such as breasts in mammography, the energy is much lower: about 30 kVp (average: 15 keV). These energies are chosen to optimize the contrast, the statistics and the dose delivered by controlled protocols.
The achievable resolution in medical imaging is driven by new parameters related to the dose and the acquisition time.

Definition: Dose

The absorbed dose is the amount of energy deposited by the radiation in the sample.

$$D = \Phi E \mu_{en}/\rho \tag{1.5}$$

with Φ the fluence $[photons/m^2]$, E the energy and μ_{en}/ρ the mass energy absorption coefficient.
The dose is expressed in Gray (Gy) which is an energy (in Joules) per mass unit (in kg).

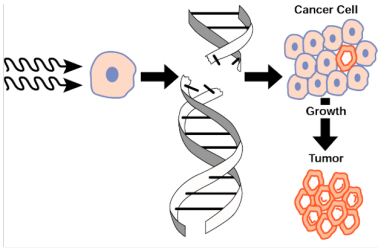

Figure 1.18: Process from DNA damage to cancer. (image from https://serc.carleton.edu/)

X-rays are a ionizing radiation which means that they have the power to break molecules bonds such as DNA bonds. When that happens, the cell either dies, repairs the DNA or incorrectly repairs the DNA leading to a mutation that can turn the cell into a cancer cell (see Figure 1.18).

The more radiation the cells receive, the more chance there is that one of them that turns into a cancerous cell.
Therefore, limiting the dose to the minimum amount possible is very important in x-ray imaging. However, as discussed in the previous section, the lower the number of photons per pixel, the lower the image quality. The consequence is that the size of the pixel used cannot be as small as in other applications if we want to limit the amount of radiation deposited in the patient tissues while still having enough signal in each pixel (i.e. if the rain is lighter you need a bigger bucket to get as much water as under heavy rain).

Another limitation related to imaging a patient is that we need a fast acquisition. We want the acquisition to be sufficiently fast for the sample not to move during the integration of an image. We also want this acquisition to be very fast in tomography if we want to acquire the thousands of images required for volume reconstruction in a reasonable amount of time. Doing so requires two things: a source that can emit a sufficient x-ray flux (number of photons per surface per second) and a detector capable of integrating images quickly. The main inconvenience to having a source that emits such a flux is that it will have a big emitting spot that blurs the image and also limits the achievable resolution as represented in Figure 1.19. A large spot size means that the rays passing through each point of the sample arrive from various incident angles and will therefore hit the detector on a spread area. This area is what we will call the projected source. This projected size S_p depend on the source spot size S_s, the distances between the source, the sample and the detector:

$$S_p = S_s \frac{distance\_sample\_detector}{distance\_source\_sample} \tag{1.6}$$

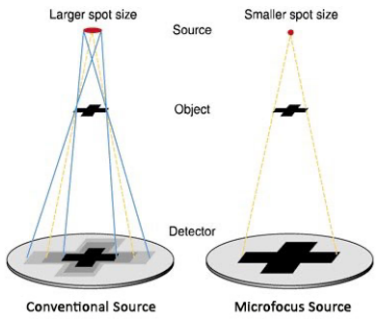

Figure 1.19: Influence of spot size on the projected image. (from https://www.axt.com.au/)

Also, as defined earlier, the bigger the source, the smaller the spatial coherence length.

To conclude, we have seen 3 types of set-ups:

1. Synchrotron set-ups that can give a highly coherent monochromatic beam with a high flux which allows to do high resolution imaging with a low noise.
2. Laboratories micro-CT that have polychromatic sources of various sizes allowing to get a fairly high resolution.
3. Clinical set-ups that usually have big polychromatic sources to get fast acquisitions. They have a very limited resolution related to the need to keep a low dose but high SNR.

The direct transfer of a technique from the first to the third would mean varying greatly almost all parameters. In order to achieve it at some point, a first transfer to laboratory set-ups is necessary as an intermediary step. The current work focuses on this first step, keeping the final objective in mind to choose coherent parameters for the final transfer.

1.2.3 Computed tomography

Before finally entering the technical details of phase contrast imaging, a last principle of conventional x-ray imaging needs to be introduced: computed tomography.

Unlike simple projection acquisition that gives a 2D image where the information about the interior of the sample are integrated on the propagation direction, Computed Tomography (CT) is an imaging procedure that allows to retrieve a 3D volume information about a sample.

The principle of x-ray tomography, summed up Figure 1.20, is that the sample is placed between the source and detector and a set of acquisitions is obtained with a varying orientation of the sample by either rotating it on its axis or by rotating the source and detector around it. From the projection images obtained, sinograms are extracted by combining the same line of pixels over all the orientations of the acquisition. We obtain as many sinograms as there are pixels parallel to the axis of rotation of the acquisition. Then from each sinogram, a slice is reconstructed, recreating the 3D volume when all the sinograms have been processed.

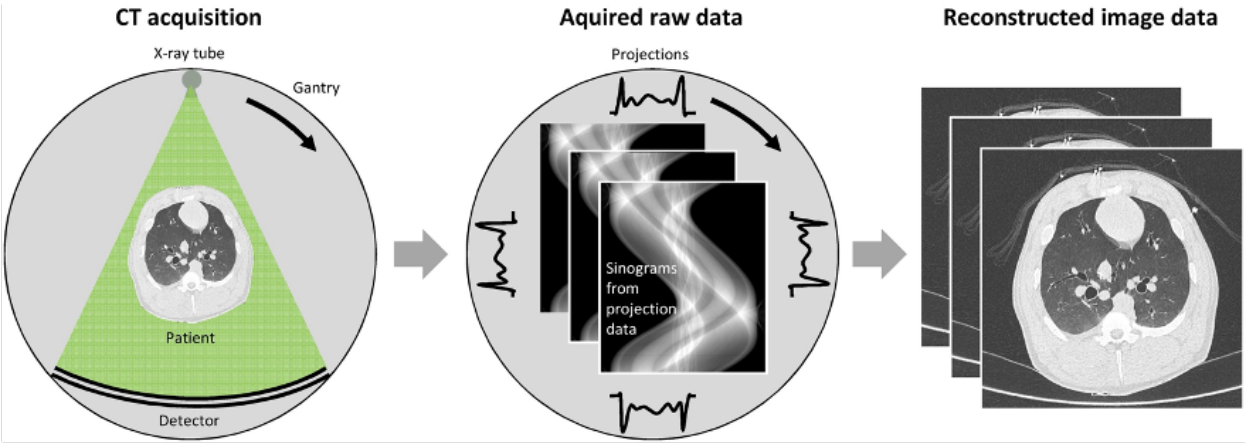

Figure 1.20: Outline of tomographic global process. (Image from Stiller [37]).

The reconstruction process from the sinogram to the slice is sketched in Figure 1.21. The first step is to make use of the Fourier slice projection theorem which states that the Fourier transform of a projection along one direction is equivalent to one line of the 2D Fourier transform of the slice crossing the frequency origin and in the same orientation as the projection. It means that by taking the Fourier transform of each line of the sinogram we can fill the Fourier space with the corresponding rotating lines as shown in Figure 1.22.

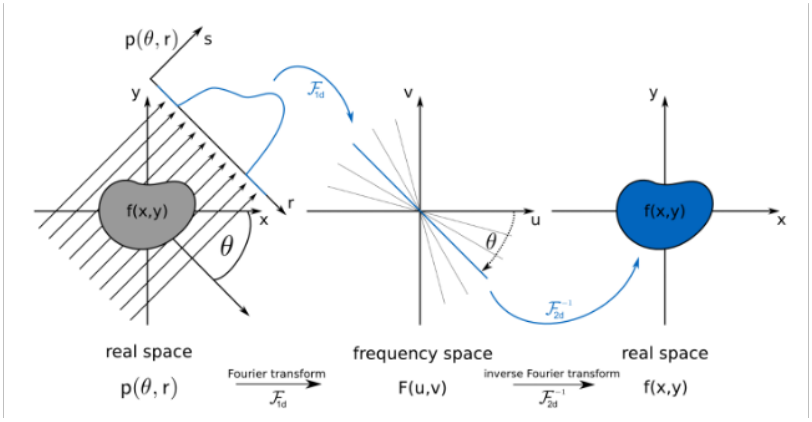

Figure 1.21: Outline of tomographic reconstruction process through slice-projection theorem and back-projection. (Figure from Department of Physics Munich School of Bioengineering Technical University of Munich X-ray Computed Tomography Advanced Lab Course No. 79)

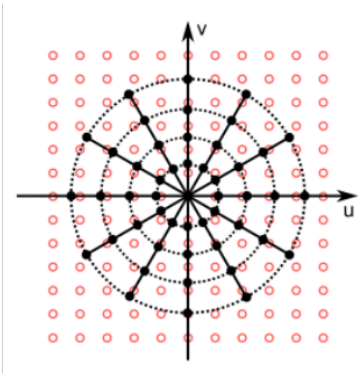

Figure 1.22: Tomography k-space representation.

As represented on that figure, it means that the information retrieved for low frequencies (close to the center of the space, to the 0 frequency) is a lot more dense than for high frequencies. When taking the inverse Fourier transform to retrieve real space information, this will give rise to low frequency artefacts. To limit those, a 2D filter is usually applied to the Fourier space image. The different kinds of filters are presented in Figure 1.23. The most 'basic' one is the Ramp filter or "Ram-Lak" filter which gives a linear filtration. However, other filters shape have proven to give a better visual quality reconstruction and might be used depending on the data and acquisition device for a better result.

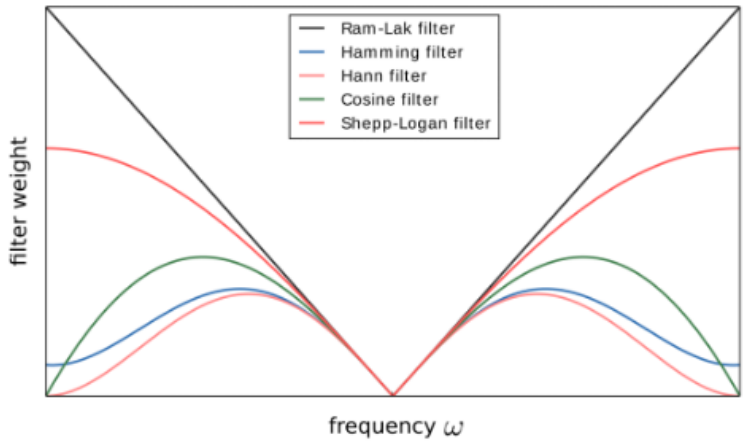

Figure 1.23: Filters used in filtered back-projection tomography.

This reconstruction process is commonly used for simple radiography projections with attenuation contrast. The reconstructed information then corresponds to the linear attenuation coefficient of the sample and is expressed in Hounsfield units $HU = 1000.(\mu - \mu_{water})/(\mu_{water})$ with the linear attenuation coefficient of water as a reference. However this process can be applied to other kinds of information obtained from sample projections like phase or dark-field images.

1.3 Phase contrast imaging

Now that we have placed phase contrast and dark-field imaging in a the clinical context, introduced the instruments and principles of

conventional radiography, we will see how to go from simple attenuation images to multi-contrast imaging, how these contrasts are associated to physical phenomena. Finally, different techniques allowing to retrieve dark-field and phase from x-ray imaging experiments will be presented.

Firstly, the main notations used in the mathematical formulas of this part are:

Notations

Variables:

- n: complex refractive index
- δ: refractive index real part decay
- β: refractive index imaginary part
- μ: linear attenuation coefficient
- α: angle of refraction
- α_{df}: average opening angle of multiple refraction
- k: wavenumber
- ϕ: phase
- z: spatial axis in the direction of propagation
- x, y : spatial coordinate perpendicular to propagation
- k_x, k_y: Fourier space coordinates (angular frequency)
- $\mathbf{f} = (f_x, f_y)$: Fourier space coordinates (frequency)
- I: intensity field
- I_r: Reference image of the optical elements without sample
- I_s: Sample image with the sample
- t : sample thickness

Operators:

- ∇: gradient operator
- $Re\{\}$: Real part
- $\mathcal{F}$: Fourier transform
- $\mathcal{F}^{-1}$: inverse Fourier transform

1.3.1 From interactions to contrast

In section 1.2.1 we have described interactions in the particle model but there is one phenomenon that is difficult to explain with particles interactions even though it is observable: refraction. Indeed, how come the particles can be locally coherently scattered in the same direction?

To understand this phenomenon we will enter the wave world and focus on the elastic Rayleigh scattering. This interaction is described in the wave model as follows: upon entering a material, the electromagnetic wave encountering scatterers (electrons) will be partly absorbed and re-emitted in all directions, superimposed with each other and with the incident wave-field. These scatterers being infinitely numerous in matter, this phenomenon is quasi-continuous and induces a slowly varying phase difference in the wave field. The importance of the phenomenon, associated to the phase shift that is induced, mainly depends on the wavelength and the electron density. This phase difference is directly proportional with the angle of refraction of the x-rays.

The interaction described above along with the attenuation are quantified altogether by the already mentioned complex refractive index: $n = 1 - \delta + i\beta$. The real part of the index is related to the phase shift and the imaginary part to the attenuation (which is connected to the attenuation coefficient through: $\mu = 2k\beta$).

Remark: what about reflection?
The reflection phenomenon that is often observed with visible light was not mentioned in this section because at x-ray energies, this phenomenon is negligible for light elements without a crystalline structure.

The information that is detected in a beam intensity is related to a number of photons hitting each pixels of the detector. It also corresponds to the amplitude of the wave arriving at the detector. In absence of any sample the beam reaching the detector is quasi-homogeneous. But, as mentioned in section 1.2, the initial beam will be altered by the presence of the sample: it is attenuated and refracted. Figure 1.24 presents 3 different kinds of contrast that are studied in multi-modal x-ray imaging associated to the different physical phenomena:

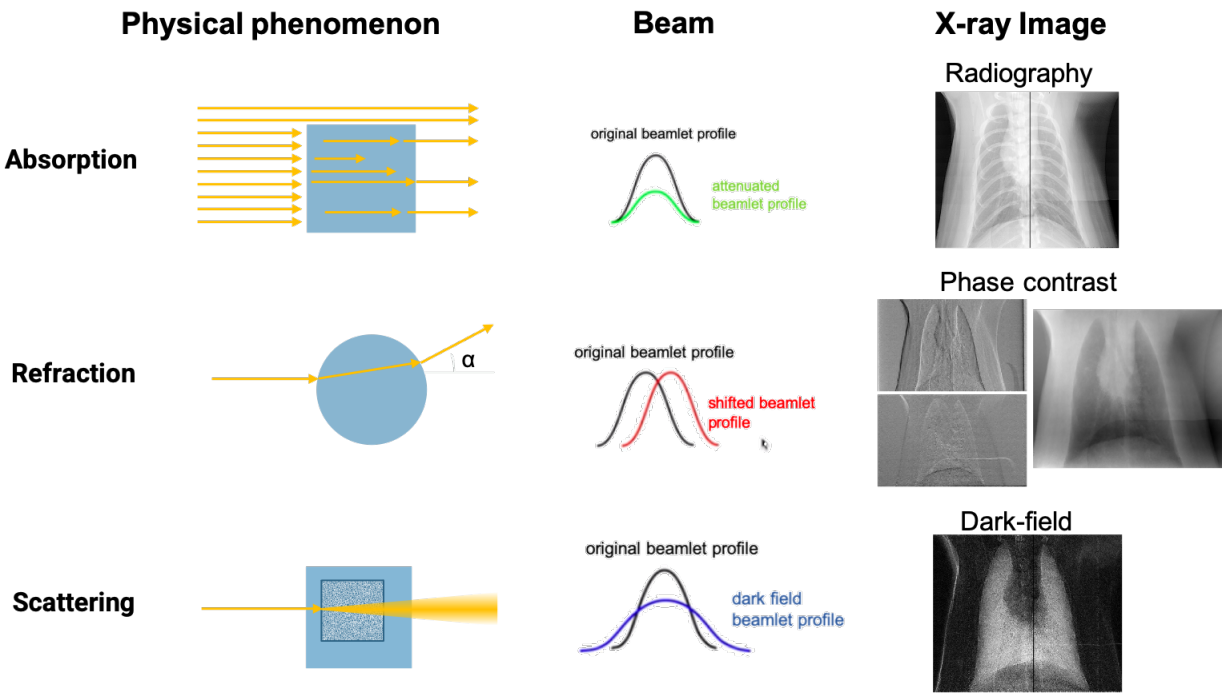

Figure 1.24: Physical phenomenon associated to different types of contrasts.

- Part of the beam will be attenuated in the sample meaning that less photons will arrive at the detector corresponding to a local decrease in intensity. This **attenuation** is quantified by the linear attenuation coefficient μ and directly related to the imaginary part β of the refractive index n. It depends both on the nature of the material and the energy of the beam. The projection radiography image conveys integrated information of all the traversed tissues. It corresponds to the conventional radiography that is used at the hospital where, the more the tissues are attenuating, the whiter they appear on the image. For example, calcium in bones absorbs X-rays the most so bone looks white.
- The beam will be locally slightly deflected at the interface between different materials. This deviation is quantified by the parameter δ, corresponding to the decay from unity of the real part of the refractive index n. This real part is the one used in classical physics

for the Snell-Descartes law which computes the deviation angle i_2 of a ray at an interface between two media of refractive index n_1 and n_2 arriving with an incident angle i_1 as presented Figure 1.25:

$$Re\{n_1\}sin(i_1) = Re\{n_2\}sin(i_2) \tag{1.7}$$

The information we actually have access to is the total **refraction angle** after the sample, i.e. the difference of direction between the incident angle and the deflected angle after the sample. This refraction angle α is proportional to the **phase difference** ϕ accumulated through the sample as translated by eq. 1.8:

$$\alpha = \frac{1}{k}\nabla\phi \tag{1.8}$$

The phase difference accumulated in the sample is connected to the refractive index of the traversed materials through the relation:

$$\phi = -k\int_z \delta(z)dz \tag{1.9}$$

Depending on the method used to retrieve the phase information, we can obtain 2 images representing the deflection angle projected in the 2 directions perpendicular to propagation. No refraction will appear in medium grey and, for vertical refraction for example the rays refracted toward the top will appear brighter and the ones towards the bottom darker (or vice-versa). The same principle applies for horizontal refraction and rays going left or right. When acquiring refraction images, or phase gradient images (as they are proportional their contrast visualization is identical) one can integrate those images to obtain the phase image. Some other methods allow to retrieve the phase Laplacian which is then integrated twice to obtain the phase image.

- The main source of the **dark-field** signal is also related to the refraction phenomenon but in the case where there are so many interfaces that, instead of resulting in a local deflection of the beam, it results in a spreading of that beam due to multiple refraction on micro-structures surfaces. When part of the sample is composed of numerous dense micro-structures that are too small to be directly observed on the image, i.e. when the structures are smaller than the resolution of the system, they still distort the image, scattering slightly the beam that is traversing them, spreading it into a very small angular opening cone. This average angle opening α_{df} is related to the number of structures N encountered by the beam and the difference in refractive indices of the particles $\delta^{(1)}$ and their environment medium $\delta^{(2)}$ by the relation [38]:

$$\alpha_{df} = 2|\delta^{(1)} - \delta^{(2)}|\sqrt{N\left(log\left(\frac{2}{|\delta^{(1)} - \delta^{(2)}|}\right) + 1\right)} \tag{1.10}$$

This signal is often associated to a loss of visibility or a local 'blurring'. This relationship between the opening angle and the induced blurring on the image will be further developed in the second chapter. It is the loss of visibility related to the multiple scattering that is usually displayed in dark-field contrast images.

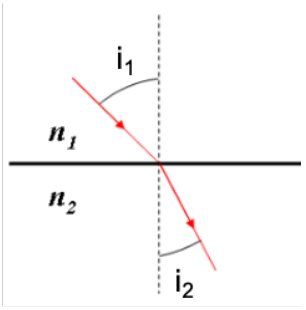

Figure 1.25: Schematic of the refraction of a ray at the interface between two media.

1.3.2 Phase contrast and dark-field imaging techniques

While attenuation is directly visible on simple acquisitions, phase and dark-field appear more as small artifacts in the images and retrieving their signal is not as straightforward. In this section, different existing techniques will be introduced with their principle, advantages and limitations and the recent progresses made toward clinical transfer. These techniques can be divided into two categories: the techniques that were developed for synchrotron use and make use of some of its core properties to work; and the more recent ones that were designed for a transfer to conventional laboratory sources, freeing themselves from synchrotron features requirements.

Early synchrotron techniques:

- Propagation-based imaging
- Analyzer-based imaging

Techniques for a transfer on conventional laboratory source:

- Grating interferometry
- Edge illumination
- Mesh-based imaging
- Modulations-based imaging

This list is not exhaustive and numerous variants exists, we introduce here the most developed and publicized ones.

Early synchrotron techniques

• Propagation based imaging and Holography

The most popular synchrotron technique today is Propagation Based Imaging (PBI). Its success is no doubt due to its very simple experimental set-up, the rapidity of the acquisition and the simple numerical phase retrieval processing.

As presented Figure 1.26, the PBI set-up only involves a source and a detector. The key features of this method are the spatial coherence of the source and the propagation distance between the sample and the detector, apart from that, the set-up is similar to one of conventional radiography.

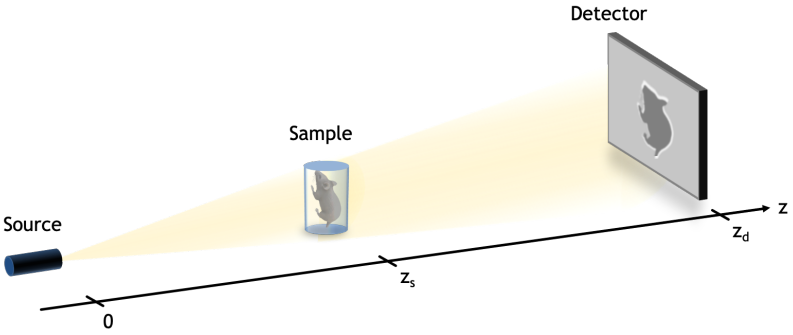

Figure 1.26: Propagation-based imaging set-up.

The principle is that, thanks to the spatial coherence of the source, upon propagation, the waves distorted in the sample will create interference patterns that are more and more prevalent as the distance between the sample and the detector increases. Those interference fringes appear as white and black lines contouring the sample, it is what we call "edge enhancement". This interference pattern, appearing as intensity variations on the acquisitions, are proportional to the phase Laplacian of the waves distorted by the sample. To retrieve the phase information, various methods have been developed and optimized around the world but the fundamental one is the so-called 'Paganin method' [39]. It is based on the Transport of Intensity Equation (TIE) in the paraxial approximation.

Definition: Paraxial approximation

The paraxial approximation states that the particles path follows a direction with only a very small deviation from the optical axis.

When a wavefield of intensity I and phase ϕ propagates along an axis z, the TIE describes its evolution:

$$-k\frac{\partial I(x,y)}{\partial z} = \nabla_\perp \cdot [I(x,y)\nabla\phi(x,y)] \tag{1.11}$$

x and y are the spatial coordinates in the plane perpendicular to the propagation axis z. An extensive development of this equation including derivation of the equation and its use with different approaches can be found in the very well written review by Zuo et al. [40].
The resolution of this equation to extract the phase information proposed in [39] assumes a single material sample. This approximation allows to assume a constant δ and β to solve the equation from only one acquisition. This assumption implies that the phase is proportional to the thickness t as Equation 1.9 is simplified to: $\phi = \delta t$. The equation to extract the thickness from the TIE then becomes:

$$t(x,y) = -\frac{1}{\mu} log\left(\mathcal{F}^{-1}\left\{\frac{\mathcal{F}\{I_s(x,y)/I_r(x,y)\}}{1-(z_2\delta/\mu)(k_x^2+k_y^2)}\right\}\right) \tag{1.12}$$

Where I_s is the sample image acquired with the sample and I_r is the reference image corresponding here to the white field without the sample, used for normalization.

Because of the strong single material hypothesis, the retrieved image does not give a quantitative measurement, however, it still gives a very good contrast between various materials.

In order to get free from this assumption and get quantitative results, a variant of this method was invented with several propagation distances z (between the sample and the detector as shown in Figure 1.27) and based on the Contrast Transfer Function (CTF) [41]:

$$\phi(x,y) = \frac{1}{I_r}\mathcal{F}^{-1}\left\{\frac{\sum_z \left[I_s^{(z)} - I_r - G^{(z)}(\mathbf{f})\mathcal{F}\left\{\nabla_\perp(\phi(x,y)\nabla_\perp I_r)\right\}\right] H^{(z)}(\mathbf{f})}{\sum_z \left(H^{(z)}(\mathbf{f})\right)^2}\right\} \tag{1.13}$$

Where $\mathbf{f} = (f_x, f_y)$ is the Fourier space vector [2], $G^{(z)}(f) = \frac{\lambda z}{2\pi} cos(\pi\lambda z f^2)$ and $H^{(z)}(f) = 2sin(\pi\lambda z f^2)$. In this method, the equation is solved iteratively, neglecting the term containing the phase for initialization.

2: The variables used in Fourier space are sometimes the frequency noted **f** or **u** or the angular frequency **k**=2π**f**. As much as we try to harmonize the notations, it was chosen to keep the original article notations when possible.

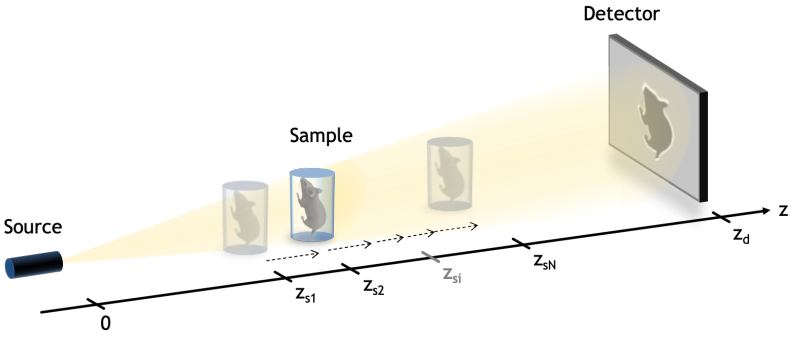

Figure 1.27: Holography imaging set-up. A coherent beam traverses the sample and propagates a certain distance before reaching the detector. Interference fringes due to wave perturbation in the sample appear on the detector plane and vary according to the distance of propagation. Several images with various distances of propagation or only one position can be taken.

Due to the high spatial coherence requirement, the transfer of this technique to other sources than synchrotron was mainly limited to high resolution imaging [42] using mostly liquid metal jet X-ray sources [43]. Imaging of patients can possibly be done with high energy compact source such as the thomX project [44]. Nevertheless the cost of such source, and the fact that patients would have to be rotated for 3D imaging will limit the PBI spread.
Moreover, PBI is sensitive to the phase Laplacian that introduces reconstruction artifacts when imaging materials presenting a slowly varying density and low spatial frequencies [7].
Finally, retrieving dark-field from PBI images just started to be investigated and appears to be limited to observing its effect at the edges of the sample [45, 46].

- **Analyzer based imaging**

The first phase gradient sensitive technique in history, Analyzer Based Imaging (ABI), also known as diffraction enhanced imaging, is based on highly selective analyzer crystals.
Its experimental configuration consists of a monochromator upstream of the sample and an analyzer crystal positioned according to the Bragg geometry between the sample and the detector, as shown in Figure 1.28

This analyzer crystal acts as an angular filter for the radiation coming from the sample. When the x-rays are refracted by an object, the angle of incidence on the analyzer crystal is changed. When the x-rays reach the analyzer crystal, the Bragg diffraction condition is satisfied only for a small range of angles. Thus, when the scattered or refracted rays have incident angles outside this range, they are not reflected and do not contribute to the signal. By adjusting the tilt angle of the analyzer crystal, the refraction angle and small angle scattering can be extracted [47, 48].

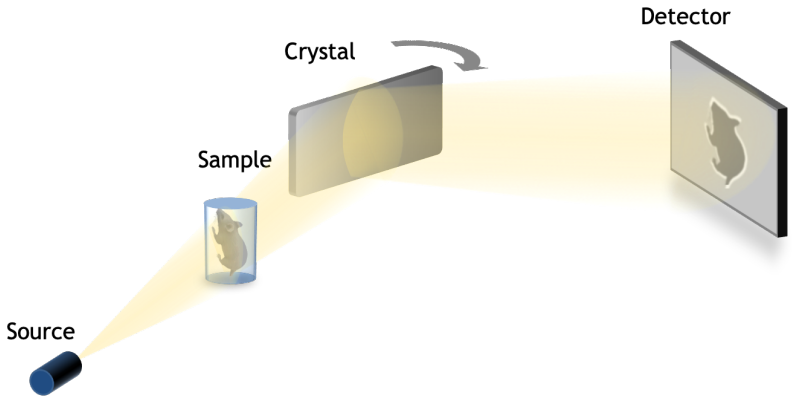

Figure 1.28: Analyzer-based imaging set-up. A monochromatic beam traverses the sample. Then it arrives on a Laue crystal that only reflects the beam arriving with a precise incident angle toward the detector. The crystal can be rotated to acquire several images with various reflection angles to retrieve the refraction from the sample.

This Phase Contrast experimental method proved to be a very sensitive technique [49] and feasible at low dose deposition to the sample as was demonstrated in [10].

The method has been successfully implemented with laboratory sources but at the cost of extremely long exposure times (up to several hours) due to the low flux after monochromatization [50]. Moreover the beam stability is difficult to maintain even at synchrotrons. These characteristics do not make this technique a good candidate for transfer to conventional laboratory sources and very few works have been done towards this direction.

Techniques for clinical applications

- **Grating interferometry**

Grating Based Imaging (GI) is an x-ray PCI technique based on the use of grating interferometers. It has been successfully adapted from visible light grating interferometry [51]. Fairly recent, this technique has become popular in many fields because of its good adaptability to conventional x-ray tubes. The principle of GI is a phenomenon called the Talbot effect (observed in 1836 by the English inventor Henry Fox Talbot), where a periodic wave repeats its pattern at certain distances in the Fresnel regime.

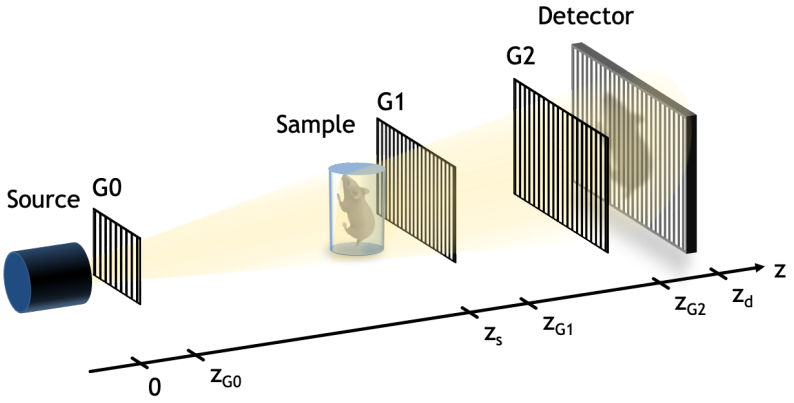

Figure 1.29: Grating interferometer imaging set-up. A beam from a very focused source or from a source collimated by a G0 grating is emitted towards the sample. A grating G1 placed before or after the sample creates a Talbot carpet interference pattern. The grating G2 filters the peaks of intensity that have been deviated from the axis before the detector. Several acquisitions are acquired with various positions of G1 and G2.

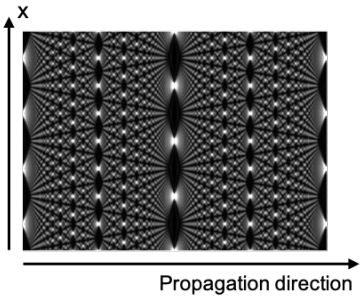

Figure 1.30: Talbot carpet pattern created by phase gratings.

Figure 1.29 presents a GI set-up on a conventional laboratory source. An X-ray grating interferometer consists of two gratings (G1 and G2), a detector, and, in the case of conventional x-ray source, an additional grating G0 that acts as a collimator creating multiple small x-ray sources. G1 is usually a phase grating and G2 an absorption grating.

G1 is used to split the beam creating periodic interference patterns varying with distance. This interference pattern is called the 'Talbot carpet' as shown in Figure 1.30. The interference pattern created from the waves re-emitted through G1 gives periodic peaks of intensity at characteristic distances. The detector is placed at one of theses characteristic distances, usually where the intensity peaks are higher. When the sample is placed in the beam, these interference patterns will be distorted due to attenuation, refraction and scattering. When placing an attenuation grating in front of the detector with the same period as the original interference pattern, the phase variations are translated into intensity variations as the peaks of intensity no longer fall in the space between two bars of G2. Taking several acquisitions with several positions of the gratings allows to retrieve the precise refraction angles as well as the attenuation and spreading of dark-field.

There are two types of interferometers: the most common is a 1D interferometer that consists of gratings made up of parallel lines and the 2D grating interferometer designed with two-dimensional patterns [52]. Besides this latter proof of feasibility, it is difficult to find real application of this 2D interferometers.

In 2006 Pfeiffer et al. [30] demonstrated the possibility of using the method on conventional laboratory sources and a new field was born with tens of teams around the world working on this set-up.
Albeit presenting a good sensitivity, this technique requires complex experimental set-ups difficult and expensive to manufacture especially for large fields of view. However, recent advances have shown impressive results on human patients using grating interferometry dark-field imaging [25, 53].
Even more recently, the same teem published the first results on the implementation of the technique on a clinical CT scanner [54]. This proof of concept on phantoms still needs to be optimized in order to reduce the acquisition time for it to be done while patients hold their breath. This technique is the one closest to be really available for clinical routines.
Despite the set-up's precision requirement and stability, it was proven that, given the means and materials, it was possible to implement it on a tomography set-up.

The remaining obstacles that can be imputed to GI for complete 3D clinical adaptation are:

- its limited dose efficiency as several position of the gratings are required to obtain each projection and part of the flux going through the sample will not be used to produce the image as they will be absorbed in G2;
- its acquisition time which is still too long for tomography;
- its fabrication which is tedious and expensive;
- its ability to retrieve the refraction only in one direction, making it insensitive to variations that are parallel to the gratings and causes

bad performance in terms of noise [55] (noise power spectrum diverging with low frequency) with tomographic reconstruction due to a bad integration for the phase.

- **Edge illumination**

Initially developed as "coded aperture" [56] at synchrotrons and adapted to conventional laboratory sources [57] it is now called Edge Illumination (EI) since 2013 [58]. It is based on the observation that by illuminating only the edge of the detector pixels, a high sensitivity to phase effects is obtained. The effect obtained is comparable to the ABI with a fine angular selection on the direction of the photons.
Figure 1.31 shows a typical Edge Illumination set-up. The method uses a pair of masks, one before the sample and the other close to the detector. Although the configuration may appear similar to that of a grating interferometer, the physical principle is different. The spacing between the bars of the grids is wider than for GI and instead of creating interference patterns the grid placed in front of the sample (G0) simply splits the beam into thin vertical beamlets. In absence of the sample, each of those beamlets will hit the center of each column of the detector. A second grid is placed in front of the detector, collimating vertically part of the pixels, reducing their individual field of view. When the sample is inserted, the rays that are deviated will no longer arrive in the free spaces of G1, changing the intensity received by the detector. Displacing G1 slightly on one side and the other will allow to retrieve the local refraction of the beam in the direction perpendicular to the grids and the dark-field scattering.
The use of such a simple configuration, as opposed to ABI, eliminates the need for a monochromatic beam.

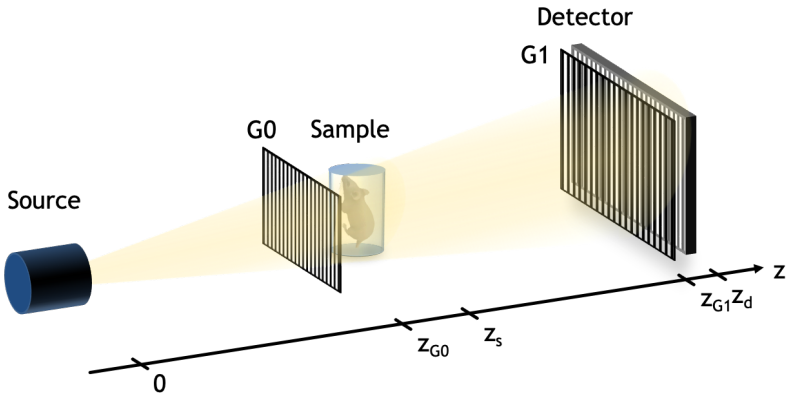

Figure 1.31: Edge illumination imaging set-up. A beam emitted toward the sample is first split into thin line beamlet by a vertical grid G0. Those beamlet go trhough the sample before propagating to the detector plane where a second grid G1 filtering the beamlets that have been deflected by the sample. Several acquisitions are acquired with various positions of G0 and G1.

It has been shown that this technique requires only low spatial and temporal coherence. The method has been successfully implemented on conventional x-ray sources [59].
Though its set-up is simpler and the requirements in terms of coherence are smaller, EI suffers from some of the same limitations as GI for 3D: dose, acquisition time and difficulty to rotate around the sample/patient. This technique is indeed better suited for pre-clinical studies than for *in vivo* radiological applications because of the high dose delivered to the sample since part of the radiation passing through the sample is stopped by the second slit. Another limitation remains the detection of

the unilateral phase gradient only (even if 2D implementation exists [60] their use remains scarce) and thus the complexity to perform 3D imaging with this device.

• **Mesh-based imaging**

In 2008, in the search of a technique requiring less exposure than GI and a simpler acquisition set-up, Wen at al. [61] invented spatial harmonic imaging. It has rapidly gone from a 1D to a 2D differential phase contrast modality [62].
The experimental set-up shown in Figure 1.32 consists simply of a 2D grid (or mesh) placed close to the sample in the path of the beam. Only two acquisitions are needed, one with only the grid in the path of the beam, to collect the reference image (I_r), and one with the sample added in the path of the beam (I_s). Ideally, the grid should entirely absorb the rays and be as thin as possible.

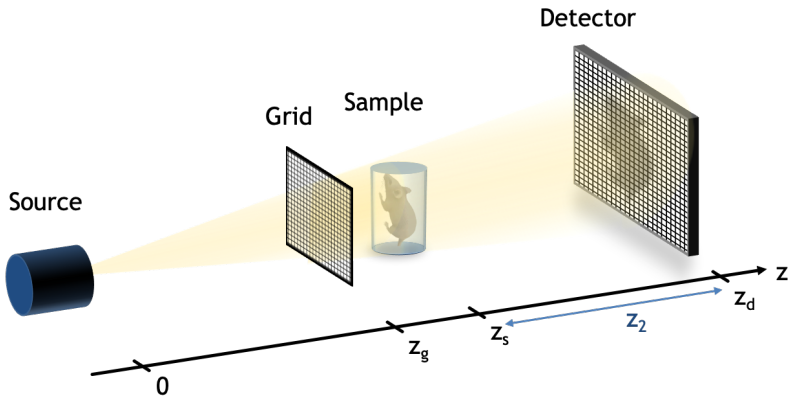

Figure 1.32: Mesh based imaging set-up. The beam is modulated by a 2D grid before reaching the sample. The beam then propagates to the detector carying informations about the grid ans the sample. Several images can be acquired with different positions of the grid.

The resulting sample image acquired multiplies the effect of the sample with the effect of the grid. Therefore, when going through Fourier transformation, the effects of the sample are convoluted with a 2D Dirac comb (Fourier transform of the mesh) and, by isolating different harmonics of the Fourier transforms of the sample and reference images, it is possible to retrieve attenuation, scattering and differential phase contrast images of the samples.
Figure 1.33 presents an example of a simulated sample image of a phantom with a grid and the associated Fourier transform. On the Fourier transform image, we can see clearly the different harmonics due to the mesh. Those harmonics are isolated by band pass filters, such as the blue and red circles drawn on the image, with radii (r) smaller than the separation width (SW) of the harmonics. After filtering the different (m,n) harmonics, their real space images $I_{s;m,n}(x,y)$ can be retrieved. Because the mesh is not composed of perfect delta Dirac functions, those images can be corrected by the same harmonic image of the reference image $I_{r;m,n}(x,y)$ to obtain: $I_{m,n}(x,y) = I_{s;m,n}(x,y)/I_{r;m,n}(x,y)$. The information contained in that harmonic image can be written as:

$$I_{m,n}(x,y) = I_0(x,y)S_{m,n}(x,y)\exp(i\psi_{m,n}(x,y)) \tag{1.14}$$

where $I_0(x,y)$ is the intensity transmitted through the object, $S_{m,n}(x,y)$ is the real-valued scattering amplitude and $\psi_{m,n}(x,y) = Mz_2\mathbf{g}_{m,n}.\boldsymbol{\alpha}(x,y)$ is proportional to the phase derivative in the $\mathbf{g}_{m,n}$ direction. Here M is

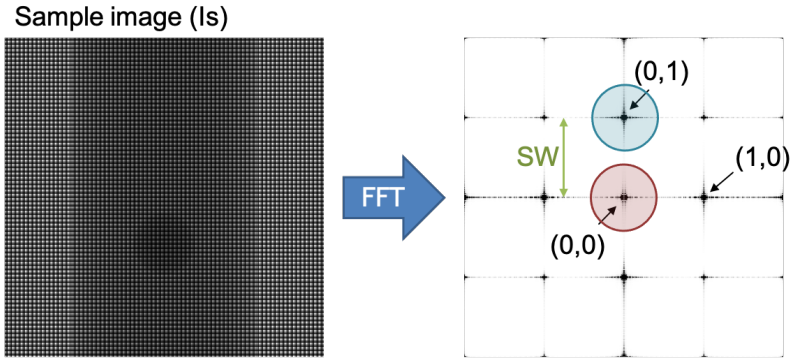

Figure 1.33: Mesh-Based imaging phase retrieval principle. Simulated sample image with a phantom and a grid. The Fourier transofrm of this image contains the fourier transform of the sample convoluted to a Dirac comb. The harmonics contain various pieces of information about the sample.

the magnification, z_2 is the propagation distance between the sample and detector and $\boldsymbol{\alpha}(x,y)$ is the refraction angle.
From eq. 1.14 the sample transmission is obtained by taking the 0^{th} harmonic $I_0(x,y) = I_{0,0}(x,y)$.
When taking the (0,1) and (1,0) harmonics we get:

$$I_{0,1}(x,y)/I_0 = S_{0,1}(x,y)\exp(i\psi_{0,1}(x,y)) \tag{1.15}$$

Then $S_{0,1}(x,y)$ is the norm of this complex ratio and its angle gives $\psi_{0,1}(x,y) = Mz_2\mathbf{g}_{0,1}.\boldsymbol{\alpha}(x,y) = Mz_2\alpha_x(x,y)$. From which the refraction along the x axis $\alpha_x(x,y)$ can be easily extracted. The same treatment on the (1,0) harmonic gives the refraction angle along the y axis $\alpha_y(x,y)$. A more complex even though quite similar harmonic-based method also allows to retrieve the dark-field signal.

This method was developed for conventional laboratory sources from the very beginning, first with simple 1D grids that gave only one phase derivative at a time [61, 63] but was rapidly adapted to 2D phase derivative by using meshes instead of simple grids [62]. It was also very rapidly used for *in vivo* imaging [64]. This methods appeared to be extremely promising for *in vivo* imaging and clinical transfer however, it appears that very few works were carried on during the following years and very little improvements to the technique were made. In 2019, it was proven that the technique gives quantitative phase images with a conventional source [65] and some works have been done to increase the retrieved images resolution [66] which was so far limited to the distance between two wires of the mesh.

• **Modulations-based imaging (Or speckle)**
Randomly distributed phase modulations techniques were developed in 2012 [1, 2] at synchrotrons, using the "speckle phenomenon" to create a randomly distributed intensity pattern which modifications upon introduction of the sample would give its phase information.

Definition: Speckle

In optics, speckles are random granular patterns that are produced by a very coherent beam when deflected by an element with a rough surface (such as sandpaper).

The experimental set-up of Modulations-Based Imaging (MoBI) is shown in Figure 1.34.

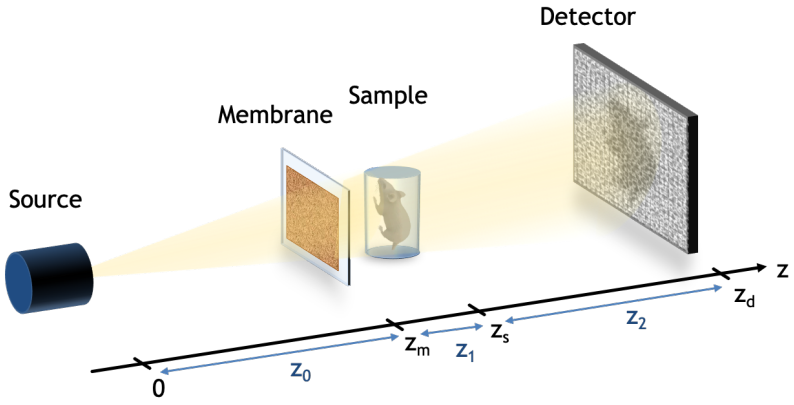

Figure 1.34: Modulations-based imaging set-up. The beam is modulated by a randomly distributed granular membrane before reaching the sample. Then it propagates to the detector distorted by the membrane and the sample. Several images can be acquired with various positions of the membrane.

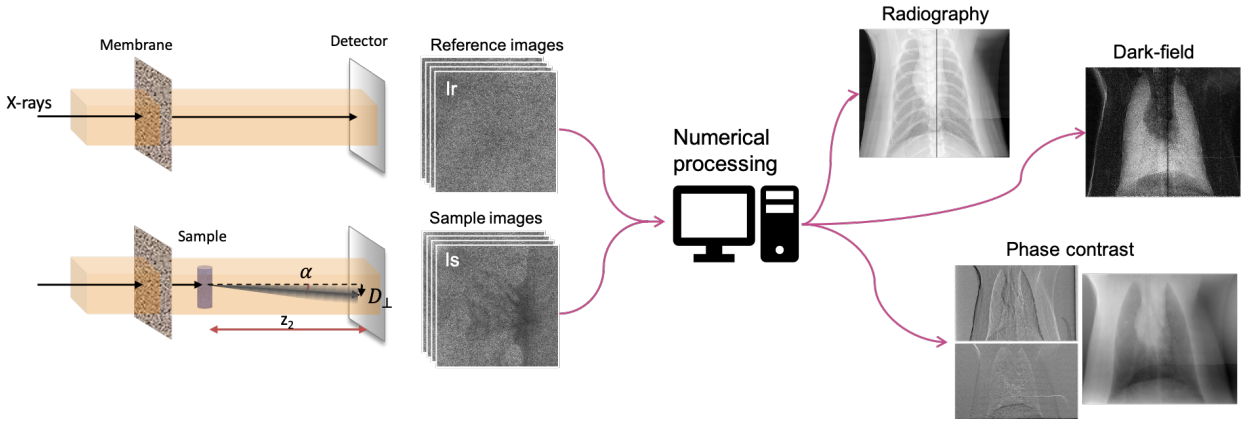

Figure 1.35: MoBI principle outline. From several acquisition of the membrane alone and membrane plus sample in the path of the beam, a numerical processing allows to retrieve attenuation dark-field and phase contrast images.

The experimental set-up only requires the sample, an x-ray imaging detector and a randomly distributed granular membrane with structures of a few pixels in size.
The principle of MoBI is to follow the deflection of the beam's rays due to the object. To do so, a first image reference, I_r, is acquired with the membrane placed between the source and the detector, generating a random intensity modulations pattern as shown on Figure 1.35. Then a sample image, I_s, is acquired when an object is added in the path of the x-ray beam. MoBI is based on the tracking of the local distortions of the random pattern observed when comparing I_s to I_r. This comparison allows to retrieve the attenuation, refraction maps and dark-field signal. As mentioned before, the refraction is proportional to the phase derivative. The phase image (ϕ) can then be retrieved by integrating the refraction maps. Those steps can be done using different techniques and algorithms that are described in Chapter 3. In order to improve the quality of the result it is possible to take several pairs of acquisitions (with and without the sample), moving the membrane between each pair of acquisitions.

This set-up, besides its simplicity of implementation, has the following main advantages:

- no field of view limitation other than the detector (the random mask is easy to manufacture)
- no resolution limitation other than the optical system

- being radiation dose efficient because no absorbing element is used between the sample and the detector meaning that all photons passing through the sample are eventually contributing to the image formation.

On conventional laboratory systems, because the speckle phenomenon is difficult to produce, a new kind of membrane had to be invented using high Z atomic element (3D printed or powders deposition) to produce randomly distributed intensity modulations. This process has been patented (Patent number: WO2021005283 [67]). Contrary to Coded Aperture systems [68] or EI that use binary masks (either letting the beam through, unmodulated, or blocking it completely), the MoBI masks introduce an intensity modulation encoding each pixel of the image meaning that sub-pixel precision is easier to obtain. Despite being easier to manufacture than coded aperture masks, and being easier to use (no need of precise alignment), due to the introduced modulations being isotropic, it does not suffer from any frequency problems related to preferential direction detection like in Mesh Based Imaging and is sensitive to any directional structure.

To summarize, the experimental complexity of PCI and Dark-Field is translated in MoBI to the numerical processing side. This practical simplicity holds promise for the feasibility of a rotation gantry. Then through image analysis method, we can track the modulations displacements caused by the refraction of the sample directly in two directions.

Very recently, a new method in between MoBI and EI has emerged based on Hartmann Wavefront Sensors [69]. This techniques uses a highly absorbing plate with punched holes to split the beam into very thin beamlets and then track their displacements on the detector plane. The main difference with MoBI is that the sample is not entirely illuminated at once due to the binary 'modulation' of the beam. This method though very recent and therefore still rare in the literature appear to have various advantages and was already proven to work with a laboratory liquid-metal jet source [70].

1.3.3 Summary of the pros and cons

The phase-sensitive techniques described above differ in their technical complexity, the use of x-ray optics, the readout process, and the method of extracting the signals to detect and to measure the phase contrast. Thus, all these modalities face various limitations for the transfer to clinical devices.

Table 1.2 summarizes the advantages and disadvantages of each technique. PBI and ABI both require highly coherent sources (mainly spatial coherence for PBI and temporal coherence for ABI) and very few work mention their use for extracting the dark-field signal in the literature. In addition ABI has a complex set-up that requires a lot of flux and is therefore difficult to implement with conventional x-ray tubes. PBI has a very simplistic set-up but the source spatial coherence requirement make its transfer to clinical tomography devices impossible. GI, EI and MBI have proven to be transferable to conventional sources however, GI and EI have quite complex set-ups and are only sensitive to the gradient in one

direction while MBI has a simple set-up sensitive to two directions. The main limitations of MBI remain its limited resolution and sensitivity.

Table 1.2: Summary of different features of the PCI techniques

PCI technique	Coherence requirement	Phase sensitivity	Dark-field sensitivity	Set-up complexity	Transfer to conventional source (x-ray tube)
Propagation-based imaging	High	High (Laplacian)	Very limited	Simple (Source coherence requirement)	Liquid-metal jet (expensive) or micro-focus (limited flux)
Analyzer-based imaging	High	High (1D gradient)	Good (1D)	Medium (Crystal analyzer)	Yes but very limited flux
Grating interferometry	Low	High (1D gradient)	Good (1D)	Complex (Gratings fabrication and alignment)	Yes
Edge illumination	Low	Medium (1D gradient)	Good (1D)	Medium (Grid alignment)	Yes
Mesh-based imaging	Medium	Medium (2D gradient)	Medium	Simple (Mesh fabrication)	Yes
Modulation-based imaging	Medium	Medium (2D gradient)	Good (2D)	Very simple (random mask)	In progress

Finally, we decided to work with MoBI because the set-up, despite requiring a high stability, is very simple. It is sensitive to 2D variations, does not appear to require a high coherence of the source and the entire beam going through the sample is used for image formation making it quite dose efficient. For those reasons, MoBI is a very interesting candidate for the transfer to clinical devices.

As was mentioned above, despite all those experimental qualities, the challenges of MoBI remain the numerical extraction of the various signals from the acquisitions obtained with conventional laboratory set-ups. While extracting those signals from high resolution, low noise acquisitions was already proven to work efficiently, the transfer of this method to less coherent, polychromatic, low resolution set-ups with the lowest possible dose remains a big challenge.

The main goals of this work are then the optimization of the experimental set-up to obtain the acquisitions from which the signals will be the better extracted and get the most efficient numerical processing to extract the signals of interest.

Résumé du Chapitre 1 en Français

Dans ce chapitre, nous introduisons le contexte médical et physique au coeur du sujet de thèse.
Après un bref historique de l'imagerie clinique de routine aujourd'hui, nous développons l'intérêt de l'imagerie x en contraste de phase et en champ sombre pour le diagnostic et les études cliniques notamment pour l'imagerie ostéo-articulaire et pulmonaire. Dans un second temps, une description des phénomènes physiques mis en jeux et des éléments technologiques utilisé en imagerie par rayons x permettent de mettre en évidence les défis du projet de thèse. Les rayons x et leurs interactions avec la matière seront définis avant une description des caractéristiques de différentes sources et différents détecteur de rayons x.
Enfin, une vue d'ensemble des méthodes d'imagerie en contraste de phase est donnée avec leur applicabilité à la clinique.

Aujourd'hui, la radiographie, l'imagerie par résonnance magnétique et l'échographie sont les méthodes d'imagerie les plus utilisées en routine clinique. En fonction de ce que l'on veut observer une technique va être préférée à une autre car elles ont des caractéristiques très différentes. Cependant, pour l'imagerie osteo-articulaire ou pulmonaire, chacune possède des limitations. La radiographie permet de voir correctement les os et leurs lésions mais fournissent un contraste très faible des autres tissus. L'IRM permet d'avoir un bon contraste des tissus mous mais donne difficilement des informations sur les tissus rigides tels que les os ou le cartilage et rend difficilement un contraste dans les poumons qui sont pauvre en atomes d'hydrogène. De plus, l'IRM a une résolution limitée et un coût élevé. L'échographie a un très faible coût et un bon contraste des tissus mous mais ne pénètre pas l'os et permet uniquement d'obtenir des informations sur les structures peu profondes. L'imagerie x en contraste de phase et en champ sombre présente des avantages qu'aucune de ces techniques ne combine : un contraste aussi bien dans les tissus mous que les tissus rigides, la possibilité d'avoir une résolution élevée et un coût limité lorsque nous parviendrons à développer une technique fonctionnelle sur de simples appareils de radiographie.

Les rayons x sont des radiations lumineuses de très haute énergie qui sont capables de traverser la matière et d'interagir avec elle. Les photons qui les composent peuvent être déviés ou bien absorbés dans les matériaux et ces phénomènes auront une répercussion sur le faisceau sortant de l'échantillon qui sera par conséquence dévié ou moins intense selon la quantité de photons absorbés. Ce sont ces modifications du faisceau qui seront détectées et qui permettront d'obtenir des images avec différents contrastes.

Pour produire ces rayons x, il existe différents types de sources mais celles qui nous intéressent ici sont la source synchrotron (qui a permis d'inventer l'imagerie x en contraste de phase) et les tubes à rayons x (utilisés dans les appareils cliniques conventionnels). La source synchrotron produit un flux de photons extrêmement intense ce qui permet de se placer très loin de la source pour optimiser la cohérence spatiale et de filtrer les énergies pour obtenir une cohérence temporelle. Les tubes à rayons x sont beaucoup moins puissants ce qui ne permet pas de filtrer le faisceau pour optimiser la cohérence temporelle. Ils ont aussi généralement un point d'émission étendu qui limite la cohérence temporelle du

faisceau.
Pour détecter les rayons x, il existe également différents types de détecteurs mais nous nous concentrons sur les deux types utilisés dans cette thèse : les détecteurs à comptage photonique et les détecteurs en intégration d'énergie avec scintillateur. Les premiers permettent de compter les photons individuellement et d'obtenir un signal électrique proportionnel au nombre de photons. Ils ont une fonction de dispersion nulle (le signal ne "fuite" pas sur les pixels alentours) mais ont généralement une taille de pixel plus importante. Les détecteurs à scintillateur en intégration d'énergie ont une première plaque qui transforme les rayons x en lumière visible avant détection de celle-ci. A cause de cette première transformation, le rayon reçu en une certaine position peut dériver légèrement avant d'être transformé en signal électrique. Ces détecteurs peuvent cependant avoir une résolution très élevée.

Au synchrotron, nous travaillons avec un faisceau d'une grande cohérence et un flux très important ce qui permet d'utiliser des détecteurs avec une très grande résolution (petite taille de pixels). Dans des conditions cliniques, la taille de la source risque de flouter l'image de l'échantillon et le faible flux nécessite l'utilisation de grands pixels pour obtenir une statistique suffisante. De cette manière, il est impossible d'obtenir une résolution comparable à celle du synchrotron et le travail nécessaire à la récupération de la phase sur les images qui n'induit que de très faibles transformations de l'image est rendu extrêmement compliqué. Les appareils de laboratoire permettent généralement d'obtenir un entre deux. Ils ont une source polychromatique mais avec un point d'émission plus petit que les source d'hôpital. Leur configuration permet d'avoir une bonne distance de propagation entre l'échantillon et le détecteur ce qui permet d'avoir un grandissement important et une résolution importante au niveau de l'objet. Pour ces raisons, le transfert de notre technique synchrotron ne se fait pas directement sur des appareils cliniques mais dans un premier temps sur des appareils de laboratoire.

En radiographie conventionnelle, le signal observé est lié à l'atténuation des rayons x dans l'échantillon. En contraste de phase on va s'intéresser aux signaux liés à la phase. La première chose à comprendre est que la phase est directement liée au phénomène de réfraction. En effet, le gradient de la phase est proportionnel à l'angle de réfraction du faisceau sortant de l'échantillon. Ce que nous nommerons le contraste de phase correspond donc au déphasage local ou à la réfraction locale induite par l'échantillon en chaque point. Le second signal auquel nous nous intéressons, et qui est également lié à la phase, est la diffusion aux petits angles. Elle est produite par la traversée de nombreuses interfaces par le faisceau. Ce signal, qui produit une image que nous appelons "champ sombre" (dark-field en anglais) donne des informations sur la présence de nombreuses microstructures dans l'échantillon.

Parmi les techniques de contraste de phase existantes, l'imagerie par propagation ou l'holographie est la plus utilisée au synchrotron grâce à sa simplicité expérimentale. Elle nécessite simplement de placer l'échantillon dans le faisceau et de placer le détecteur suffisamment loin après pour voir des franges d'interférence due au déphasage de l'échantillon apparaître. Ce phénomène se produit grâce à la cohérence du faisceau synchrotron mais ne fonctionnera pas avec les tubes à rayons x utilisés en clinique. Parmi les autres méthodes qui sont investiguées pour un

transfert clinique aujourd'hui, on peut citer les interféromètres par réseau ou bien l'illumination de bord. Ces techniques sont très prometteuses mais ont encore de nombreux inconvénients, notamment leur montage expérimental complexe.
Nous travaillons sur une méthode synchrotron initialement nommée imagerie par tavelure (speckle-based imaging) que nous avons renommé récemment imagerie par modulations. La méthode consiste à insérer une membrane avec des structures aléatoires dans le faisceau pour obtenir un motif de référence. En insérant un échantillon à sa suite dans le faisceau, on va observer une modification de ce motif lié à l'atténuation du faisceau mais aussi un déplacement local du motif lié à la réfraction et un floutage lié à la diffusion aux petits angles.

L'objectif principal de cette thèse est donc d'adapter l'imagerie par modulations à des dispositifs de laboratoire en vue d'un futur transfert sur des appareils cliniques.

Simulation of modulations-based imaging

2

The development of MoBI for clinical set-ups is twofold:

1. a set-up optimization to be able to extract as much information as possible with the lowest level of noise and artefacts.
2. the creation of the most efficient numerical process to extract the signal and filter out noise and artefacts.

These steps are associated with a deep understanding of all experimental parameters and their influence on the result.

To reach that goal, a simulation is a very powerful tool because it allows to study the influence of various features of the set-up in a completely 'controlled' environment. It is also a way to test signal retrieval algorithms as the result expected can be predicted in the simulation.
After considering the already existing software programs available for phase contrast imaging simulations, I decided to develop a new one, dedicated to MoBI where all the desired parameters would be flexible and the computation time would be reasonable. We named this tool PARESIS [1] .
This chapter, after a first part giving a touch on the existing tools for simulations of phase contrast imaging, contains details about the skeleton of the created simulation software with the relevant resources, the validation tests that were done and some of the set-up optimization work it allowed to do.

Before starting, here are the notations used in this Chapter:

Notations

Variables:

- n: complex refractive index
- δ: refractive index real part decay
- β: refractive index imaginary part
- μ: linear attenuation coefficient
- λ: wavelength
- $k = 2\pi/\lambda$: wavenumber
- ϕ: phase
- B : absorption
- ψ: wave function
- $\mathcal{T}_{obj}$: transfer function
- $D_\perp = D_x, D_y$: intensity displacement in the detector plane related to refraction
- δ_x, δ_y: local displacements
- D_f: Dark-field
- α: angle of refraction
- α_{df}: average opening angle of multiple refraction
- σ: standard deviation

2.1 State of the art 46
Existing software programs . 46
Previous similar works 47
Useful resources 48
2.2 The PARESIS software 50
Physical models and principles 50
Membrane geometry 55
Implementation and features 58
2.3 Validations and limitations . 65
Phase effects validation on a monochromatic synchrotron set-up 65
Phase effects validation on a polychromatic laboratory set-up . . . 68
Comparison of the dark-field simulation to a synchrotron experiment 70
Limitations 70
2.4 Optimization of MoBI based on simulations 72
Influence of the number of membrane positions 72
Influence of the number of photons per acquisition 73
Influence of low energy filtering 74
Conclusion 76
Résumé du Chapitre 2 en Français 78

1: PARESIS: Python rAy-tRacing and frEsnel program for Speckle Imaging Simulation

- z: spatial axis in the direction of propagation
- x, y : spatial coordinate perpendicular to propagation
- k_x, k_y: Fourier space coordinates (angular frequency)
- $\{P\}$: set of membrane positions
- z_0: distance between the source and the membrane
- z_1: distance between the membrane and the sample
- z_2: propagation distance between the sample and the detector
- I: intensity field
- I_r: Reference image of the optical elements without sample
- I_s: Sample image with the sample
- t: thickness of the sample

Operators:

- P: fresnel propagator in real space
- $P^{(F)}$: Fresnel propagator in Fourier space
- $*$: convolution product
- ∇: gradient operator
- $Re\{\}$: Real part
- $\mathcal{F}$: Fourier transform
- $\mathcal{F}^{-1}$: inverse Fourier transform
- $\iint_{(x,y)} ..dxdy$: 2D surface integral
- $\sum_i$: sum of the following quantity for i in a set.
- log: natural logarithm
- e: exponential function

2.1 State of the art

In this first section, reviews the already existing software programs and resources that inspired the development of our own simulation program. For our purposes, we were searching for a program with the following characteristics:

- Quantitative phase effects simulation
- Realistic noise representation
- Possibility to implement complex geometries for the sample and membrane
- Possibility to simulate a Synchrotron source and a laboratory polychromatic source
- Take into account the influence of the source spot size
- Possibility to simulate the detector point spread function
- Rapid computation
- Possibility to implement the dark-field phenomenon
- User friendly

2.1.1 Existing software programs

SHADOW is one of the oldest synchrotron x-ray simulation software. The first version already based on Monte Carlo (MC) methods was finalized in 1982 and the first publication concerning its principle was published in 1984 [71]. Since then, the Shadow software has known continuous improvement [72] and is now interfaced in the OASYS platform [73]. A second software for synchrotron optics simulations is embedded in

OASYS with a wave optics approach more appropriate to simulate interference phenomena: SRW[74] (Synchrotron Radiation Workshop) which is based on a Fresnel propagator method similar to the one that will be described in the next section. This software, albeit being widely used and validated, is limited to synchrotron experiment simulations.
At the beginning of the 2000s, the CERN (European Organization for Nuclear Research) developed a software toolkit that allowed to compute the path of various particles in matter called Geant4 [75]. Also based on Monte Carlo methods, it makes use of the interaction cross sections of the particles with materials. GATE [76] (Geant4 Application for Tomographic Emission) is a platform that interfaces the Geant4 libraries to perform various kinds of simulations, from nuclear medicine imaging to dose calculations, computed tomography and radiotherapy. The adaptation of the code for phase contrast imaging was not originally possible as it considered only particle interactions such as absorption and inhomogeneous scattering, it could not reproduce wave effects such as interference fringes (i.e. refraction). However, recent works have been completing the MC simulations with wave phenomena using mixed approaches with Snell-Descartes' Law to compute refraction [77] even for polychromatic sources [78]. Using GATE to simulate various phase contrast imaging experiments have therefore become possible but with one main drawback: the computation cost of MC simulations is tremendous. It requires a lot of time and very powerful machines as it computes the path of each particle individually when there can be several millions of them to form a single image.

Definition: Monte Carlo simulations (MC)

Monte Carlo simulations are used to model the probability of different outcomes in a process that cannot easily be predicted due to the intervention of random variables.

During the past decades, other software programs for synchrotron simulations have been developed to complement or concurrence the already existing ones. For example, we can cite PHASE [79] based on Fourier optics, McXTrace [80] based on MC simulations or Syris [81] based on the Fresnel propagation process similarly to what will be described in the next section. However, all these existing software programs have been designed for specific conditions and lack the flexibility that we require to correctly simulate the MoBI experiments that we are interested in for this project.

After considering all those tools, it was decided to implement our own simulation program in Python to be able to fully adapt it to our experimental conditions and deeply understand the founding principles of its implementation.

2.1.2 Previous similar works

The implementation of simple simulation programs for the study of specific phase contrast imaging methods has already been attempted by other teams around the world. Mostly they were developed for laboratory set-ups with x-ray tubes as they are the less treated with already existing

software programs.
In each context, the different teams would choose different physical pipelines depending on the precision, the physical phenomena prevalence of their experiment and the rapidity of the desired code.
Some of the most popular ways to simulate propagation phase effect (for PBI) are by combining MC methods with wave propagators [82, 83] or adapt MC to take into account the Huygens-Fresnel principle [77, 84]. Similar combinations were also used for specific simulation of grating interferometers [85, 86] or edge illumination experiments [87].
An American team developed their own code for the simulation of mesh-based imaging based on a similar approach to the ray-tracing one that will be described in the next section [88].
A french team recently created their simulation code for Hartman Wavefront Sensor imaging using a Fresnel propagator method similar to one of the models used in our program [89].

Finally, for specific simulations of MoBI, only three works were found. The first one, by Zdora et al. [90], was based on Fresnel propagation and intended to study the influence of the spectrum bandwidth on the MoBI experiment. However, the simulated spectrum was not based on a real source and would therefore not be able to reproduce real experiments. A second work was done very recently, also based on Fresnel propagator to study the dark-field signal introduced in the modulations with different characteristics of a porous material [91]. This one is amongst the very few works that were found to simulate dark-field signal due to multiple scattering in a porous material. To simulate it, the material was based on a packed sphere geometry that was described at very high resolution (as the spheres size was only a few microns) and was very computationally expensive. The last even more recent work compared a MC approach and a TIE based propagation approach for MoBI [92]. In this case, interested in simulating large samples in a cone beam geometry, they used a multi-slice approach to account for the sample geometric deformation due to the cone beam.

The work that was done here on the PARESIS software is partly similar to the ones by Zdora et al. as one model uses the same Fresnel propagator method but with many additional features.

Remark: Visibility and dark-field.
In some articles, the dark-field is simply defined as a loss of visibility due to the sample. In the case of a polychromatic beam, this visibility can be altered by beam hardening in the sample. This phenomenon is related to attenuation in the sample and is more an artifact than a new information which is why it is not the kind of 'dark-field' we are interested in in the present thesis work.

2.1.3 Useful resources

The implementation of our own simulation software required two main datasets: one with the sources energy spectra and one with materials complex refractive index for the energies and materials of interest.

- **Source spectrum data**

X-ray tube spectra can be either measured or simulated. The direct measurement of the spectrum requires special equipments and allows to determine the spectrum only in precise conditions and geometries [93] which is too restrictive for the cases that we wanted to study.

Most of the existing x-ray tube spectrum simulations are based on Monte Carlo simulation of the electron's interactions with the anode material [94, 95] and the reference toolkit for this method is BEAMnrc [96]. But as mentionned before, MC methods require a big computation power

and a lot of time which is counterproductive for our goal to create a fast computation program.

In between simulations and experimental measurements there is the semi-empirical approach. From a base of several measured spectra or Monte Carlo simulated ones, others can be interpolated to fit various geometries using spline interpolation as it is the case for the TASMIC method [97] used in the SpekTr toolkit [98]. This toolkit is available as Matlab functions or with a user interface but cannot be directly integrated in a Python code.

In other cases, some features are adapted to fit the experimental results. In the Birch and Marshall method [99], the bremmstrahlung cross-section is tuned to adapt the spectrum to various experimentally measured spectra [100, 101]. Based on a similar method but extended to wider cases and higher tube voltage SpekCalc software is available with a user interface [102]. More recently, a new improved version of the semi-empirical method was developed and implemented into a free Python toolkit: SpekPy [103].

This last software, SpekPy, is the one that is used in our PARESIS program as it is a very accurate user-friendly python toolkit.

- **Materials refractive index coefficients**

The refractive index coefficients responsible for attenuation β and refraction δ depend both on the material composition and the beam energy. Those coefficients are related to the atomic scattering factors (f_1, f_2) which are measures of the scattering powers of individual atoms related to the absorption strength of the material (f_2) and the non absorbing interactions (f_1) related to the interaction cross-sections [104, 105] (already mentioned in the first Chapter). The relations between refraction coefficients and scattering power are:

$$\delta = \frac{n_a r_e \lambda^2}{2\pi} f_1 \tag{2.1}$$

$$\beta = \frac{n_a r_e \lambda^2}{2\pi} f_2 \tag{2.2}$$

where r_e is the electron radius, λ is the wavelength, $n_a = \rho \mathcal{N}_a / M_a$ is the number density with ρ the material density, $\mathcal{N}_a$ the Avogadro number and M_a the molar mass.

The standard method for computing those coefficients today is described by Chantler [105] and implemented in the online software NIST [106] which can give form factors, attenuation and scattering cross-sections. From those data, is is possible to retrieve the δ and β coefficients.
The Melbourn University derived this method in another online software (TS Imaging) that gives directly the δ, β coefficients for a variety of already implemented human tissues or customized materials. This website was used to create the database used in PARESIS.

To the best of our knowledge, two toolkits for getting refractive index coefficients exist for Python implementation: xraylib [107] and xraydb. Xraylib coefficients are computed from coefficients extracted from various datasets for the different interactions [108, 109]. It is implemented in C

but is available as a toolkit for various programming languages including Python.
Xraydb is also based on coefficients extracted from various databases, similar to xraylib but with an additional source [106].

The use of those libraries for the PARESIS software was investigated but due to difficulties of implementation or divergence of results for compound materials compared to the data obtained with the TS Imaging website, they are not kept in the current version. More tests should be ran in the future to implement one of those toolkit in PARESIS for an easy use of other materials than the ones already in the local database.

2.2 The PARESIS software

Remark: PARESIS meaning
Some would think that "paresis" is a condition where the muscles movements are weakened but no it actually means "Python rAy-tRacing and frEsnel program for Speckle Imaging Simulation". Even though we no longer speak of 'speckles' ('modulations' now) it was chosen to keep the name.

The PARESIS software that I developed for MoBI optimization is flexible as it can simulate synchrotron experiments as well as laboratory and clinical devices and various samples and membranes geometries with different materials. In this part, the simulations framework from the source spectrum simulation to the detector characteristics will be developed. We need first to introduce the two physical models that are implemented to compute the distortions of the wavefront between the source and the detector, going through various elements.

2.2.1 Physical models and principles

The physical interactions involved in phase contrast imaging have already been presented in the first chapter but we will now see two mathematical schemes to describe them. The first model is based on the wave optics Fresnel propagator method as described in Paganin et al. [110]. The second one is based on classical optics ray tracing in a numerical pixelated geometry.

Fresnel propagator model

In both models we start by making use of the projection approximation. This approximation, which is most of the time valid when the object is thin in comparison to the propagation distance, states that the description of the wave through an object can be described as phase shift and attenuation following straight lines through the object. Another way to see it is by saying that the deflection inside the object volume is negligible and that we only retrieve the total deflection at the exit surface. In practice, that means that we can calculate the phase shift ϕ and the absorption B through the entire object at once with the relations:

$$\phi(x,y) = -k \int_z \delta(x,y,z)dz \tag{2.3}$$

$$B(x,y) = k \int_z \beta(x,y,z)dz \tag{2.4}$$

where x and y are the spatial coordinates in the plane perpendicular to the propagation direction z, δ and β are the indices for refraction and absorption introduced in the Chapter 1, $k = 2\pi/\lambda$ is the wave number.

The numerical calculation of these distortions was achieved by creating pixelated thickness maps of each material of the image. Then for each pixel (x,y), the phase shift and attenuation associated to each material (mat) and its traversed thickness (t_{mat}) along z are summed to obtain the total phase shift and attenuation:

$$\phi(x,y) = -k \sum_{mat} \delta_{mat} t_{mat}(x,y) \tag{2.5}$$
$$B(x,y) = k \sum_{mat} \beta_{mat} t_{mat}(x,y)$$

The δ, β coefficient are extracted for the considered energy and materials from an Excel table that is filled with data from the TS Imaging website of Melbourne University.

Remark: Projection approximation and multi-slice approach.
This approximation has limitations as it was shown in [111] and for larger objects or coherent sources, the result may be slightly biased. Then, a way to have a more precise calculation is by using a multi-slicing method [92, 112]. The principle is that the object is going to be divided into virtual slices along the propagation direction. Those slices can be considered as a series of objects on which we can apply the projection approximation to compute the phase and attenuation and propagate the wave-field between each slice. In our simulations, it was estimated that the distortions occurring in the sample could be neglected and no such multi-slice approach was implemented so far.

Wave models for coherent x-rays can be derived starting from Maxwell's equations as is described and detailed in Paganin et al. [110]. The starting point of the model is to write the wave equation of the beam:

$$\psi(x,y,z) = e^{i(k_x x + k_y y + k_z z)} \tag{2.6}$$

where x and y are the coordinates on the perpendicular plane, k_x, k_y and k_z are the vector components of the wave vector. Before the wave reaches any object, it can be considered that the wave vector is along the propagation direction, therefore, eq. 2.6 becomes:

$$\psi(x,y,z) = e^{ik_z z} \tag{2.7}$$

Then, when a wave goes through an object, it will be partly locally absorbed and its phase shifted. A simple way to calculate those phase alterations is through a transfer function $\mathcal{T}_{obj}$ that is calculated from the phase shift and attenuation from eq. 2.5:

$$\psi(x,y,z_{after\_object}) = \mathcal{T}_{obj}\psi(x,y,z_{before\_object}) \tag{2.8}$$
$$\mathcal{T}_{obj} = e^{i\phi(x,y) - B(x,y)} \tag{2.9}$$

Once the wave carries the object information, it will undergo other modifications during propagation (z_2) to the detector plane. The experiments of interest here being mainly limited to the Fresnel domain under the paraxial approximation, that propagation can be described by the "Fresnel Propagator" [110]. There are two formulations of that propagator. One in the real space:

$$\psi(x,y,z_{objet} + z_2) = P(x,y,z_2) * \psi(x,y,z_{objet}) \tag{2.10}$$
$$P(x,y,z_2) = \frac{e^{ikz_2}}{4\pi^2} \iint_{-\infty}^{\infty} e^{-iz_2(k_x^2+k_y^2)/(2k)} e^{i(k_x x + k_y y)} dk_x dk_y \tag{2.11}$$

with $*$ the convolution product operator, P the real space Fresnel propagator and z_2 is the distance of propagation. This calculation includes a convolution which induces a big computation cost while the second one is a simple multiplication in the Fourier space as shown in eq. 2.12:

$$\psi(x, y, z_{objet} + z_2) = P^{(F)}(x, y, z_2).\psi(x, y, z_{objet}) \tag{2.12}$$

$$P^{(F)}(x, y, z_2) = e^{ikz_2}\mathcal{F}^{-1}\left\{e^{-\frac{iz_2}{2k}(k_x^2+k_y^2)}\right\}\mathcal{F} \tag{2.13}$$

Remark:
The same calculation would be used to compute the propagation between slices in the multi-slicing model.

where $P^{(F)}$ is the Fresnel propagator in Fourier space.

It was mentioned in the first chapter that depending on the experiment we have either a parallel or a cone beam geometry. The cone beam geometry will have a big influence on the interference fringes that will be observed at a distance z_2. To account for it, we can use the Fresnel Scaling Theorem as described in the annex of Paganin et al. [110] from which is extracted the Figure 2.1. This theorem states that the interference fringes that will appear in a cone beam at a distance z_2 are identical to those that would appear at a distance $z_{eff} = z_2/M$ in a parallel beam. Where M is the magnification. This means that we can use the same propagation method by taking a propagation distance z_{eff} instead of using directly z_2.

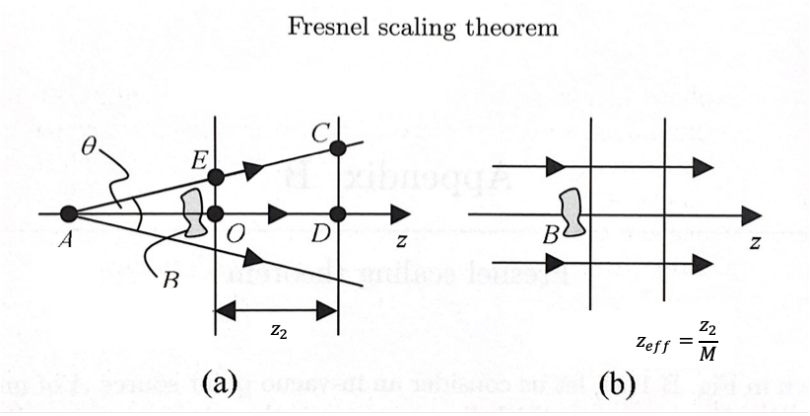

Figure 2.1: Fresnel scaling theorem as illustrated in Paganin et al. [110].

After propagation to the detector plane, the wave function can be converted to intensity with the following relationship:

$$I(x, y) = |\psi(x, y)|^2 \tag{2.14}$$

Ray-tracing model

In this second approach, the intensity field is directly considered, split into a pixelated frame. The intensity after the object I_{ao} can then be calculated as:

$$I_{ao}(x, y) = I_{bo}(x, y)e^{-2B(x,y)} \tag{2.15}$$

where I_{bo} is the intensity before the object. From the phase shift, the refraction angle α of each ray going through a square pixel (x,y) can be computed as:

$$\alpha(x, y) = \frac{1}{k}\nabla(\phi(x, y)) \tag{2.16}$$

And using that angle map, the redistribution of intensities from virtual pixels (x,y) after the object to virtual pixels (x_d, y_d) on the detector plane

after propagation over a distance z_2 can be calculated:

$$I(x_d, y_d) = \left\{ \sum_{x,y} I(x,y) w_\cap \; ; \; w_\cap = (x_d, y_d) \cap (x,y) + z_2 tan(\alpha(x,y)) \right\} \tag{2.17}$$

Here, the beam is virtually sliced into pixel-size beamlets. When, after propagation, the refracted beamlet hits partly neighbouring pixels, its intensity is consequently allocated to those pixels as is sketched in Figure 2.2.

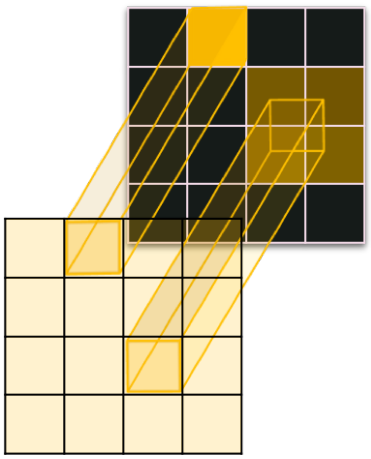

Figure 2.2: Beamlets redistribution due to refraction after propagation.

These were the theoretical models for a monochromatic case in an ideal world with no experimental flaws or errors. For a more realistic simulation, other elements will be detailed in the following sections.

Polychromatic case

In the previous sections, we have introduced two physical model equations. In those equations, many parameters $(\delta, \beta, k, \phi, B)$ are varying with the energy. In order to consider the polychromatic character of some of our sources, there is a simple way to proceed. We follow the previously described pipelines several times for every energy E of the spectrum that we want to consider and then combine their resulting intensity weighted by their frequency of occurrence w_E in the source spectrum:

$$I(x,y) = \sum_E I_E(x,y) w_E \tag{2.18}$$

As mentioned in the previous section, this spectrum is easily obtained in Python with the SpekPy library.

Dark-field model

The dark-field phenomenon related to multiple refraction in the sample has already been introduced in the first chapter. For reminder, the average scattering opening angle α_{df} of a beamlet going through a porous material can be written:

$$\alpha_{df} = 2|\delta^{(1)} - \delta^{(2)}| \sqrt{N \left(log \left(\frac{2}{|\delta^{(1)} - \delta^{(2)}|} \right) + 1 \right)} \tag{2.19}$$

where N is the number of particles encountered by the ray and $\delta^{(1)}, \delta^{(2)}$ the refractive indices of the particles and their environment. To get the average number of spheres crossed in a thickness t of the sample, we need the sphere radius R and the volume fraction occupied by the spheres f_s. From that, we can get the number of spheres occupying a unit volume N_{vol} as:

$$N_{vol} = \frac{f_s}{V_s} = \frac{f_s}{\frac{4}{3}\pi R^3} \tag{2.20}$$

where V_s is the volume of one sphere. From there, we can say that the number of spheres crossed in a unit segment is:

$$N_{seg} = \sqrt[3]{N_{vol}} = \sqrt[3]{\frac{f_s}{\frac{4}{3}\pi R^3}} \tag{2.21}$$

So for a segment of thickness t the number of spheres N encountered is:

$$N = tN_{seg} = \frac{t}{R}\sqrt[3]{\frac{3f_s}{4\pi}} \tag{2.22}$$

The local blurring G induced by this scattering is related to the opening angle α_{df} [113]:

$$G(x,y) = \frac{1}{2\pi(\alpha_{df}(x,y)z_2/2)^2} e^{-\frac{x^2+y^2}{2\alpha_{df}(x,y)z_2/2)^2}} \tag{2.23}$$

This local blurring was implemented in the ray-tracing version similarly to the refraction. As sketched in Figure 2.3, part of each beamlet intensity is spreading on the neighbouring pixels following a Gaussian blur defined by G, its intensity is redistributed in consequence.

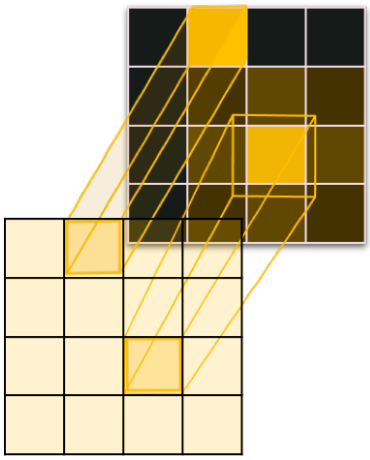

Figure 2.3: Beamlets redistribution due to dark-field blurring after propagation.

Definition: Gaussian shape - Gaussian blur.

A Gaussian shape is a symmetrical curve or scalar field representing the normal distribution. The graph of a Gaussian is a characteristic symmetric "bell curve" shape as shown on Figure 2.4. It is mathematically defined as:

$$G(\mathbf{x}) = Ae^{-(x-\mu_G)/(2\sigma^2)} \tag{2.24}$$

Where A is the amplitude of the curve (the highest value), $\mathbf{x}$ is the spatial coordinate (scalar in 1D or vector in 2D), $\boldsymbol{\mu_G}$ is the average value of the distribution i.e. the position of the center of the 'bell' and $\boldsymbol{\sigma}$ it the standard deviation of the distribution related to the width of the 'bell'. In 2D, the shape is not necessarily isotropic, it can be elongated in one direction however in most of the cases considered in this manuscript, it will not be the case and we will use a scalar value for σ to describe the size of the shape in both directions. This value sigma is directly connected to the Full Width Half Maximum (FWHM) of the Gaussian curve as $FWHM = 2.355 \times \sigma$. This quantity will often be used to describe the Gaussian shape.

A Gaussian blur is the convolution of an image with a Gaussian shape. This process will result in a smoothly blurred image.

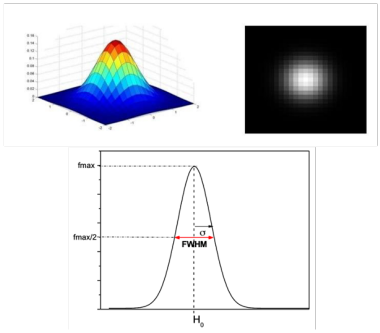

Figure 2.4: 2D and 1D Gaussian shapes representations.

Final processing to get a realistic image

The final parameters to include in the simulations are the source blurring, the detector pixel size sampling, the detector PSF and the statistical noise as outlined in Figure 2.5.

The source blurring is computed on the final intensity image as a convolution of the obtained image with the projected source shape. The source shape is assimilated to a Gaussian and its size is calculated as the

Figure 2.5: Outline of realistic image degradation for simulations: source blurring, pixel size down sampling to detector pixel size, detector PSF blurring and additional shot noise.

projection of the focal spot in the detector plane. It is usually based on the full width half maximum value given by the constructor.

For a more accurate calculation, the pixel size of the simulation is smaller than the detector pixel size so the first step is to re-sample the image at the correct pixel size. This "oversampling" of the simulation will be discussed in section 2.2.3.

Next comes the convolution with the detector PSF. Very similarly to the source, the detector PSF is assimilated to a Gaussian shape and homogeneously convoluted to the image.

In this first version, the source and detector blurring are assimilated to Gaussian blurs but this shape could be easily modified to fit more precisely defined systems PSF.

Finally, the shot noise (due to the random process of photons hitting the detector) is added. It follows a random Poisson statistic where the variance is considered to be the number of photons arriving in each pixels as was mentioned in first chapter. The detector electronic noise was not implemented as it is very difficult to model and is usually less important than the shot noise.

2.2.2 Membrane geometry

A task that proved a lot more complicated than could be expected is the membrane geometry simulation. We use randomly structured masks but what do they look like exactly? How do we reproduce their geometry numerically?

- **Characterization**

The first step was the characterization of our membranes. MoBI can be done with any kind of membranes but the ones we are working with are mainly sandpaper at the synchrotron or metal powders fabrications [67] for x-ray tube experiments. The powder-based ones are made by simply depositing metal powders on double sided tape on a PMMA[2]

2: PMMA = polymethyl methacrylate. It is a kind of engineering plastic.

thin plate. We already had an estimated idea of the size of the various grains we had been using but what about their shape? In order to have a more precise idea, we used a transmission optical microscope to try to visualize them at high resolution as shown Figure 2.6. The microscope used was a Olympus BX 50 with a x5 lens resulting in a pixel size of 0.65 µm. Because that kind of membrane is not transparent to visible light, we only obtain the contour of the grains. Thanks to their small size, the focal plane was thick enough to focus on various grains and get sharp focused edges.

As we see, the sandpaper grains have sharp random geometries. The copper powder is very dense so a few grains were deposited more spread on a plate to try and better observe their shape as shown in the small insert of the Copper powder membrane. We can see that the grains shape is quite complex for this powder.
Good news was that the bronze powder (provided by GoodFellow UK) has almost perfect spherical grains. It was therefore decided to work with that membrane.

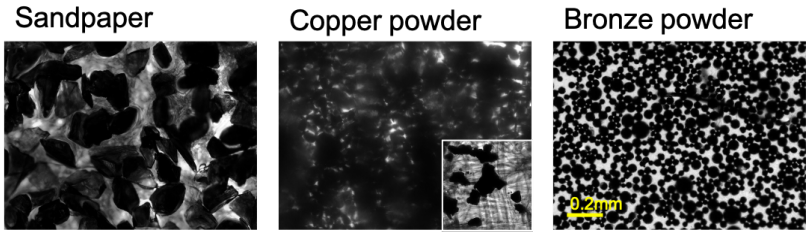

Figure 2.6: Three membranes observed with an optical microscope: one simple sandpaper sheet and two metal powder homemade membranes.

A granulometry study was done on the bronze membrane microscope images following the pipeline described in Figure 2.7 using the FIJI software.
First, the spheres are segmented from the background using a simple threshold. Then we use the Watershed function to separate adjacent particles that appear merged. Briefly, the idea of this algorithm is to find the center of each particles by erosion of the image, then filling the particles with imaginary water starting from those centers. When two wells of water touch, the algorithm 'builds a dam' to separate them.
The last step is to analyze those individual particles, counting them and measuring their areas.

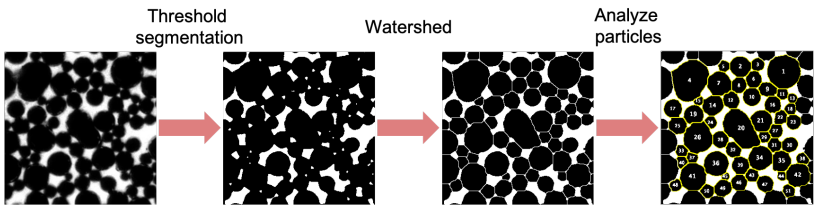

Figure 2.7: Granulometry pipeline with FIJI: threshold segmentation completed by a watershed and particles characterization.

- **First try with blender**

From this very basic segmentation a first idea was to analyze the sphere radius distribution and to try to simulate a surface covered with spheres of random radius following that distribution.

Figure 2.8 outlines the process of this membrane generation. From the segmented image, a distribution of the spheres radius with their frequency

of appearance was plotted and fitted with a Gaussian distribution.
A simulation was then done using the software Blender. Blender is a free software meant to create animated films, virtual reality, and motion graphics. We used this software to simulate a scene where a large number of spheres, with radii following the previously defined distribution, fell onto a surface delimited by vertical walls. Once the spheres were stable only the spheres in contact with the surface were kept as if they were the ones that would stick to the double sided tape. As shown on the figure, this method gave very satisfactory results in term of resemblance to the original membrane.
From this simulation, the position and radius of each sphere was extracted and stored in a text file that would in turn be read by the simulation software that creates thickness maps from those information.

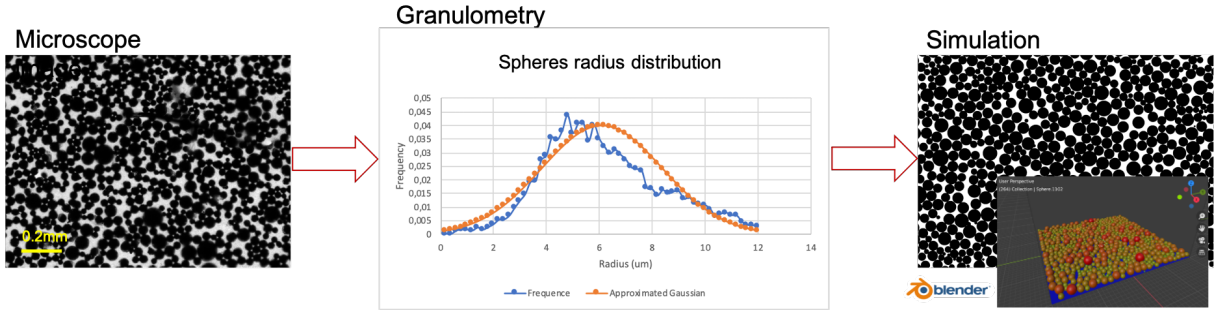

Figure 2.8: Outline of the process to simulate the membrane with blender. After acquiring microscope images of the membrane, a granulometry study was realized fith FIJI extracting the spheres radius distribution. This distribution is associated to a gaussian distribution that is used to simulate a bunch of spheres falling on a surface using Blender.

This method, even though it gave satisfactory result, had one main limitation: the computation of the membrane simulation took an extremely long time for very limited fields of view.

- **IMorph sphere meshing**

A second method was then investigated to segment and recreate the membrane geometry from a spherical mesh. This was done using the iMorph software [114]. The beginning of the pipeline is the same as for segmentation using FIJI: images are binarized with a threshold determined by Otsu algorithm. Then, a circular mesh is obtained with the following steps:

1. a distance map of the binary image is computed separating grains and background,
2. using a heap, pixels are sorted by their distance to a border value
3. starting from the pixels associated with the broader distances, disks are drawn centered around these pixels. If a pixel is already assigned to another disk, the pixel is discarded as a possible center.
4. the disks are saved in a result image and their area become background on the binary image.
5. repeat all the above to fill the image with smaller spheres until you reach a limit disk size.

A result of this segmentation is shown in Figure 2.9 c). From this segmentation, spheres radii and positions could be extracted. d) shows the distribution of measured radii.

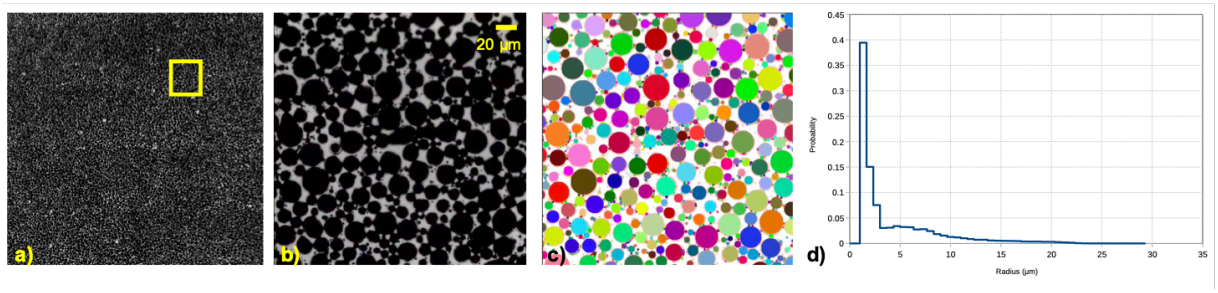

Figure 2.9: Membrane segmentation with IMorph. a) The microscope image acquired, b) an insert from this image with visible spherical grains, c) the same area where a coloured segmented spherical mesh is represented. d) The segmented spheres radii distribution.

This method, applied on very large membrane images, allowed to create virtual membranes for the simulation with a wider field of view. In the case where even this field of view was not enough, several segmented membranes were stitched together.

The advantage of recreating the thickness maps from spheres radii and coordinate is that we can play with this parameter. If we want to see the effect of bigger spheres, we simply need to scale the coordinates with the spheres radii.

2.2.3 Implementation and features

In this last section, some more details about the software implementation are given to better understand its functioning and how to use it. Among those, we discuss

- the sample geometry modelling and its geometry sampling size depending on the physical model used;
- the polychromatic source energy sampling
- the processing time of the entire simulation
- the software input and output interface

• Sample geometry sampling

In the real world, the surfaces of objects are continuous. In the numerical world, the information about this surface can either be defined by a function (as B-splines) or split into a finite number of very small surfaces each being assigned a constant value. And in the numerical imaging world, the acquired image of the sample is split into pixels defined by the detector characteristics.

While in MC simulations B-splines are often used, in analytical simulations, the sample geometry is usually approximated by a voxelized geometry. In our simulations, the samples geometries are defined by thickness maps of the different materials constituting it. This definition is possible thanks to the projection approximation. Because we only consider the phase shift and attenuation in the exit plane of the sample, summing the contributions of all the tissues encountered in a straight line (the order of the materials is of no importance).

Figure 2.10 represents all the phantoms geometry that have been implemented in the software so far. Their thickness maps are calculated for each pixel from configured size parameters such as the radius or

center positions of the spheres. In addition to simple geometric phantoms, the geometry of a contrast phantom used in tomography was designed. Finally, the Shepp Logan geometry can be simulated using the python library Phantominator. Other more complex sample geometries

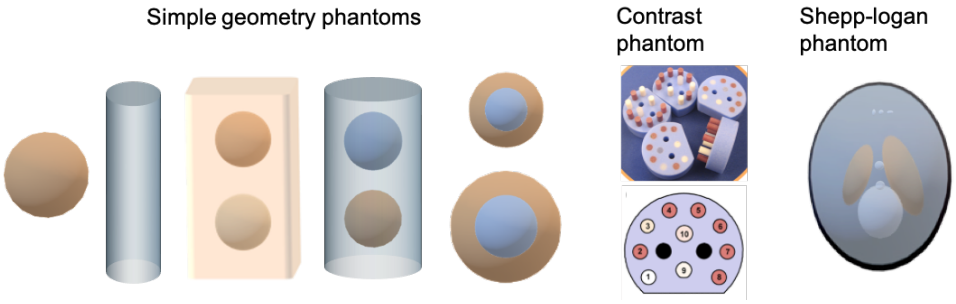

Figure 2.10: Implemented phantoms geometry.

could be easily added from high resolution segmentation of tomographic volumes.

In order to obtain the most precise simulation, this geometry often needs to be 'oversampled' compared to the detector sampling as Figure 2.11 illustrates. We will define the oversampling factor as the factor by which the detector pixel size is divided in the simulation.

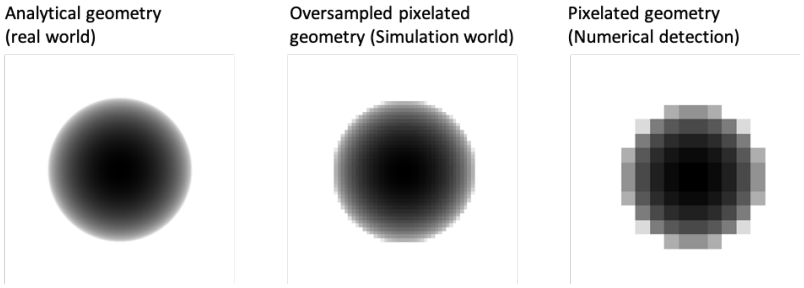

Figure 2.11: Illustration of numerical sampling of a sphere sample compared to the analytical truth.

The minimum oversampling factor required to obtain a realistic result have been studied in the wave optics model with a Fresnel propagator by Häggmark, Shaker, and Hertz [115]. According to them the maximum pixel size dx required to properly simulate propagation through Fourier space is:

$$dx < \frac{\sqrt{\lambda z_2}}{2} \tag{2.25}$$

Let's take the example of a simple propagation image of a nylon wire of 300 µm diameter placed at 20 cm from a 5 μm focal spot source at 30 keV. Lets place the detector 80 cm after the sample with a pixelsize of 50 μm and a PSF FWHM of 2.8 pixels.

In those conditions the maximum sampling computed with eq. 2.25 is 1.28 μm.

Figure 2.12 shows a simulated propagation image of this nylon wire. The noise addition was removed for visibility purposes. Profiles extracted from this same image where the simulation was sampled at different pixel sizes (dx) are displayed. It shows that the result converges when dx decreases. In agreement with the above mentioned condition, the

difference between profiles obtained with dx smaller than 1.28 μm are identical.

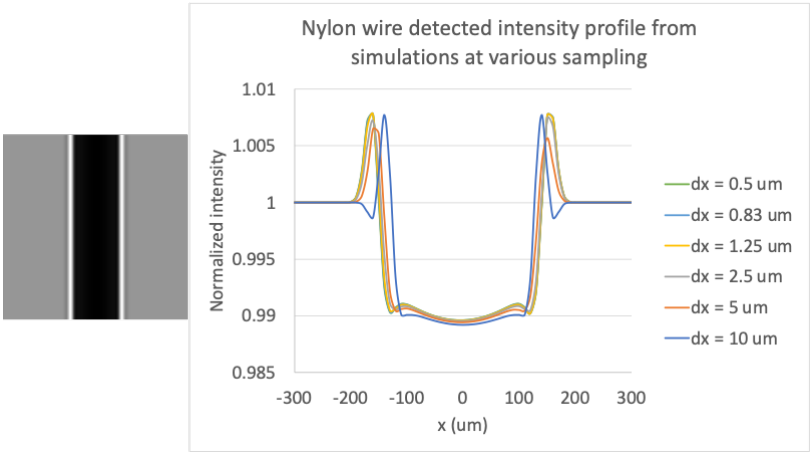

Figure 2.12: Nylon wire propagation profile with decreasing sampling size dx (i.e. increasing oversampling factor compared to the detector) in the Fresnel model.

For the ray-tracing (RT) simulation however, because there is no use of the Fourier space, the Shannon criteria, stating that the simulation sampling should be twice the detector sampling, is enough.

The same simulation of the 300 µm diameter nylon wire was done with the ray-tracing model at different sampling sizes. The detector pixels size in the sample plane is 10 µm. Results are presented in Figure 2.13. As expected, the results converges a lot faster than in the Fresnel case and appear to be consistent already with the 5 μm sampling which correspond to an oversampling factor of 2 compared to the detector.

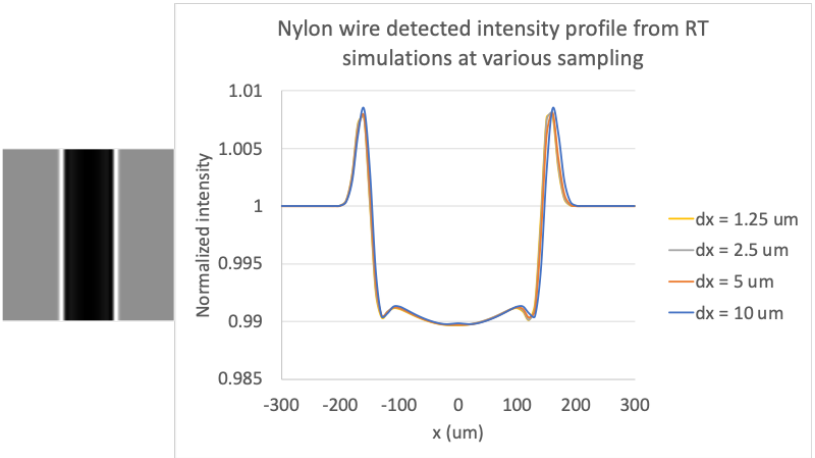

Figure 2.13: Nylon wire propagation profile with decreasing sampling size dx (i.e. increasing oversampling compared to the detector) in the Ray-tracing model.

- **Source energy sampling**

When simulating a polychromatic source, we mentioned that the calculation of the propagation was repeated with all the energies of the spectrum. This spectrum being continuous in reality, there is of course a sampling of it in the digital world. As represented in Figure 2.14, this spectrum sampling can be done every keV or every 10 keV (or every n keV as chosen by the user). This will of course influence the precision of the calculation and the consideration of the beam hardening but also the computation time. Here we can see that when diminishing the energy sampling size dE, in all likelihood, results converge (dE=0.5 keV is superimposed with de = 2 keV). When looking at the NRMSE (defined

below) of those profiles, taking dE = 0.5 keV as reference, we get an error of about 30 % for the monochromatic case and the dE = 20 keV. The error drops to 5 % at 10 keV, 1% at 5 keV and gets lower than 0.03 % at 2 keV. Because the calculation of the propagation is one of the most costing step, the computing time increases almost linearly with the number of spectrum samples. Choosing between the precision and computing time will be determined by the requirements of the simulation.

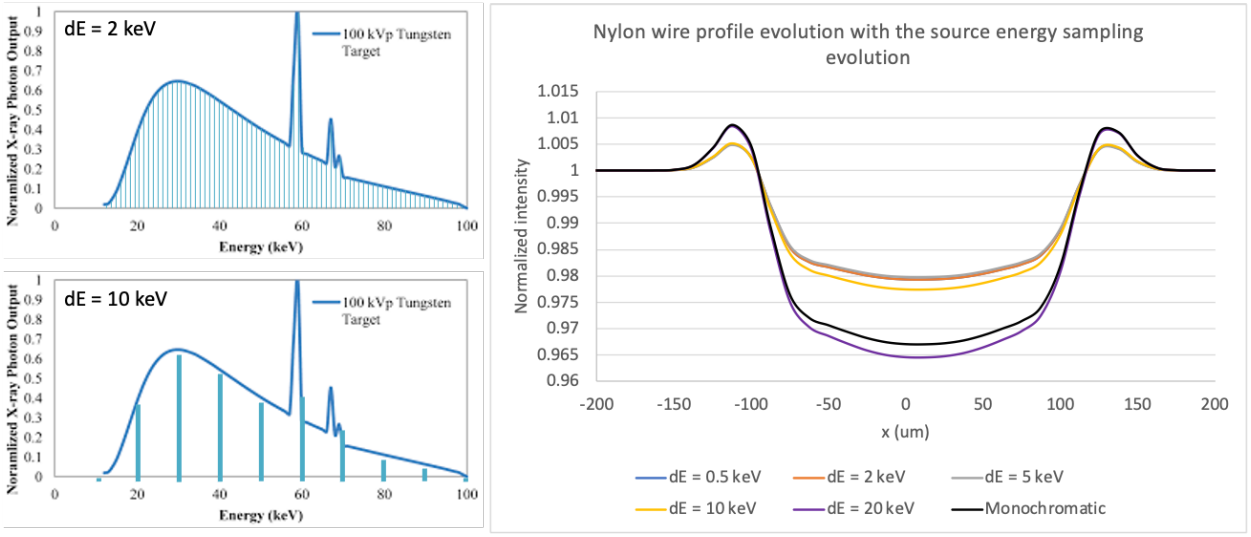

Figure 2.14: Schematic of spectrum sampling with energy bins of 2 keV and 10 keV. Nylon wire propagated profiles with different spectrum energy sampling dE.

Definition: Normalized root mean squared error.

Root mean squared error (RMSE) and normalized root mean squared error (NRMSE) are metrics that quantifies the error between two sets of data, usually an experiment and a theoretical "ground-truth" set. They are mathematically defined as follows.

$$\text{RMSE} = \sqrt{\frac{\sum_{i=1}^{N}\left(I_{exp}^{(i)} - I_{theo}^{(i)}\right)^2}{N}} \tag{2.26}$$

$$\text{NRMSE} = \frac{\text{RMSE}}{\max(I_{\text{theo}}) - \min(I_{\text{theo}})} \tag{2.27}$$

The NRMSE will be used in several experiment of this manuscript, usually to compare profiles extracted from images.

- **Processing time**

The processing time depends on various simulation parameters. As just mentioned, the source sampling in the polychromatic case will influence it but many other parameters are to be taken into account.

A first one is the simulation physical model. The Fresnel Propagator model (FP), uses simple Fourier transform multiplication while the Ray-Tracing model (RT) computes the beamlet distribution pixel by pixel which takes a lot longer. However in the case of low resolution experiments simulations, the spatial sampling requirements for the RT model is only twice the detector resolution while the one for the FP model is defined by the wavelength and propagation distance and often

requires a very small pixel size. Therefore, in some cases, simulating a final NxN image will require to compute a 2Nx2N simulation with RT and a 8Nx8N simulation with Fresnel as it was the case for the case described at the beginning of this section. Then, the FP model might become less advantageous than the RT one. Then of course the desired final field of view NxN is a major parameter to take into account for the computation time.

A second one that is quite important too, is the creation of the membrane geometry. It is a quite time consuming step. When loading the geometry from the spheres coordinates (and therefore be able to change its size and number of layers) the algorithms recreates the thickness map by computing it for every sphere one at a time. Therefore, the smaller the spheres, the more individual geometries it needs to create and the longer it takes. It also increases with the number of layers required and the field of view.

Because in some cases, the simulation was taking a very long time, we searched for a way to make the code faster. We could greatly improved the propagation processing time for ray-tracing model by the use of NUMBA which is an alternative to conventional python compiler for simple python functions. It allowed to decrease the total computation time by two to three orders of magnitude. In addition, parallelization of the computation over the energies of the spectrum is currently being implemented.

- **Software interface - Input**

Figure 2.15 summarises all the parameters that need to be defined for a simulation. The general experiment geometry, the distances and various elements that are part of the set-up, the type and parameters of the source and the detector and the characteristics and geometries of the membrane and sample of interest.

Ideally, someday, the software should have a user-friendly interface with buttons and simple fields to fill. For now, all the input parameters are chosen in xml files with a precise syntax as shown in Figure 2.16. The experiment geometries and constituting elements are defined in the Experiment.xml. Those elements are: the distances between the source, membrane, sample and detector ; the average number of photons emitted in a solid angle corresponding to one pixel of the detector ; if the experiment is done in vacuum or air ; the name of the elements defined in the other xml files. It also contains the information of whether the detector has a carbon fiber protective plate or not.

Then, in the Source.xml, monochromatic or polychromatic sources can be defined with their size corresponding to the FWHM of the emitting spot. For a monochromatic source, only the energy in keV must be given. For the polychromatic source, the voltage is required and additional features can be added:

1. a target material of the anode: Tungsten (W), Rhodium (Rh) or Molybdenum (Mo). If none is given the default material is Tungsten.
2. an exiting filter such as a Beryllium window or an Aluminum filter that will harden the spectrum (increasing its average energy value).
3. the energy sampling that was described in a previous section.

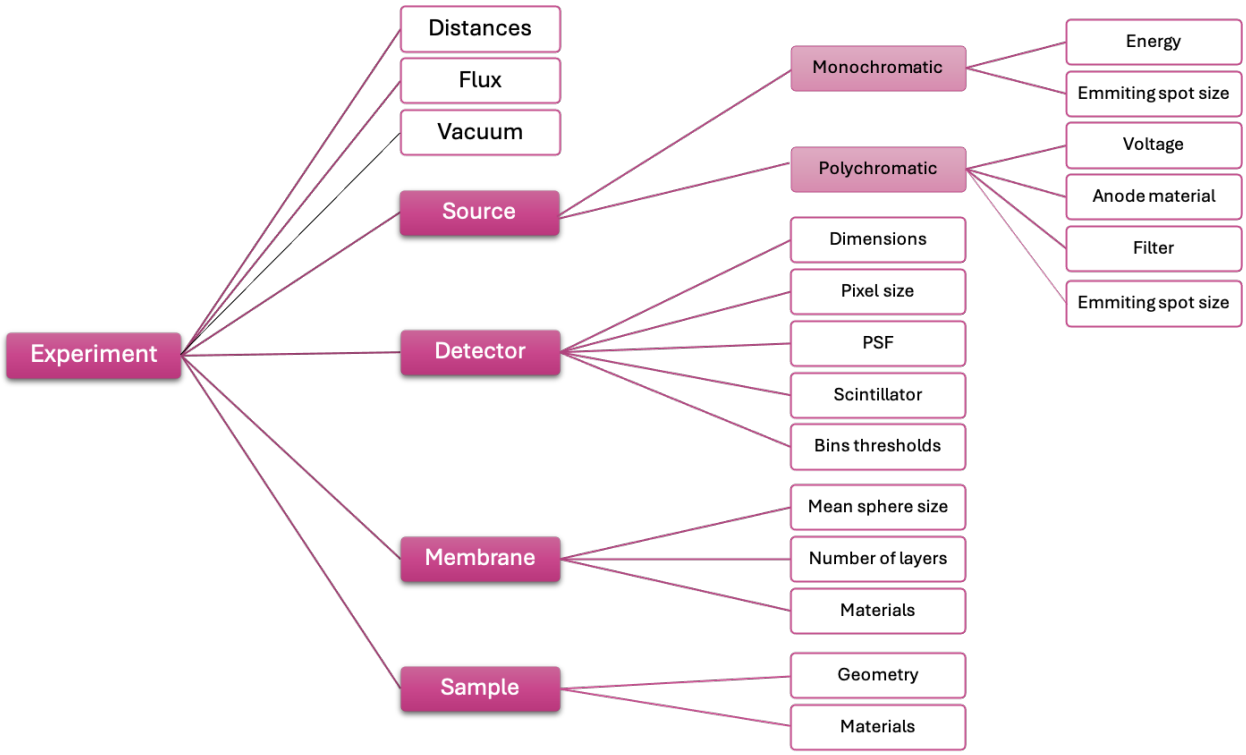

Figure 2.15: Summary of all the flexible parameters to define in the simulation.

The Detector.xml contains detectors characteristics, some that are mandatory: its dimensions in pixels, its pixel size and its PSF standard deviation. In addition, it is possible to specify if the detector is a photon counting or indirect integrating detector. In the case of a detector with a scintillator, it is also possible to specify the thickness and material of this scintillator. These last pieces of information are used to compute the probability of absorption of a photon in the scintillator depending on its energy.

Finally, in the Sample.xml there are all the specifications required to create the virtual samples and membranes. All those elements will have a list of materials constituting them and a geometry function indicating which function to use in order to create their geometry. Then, depending on the function, some additional parameters might be required such as the radius and orientation for the cylinder or the number of layers and mean sphere radius for the membrane.

- **Software interface - Output**

During the simulation, some information is displayed on the terminal for the user to check some parameters and the consistency of the simulation. The other outputs are displayed inFigure 2.17:

- Sample images set $\{I_s\}$
- Reference images set $\{I_r\}$
- Propagation image
- White field image
- Text file with all experiment and algorithm parameters.

For more details about the code, a documentation was generated using Sphinx and is available at the adress: https://quenotl.github.io/PARESIS/.

Experiment.xml

```
<listExperiment>
    <experiment>
        <name>Fil_Nylon_ID17</name>
        <distSourceToMembrane unit="m">144</distSourceToMembrane>
        <distMembraneToObject unit="m">1.6</distMembraneToObject>
        <distObjectToDetector unit="m">3.6</distObjectToDetector>
        <membraneName>Mask_CuSn_From_txt_config1</membraneName>
        <sampleName>filNylon</sampleName>
        <sampleType>AnalyticalSample</sampleType>
        <detectorName>sCMOS_ESRF</detectorName>
        <sourceName>id17</sourceName>
        <meanShotCount>30000</meanShotCount>
        <inVacuum>True</inVacuum>
    </experiment>

    <experiment>
        <name>id17_ContrastPhantom</name>
        <distSourceToMembrane unit="m">144</distSourceToMembrane>
        <distMembraneToObject unit="m">1.6</distMembraneToObject>
        <distObjectToDetector unit="m">3.6</distObjectToDetector>
        <membraneName>Mask_CuSn_From_edf</membraneName>
        <sampleName>ContrastPhantomID17</sampleName>
```

Sample.xml

```
<sample>
    <name>filNylon</name>
    <myType>sample_of_interest</myType>
    <myGeometryFunction>CreateSampleCylindre</myGeometryFunction>
    <myRadius unit="um">1000</myRadius>
    <myOrientation unit="degree">30</myOrientation>
    <myMaterials>Nylon</myMaterials>
</sample>

<sample>
    <name>Mask_CuSn_From_txt</name>
    <myType>membrane</myType>
    <myGeometryFunction>getMembraneSegmentedFromFile</myGeometryFunction>
    <myMembraneFile>Samples/Membranes/CuSn.txt</myMembraneFile>
    <myPMMAThickness unit="um">4000</myPMMAThickness>
    <myMaterials>CuSn,PMMA</myMaterials>
    <myMeanSphereRadius>15</myMeanSphereRadius>
    <myNbOfLayers>2</myNbOfLayers>
</sample>

<sample>
    <name>PMMA_sphere</name>
    <myType>sample_of_interest</myType>
    <myGeometryFunction>CreateSampleSphere</myGeometryFunction>
```

Source.xml

```
<source>
    <name>id17</name>
    <myType>Monochromatic</myType>
    <mySize unit="um">10</mySize>
    <myEnergy unit="kev">52</myEnergy>
</source>

<source>
    <name>simap</name>
    <myType>Polychromatic</myType>
    <mySize unit="um">8</mySize>
    <sourceVoltage unit="kVp">40</sourceVoltage>
    <filterMaterial>Be</filterMaterial>
    <filterThickness unit="mm">0.2</filterThickness>
    <myEnergySampling unit="keV">0.5</myEnergySampling>
    <myTargetMaterial>W</myTargetMaterial>
```

Detector.xml

```
<detector>
    <name>sCMOS_ESRF</name>
    <myDimensions>
        <dimX>200</dimX>
        <dimY>200</dimY>
    </myDimensions>
    <myPixelSize unit="um">6</myPixelSize>
    <myPSF unit="pixel">1</myPSF>
</detector>

<detector>
    <name>flatPanelSimap</name>
    <myDimensions>
        <dimX>300</dimX>
        <dimY>400</dimY>
    </myDimensions>
    <myPixelSize unit="um">50</myPixelSize>
    <myPSF unit="pixel">1</myPSF>
    <photonCounting>True</photonCounting>
    <myScintillatorMaterial>CsI</myScintillatorMaterial>
    <myScintillatorThickness unit="um">600</myScintillatorThick
```

Figure 2.16: xml files used for input parameters of the simulation program.

The program is shared on the gitHub: https://github.com/quenotl/PARESIS where a detailed user guide is provided.

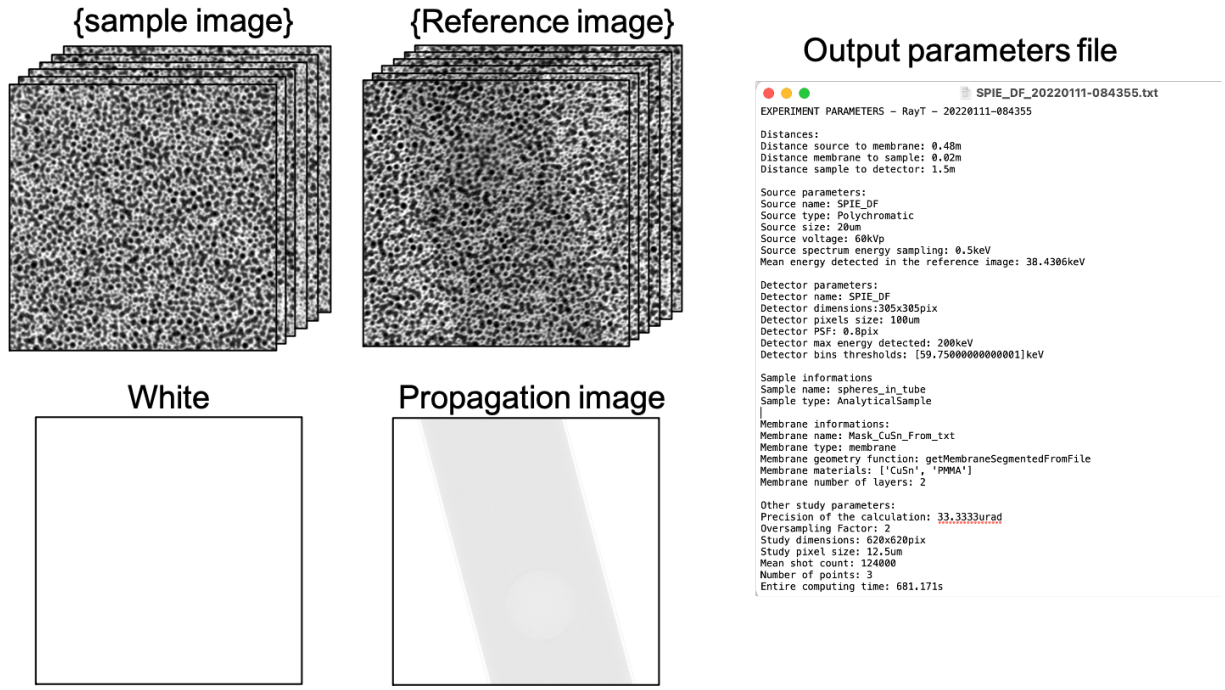

Figure 2.17: Example output of the simulations: sample and reference images set, propagation image, white field and a text file with a summary of the experiment and algorithm details.

2.3 Validations and limitations

The phase simulations were validated on both synchrotron and laboratory x-ray tube cases with simple nylon wires as the samples. The simulated images were compared to real experiments and with results obtained with GATE MC simulations. These results were published in Physics in Medicine and Biology [116] .
Dark-field validations were only done on a synchrotron experiment and are not yet published.

[116]: Laurene Quenot, Emmanuel Brun, Jean Michel Létang, and Max Langer. 'Evaluation of simulators for x-ray speckle-based phase contrast imaging'. In: *Physics in Medicine & Biology* (2021)

2.3.1 Phase effects validation on a monochromatic synchrotron set-up

A first validation of the simulation code was done for a synchrotron experiment case. The experiment was done at the ID17 beamline of the ESRF with the following parameters:

Experiment 2.1: Nylon wire - ID17

- Distance source to membrane (z_0): 138 m
- Distance membrane to sample (z_1): 1.5 m
- Distance sample to detector (z_2): 3.6 m
- Source: ID17 - 33 keV
- Detector: CCD camera with magnifying optics → effective pixel size of 3 µm
- Membrane: 2 layers of CuSn spheres of 100 µm average size on PMMA plates (the same that was characterized with the

microscope and used for the simulations).
- Sample: Nylon wire of 140 µm
- Number of membrane positions acquired: 10

To compare the phase retrieval results that could be obtained with the simulations, the Unified Modulated Pattern Analysis algorithm (UMPA) developed by Zdora et al. [117] was used as it does not require any assumptions on the sample. This phase retrieval method will be introduced in the Chapter 3.

Figure 2.18 shows the propagation, sample and reference images of this nylon wire from experiment and simulations. The first observation is that all three simulation methods give visually identical results. For the membrane images, we can see that the simulated modulations appear sharper and more contrasted than the experiment one. This might be due to the tape used to glue the grains to the PMMA that may diffuse a lot and that is not taken into account in the simulations. When looking at the retrieved displacement maps [3] now, we can see that, once again, all simulated images give visually identical results similar to the experiment even though this last one appear noisier. This is probably related to the loss of visibility noticeable in the I_r and I_s images. As the modulations are less contrasted, it is more difficult to track their displacements.

3: **Remark:** We use here the term displacement maps to describe the retrieved information. As mentioned in the first chapter, in the conditions considered in this work, the displacement is proportional to the refraction angle. Therefore, these 'displacement maps' are identical to what could be called 'refraction maps' as their relative image contrasts are proportional. The only difference would be the absolute values of the grey scale.

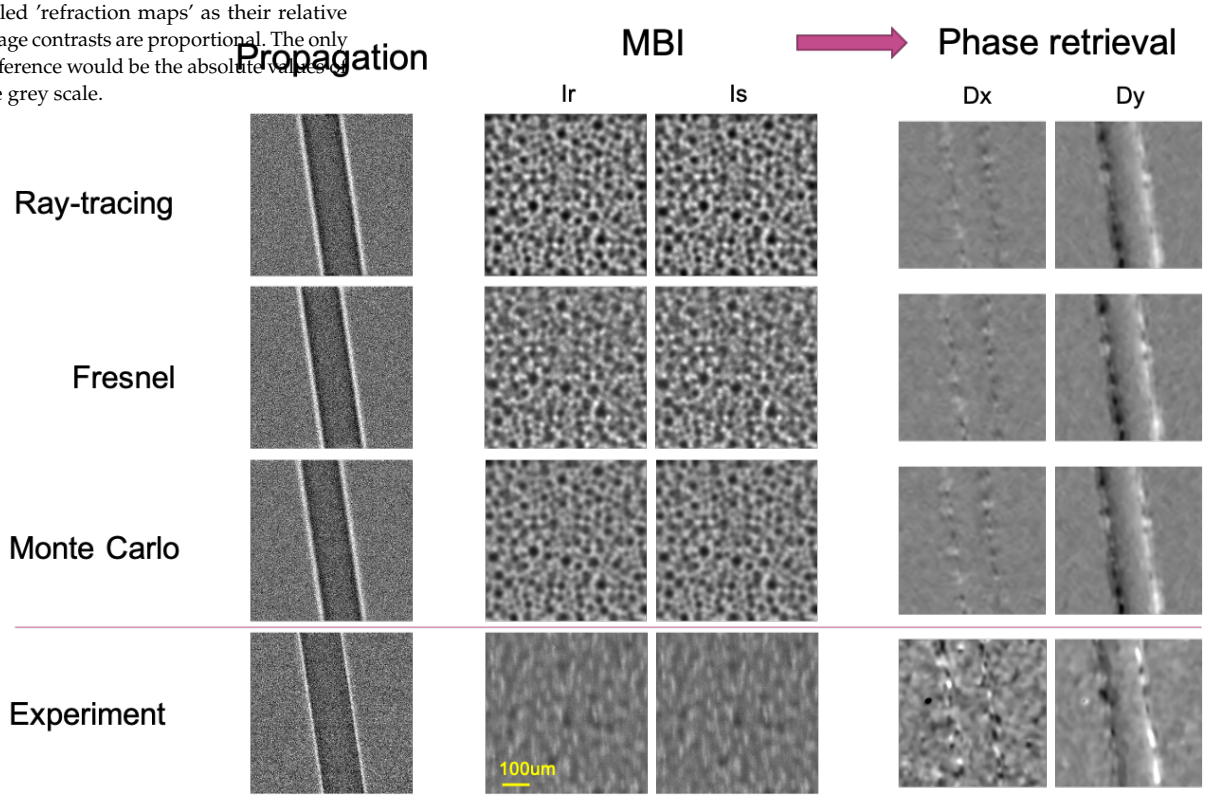

Figure 2.18: Monochromatic nylon wire sample, reference and propagation images. The images are from a real experiment and 3 simulations: the two models previously introduced (RT and Fresnel) and a Monte Carlo approach from the GATE software. The Dx and Dy retrieved displacement maps were obtained with the UMPA algorithm.

Figure 2.19 presents profiles extracted from the previous images. (a) shows profiles from the propagation images from lines perpendicular to the nylon wire and averaged over 20 consecutive lines to reduce the effects of noise. This confirms that the simulations give quantitatively

identical results and are quite similar to the experiment. A normalized root mean squared error was computed on those profiles comparing the simulated profiles to the experimental one on the varying part (not the noise outside the sample). The results show that the error between each simulation method and the experiment is about 13%.

The second graph from Figure 2.19 shows profiles from the displacement maps Dy averaged over 30 lines perpendicular to the nylon wire. It shows that the retrieved displacements from the simulations are agreeing with the experimental ones. The experimental profiles appear to have a slight offset which might be due to a small involuntary movement of the membrane between the reference and sample images acquisitions. This is the kind of experimental variability that cannot be taken into account in the simulations and renders this experiment always more unpredictable than the simulation.

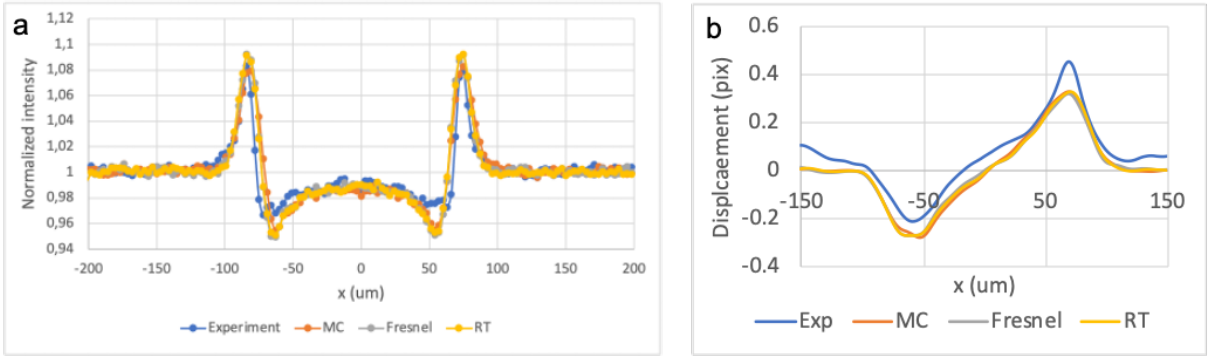

Figure 2.19: Profiles extracted from lines perpendicular to the nylon wire from the propagation images (a) and from the displacement images Dy (b).

These results are proof that the simulation software developed with both ray-tracing and Fresnel propagator models provide results of similar quality than GATE. In addition, those results are in very good agreement with the synchrotron monochromatic experiment and display quantitative refraction. The remaining difference between the simulated and experimental propagation profiles might be due to the simplified shape of the detector PSF which plays a very important role in the detected intensity as shown in Figure 2.20. This figure also shows that at very high system resolution the different simulation methods show some contrast variations that are erased by the PSF. This is particularly true for the Fresnel model as it is expected to compute interference fringes while MC and RT simply compute refraction.

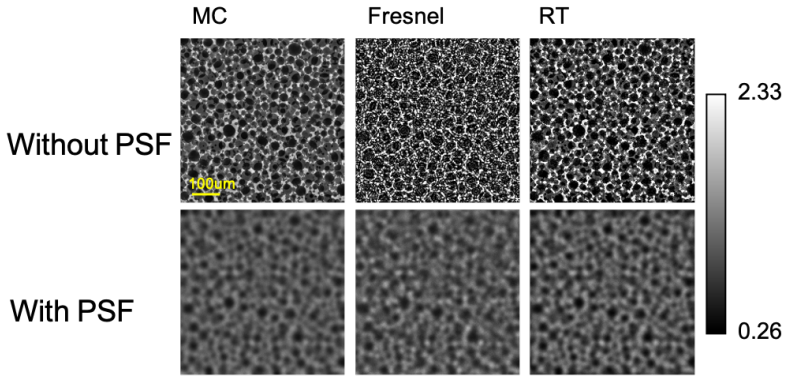

Figure 2.20: Reference images simulations with and without taking into account the detector PSF.

2.3.2 Phase effects validation on a polychromatic laboratory set-up

A similar nylon wire experiment was done on a laboratory set-up. The set-up was mounted in an EASYTOM XL Micro machine from RX Solutions.

Experiment 2.2: Nylon wire - Laboratory micro-CT

- System: adapted EASYTOM XL tomographic set-up from RX Solution, France
- Distance source to membrane (z_0): 4.15 cm
- Distance membrane to sample (z_1): 2.15 cm
- Distance sample to detector (z_2): 62.2 cm
- Source: micro-focus tungsten rotating anode with a focal spot of 5 μm FWHM and operating at 40 kVp with a 200 µm thick beryllium existing window.
- Detector: Flat panel with a pixel size of 127 µm with a 2.5 mm thick carbon fiber protective plate.
- Membrane: 2 layers of CuSn spheres of 100 µm average size on PMMA plates (the same that was characterized with the microscope and used for the simulations).
- Sample: Nylon wire of 200 µm of diameter.
- Number of membrane positions acquired: 25.

The air volume present between the source and the detector was taken into account as it absorbs significantly the low energies.

Figure 2.21 presents the simulated images and experimental ones obtained in simple propagation and with the membrane. As for the monochromatic case, the simulated images appear almost identical and very similar to the experiment. Profiles were once again extracted from the propagated images without membrane and are displayed on the graph. In this case the NRMSE computed between the simulated and experimental profiles are close to 8 %.

In this polychromatic case, the beam hardening due to various elements of the set-up plays a crucial role. Figure 2.22 presents the simulated profiles of the propagated nylon wire image when taking into account various elements of the chain. Those elements are the source exiting window which is composed of a 200 μm thick Beryllium film, the air volume between the source and detector and the detector protective plate made of a 2.5 mm thick carbon fiber. These will attenuate the beam homogeneously in the (x,y) plane but differently according the the photons energy. The low energies will be absorbed significantly on their way to the detector which means that the detected spectrum mean energy will be higher than the emitted spectrum. In addition, the detector scintillator (600 μm of CsI) efficiency was taken into account with its probability of absorption for each photon energy.

The left hand side plot, shows that the various elements will greatly influence the profiles of the wire on the propagated image. This difference is due to the beam hardening induced by the attenuating elements. The detector plate appear to be the more important element as we can see the difference between the yellow and gray profiles with and without it. The

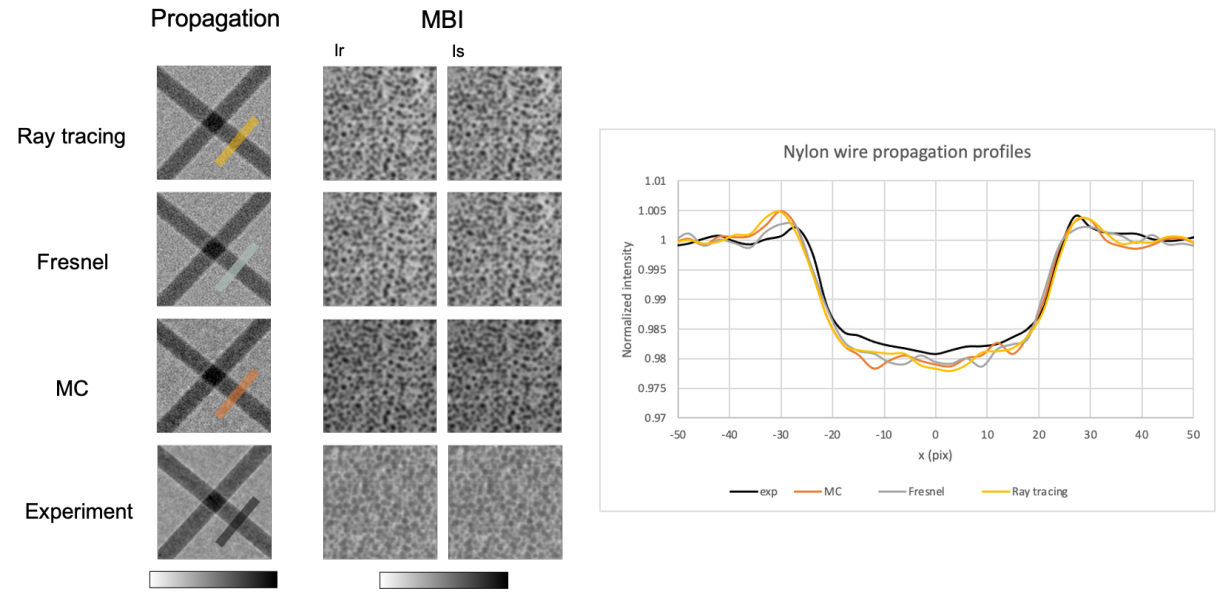

Figure 2.21: Propagation sample and reference images from polychromatic simulations and an experiment. Extracted profiles from the propagation images.

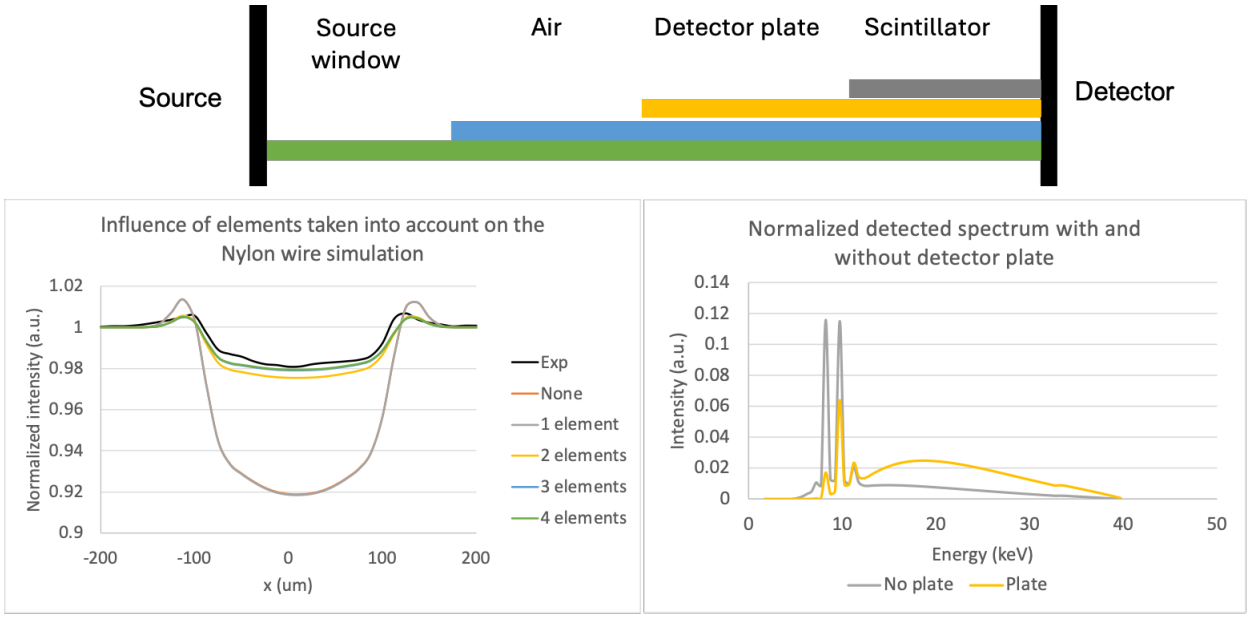

Figure 2.22: Profiles of the simulated nylon wire compared to the experiment when taking into account various elements of the chain. Profiles with only the sample and no other elements (None), then, adding the efficiency of the scintillator (1 element), adding the detector protective plate (2 elements), adding the air volume (3 elements) and finally adding the source beam exiting window (4 elements). The second graph shows the normalized spectrums from the intensity detected in the white image at each energy with and without the detector plate.

spectrum detected in those two cases is represented on the right hand side graph. We can see that, in presence of the plate, the high energies are a lot more intense than without it.
This demonstration was done with the ray-tracing simulation but other models give identical results.

These studies proves two important things:

1. The developed program allows to simulate very accurately polychromatic experiments

2. In the polychromatic case, all the absorbing elements that might be in the path of the beam will have a big impact on the detected propagated image.

2.3.3 Comparison of the dark-field simulation to a synchrotron experiment

The dark-field model is only implemented in the ray-tracing approach which is therefore the only one being compared to the following experiment. The experiment considered here was also done on the ID17 beamline at the ESRF.

Experiment 2.3: Glass beads tube - ID17

- Distance source to membrane (z_0): 138 m
- Distance membrane to sample (z_1): 1.5 m
- Distance sample to detector (z_2): 3.6 m
- Source: ID17 - 29 keV
- Detector: Photon counting Eiger from Dectris with pixels of 75 µm
- Membrane: Sandpaper stack
- Sample: Tube filled with glass beads (SiO2) of 100 µm of diameter.
- Number of membrane positions acquired: 15

For the simulations, it was assumed that the beads were arranged in a random packing occupying 64 % of the volume. A cone geometry filled with constant radius beads was simulated.

From simulated and experimental acquisitions, the dark-field signal was retrieved using an algorithm called LCS[4] .

4: LCS stands for Low Coherence System algorithm. It is a phase and dark-field retrieval algorithms that I developed that proved to be very fast and sensitive to small displacement. It will be described in the chapters 3 and 4.

Figure 2.23 shows the simulated cone geometry and the dark-field image retrieved from the simulation along with the dark-field from the experiment. The extracted profiles from both simulation and experiment are plotted on the graph. We can see that the values are very close to each other and the computed NRMSE is below 12%. The experimental signal appears slightly stronger close to the center. It might be due to a complementary source of scattering that was not taken into account or to the difference in noise present in the acquisition and simulation.

This results is a first confirmation that the simulation method for dark field is realistic and that the model is quantitative.

2.3.4 Limitations

To conclude on this simulation program, it appears appropriate to mention its limitations.

Among these, the membrane blurring due to the source can be mentioned. The source blurring is modeled by computing its projected shape as illustrated in Figure 2.24. The shape projected in the detector plane depends on the distances between all elements. Because this blurring can

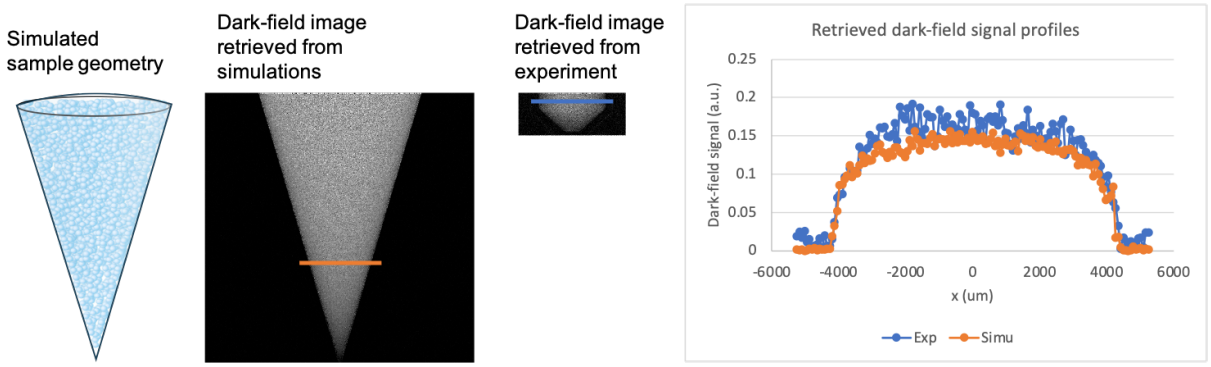

Figure 2.23: Dark-field simulation compared to the experiment. Glass beads cone geometry. Retrieved dark-field from the simulations. Retrieved dark-field from the experiment. Plot of the dark-field extracted profiles.

only be applied to the final intensity image, only one projected source shape could be defined for the sample and membrane. It was decided to use the position of the sample in the program but this causes the blur to the membrane image to be under-estimated.

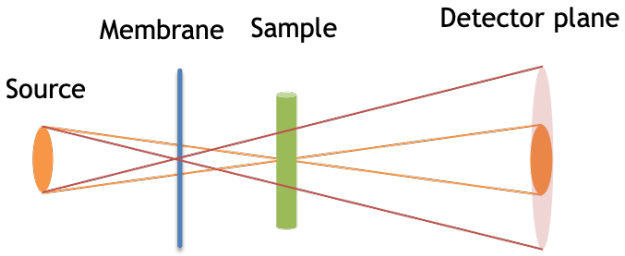

Figure 2.24: Schematic of the source projected shape in the detector plane with respect to the sample (orange) and to the membrane (red).

A second limitation of the code is its absence of consideration of geometric deformation when considering large samples in a cone beam geometry. In our models, it was mentioned that we use the projection approximation that approximates the ray path in the sample to be following parallel straight lines. However, as illustrated in Figure 2.25, in the case of large samples, the cone beam rays do not follow parallel lines in the sample. This cone beam will induce a geometric deformation of the sample image detected compared to a parallel beam case. This geometric deformation of large samples in cone beams is not treated in our simulations as the samples we are interested in are usually very small compared to the propagation distances. In order to compensate for it we should create the sample geometry accounting for this deformation.

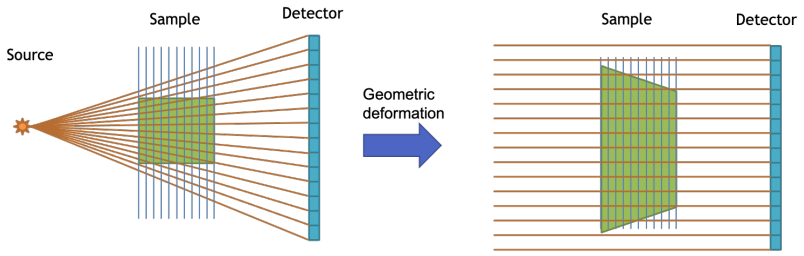

Figure 2.25: Schematic of the sample geometric deformation to take into account in the case of a cone beam geometry and a thick sample.

It should also be mentioned that the simulation deals badly with samples that have very sharp edges such as a cube with faces parallel to the propagation axis.

2.4 Optimization of MoBI based on simulations

The work presented in this section was done together with Robin Gallix, a Master 2 intern partly under my supervision.

Since its implementation and validation, the program has been used in different specific set-up optimization studies. The optimization studies that were conducted and their analysis are experiment-specific and transfer to other cases must be analyzed while taking a step backwards. The main parameters that have been studied so far are:

1. The influence of the number of membrane positions and total acquisition dose on the refraction and phase images.
2. The influence of the number of photons per acquisition.
3. The influence of low energy filtering on the displacement maps of very attenuating samples.

2.4.1 Influence of the number of membrane positions

This first study was for a laboratory set-up with the following characteristics:

Experiment 2.4: Phantom pairs of spheres - Simulation

- Distance source to membrane (z_0): 8 cm
- Distance membrane to sample (z_1): 2 cm
- Distance sample to detector (z_2): 70 cm
- Source: 8 µm FWHM micro-focus Tungsten anode at 40 kVp with a 4 mm aluminum filter
- Detector: photon counting Eiger with 75 μm pixels and a PSF of 1
- Membrane: CuSn powder membrane
- Sample: Pairs of spheres of different sizes, a sphere of cartilage, superimposed with a sphere of muscle

The dose, as defined in Chapter 1 is related to the energy, the mass attenuation coefficient and the fluence. The fluence is defined as a number of photons per meter square. In the simulation program, the defined value is the number of photons per pixel leaving the source so a number of photons per pixel surface S_{pix}. The relation between the fluence Φ and the number of photons N is then quite simple: $\Phi = N/S_{pix}$. Then we can compute the number of photons per pixel for a given dose D:

$$N = \frac{DS_{pix}}{E\mu_{en}/\rho} \tag{2.28}$$

Here $S_{pix} = 75 \times 75\mu m^2$, E is the mean spectrum energy: about 30 keV and $\mu_{en}/\rho = 0.156$ mass attenuation coefficient of water at 30 keV.

The simulation was done for two dose values: 0.1 mGy and 1 mGy for the total acquisitions and was repeated for various number of membrane positions. This means, as described in Table 2.1, that the more membrane positions used , the fewer photons per individual exposure we get, but in total, the number of photons used for the experiments at identical dose were constant.

Number of membrane positions	N photons per pixel per position	Total photons per pixel in total experiment
3	25 000	75 000
5	15 000	75 000
7	10 000	75 000
13	5 800	75 000

Table 2.1: Summary of the number of photons per pixel per position in each acquisition depending on the number of membrane positions.

From those simulated experiments, the refraction and phase were retrieved with the LCS algorithm. Results at 0.1 mGy are shown in Figure 2.26. This result shows that at constant dose, the higher the number of membrane positions, the lower the noise in the refraction and phase reconstruction. This evolution however does not appear to be linear.

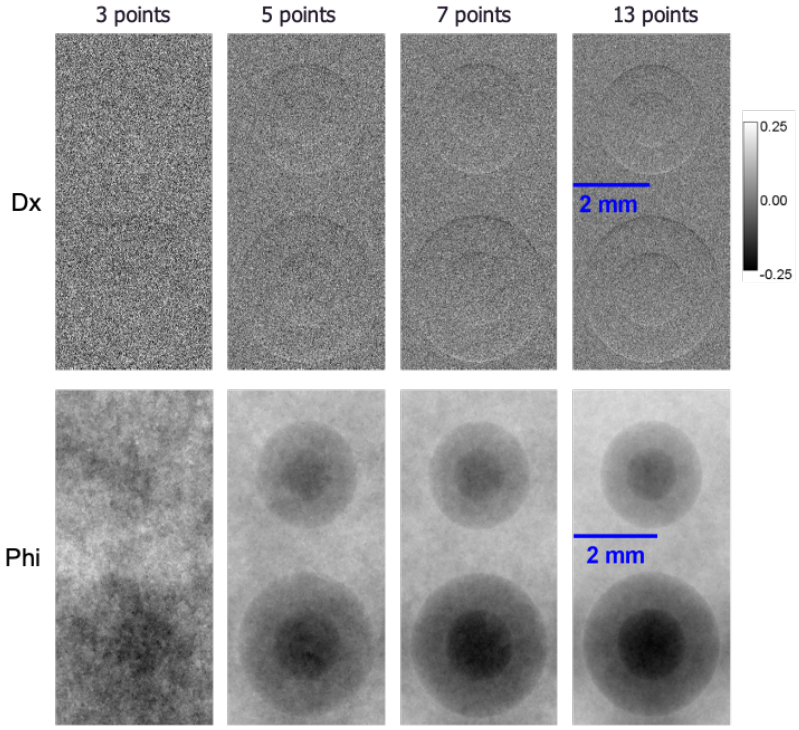

Figure 2.26: Refraction and phase images of a simple phantom retrieved from simulated images. Simulations comprised a constant total number of photons on the set of acquisition simulated but with an increasing number of membrane positions (75 000 photons per pixel in average = 0.1 mGy).

Figure 2.27 shows the same refraction and phase images but from simulations at 1 mGy. The same evolution of the image quality with an increasing number of membrane positions is observed. The noise present in the refraction images can be quantified by the standard deviation of the noise present in the background of the image where there should be no intensity variation due to the sample. Figure 2.28 shows the evolution of this noise with an increasing number of membrane positions (or measurement points) for the two dose experiments. We can see that the noise decreases but with a curve that is far from linear. The noise is very important with only 3 measurements but decreases very rapidly when reaching 5 and 7 points. We can also note that for a dose that is ten times higher, the resulting image does not have ten times less noise.

A similar experiment was done at the ESRF on the ID17 beamline. A nylon wire was imaged with an increasing number of membrane positions but decreasing exposure time (i.e. decreasing photons per pixels per acquisition). Results are presented in Figure 2.29. The experimental results confirm what was seen with the simulations: increasing the number of membrane points with lower exposure time per acquisition gives less noisy phase images.

2.4.2 Influence of the number of photons per acquisition

With identical simulation parameters (exp. 2.4 p. 72), a study with a constant number of membrane positions (10 positions) but an increasing

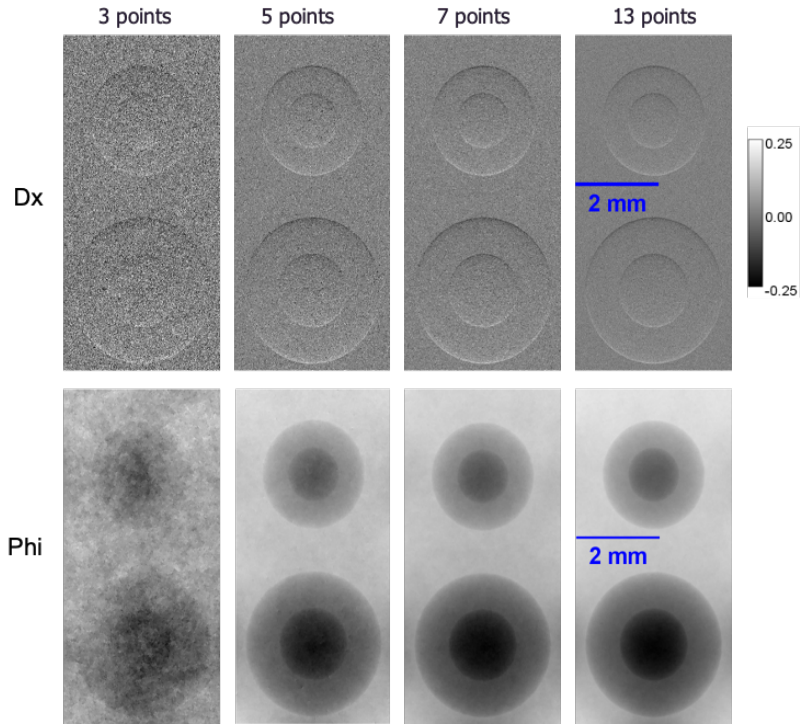

Figure 2.27: Refraction and phase images of a simple phantom retrieved from simulated images. Simulations comprised a constant total number of photons on the set of acquisition simulated but with an increasing number of membrane positions (750 000 photons per pixel in average = 1 mGy).

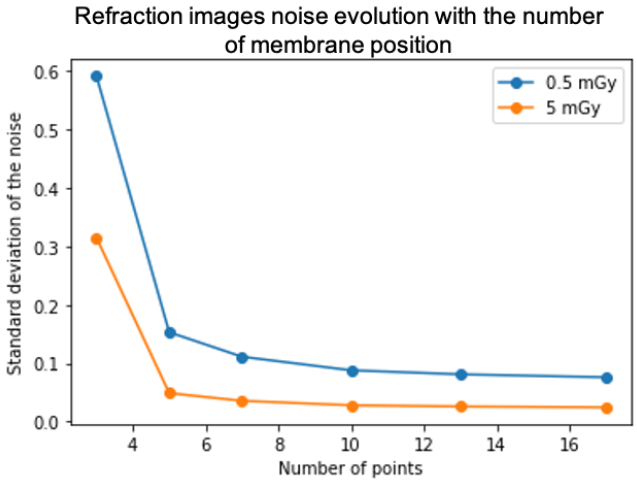

Figure 2.28: Evolution of the standard deviation of the noise in the background of the displacement maps with an increasing number of membrane positions as presented on the two previous figures.

the number of average photons per pixel per acquisition was performed. From the retrieved displacement maps, the noise standard deviation was extracted and is displayed on Figure 2.30. As is shown, the noise reduction in the displacement map is not linear with the number of photons (i.e. the dose). This parameter will be crucial when considering imaging real patients for the balance between the dose received by the patient and the visibility of the structures in the images. Note that the visibility is a tricky concept and cannot be fully described by this noise quantification. Still the results will be correlated.

2.4.3 Influence of low energy filtering

As mentioned in the previous section, in polychromatic cases, the elements present in the path of the beam will induce a modification of the

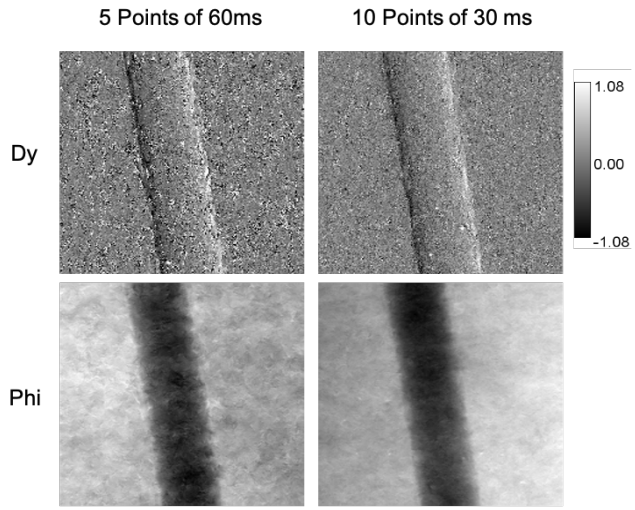

Figure 2.29: Displacement maps and integrated phase of a nylon wire from a synchrotron monochromatic experiment. Two acquisition schemes were followed one with 5 membrane positions, the other with 10 membrane positions but with the same total exposition time.

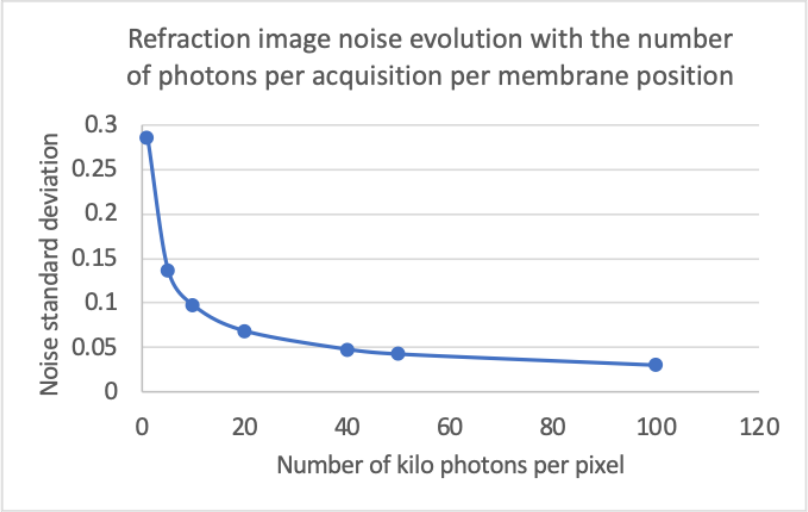

Figure 2.30: Evolution of the noise in displacement maps when increasing the number of photons per pixel per acquisition with 10 membrane positions.

spectrum, increasing its average value. It was observed that in polychromatic cases, with strongly absorbing samples, an artefact appears in the retrieved images. The same experimental conditions as in the previous experiment (exp. 2.4) are used but instead using spheres made of bone of 2 mm of diameter as the samples. It remains a small sample but bone is highly absorbing at low energies as delivered by the tungsten anode at 40 kVp.

Simulations and phase retrieval were computed with an increasing aluminum filter thickness placed just after the source. Results are displayed on Figure 2.31. We can see that, without any filtering, there are a lot of noisy artifacts in the sphere and when increasing the thickness of the aluminum filter, the artifact decreases. This artifact evolution was quantified using the standard deviation measured in a square in the sample (see blue square) as this noise appears a lot stronger than the displacement measured there. This quantity is displayed on the graph of the figure. It shows that the noise decreases when increasing the aluminum filter thickness until it reaches a plateau that corresponds to the shot noise that we also get in monochromatic cases. This artifact is probably due to beam hardening in the sample that will distort the membrane modulations in the sample image. This phenomenon is reduced when

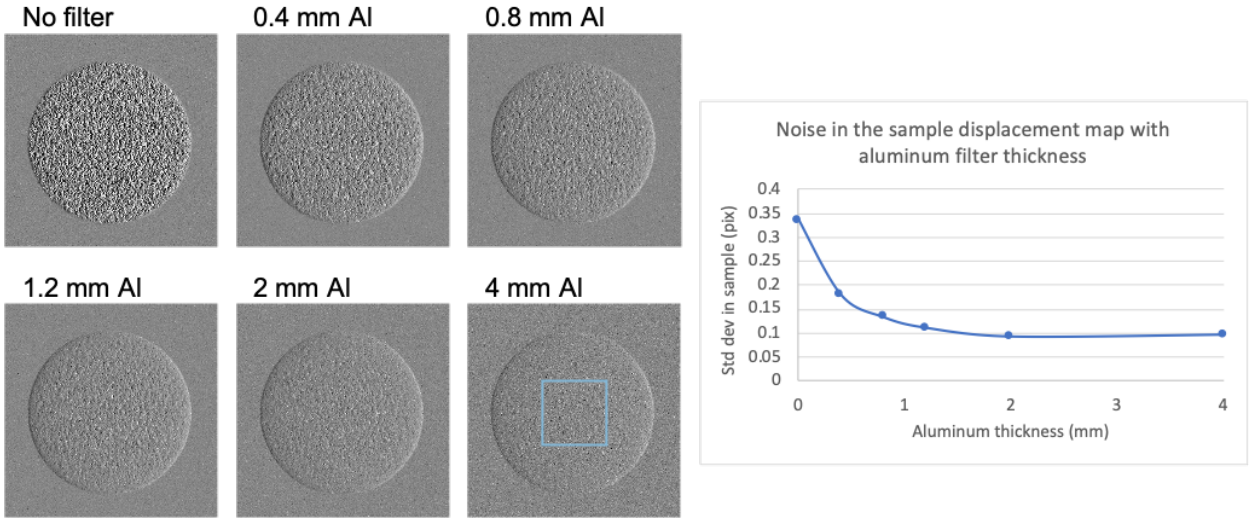

Figure 2.31: Displacement maps of a bone sphere from simulation with an increasing aluminum filter thickness behind the source. Plot of the standard deviation of an area inside the sample (illustrated by the blue square on the last image) from the different images.

using an aluminum filter as it already attenuates a lot the low energies as shown on Figure 2.32 (a).
Figure 2.32 (b) plots the fraction of the flux reaching the detector when increasing the aluminum thickness. It starts at 0.6 without the aluminum filter as part of the flux is already absorbed in air. It is interesting to notice that, up to a certain point, filtering the low energies gives better results even if the flux is highly reduced. It appears however that, in this case, above 2 mm of aluminum the standard deviation in the sample stops decreasing, probably replacing the beam hardening artifact by shot noise. This is due to a too a small flux reaching the detector as we can see that with 4 mm of aluminum, only 0.3 % of the beam reaches the detector.
Figure 2.32 (c) displays the average spectrum energy and the standard deviation of the spectra reaching the detector with the increasing aluminum thickness. As the thickness increases, the mean energy increases and the standard deviation decreases which means that the temporal coherence length increases. It is hard to affirm with certainty which of those is correlated to the reduction of the artifact. We can however make the hypothesis that it is the standard deviation of the spectrum that is responsible for it. If the artifact is indeed due to beam hardening in the sample, distorting the modulations when the low energies are being absorbed, we can assume that with a narrower energy bandwidth, this distortion will be reduced.

2.4.4 Conclusion

To conclude this part, after listing our simulation needs for MoBI optimization and an extensive look at the existing resources, I decided to implement our own simulation software. Table 2.2 summarizes the initial specifications for the simulations and how PARESIS meets them.

As summarized in Table 2.2, the initial specifications have been largely respected and I managed to deliver a software that is a great tool to start the optimization of MoBI!

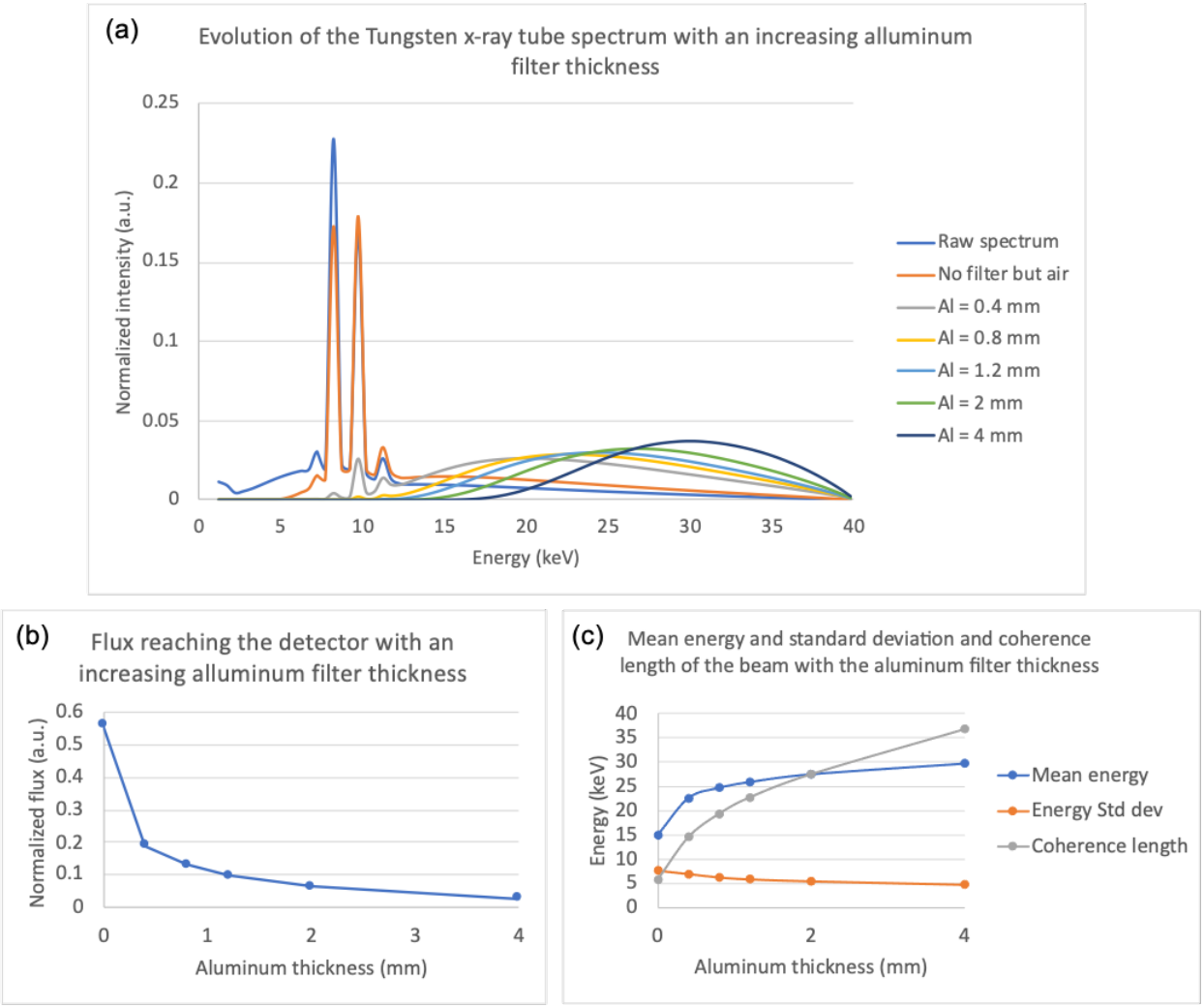

Figure 2.32: a) Normalized spectrums reaching the detector in the white field with increasing thickness of the aluminum filter. b) Fraction of the initial emitted flux reaching the detector with increasing thickness of the aluminum filter. c) Mean energy and standard deviation and transversal coherence length of the beam.

Following its elaboration, the influence of various parameters have been investigated such as such as:

- the number of membrane positions : it is better having numerous membrane positions than a lot of photons per acquisition,
- the number of photons per acquisition : a higher number of photons leads to less noisy phase images but with a non linear relationship,
- the influence of a polychromatic source and low energy filters: beam hardening artifacts appear with a polychromatic source that can be reduced by using low energy filters.

Table 2.2: PARESIS software final appraisal compared to initial specifications.

Specification	Assessment
Quantitative phase effect simulation	Validated on synchrotron and laboratory set-up
Realistic noise representation	Shot noise following the standard Poisson statistic
Possibility to implement complex geometries for the sample and membrane	Geometries easily modelled from pixelated thickness maps (possibility to add complex segmented geometries). Geometric deformation for large sample in cone beam geometry not taken into account.
Take into account the influence of the source spot size	Calculation of the projected size with respect to the sample and assimilation to a Gaussian blurring. Not precise for the membrane blurring.
Possibility to simulate the detector point spread function	Assimilation to a Gaussian blurring
Rapid computation	Thousands of times faster than MC simulations
Possibility to implement dark-field phenomenon	Done with the ray-tracing model
User friendly	Not trivial to use but user guide available

Résumé du Chapitre 2 en Français

Ce second chapitre présente le travail réalisé sur les simulations pour optimiser l'expérience d'imagerie par modulations. Après un état de l'art des logiciels de simulations d'imagerie x en contraste de phase existant, le programme que j'ai développé spécifiquement pour simuler notre expérience est décrit. Les modèles physiques ainsi que les paramètres expérimentaux considérés sont détaillés. Les deux dernières parties présentent les validations de l'outil faites à travers des comparaisons avec des résultats expérimentaux et les travaux d'optimisations de l'expérience qu'il nous a permis de faire.

Parmi les logiciels permettant de modéliser des expériences d'imagerie en contraste de phase SHADOW, GATE, OASYS, SRW, aucun ne semblait présenter la flexibilité pour modifier simplement les paramètres que nous voulions utiliser ou la rapidité de calcul qui permettrai de faire des études à la chaîne sur ces paramètres. D'autres travaux indépendants réalisés pour des simulations similaires ont été considérés mais ceux-ci ne sont pas en libre accès et manquent des paramètres clés à prendre en compte pour un résultat suffisamment proche de la réalité. Finalement, il fut décidé de créer notre propre programme de simulations en utilisant les ressources disponibles telles que NIST pour la composition des matériaux et leurs indices de réfraction ou bien SpekPy pour la génération des spectres de tubes à rayons x.

J'ai implémenté deux modèles physiques dans notre programme. Le premier basé sur la physique ondulatoire et utilisant un propagateur de Fresnel, le second basé sur de l'optique géométrique et du tracé de rayons. Le programme permet de prendre en compte de très nombreux paramètres expérimentaux tels que le bruit photonique lié au nombre de photons reçus par le détecteur, la taille de la source et la fonction de dispersion du détecteur, l'ajout de filtres devant la source ou le cas d'une expérience dans le vide et bien d'autres. Nous avons ensuite comparé les résultats obtenus avec ce programme à des simulation réalisée avec GATE et à deux vraies expériences : une expérience synchrotron monochromatique et une expérience de laboratoire avec un faisceau

polychromatique. Cette comparaison a permis de valider la quantitativité des simulations dans ces deux configurations.

Finalement, nous avons pu commencer les travaux d'optimisation de l'expérience grâce à ces simulations. Parmi les études réalisées nous avons pu montrer que :

- Acquérir plusieurs positions de membranes avec de courtes durées d'exposition plutôt que l'inverse augmente la qualité des images de phases récupérées;
- L'augmentation de la durée d'exposition des acquisitions n'induit pas une diminution linéaire du bruit dans les images de phase obtenues;
- Filtrer les basses énergies du spectre polychromatique permet de réduire les artéfacts liés au durcissement de faisceau dans les échantillons très absorbants.

Phase retrieval 3

The transfer of MoBI to the clinics requires optimization of the set-up but also of the phase retrieval post processing. The goal is to make it highly sensitive, fast, robust to noise (that increases if we want to reduce the dose to the patient) and adapted to the set-up constraints such as a polychromatic wide spot source and low resolution detector. In this chapter, after a presentation of the phase-retrieval algorithms state of the art, the different phase retrieval possibilities that were investigated will be presented along with the results and performances of the one that proved more promising. The last section contains an extensive comparison of phase retrieval algorithms in various configurations.

3.1 State of the art 81
Explicit tracking 83
Implicit tracking 85
Integration methods 87
3.2 Fourier transform analysis of Fresnel interference patterns applied to MoBI 89
Ambiguity function to TIE . 89
Contrast transfer function multi-energy method 90
3.3 Development of a new algorithm optimized for low coherence systems 94
Theoretical development . . . 94
First validations on a synchrotron experiment 95
Studies on conventional laboratory set-ups 98
3.4 Comparison of algorithms . 107
Synchrotron biomedical case 107
Synchrotron quantitative measurements 110
Conventional source imaging114
Summary of the comparison of the algorithms 116
Note on integration algorithms 117
3.5 Conclusion 118
Résumé du Chapitre 3 en Français 119

3.1 State of the art

This part introduces the phase retrieval algorithms existing before I started the thesis work with their advantages and drawbacks.

As a reminder, MoBI works through the observation of the modification of a random pattern due to refraction through an object. The reference image (I_r) containing only the random pattern is obtained by inserting a randomly structured membrane in the x-ray beam. The sample image (I_s) is then acquired by adding the sample in the path of the beam downstream the membrane. The refraction angles information α is directly associated to the amplitude of the displacement $D_\perp = (D_x, D_y)$ of the pattern modulations. This acquisition method is represented in Figure 3.1. Usually, for better statistics and higher sensitivity[1] , several pairs of acquisitions (I_r, I_s) are acquired with different membrane positions.
As shown on the plot of Figure 3.1, when taking profiles on the reference and sample image, the difference between both will be a loss of intensity due to attenuation and a displacement of the modulations due to refraction. For now we focus on phase effects and neglect the dark-field phenomenon, its influence will be described in the next chapter.

1: We define the sensitivity as the ability to extract a significant signal out of noise.

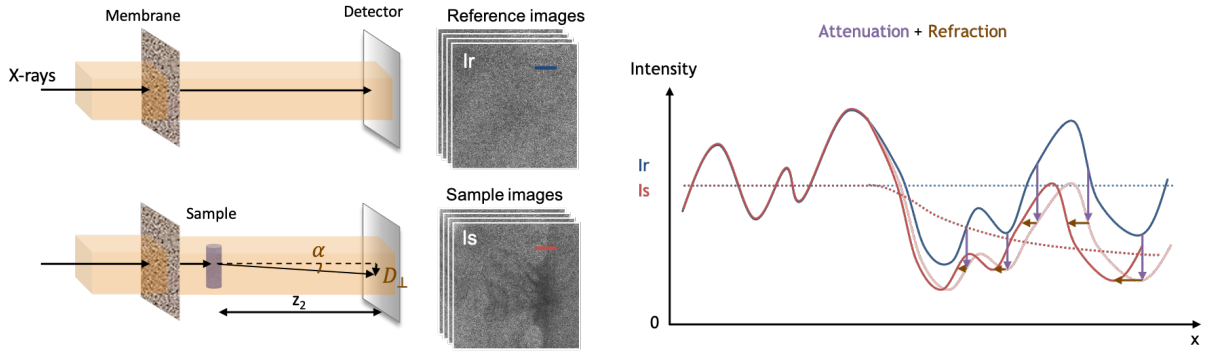

Figure 3.1: MoBI acquisition principle. A set of reference images is taken in presence of the membrane at different positions (Ir) and a set is acquired with the sample inserted in the path of the beam (Is). The plot shows small profiles extracted from a sample and reference images. The profile of Is is lower due to attenuation and the membrane modulations are slightly shifted due to refraction.

Before starting, here are the mathematical and experimental notations used in this chapter.

Notations

Variables:

- n: complex refractive index
- δ: refractive index real part decay
- β: refractive index imaginary part
- μ: linear attenuation coefficient
- λ: wavelength
- $k = 2\pi/\lambda$: wavenumber
- $D_\perp = D_x, D_y$: intensity displacement in the detector plane related to refraction
- α: angle of refraction
- ϕ: phase
- z: spatial axis in the direction of propagation
- x, y : spatial coordinate perpendicular to propagation
- k_x, k_y: Fourier space coordinates (angular frequency)
- $\mathbf{f} = (f_x, f_y)$: Fourier space coordinates (frequency)
- $\{P\}$: set of membrane position
- z_0: distance between the source and the membrane
- z_1: distance between the membrane and the sample
- z_2: propagation distance between the sample and the detector
- I: intensity field
- I_r: Reference image of the optical elements without sample
- I_s: Sample image with the sample
- I_{obj}: intensity attenuation due to the sample
- T: transmission of the sample
- t: thickness of the sample

Operators:

- ∇: gradient operator
- $Re\{\}$: Real part
- $\mathcal{F}$: Fourier transform
- $\mathcal{F}^{-1}$: inverse Fourier transform
- argmax_{param}: maximum argument when varying param
- argmin_{param}: minimum argument when varying param
- $\iint_{(x,y)} ..dxdy$: 2D surface integral
- $\sum_i$: sum of the following quantity for i in a set.
- log: natural logarithm
- e: exponential function

There are two kinds of algorithms allowing to retrieve the displacements from the acquisitions: explicit and implicit speckle tracking methods[2] . Figure 3.2 summarizes the existing algorithms for phase retrieval (not dark-field extraction even though some are completed with a dark-field part as it will be described in the next chapter). Phase retrieval algorithms can be separated into two categories: explicit and implicit algorithms. Most of them give displacement maps (that can be integrated in a second step to retrieve the phase image) except the SMOST algorithm that gives directly a phase image. All these algorithms will be described in this

2: Remark: As mentioned in the first chapter, the "Speckle" term corresponds to a physical interference phenomenon that occurs with highly coherent sources. In less coherent cases we no longer look at 'speckles' but at simple intensity modulations patterns. However, the tracking principle remains the same and the technique was initially invented with speckle modulations hence the misuse of language.

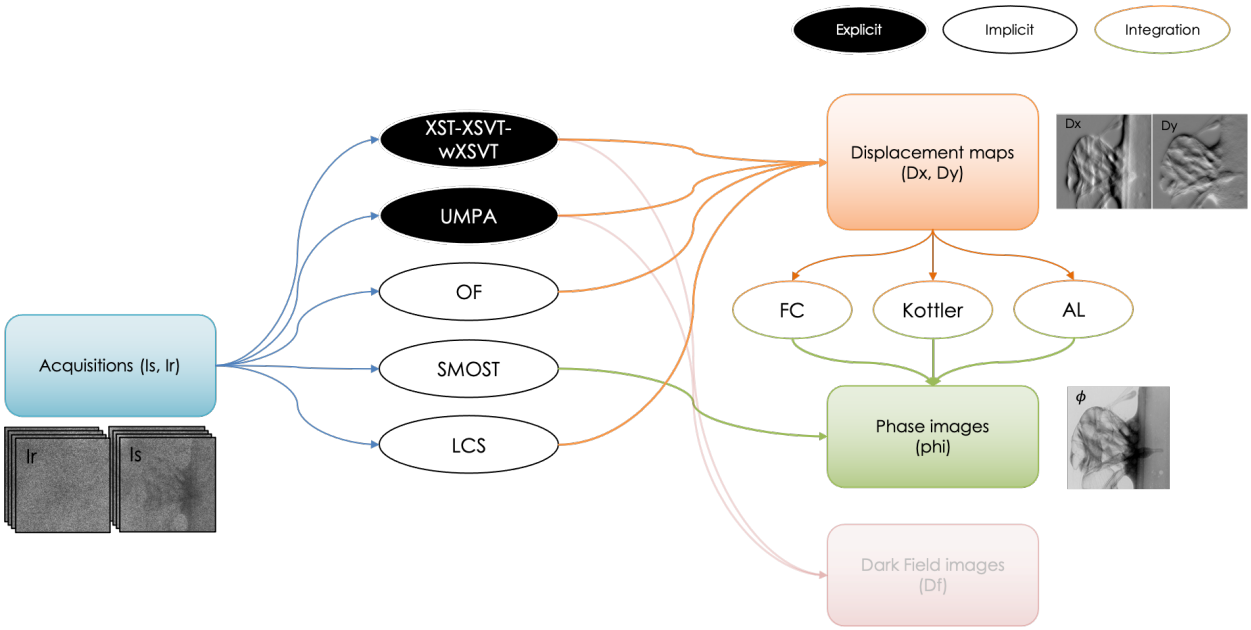

Figure 3.2: State of the art of the implicit and explicit phase retrieval algorithms and integration methods.

section except for the LCS that was created during the PhD and will have a dedicated section.

3.1.1 Explicit tracking

Explicit speckle tracking methods consist in following the local displacement of the patterns by comparing small groups of pixels from the reference images and the sample images around a pixel of interest, searching for the displacement that leads to the best match of the modulations. The operation is repeated for every pixel of the image. Among those algorithms there is a "family" that was derived from the initial x-ray speckle tracking (XST) algorithm and the unified modulated pattern analysis.

X-ray Speckle Tracking (XST) and X-ray Speckle Vector Tracking (XSVT)

The first phase retrieval algorithm, called single shot x-ray speckle tracking (XST), was developed in 2012 [1], similar to the one developed in 2011 for an attenuation grid method [2, 118]. It used only one pair of sample/reference images and involves calculating the local maximum of cross correlation of small windows w from I_s and I_r around each pixel (x_0, y_0) to find the local modulation displacement $D_\perp(x_0, y_0)$:

$$D_\perp(x_0, y_0) = \underset{\delta_x, \delta_y}{\operatorname{argmax}} \iint_{(x,y)\in w(x_0,y_0)} I_s(x, y) I_r(x + \delta_x, y + \delta_y) dx dy \quad (3.1)$$

The window w has a defined size $2N_w+1$ around each pixel (x_0, y_0) where N_w is the maximum distance pixel to consider. The cross-correlation between the two windows is calculated with varying δ_x, δ_y within a range $[-D_{max}, D_{max}]$ chosen according to the experiment conditions. The

maximum of the obtained 2D cross-correlation function gives the values of δ_x, δ_y that correspond to the displacement at the position (x_0, y_0). This calculation is repeated for each pixels of the image. In order to relax the effects of attenuation, the intensities can be locally normalized by the average attenuation over the considered window in the sample and reference images.

A second similar algorithm, x-ray speckle vector tracking (XSVT)[119], was developed for several pairs of acquisitions where the membrane was randomly displaced between each pair of acquisitions leading to higher sensitivity. This method, instead of comparing windows of pixels to find the displacement at each position, compares a vector of single pixels with coordinates (x_0, y_0) from each sample image to a vector from the reference images set. This sample image vector is then compared to the reference image vectors from neighboring pixels, distant of δ_x, δ_y from (x_0, y_0) within $[-D_{max}, D_{max}]$, tracking once again the maximum correlation. Numerical interpolation is used to reach a sub-pixel resolution.

In order to increase the resolution, another acquisition scheme was developed: x-ray speckle scanning (XSS)[120]. This involves acquiring a large number of reference images with sub-pixel steps around each position. The vector of the sample image is then compared to the vectors of these reference acquisitions shifted with very small steps to find the one that would best match the displacement due to refraction. This method however requires a huge amount of data to acquire, store and process, and very precise motors. It is why it was not considered for the transfer to clinical set-ups and will not be discussed further in this work.

The XSVT method was then extended by coupling with the XST window one, leading to a comparison of windows over several pairs of acquisitions with multiple positions $\{P\}$ of the membrane [121]. This XST-XSVT method can be described by the equation:

$$D_{\perp}(x_0, y_0) = \underset{\delta_x, \delta_y}{\operatorname{argmax}} \sum_{p \in \{P\}} \iint_{x,y \in w(x_0,y_0)} I_s^{(p)}(x, y) I_r^{(p)}(x + \delta_x, y + \delta_y) dx dy \tag{3.2}$$

A sub-pixel displacement can be obtained by fitting a Gaussian shape to the cross-correlation curve and taking the maximum of this Gaussian shape. It can also be enhanced by oversampling the windows through quadratic interpolation. Mainly used for metrology, these algorithms were reviewed with experimental details in [122, 123].

More recently, in search of a better computational efficiency and of an algorithm more robust to noise, wavelet x-ray speckle tracking (WXSVT) was developed[124]. It uses a wavelet transform which consists in decomposing the signal into a finite number of signals, each containing a range of frequency from the initial data. It allows to filter out very high frequency noise simply by getting rid of the very high frequency signal. Then it calculates an euclidean distance in the wavelet domain to retrieve displacement using vectors of pixels from the different membrane positions acquisitions as in the XSVT algorithm.

Unified Modulated Pattern Analysis (UMPA)

The unified modulated pattern analysis (UMPA) is a method similar to the mixed XST-XSVT: from multiple acquisitions at random membranes positions and window comparison. This one is based on the minimization of the local mean squared error of a cost function $\mathscr{L}(x_0, y_0)$[117]:

$$\mathscr{L}(x_0, y_0; T, \delta_x, \delta_y) = \sum_{p\in\{P\}} \iint_{x,y\in w(x_0,y_0)} \left[T(x,y) I_r^{(p)}(x+\delta_x, y+\delta_y) - I_s^{(p)}(x,y)\right]^2 dxdy \tag{3.3}$$

$$D_\perp(x_0, y_0), T(x_0, y_0) = \underset{\delta_x,\delta_y;T}{\operatorname{argmin}} \mathscr{L}(x_0, y_0; T, \delta_x, \delta_y) \tag{3.4}$$

Minimizing the cost function when varying δ_x, δ_y and T gives the displacements and transmission in each pixels. This cost function can also be completed with a dark-field coefficient as it will be developed in the next chapter.

More details about explicit algorithms, their technical challenges and algorithmic implementations can be found in the review article by Zdora [125].

The main drawback of these explicit methods is their computational cost. Without very powerful computers, retrieving the phase for a radiography takes hours. When working with tomography, each projection must be processed individually which, even with multiprocessing, could take weeks and that is not conceivable for clinical applications. The need of inventing faster phase retrieval is what led to investigating implicit methods.

3.1.2 Implicit tracking

Implicit speckle tracking is based on the conservation of the optical flow and the transport of intensity equation (TIE). This equation already briefly mentioned in the first chapter for the PBI method has a whole tutorial dedicated to it for various cases of phase retrieval problems [40]. Based on the energy conservation law and the Helmotz equation and valid under the paraxial approximation, its use for phase retrieval was first proposed for visible light problems where it was used to described the propagation of an intensity I on a distance z_2 (as for the PBI case)[126]. This version of the TIE is written:

$$I(x,y,z) - I(x,y,z+z_2) = -\frac{z_2}{k}\nabla_\perp \left[I(x,y,z)\nabla_\perp\phi(x,y,z)\right] \tag{3.5}$$

Where ϕ is the phase shift present in the wavefront at the position z.

Optical Flow algorithm (OF)

In 2018, Paganin et al. [127] proposed a version of the TIE adapted to the MoBI problem assuming a non absorbing sample to respect the

conservation of energy hypothesis:

$$I_s(x,y) - I_r(x,y) \approx \frac{z_2}{k}\nabla_\perp \cdot [I_r(x,y)\nabla_\perp \phi(x,y)] \tag{3.6}$$

Using the relationship between the phase shift ϕ, the refraction angle $\alpha_\perp$ and the intensity displacement $D_\perp$ after a propagation distance z_2:

$$\nabla_\perp \phi = k\alpha_\perp = \frac{k}{z_2} D_\perp \tag{3.7}$$

equation 3.6 can be re-written:

$$I_s(x,y) - I_r(x,y) \approx \nabla_\perp \cdot [I_r(x,y) D_\perp(x,y)] \tag{3.8}$$

From the previous equation, a simple way to extract the displacements is by using Fourier transforms as follows:

$$D_\perp(x,y) = \frac{i}{I_r(x,y)} \mathcal{F}^{-1}\left\{(k_x,k_y)\frac{\mathcal{F}\{I_r(x,y) - I_s(x,y)\}}{k_x^2 + k_y^2}\right\} \tag{3.9}$$

This resolution method from the TIE was named Optical Flow (OF) as it was the first method based on this theory. It has two main advantages:

- the numerical resolution is extremely fast and computationally efficient as it computes simple image Fourier transforms and multiplications.
- the resolution theoretically requires only one pair of acquisition (I_r, I_s).

Two important drawbacks of this method are:

- it assumes a non absorbing sample which is very rarely the case especially when considering clinical samples with dense structures.
- the use of Fourier transforms induces low frequency artifacts especially because the denominator will be 0 at the center frequency.

In order to overcome these two inconveniences, numerical "tricks" can be used. The absorption due to the sample can be partially corrected by using a slightly blurred image obtained from the I_s/I_r ratio. This approximated attenuation image is then used to correct the sample images. The problem with that method is that the blurring induces artifacts at the edges of the sample that might get the upper hand over the phase effects that we are actually trying to retrieve.
The low frequency issue can simply be addressed by using a high pass filter in the Fourier domain. The results that are obtained with this algorithm are images of very good quality. However, an interrogation persists concerning the separation between the phase signal and a filtered absorption, as it does give quantitative results [128] .

[128]: Helene Rouge-Labriet, Laurene Quenot, Sylvain Bohic, Barbara Fayard, David M Paganin, Emmanuel Brun, and Sebastien Berujon. 'Comparison of X-ray speckle-based imaging deflection retrieval algorithms for the optimization of radiation dose'. In: *Physics in Medicine & Biology* 66.6 (2021)

Single Material Object Speckle Tracking (SMOST)

Very similarly to what is done in the single material case of PBI, for SMOST, the TIE is written to describe the intensity evolution over propagation. In MoBI's case it describes the evolution of intensity in our two cases: after

the membrane alone and after membrane + sample (i.e. for the reference and sample images)[129]. Assuming a single material sample, we rewrite the phase and attenuation of the sample as functions of the sample thickness and their δ, β coefficients: $\phi = -k\delta t; I_obj = e^{-\mu t}$. Dividing one expression by the other, it is then possible to retrieve the thickness as:

$$t(x,y) = -\frac{1}{\mu} log\left(\mathcal{F}^{-1}\left\{\frac{\mathcal{F}\left\{I_s(x,y)/I_r(x,y)\right\}}{1+(\delta z_2/\mu)(k_x^2+k_y^2)}\right\}\right). \tag{3.10}$$

We can notice that this formulation is perfectly identical to the single material phase retrieval method for the PBI [39]. The only difference with this method is the presence of the membrane in the sample and reference images.
Because of the use of Fourier transform, low frequency artifacts appear however they can partly be filtered out with a high pass filter.
This algorithm was proven to give very good results in synchrotron MoBI tomography experiments [129].
Unlike the previously introduced method that gave displacement maps (corresponding to phase gradient images) this method gives directly a thickness map which, under its single material assumption, is proportional to the phase.

Among the numerous algorithms introduced here, the XST-XSVT, UMPA, OF and SMOST have been centralized in a Python program. Except for the UMPA one that was collected from a GitHub repository[3] , all the algorithms were implemented in our team. The program regrouping all the previously mentioned algorithms is available in our GitHub repository POPCORN[4] . For comparison to other algorithms (XSVT and wXSVT) in the third section of this chapter, data were shared with collaborators working with these programs.

3: github.com/pierrethibault/UMPA

4: github.com/DoctorEmmetBrown/popcorn

Remark: POPCORN meaning:
Some might think that popcorn is a bunch of seeds of maize that are heated until they break open and become soft and light, usually flavoured with salt, butter, or sugar and eaten at the cinema but no. POPCORN actually means POst-processing library for Phase COntrast and spectRal x-ray imagiNg.

3.1.3 Integration methods

Phase gradient images $\frac{\partial\phi}{\partial x}$, $\frac{\partial\phi}{\partial y}$, proportional to the previously mentioned displacement maps D_x, D_y, are 2 directional complementary information sets. Contrary to many of the other PCI method presented in the first chapter, MoBI allows to access these 2D gradients. These images are already interesting because they offer a different structure visualization than attenuation images. However, it can be interesting to obtain also the integrated phase image to be able to do tomographic reconstruction of projections for example. Integrating images is not as straightforward as integrating a simple 1D function and especially when this image contains noise. Different integration algorithms exist, initially developed for different applications. In this work we mainly use three of them based on Fourier transform integration:

- Frankot and Chellapa's formula [130] (FC):

$$\phi(x,y) = \mathcal{F}^{-1}\left\{\frac{-i}{k_x^2+k_y^2}\left(k_x\mathcal{F}\left\{\frac{\partial\phi}{\partial x}(x,y)\right\} + k_y\mathcal{F}\left\{\frac{\partial\phi}{\partial y}(x,y)\right\}\right)\right\} \tag{3.11}$$

- Arnison *et al.* [131] (AL):

$$\phi(x,y) = \mathcal{F}^{-1}\left\{\frac{1}{ik_x - k_y}\mathcal{F}\left\{\frac{\partial\phi}{\partial x}(x,y) + i\frac{\partial\phi}{\partial y}(x,y)\right\}\right\} \tag{3.12}$$

- Kottler *et al.* [132]:

$$\phi(x,y) = \mathcal{F}^{-1}\left\{\mathcal{F}\left\{\frac{\partial\phi}{\partial x}(x,y) + i\frac{\partial\phi}{\partial y}(x,y)\right\} e^{i.atan(k_x/k_y)}\right\} \tag{3.13}$$

As always when going though Fourier, some frequency artifacts appear especially when the object crosses the edge of the image and its gradients do not start from zero: the boundary conditions for integration are not respected. Padding the gradient images is one way to reduce such artifacts but it is difficult to get completely rid of them. While the first two (FC and AL) have mathematically almost equivalent formulas, the third one is quite different because it contains a ramp filter that anticipates the tomographic reconstruction. Therefore, when used on simple projections it gives a very high frequency image with no quantitative possibility.

In this section we gave an overview of the phase retrieval and integration algorithms that can be used for MoBIs experiments. The next section will present new works that were done for phase signal extraction from MoBI acquisitions. The advantages and drawbacks of the different existing algorithms in various cases will be discussed later in this chapter.

3.2 Fourier transform analysis of Fresnel interference patterns applied to MoBI

In order to improve phase retrieval from MoBI acquisitions, I studied two main directions. This section introduces a first exploration.

Very similar to the work that was done in [41] for propagation based imaging, I investigated the possibility to retrieve the phase from the description of the acquisitions' intensity in reciprocal space as defined by Guigay. From this formalism, two developments were done, leading to equations to solve that should allow us to extract the phase information. One converges towards the TIE solution and a second leads to a contrast transfer function (CTF) formalism for MoBI.

For better readability, the 2D space coordinates (x,y) will be written simply x and Fourier space coordinates (f_x,f_y) just f.

3.2.1 Ambiguity function to TIE

We can write the Fourier transform of the intensity image obtained from a beam passing through the membrane (m) and the sample (s) in the near-field region using the ambiguity function based on [133]:

$$\widetilde{I}_s(f) = \int_{-\infty}^{+\infty} T_{m+s}(x - \frac{\lambda z_2}{2} f) T^*_{m+s}(x + \frac{\lambda z_2}{2} f) e^{-i2\pi x f} dx \tag{3.14}$$

Where T is the transmittance function under the projection approximation as it was defined in Chapter 2: $T_{m+s}(x) = a_{m+s}(x)e^{i\phi_{m+s}(x)}$ with $a_{m+s}(x) = e^{-B(x,y)} = e^{-\int_z \mu dz}$. Here the $m+s$ refers to the membrane and sample placed close together and considers their contributions together.
$a_{m+s}(x) = a_m(x)a_s(x)$ describes the attenuation of these objects.
$\phi_{m+s}(x) = \phi_m(x) + \phi_s(x)$ is the phase shift due to the objects.
z_2 the propagation distance between the object and the detector and λ is the wavelength.

For the reference image (only the membrane in the path of the beam) :

$$\widetilde{I}_r(f) = \int_{-\infty}^{+\infty} T_m(x - \frac{\lambda z_2}{2} f) T^*_m(x + \frac{\lambda z_2}{2} f) e^{-i2\pi x f} dx \tag{3.15}$$

Assuming slow variations of the phase we can get:

$$\begin{aligned}
\widetilde{I}_s(f) &= \int_{-\infty}^{+\infty} a_{m+s}(x - \frac{\lambda z_2}{2} f) a_{m+s}(x + \frac{\lambda z_2}{2} f) e^{i(\phi_{m+s}(x - \frac{\lambda z_2}{2} f) + \phi_{m+s}(x + \frac{\lambda z_2}{2} f))} e^{-i2\pi x f} dx \\
&= \int_{-\infty}^{+\infty} a_{m+s}(x - \frac{\lambda z_2}{2} f) a_{m+s}(x + \frac{\lambda z_2}{2} f) \\
&\qquad \times \left[1 + i\phi_{m+s}(x - \frac{\lambda z_2}{2} f) + i\phi_{m+s}(x + \frac{\lambda z_2}{2} f)\right] e^{-i2\pi x f} dx \\
&= \int_{-\infty}^{+\infty} a^2_{m+s}(x) \left[1 - i\lambda z_2 f \nabla \phi_{m+s}(x)\right] e^{-i2\pi x f} dx \\
&= \mathcal{F}\left\{a^2_{m+s}(x)\right\} - i\lambda z_2 f \mathcal{F}\left\{a^2_{m+s}(x) \nabla \phi_{m+s}(x)\right\}
\end{aligned} \tag{3.16}$$

For now, let's consider the case of a low absorbing sample: $a_s \approx 1$. Then we can write:

$$\widetilde{I}_s(f) = \mathcal{F}\left\{a^2_m(x)\right\} - i\lambda z_2 f \mathcal{F}\left\{a^2_m(x)(\nabla \phi_m(x) + \nabla \phi_s(x))\right\} \tag{3.17}$$

Similarly, for the reference image we obtain:

$$\widetilde{I_r}(f) = \mathcal{F}\left\{a_m^2(x)\right\} - i\lambda z_2 f \mathcal{F}\left\{a_m^2(x)\nabla\phi_m(x)\right\} \tag{3.18}$$

Then by substracting $\widetilde{I_r}$ to $\widetilde{I_s}$ we get:

$$\widetilde{I_s}(f) - \widetilde{I_r}(f) = - i\lambda z_2 f \mathcal{F}\left\{a_m^2(x)\nabla\phi_s(x)\right\} \tag{3.19}$$

$$= - \frac{\lambda z_2}{2\pi}\mathcal{F}\left\{\nabla[a_m^2(x)\nabla\phi_s(x)]\right\} \tag{3.20}$$

which is equivalent in real space to:

$$I_s(x) - I_r(x) = -\frac{\lambda z_2}{2\pi}\nabla_\perp[a_m^2(x)\nabla_\perp\phi(x)] \tag{3.21}$$

This concludes our first development. It is interesting to notice that this same result can be obtained from the propagation TIE. Indeed, we can write the sample image intensity when the sample and membrane are in the beam:

$$I_s(x) = a_{m+s}^2(x) - \frac{\lambda z_2}{2\pi}\nabla_\perp\left[a_{m+s}^2(x)\nabla_\perp\phi_{m+s}(x)\right] \tag{3.22}$$

When assuming low absorbing sample it becomes :

$$I_s(x) = a_m^2(x) - \frac{\lambda z_2}{2\pi}\nabla_\perp\left[a_m^2(x)\nabla_\perp(\phi_m(x) + \phi_s(x)\right] \tag{3.23}$$

And the reference image:

$$I_r(x) = a_m^2(x) - \frac{\lambda z_2}{2\pi}\nabla_\perp\left[a_m^2(x)\nabla_\perp(\phi_m(x)\right] \tag{3.24}$$

Then by substracting I_r from I_s:

$$I_s(x) - I_r(x) = -\frac{\lambda z_2}{2\pi}\nabla_\perp\left[a_m^2(x)\nabla_\perp(\phi_s(x)\right] \tag{3.25}$$

This expression is almost identical to the TIE used in the OF [127]. The main difference is the a_m^2 term that corresponds to the image of the membrane without the phases propagation effects. We can assume that the expressions would converge in the case of a slowly varying phase of the membrane or in systems with low spatial coherence where the phases effects do not appear on the image.
Because the membrane is usually a single material sample, it is possible to retrieve the $a_m^2 = e^{-\mu t}$ coefficient using the PBI equation for single material samples.

3.2.2 Contrast transfer function multi-energy method

As mentioned before, we can also develop the expressions of the reference and sample image in Fourier space into a CTF approach.

Assuming only a weakly absorbing object and slow phase variations this time, we can rewrite eq. 3.14 as:

$$\begin{aligned}
\widetilde{I_s}(f) &= \int_{-\infty}^{+\infty} a_m(x-\frac{\lambda z_2}{2}f)a_m(x+\frac{\lambda z_2}{2}f)e^{i(\phi_{m+s}(x-\frac{\lambda z_2}{2}f)+\phi_{m+s}(x+\frac{\lambda z_2}{2}f))}e^{-i2\pi xf}dx \\
&= \int_{-\infty}^{+\infty} a_m(x-\frac{\lambda z_2}{2}f)a_m(x+\frac{\lambda z_2}{2}f)\left[1+i\phi_{m+s}(x-\frac{\lambda z_2}{2}f)+i\phi_{m+s}(x+\frac{\lambda z_2}{2}f)\right]e^{-i2\pi xf}dx \\
&= \mathcal{F}\left\{a_m(x-\frac{\lambda z_2}{2}f)a_m(x+\frac{\lambda z_2}{2}f)\right\} + i\int_{-\infty}^{+\infty} a_m(x)a_m(x+\lambda z_2 f)\phi_{m+s}(x)e^{-i2\pi f(x+\frac{\lambda z_2}{2}f)}dx \\
&\quad - i\int_{-\infty}^{+\infty} a_m(x)a_m(x-\lambda z_2 f)\phi_{m+s}(x)e^{-i2\pi f(x-\frac{\lambda z_2}{2}f)}dx \\
&= \mathcal{F}a_m + i\int_{-\infty}^{+\infty} a_m(x)\phi_{m+s}(x)e^{-i2\pi fx}\left[a_m(x+\lambda z_2 f)e^{-i\pi\lambda z_2 f^2} - a_m(x-\lambda z_2 f)e^{i\pi\lambda z_2 f^2}\right]dx \\
&= \mathcal{F}a_m + i\int_{-\infty}^{+\infty} a_m(x)\phi_{m+s}(x)e^{-i2\pi fx}\left[a_m(x+\lambda z_2 f)\left(cos(\pi\lambda z_2 f^2)-isin(\pi\lambda z_2 f^2)\right)\right. \\
&\quad \left. -a_m(x-\lambda z_2 f)\left(cos(\pi\lambda z_2 f^2)+isin(\pi\lambda z_2 f^2)\right)\right]dx \\
&= \mathcal{F}a_m + i\int_{-\infty}^{+\infty} a_m(x)\phi_{m+s}(x)e^{-i2\pi fx}cos(\pi\lambda z_2 f^2)\left[a_m(x+\lambda z_2 f)-a_m(x-\lambda z_2 f)\right]dx \\
&\quad + \int_{-\infty}^{+\infty} a_m(x)\phi_{m+s}(x)e^{-i2\pi fx}sin(\pi\lambda z_2 f^2)\left[a_m(x+\lambda z_2 f)+a_m(x-\lambda z_2 f)\right]dx
\end{aligned} \tag{3.26}$$

For readability we write: $\mathcal{F}\left\{a_m(x-\frac{\lambda z_2}{2}f)a_m(x+\frac{\lambda z_2}{2}f)\right\} = \mathcal{F}a_m$

Assuming slowly varying objects we can also write: $a_m(x+\lambda z_2 f) - a_m(x-\lambda z_2 f) = 2\lambda z_2 f\nabla a_m(x)$ and $a_m(x+\lambda z_2 f) + a_m(x-\lambda z_2 f) = 2a_m(x)$.

Then we get:

$$\begin{aligned}
\widetilde{I_s}(f) &= \mathcal{F}a_m + i2\lambda z_2 f cos(\pi\lambda z_2 f^2)\int_{-\infty}^{+\infty} a_m(x)\phi_{m+s}(x)\nabla a_m(x)e^{-i2\pi fx}dx \\
&\quad + 2sin(\pi\lambda z_2 f^2)\int_{-\infty}^{+\infty} a_m(x)\phi_{m+s}(x)a_m(x)e^{-i2\pi fx}dx \\
&= \mathcal{F}a_m + i\lambda z_2 f cos(\pi\lambda z_2 f^2)\mathcal{F}\left\{\phi_{m+s}(x)\nabla a_m^2(x)\right\}
\end{aligned} \tag{3.27}$$

Similarly, for the reference image we get:

$$\widetilde{I_r}(f) = \mathcal{F}a_m + i\lambda z_2 f cos(\pi\lambda z_2 f^2)\mathcal{F}\left\{\phi_m(x)\nabla a_m^2(x)\right\} + 2sin(\pi\lambda z_2 f^2)\mathcal{F}\left\{a_m^2(x)\phi_m(x)\right\} \tag{3.28}$$

Finally, substracting I_r from I_s we obtain:

$$\widetilde{I_s}(f) - \widetilde{I_r}(f) = i\lambda z_2 f cos(\pi\lambda z_2 f^2)\mathcal{F}\left\{\phi_s(x)\nabla a_m^2(x)\right\} + 2sin(\pi\lambda z_2 f^2)\mathcal{F}\left\{a_m^2(x)\phi_s(x)\right\} \tag{3.29}$$

This equation can be solved to retrieve the phase using an iterative method, by first neglecting the first term on the right hand side, we have:

$$\phi_s^{(0)} = \frac{1}{a_m^2(x)}\mathcal{F}^{-1}\left\{\frac{\widetilde{I_s}(f)-\widetilde{I_r}(f)}{2sin(\pi\lambda z_2 f^2)}\right\} \tag{3.30}$$

And for the next iterations:

$$\phi_s^{(k)} = \frac{1}{a_m^2(x)} \mathcal{F}^{-1} \left\{ \frac{\widetilde{I}_s(f) - \widetilde{I}_r(f) - i\lambda z_2 f cos(\pi\lambda z_2 f^2) \mathcal{F}\left\{\phi_s^{(k-1)}(x) \nabla a_m^2(x)\right\}}{2sin(\pi\lambda z_2 f^2)} \right\} \tag{3.31}$$

This method presents big instabilities due to the fact that the denominator function $H_E(f) = 2sin(\pi\lambda z_2 f^2)$ is periodically equal to 0. A similar problem occured with the CTF version of the phase retrieval for PBI. The problem was then solved by taking images with various distance of propagation z_2 and summing them to obtain a function that would no longer periodically cross 0 [41, 134].

A similar method can be used here. The distance could be varied, however, this method being easy to implement at synchrotrons where the magnification is close to 1, it would be a lot less practical in laboratories or clinical set-up where the position of the sample between the source and detector would change its resolution a lot. Instead, with the development of spectral detectors, it would be interesting to vary the average energy detected or use the spectral detector bins.

How would using several energies solve the 0-crossing issue? Figure 3.3 illustrates the transformation of the denominator used to remove the 0 division issue. First our function $H_E(f)$ (red curve) is squared to avoid completely crossing the 0 axis (blue curve). However it still periodically touches it now. To avoid that, we also need to sum several squared $H_E(f)$ at different energies (or wavelength $\lambda^{(i)}$). Those functions obtained at different energies have different periods and summing them allow to get away from the 0 axis (green curve).

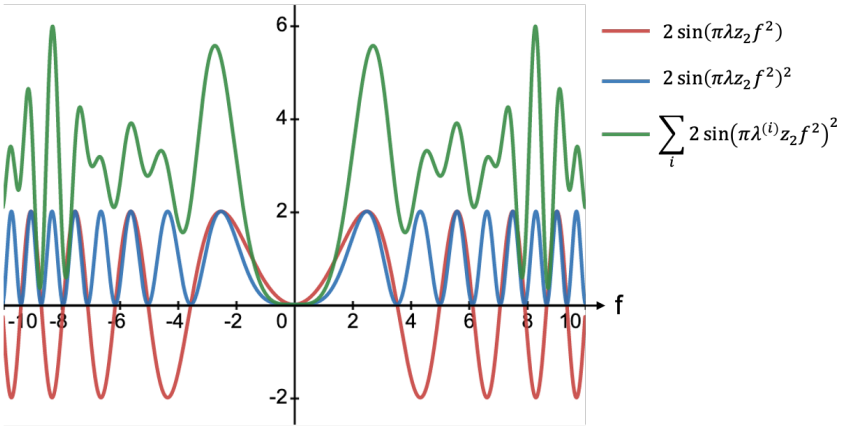

Figure 3.3: Examples of denominator function from association of acquisitions with various energies to illustrate periodic 0-crossing removal.

In practice, to achieve that, we need to multiply the numerator and the denominator of the expression in the Fourier space of Equation 3.31 by $H_E(f)$ and sum them over various energies:

$$\left\langle \phi_s^{(0)}(x) \right\rangle_E = \frac{1}{\left\langle a_m^2(x) \right\rangle_E} \mathcal{F} \left\{ \frac{\Sigma_{E_i}^{E_N} H_{E_i}(f) \left[\widetilde{I}_{s,E_i}(f) - \widetilde{I}_{r,E_i}(f) \right]}{\Sigma_{E_i}^{E_N} H_{E_i}^2(f)} \right\} \tag{3.32}$$

And for the subsequent iterations:

$$\left\langle \phi_s^{(k)}(x) \right\rangle_E = \frac{1}{\left\langle a_m^2(x) \right\rangle_E} \mathcal{F} \left\{ \frac{\sum_{E_i}^{E_N} H_{E_i} \left[\widetilde{I}_s(f) - \widetilde{I}_r(f) - i\lambda z_2 f cos(\pi\lambda z_2 f^2) \mathcal{F} \left\{ \left\langle a_m^2(x) \right\rangle_E \nabla \left\langle \phi_s^{(k-1)}(x) \right\rangle_E \right\} \right]}{\sum_{E_i}^{E_N} H_{E_i}^2(f)} \right\} \tag{3.33}$$

As can be seen in Figure 3.3, one last 0-crossing will remain as in the TIE methods at the 0 frequency. This frequency can be replaced by an infinitesimal value but a more elaborate method using the attenuation of the sample can be used as described by Langer, Cloetens, and Peyrin [135] to compensate for the frequencies close to 0.

Note that in the case of multiple energies, a_m and ϕ_s will vary slightly and the retrieved information will be an averaged value (hence the $\langle . \rangle$) as it would be with a polychromatic spectrum case. A more precise calculation could be investigating using electron density instead of phase and attenuation as they do not vary with the energy.

This theoretical work was done following interesting scientific discussions I had with the very esteemed Dr. Jean Pierre Guigay. The potential of the method is related to the fact that it would require fewer membrane positions to retrieve the phase information by making use of spectral detectors. The experimental validations are still to be done but this work will have to be carried on in a subsequent project with the appropriate means. It is now the subject of a new PhD student in the Strobe laboratory: Christopher Ninham.

3.3 Development of a new algorithm optimized for low coherence systems

In the case of attenuating samples and low coherence set-ups, the more appropriate algorithms would be the explicit ones as they do not make assumptions on the sample and do not make use of the source spatial coherence. However, they have two main limitations: their computation is very time consuming and they have a limited sensitivity due to the size of the window needed to have a limited noise. Existing implicit methods do not have that loss of resolution associated to their solution but make assumptions on the sample (no absorption or single material) and they mainly make use of the appearance of interference fringes to retrieve the phase information.

For these reasons, I worked on a new algorithm that would have a better sensitivity than the explicit ones and less hypothesis on the sample than the OF and SMOST.

3.3.1 Theoretical development

For this new implicit method, we start again from the TIE adapted to MoBI except that we add a 'loss term' I_{obj} to account for the attenuation due to the sample contrary to the optical flow where the attenuation was roughly filtered using a blurred ratio I_s/I_r that induced edge artifacts. Adding I_{obj} to the TIE we get:

$$I_r(x,y) - \frac{I_s(x,y)}{I_{obj}(x,y)} \approx \nabla \left[I_r(x,y) D_\perp(x,y) \right] \tag{3.34}$$

In this equation the right hand term can be developed into:

$$I_r(x,y) - \frac{I_s(x,y)}{I_{obj}(x,y)} \approx I_r(x,y) \nabla D_\perp(x,y) + D_\perp(x,y) \nabla_\perp I_r(x,y) \tag{3.35}$$

In this form, the first term of the right hand side (rhs) describes the interference fringes appearing with the phase Laplacian. It is the term that is used to retrieve the phase information in PBI. When working with less coherent sources, this effect gets lost and PBI no longer works. Without the membrane, the second term of the rhs would be close to 0 as the reference image would be homogeneous and therefore its gradient would be null. However, in MoBI, to compensate the loss of spatial coherence of conventional laboratory systems that will obliterate the first term, we try to maximize $\nabla_\perp I_r$ to facilitate the extraction of $D_\perp$ from the second term.
From those considerations, to simplify the resolution, we will neglect the first term corresponding to interference fringes effects. For more coherent cases it would be the same as considering the interference fringes included in the I_{obj} term. Then we get:

$$\begin{aligned} I_r(x,y) - \frac{I_s(x,y)}{I_{obj}(x,y)} \approx & D_\perp(x,y) \nabla_\perp I_r(x,y) \\ \approx & D_x(x,y) \frac{\partial I_r(x,y)}{\partial x} + D_y(x,y) \frac{\partial I_r(x,y)}{\partial y}. \end{aligned} \tag{3.36}$$

In the last equation we developed the rhs term to visualize more clearly the 2D problem. In this equation, we have 3 variables that are unknown: I_{obj}, D_x and D_y. A very simple way to solve this inverse problem is to acquire at least 3 pairs of acquisitions with different position p of the membrane to obtain a system to solve:

$$\begin{cases} I_r^{(1)}(x,y) = \frac{1}{I_{obj}(x,y)} I_s^{(1)}(x,y) + D_x(x,y)\frac{\partial I_r^{(1)}(x,y)}{\partial x} + D_y(x,y)\frac{\partial I_r^{(1)}(x,y)}{\partial y} \\ I_r^{(2)}(x,y) = \frac{1}{I_{obj}(x,y)} I_s^{(2)}(x,y) + D_x(x,y)\frac{\partial I_r^{(2)}(x,y)}{\partial x} + D_y(x,y)\frac{\partial I_r^{(2)}(x,y)}{\partial y} \\ I_r^{(3)}(x,y) = \frac{1}{I_{obj}(x,y)} I_s^{(3)}(x,y) + D_x(x,y)\frac{\partial I_r^{(3)}(x,y)}{\partial x} + D_y(x,y)\frac{\partial I_r^{(3)}(x,y)}{\partial y} \end{cases} \tag{3.37}$$

with $p \in P = \{1, ..., p_N\}, N \geq 3$.
This system requires theoretically only 3 positions to be solved but, in practice, there are some areas in the image where $\nabla_\perp I_r$ will be 0 or close to it and then the system is under-determined or imprecise. These areas will create very noisy results and to avoid this issue, more than 3 positions can be used. For each pixel, the algorithm uses a linear least squares method to solve the system.
As it was designed targeting to be used on conventional laboratory systems, we named this method the Low Coherence System algorithm (LCS) [136, 137] .

[136]: Laurene Quenot, Helene Rougé-Labriet, Sylvain Bohic, Sébastien Berujon, and Emmanuel Brun. 'Implicit tracking approach for X-Ray Phase-Contrast Imaging with a random mask and a conventional system'. In: *Optica* (2021)
[137]: Laurène Quénot, Ludovic Broche, Clément Tavakoli, Sylvain Bohic, and Emmanuel Brun. 'Towards x-ray phase contrast tomography in clinical conditions: simulation and phase retrieval development'. In: *Medical Imaging 2021: Physics of Medical Imaging*. Vol. 11595. International Society for Optics and Photonics. 2021

3.3.2 First validations on a synchrotron experiment

This algorithm was specifically designed for the low coherence cases but, as a first test, it was used on synchrotron acquisitions. In this case, the term that was neglected, corresponding to the interference patterns due to the sample, will be a part of the 'loss term' I_{obj}.

Two synchrotron experiments were tested with this algorithm. The first qualitative one is an imaging experiment of a mouse knee. The parameters of which are listed below.

Experiment 3.1: Mouse knee - ID17

- Distance source to membrane (z_0): 138 m
- Distance membrane to sample (z_1): 1.5 m
- Distance sample to detector (z_2): 11 m
- Source: ID17 - 52 keV
- Detector: CCD camera with magnifying optics => effective pixel size of 6.1 µm
- Membrane: Sandpaper stack
- Sample: Mouse knee in formalin (see Figure 3.4)
- Number of membrane positions acquired: 15.

Signals extracted from this experiment are displayed in Figure 3.5. As expected, the I_{obj} image appears to contain the absorption of the sample and the interference fringes as they can be observed in simple propagation based imaging. We call I_{obj} attenuation image even though it is a misuse of language. The displacement maps along the two axis allows us to appreciate a different contrast that can be integrated into the phase image. In this phase image, we observe some low frequency variations in

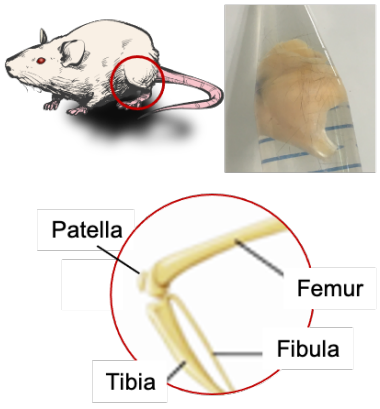

Figure 3.4: Mouse knee sample schematic and the main skeletal elements that will be visible on x-rays: patella, femur, tibia and fibula.

Figure 3.5: Mouse knee attenuation image I_{obj} and displacement maps (D_x, D_y) retrieved with the LCS along with the phase image integrated with the FC method.

the background that are due to the Fourier integration method. In the displacement maps we can see that the retrieved information has the same resolution as the attenuation image. This is an intrinsic characteristic of the implicit method. The main degradation that appears in these images is the shot noise. Because the calculation is done pixel-wise, the noise that was present in the acquisitions is directly transmitted to those images. In this case, this noise remains small compared to the actual signal and does not disturb the structures visibility. In cases with less statistics and a smaller signal, this noise might become important and some filters can then be applied to reduce it. This first experiment shows that the LCS can retrieve both the attenuation and the phase gradient information with high resolution and very good sensitivity compared to the level of noise in this high spatial coherence case.

In the first chapter, we defined the spatial coherence length (eq. 1.3 p. 17) as a quantity that determines the maximum distance between two points in the sample plane where the wavefield is still strongly correlated and can produce an edge enhancement effect. The relationship between this value and the strength of the phase signal that we can retrieve with MoBI is not straightforward as many other parameters are not taken into account (such as the propagation distance and the nature of the material). However, this spatial coherence length is correlated with the ability of the system to produce phase effects, taking into account the source size and the distance from the source to the sample. The higher this coherence length compared to the system resolution, the better chance to observe a significant phase effect. In this case $l_\perp = 55\mu m$ is much bigger than the system resolution of 6.1 µm. It explains why we get such a strong signal.

The second experiment was conducted using simple sample that allowed us to do a quantitative evaluation of the algorithm: a set of nylon wires. The experimental parameters are described below:

Experiment 3.2: Nylon wire - ID17

- Distance source to membrane (z_0): 138 m
- Distance membrane to sample (z_1): 1.5 m

- Distance sample to detector (z_2): 3.6 m
- Source: ID17 - 33 keV
- Detector: CCD camera with magnifying optics → effective pixel size of 3 µm
- Membrane: Sandpaper stack
- Sample: Nylon wires of 140 µm and 200 µm of diameter (see Figure 3.6
- Number of membrane positions acquired: 10

The displacement map perpendicular to the wires is displayed in Figure 3.7 along with their extracted profiles and theoretical ones.

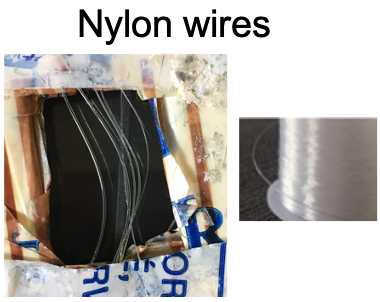

Figure 3.6: Nylon wires sample.

The theoretical profiles are computed with the following formula:

$$D_x(x) = z_2 \alpha_x(x) = \frac{z_2}{k} \frac{\partial \phi}{\partial x}(x) = -z_2 \delta \frac{\partial t}{\partial x}(x) \tag{3.38}$$

where t is the thickness of the wire along the x axis. This theoretical profile is blurred with a Gaussian kernel corresponding to the system point spread function. We can see that for the 140 µm wire, the result follows closely the theoretical profile with a NRMSE of 2.5 %. This proves that the retrieved information is quantitative which will be a great advantage for quantification studies. The second profile, for the 200 µm wire shows a very good fit of the retrieved displacement with the theoretical profile except for the highest values. In this case, we probably reached the limits of detection of the implicit algorithm that would struggle to render displacement that are bigger than the pixel. This will be an issue for very high resolution, high coherence systems and large refraction angles but as this algorithm aims at solving low resolution problems, this saturation effect will not exist in the target cases. Here the spatial coherence length is 86 µm which is once again much bigger than the system resolution of 3 µm.

These results are first proofs of the capacity of the algorithm to retrieve the phase information of a complex sample in "optimal" controlled experimental conditions. Using a simple monochromatic experiment we could compare the obtained displacements to predicted ones with low uncertainty on the model. This result showed that the LCS can give quantitative displacements in the case of small refraction.

We are here in the conditions where the source is monochromatic, it

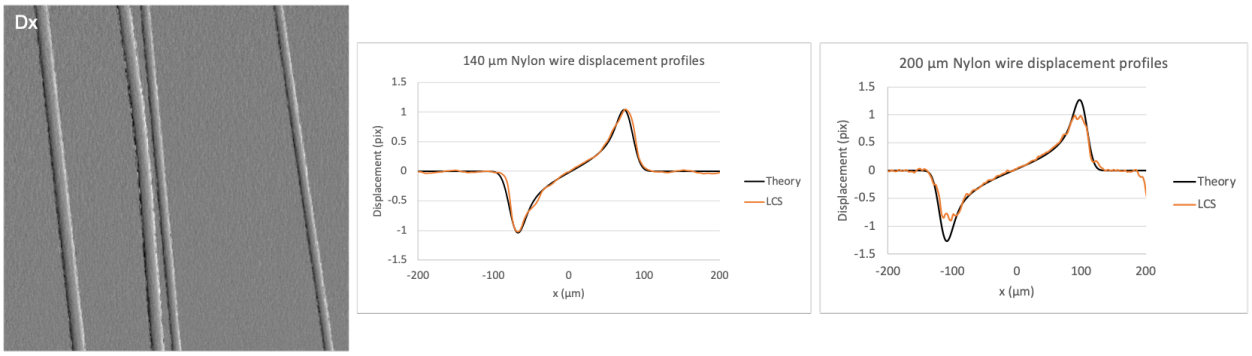

Figure 3.7: Nylon wire displacement map perpendicular to the wires orientation and their extracted profiles compared to theoretical profiles.

has a great spatial coherence and a very high detector resolution. All these parameters will be degraded with conventional laboratory set-ups, introducing new challenges.

3.3.3 Studies on conventional laboratory set-ups

After validating the algorithm on synchrotron experiments, it was confronted to conventional sources cases on several experiments. We will here present results obtained on two micro-CT set-ups with polychromatic tungsten anode sources and resolutions lower than the ones used at the synchrotron.

The fly experiment

A first experiment that will be presented here is an imaging experiment of a domestic fly on a set-up that was shared with us by the SIMAP laboratory of Grenoble. The experimental parameters are described here:

Experiment 3.3: The headless fly - Laboratory micro-CT

- System: adapted EASYTOM XL tomographic set-up from RX Solution, France
- Distance source to sample (z_0): 12 cm
- Distance sample to membrane (z_1): 6.5 cm
- Distance membrane to detector (z_2): 34.5 cm
- Source: micro-focus tungsten rotating anode with a focal spot of 4 μm FWHM and operating at 40 kVp.
- Detector: QUAD-RO CCD detector (Princeton Instruments, NJ USA) with a pixel size of 24 µm binned to a bigger pixelsize of 48 µm with a PSF of about 2.8 pixels (given from previous measurements on the equipment).
- Membrane: homemade plate of TiC grains of 100 µm average size.
- Sample: headless fly stuck to a straw with glue in air.
- Number of clean membrane positions acquired: 20.

Remark: a tomographic set-up was used but simple projections were studied.

In those conditions, the spatial coherence length of the set-up is $l_\perp = 2.5\mu m$ and the resolution of the system in the sample plane is 11 µm. We are now in conditions where the coherence length is smaller than the system resolution. It means that the phase effects are going to be much weaker than in the previously presented cases.

Before showing phase images, for readers like me who are not used to seeing fly radiographs, Figure 3.8 points out different fly anatomy structures that we can see in a fly x-ray. And to make things a little more complicated, it appears that this fly had lost its head before the experiment. What we can see is a thorax and abdomen with legs stuck on a plastic straw with liquid glue.

Figure 3.9 displays the displacement maps and integrated phase image obtained from 20 acquisitions with the LCS algorithm. In these images, we can see that, despite the low spatial coherence, the method is already

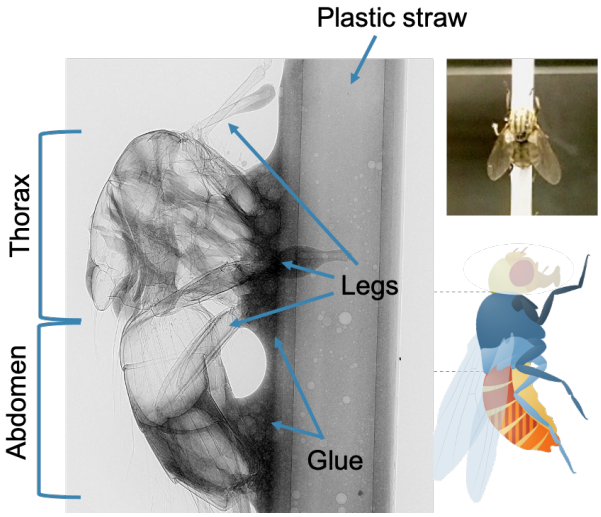

Figure 3.8: Headless fly radiograph and its structures.

sensitive to numerous details. As expected, we can see the Poisson noise in the background but in this case, it remains small compared to the retrieved signal of interest. What we can also see are small granular artifacts that are particularly visible in the most absorbing areas such as the one pointed by the yellow arrow.

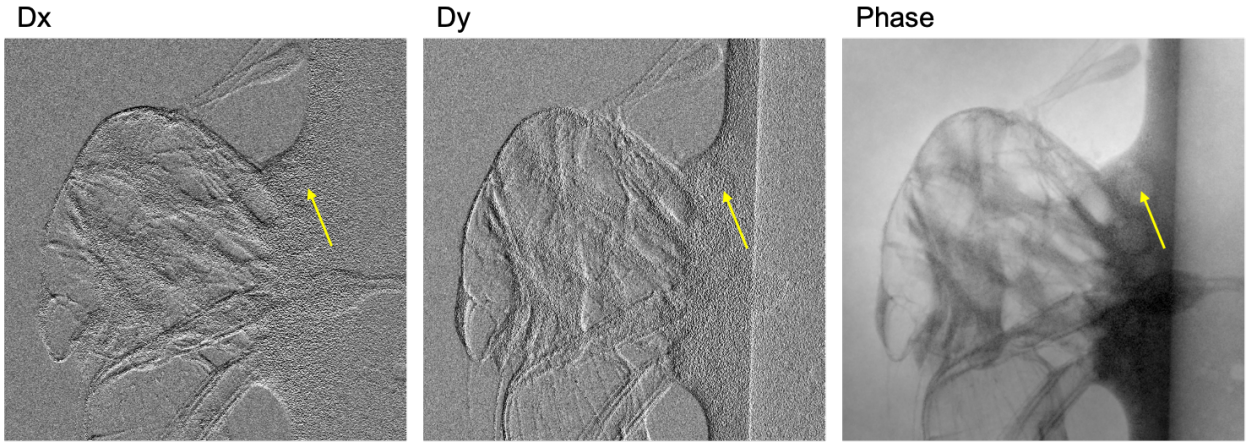

Figure 3.9: First phase gradient images of the fly retrieved with the LCS from acquisition with a conventional laboratory set-up.

We can make two hypothesis concerning the source of those artifacts:

1. It is due to beam hardening in the sample that induces a modification of the reference pattern that is not correctly accounted for in the phase retrieval method.
2. It is due to the system point-spread function that has an additional effect on the modulations gradients.

The first issue is quite complicated to compensate for, even though some works have been done for conventional tomography [138]. This lead has not yet been investigated but could be interesting for further improvements.
The second one was studied using image deconvolution to correct the blurring of the system PSF in the acquisitions (as it had been done for Mesh-Based Imaging [139]). An unsupervised Wiener deconvolution method [140] implemented in the Scikit-image Python library was used.

This function takes as parameters the image to filter and the convolution kernel to use for deconvolution. In this case, the kernel was assumed to have a Gaussian shape with a given Full Width Half Maximum (FWHM). This processing was applied to the acquisition with various FWHM in order to find an optimum. The image quality is a very difficult concept to quantify. In this case, we make use of contrast to noise ratio (CNR) and visual assessment.

Figure 3.10 shows the sample images after deconvolution with a kernel FWHM varying from 1.6 to 7 pixels. In the first images we see the edges getting sharper but from 2.8 to 7 pixels we see edge artifacts appearing, until transforming completely the image for the FWHM = 7 pixels.

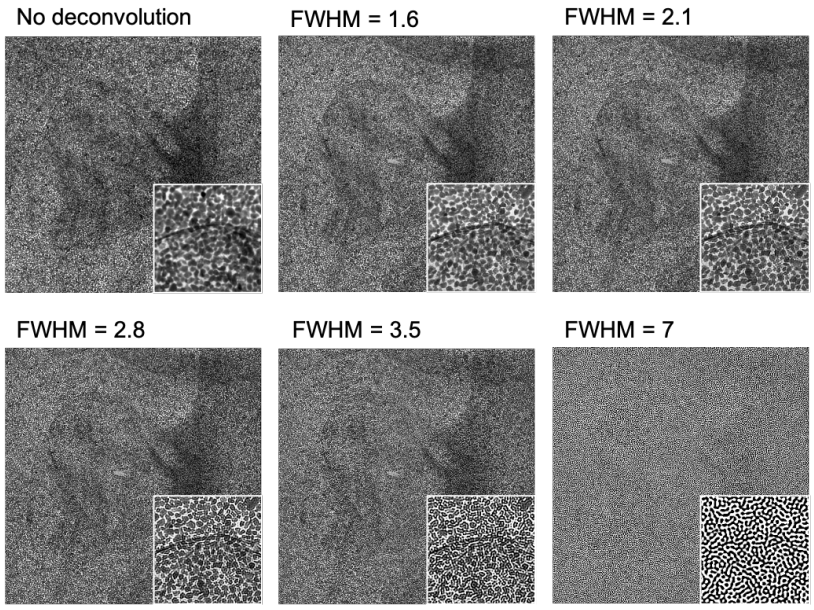

Figure 3.10: Sample images acquisitions after deconvolution by an unsupervised Wiener algorithms with an increasing full width half max (FWHM) Gaussian shaped kernel.

Displacement images and integrated phase images obtained from acquisitions after varying deconvolutions are shown in Figure 3.11. On those images, we can see that the edges of the sample are getting shaper when increasing the deconvolution kernel size before a new blurring appears with noise. When looking at the whole image, the difference may appear negligible but in the zoomed inset the difference appears clearly.

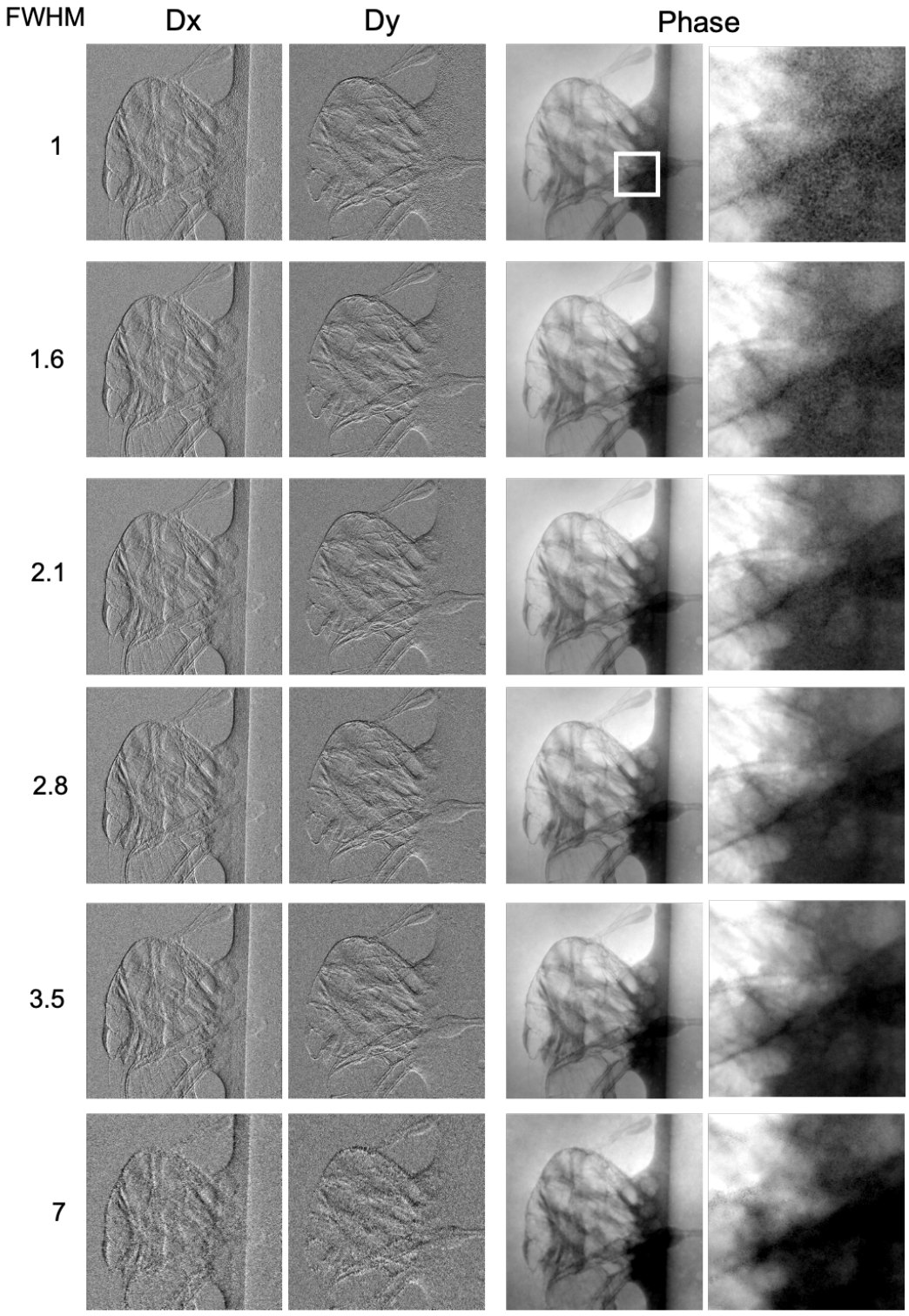

Figure 3.11: Evolution of the displacement maps and phase images retrieved with the LCS after de-blurring of the acquisitions with an increasing FWHM of the gaussian shaped deconvolution kernel.

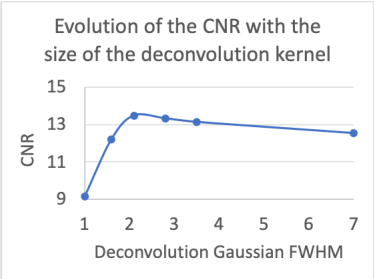

Figure 3.12: CNR measure on the phase images with increasing FWHM of the deconvolution shape.

We measured the contrast over noise ratio by comparing the measured values in a homogeneous zone in the glue and another one in the straw. Figure 3.12 presents the evolution of this CNR with the kernel size. It coroborates the visual assessment saying that the quality increases with the size of deconvolution, reaches an optimal value before decreasing again. Using this curve and the visual assessment, we can see that the best images are obtained when the deconvolution kernel FWHM is between 2.1 and 2.8 pixels. This second value corresponds to the mesured PSF of the system. This means that in order to avoid this calibration step in future works, it seems adequate to use the system PSF (when available) for this deconvolution process.

For the previous demonstrations we have used all the 20 positions of the membranes that were acquired. However, the more points are acquired, the longer is the acquisition time and the higher is the dose. Figure 3.13 shows the evolution of the retrieved displacement images when decreasing the number of positions used. We quantify the noise in those images by taking the standard deviation in an area of the background where the displacement should be 0. This noise has been converted to an angle to represent the angular sensitivity of the method when varying the number of positions. As we can see, the variation of the sensitivity is not linear with the number of acquisitions. The sensitivity improvement is quite small after 10 positions. And the noise gets really important below 6 acquisition, we can no longer consider it small with respect to the displacement that we want to measure.

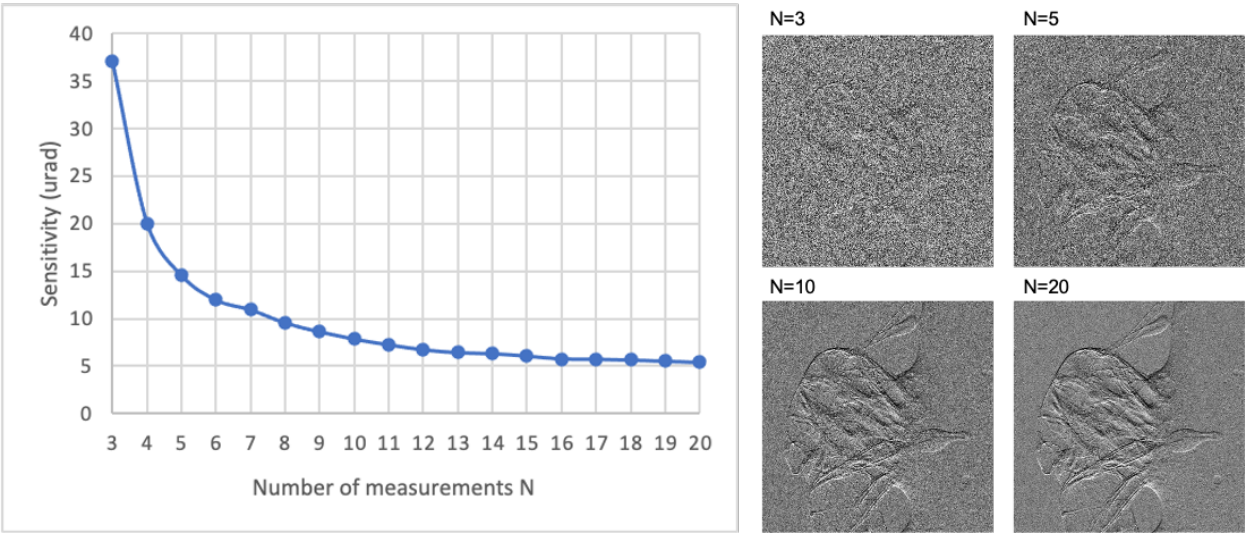

Figure 3.13: Evolution of the level of noise in refraction images with increasing membrane positions.

So, if we want to reduce the number of acquisitions, is there a way to filter the noise on the displacement maps efficiently? The most classical (and simplest) way to filter Poisson noise in an image is to use a median filter. The principle of this filter is quite simple: for each pixels it takes a window of NxN pixels around it and replaces the pixel value by the median value of all those pixels. This filter is very good at removing outliers while preserving edges. More recently, a lot of denoising and de-blurring methods based on dictionary learning have been developed [141, 142]. They are based on the following principle: natural or medical images can be represented in a sparse way with a linear combination

of only a few basic features but, theoretically, the noise cannot be. In other words, the algorithm constructs a small data-set of patches (<100 elements) from a training image set that are a linear decomposition of the variations present in the images. Those noiseless patches are then linearly recombined to match as well as possible the image to denoise. Figure 3.14 shows displacement and phase images in three cases: unfiltered, displacement maps filtered with a median filter and displacement maps denoised with our dictionary learning implementation. It shows that the level of noise in the displacement maps is indeed smaller than without filter. Our algorithm gives the lowest level of noise. However, interestingly, this denoising process appears to have a very little to no effect on the phase images. It seems that the noise present in the displacement maps is not transmitted with much intensity to the phase image integrated through Fourier.

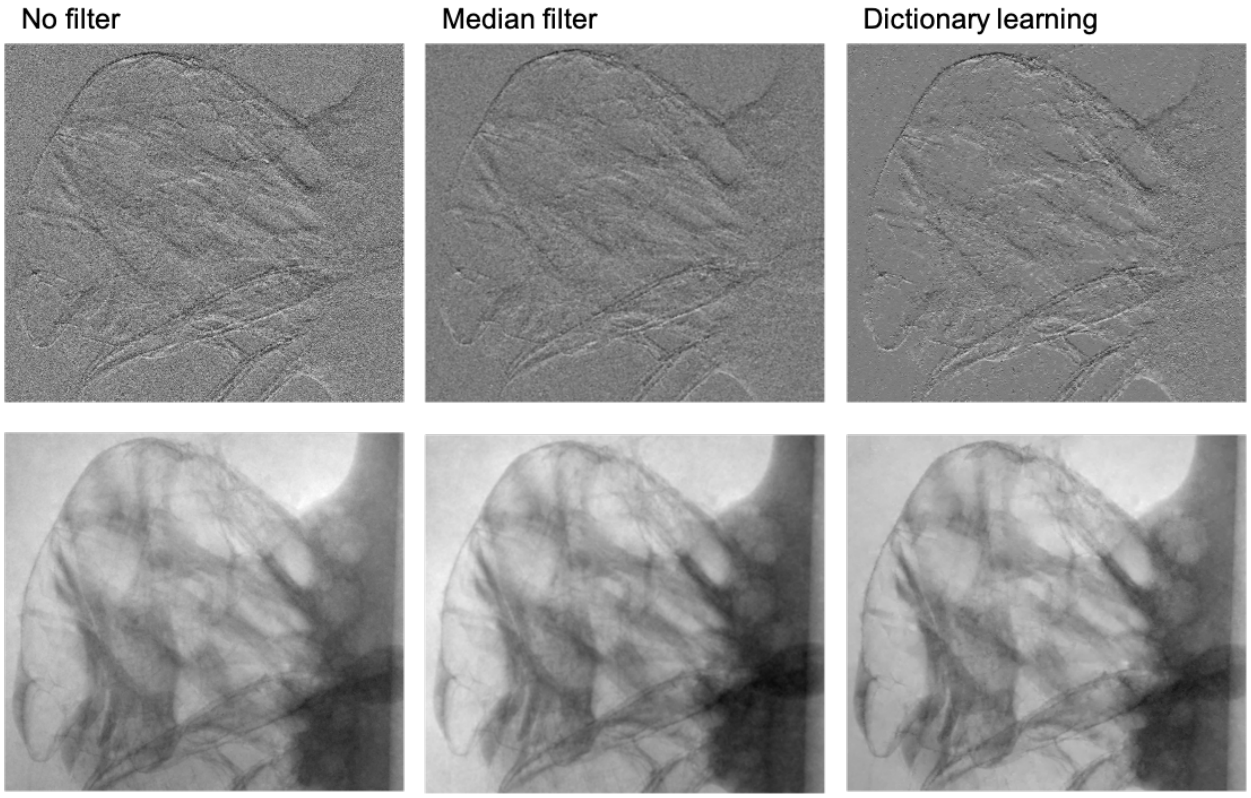

Figure 3.14: Displacement map and phase images without filters, with a median filter on the refraction image and after de-noising the refraction image with a dictionary learning method.

Finally, we wondered what would happen in similar conditions but with a lower resolution (i.e. bigger detector pixels). To "simulate" that effect, the acquisitions were binned to double the detector pixel size in both directions (a square of 4 pixels become one) creating 48 µm pixels and binned 4 times creating pixels of 192x192 μm^2. Doing this will increase the difference between the spatial coherence length and the system resolution. All 20 positions of the membrane were used and a deconvolution re-adapted to each resolution was applied. Displacement maps and integrated phase images are displayed in Figure 3.15. The first observations is that, at 96 µm, the retrieved displacements and phase still appear very sharp with a lot of visible structures. The retrieved displacements are smaller than for the 48 µm pixel size images but that

is to be expected as they are defined in pixels and the pixels are twice as big as the first ones. Even though it will be difficult to see on those small numerical/printed images, the phase images retrieved at 96 µm, despite still having a low noise level, appear less sharp than the 48 µm ones. As expected, there is a loss of sensitivity with increasing pixel size. However, it is interesting to see that at this resolution (which is getting closer to the one used in clinical devices) the very small displacements created by refraction through this very thin sample can still be detected. For the 192 µm pixel images, the results show a very poor images quality and almost no visibility of the structures. This can be explained by the fact that, with that resolution, the modulations size is barely bigger than the pixel and therefore tracking their displacement becomes impossible. For a more fair comparison, the modulations size should have been changed experimentally.

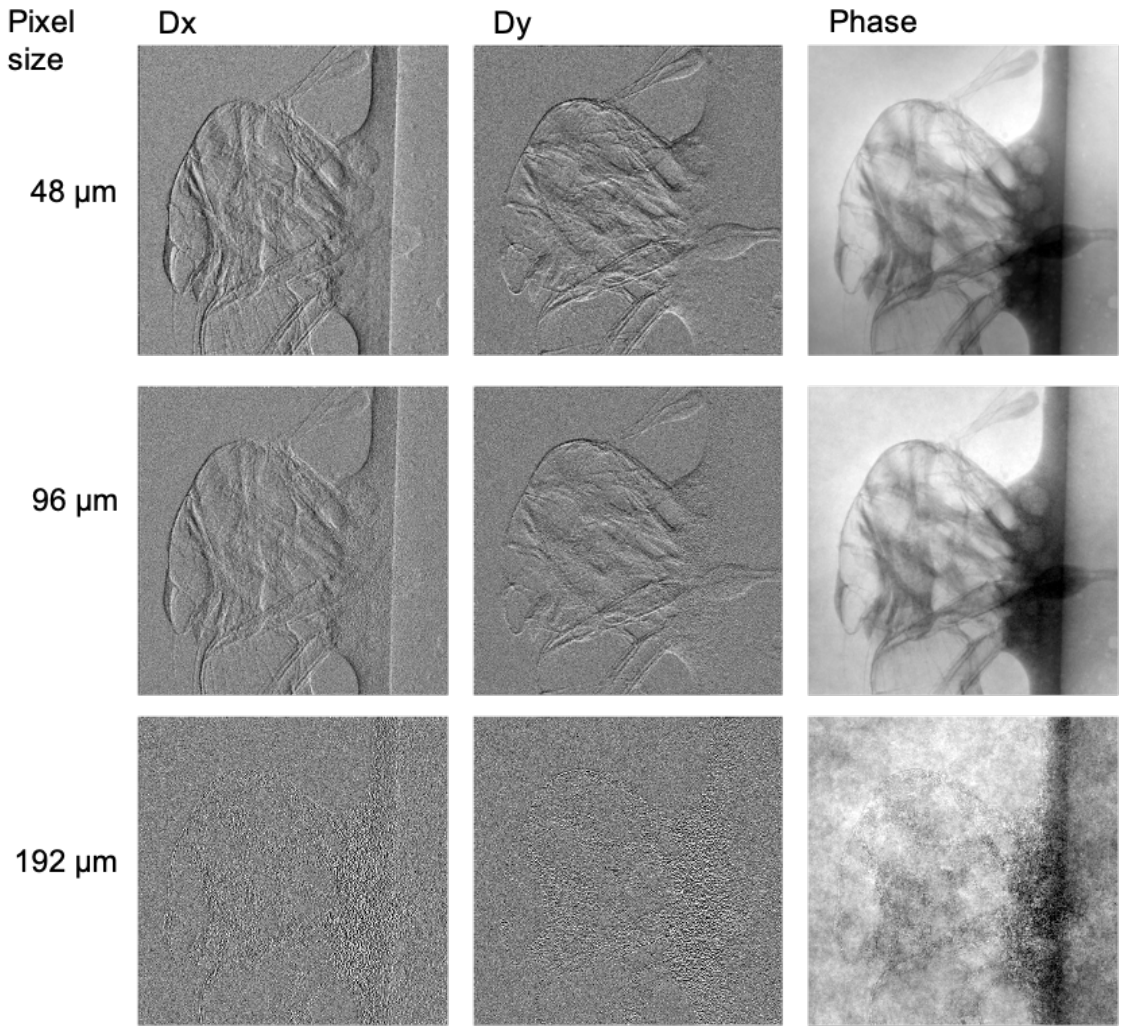

Figure 3.15: Evolution of the refraction and phase images retrieved from acquisitions with an increasing pixels size obtained through binning of the initial acquisitions.

This experiment was done in 2017, before the beginning of the current PhD work and the detector that was used got broken not late after this experiment which prevented it from being reproduced. Other experiment on conventional sources have been later attempted with little success.

Mouse knee

A second experiment was done with the same machine a few years later but with a bigger source (20 µm FWHM), another detector: a flat panel with pixels of 127 µm and another sample in the conditions described below.

Experiment 3.4: Mouse knee - Laboratory micro-CT

- System: adapted EASYTOM XL tomographic set-up from RX Solution, France
- Distance source to sample (z_0): 3.16 cm
- Distance sample to membrane (z_1): 1.44 cm
- Distance membrane to detector (z_2): 62.2 cm
- Source: micro-focus tungsten rotating anode with a focal spot of 20 µm FWHM and operating at 40 kVp.
- Detector: Flat panel with a pixel size of 127 µm.
- Membrane: homemade plate of CuSn grains of 100 µm average size.
- Sample: Mouse knee in tube.
- Number of membrane positions acquired: 25.

In those conditions, the spatial coherence is degraded even further than in the fly case. The coherence length is now down to 0.13 µm for a system resolution of 6 µm in the sample plane.

The LCS displacement maps and the phase image retrieved directly from those raw acquisitions are shown in the first line of Figure 3.16. In these first results we obtain very noisy images where the knee is barely visible on the displacement maps. On the phase image, we can see the bones appear in white. However, the phase of the bone is supposed to appear darker than the tube containing the knee. This is an artifact related to the source blurring associated to highly attenuating samples with sharp edges.

In order to try and correct it, a wiener deconvolution was applied on the acquisitions as it was done for the fly. The deconvolution kernel has to be more important in this case as it must compensate both for the detector PSF and the source blurring which projected size is about 5 pixels. The displacements and phase retrieved from the processed acquisitions are displayed in the second raw of Figure 3.16. We can see that the phase of the bone now appears in black as it should be however the images are still very noisy and do not allow us to see a lot of details.

In an attempt to understand the reasons behind this disappointing result and try to improve it, the sample and reference images were given a closer look. When taking a sample image and dividing it by its corresponding reference image, in the area outside the sample, only shot noise should be observed as the modulations of the membrane should cancel each other. However, as shown in Figure 3.17 we see a roughcast shadow effect in this area. This is due to set-up instabilities that induce a sub-pixel displacement of the membrane between the acquisition of the sample and reference images that no longer perfectly match each other. To correct this, a sub-pixel registration of the reference images on the sample images was attempted using the SimpleITK Python library. The ratio of the sample

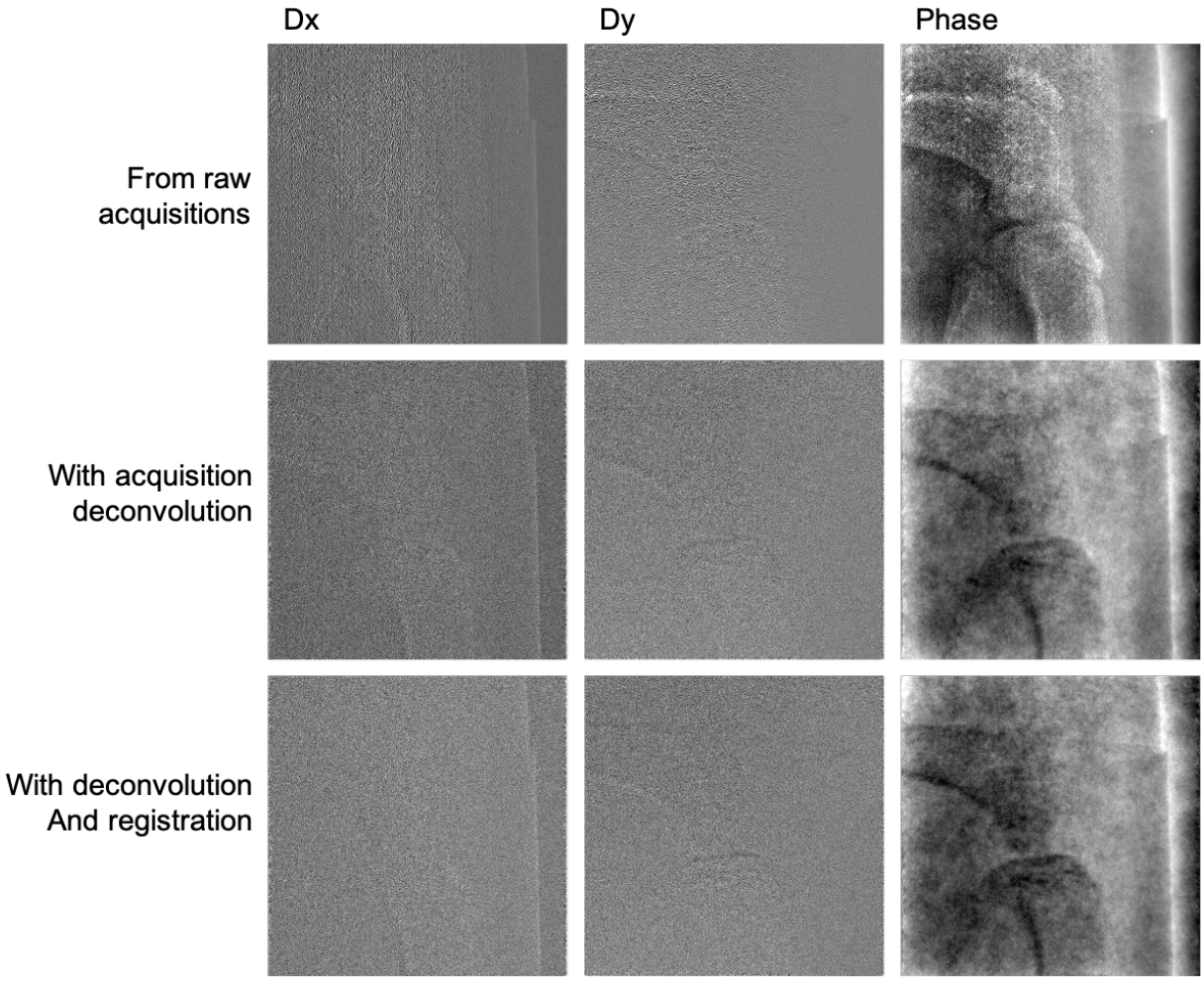

Figure 3.16: Displacement map and integrated phase retrieved from raw acquisitions (first raw) from acquisitions after deconvolution (middle raw) and from acquisitions after registration and deconvolution (bottom raw).

and reference images after registration is showed in Figure 3.17. It appears to have lost its roughcast shadow effect, however, as shown in the last raw of Figure 3.16, the retrieved displacement and phase images are not really improved. This means either that our registration is not good enough and might distort the modulations or that there is another parameter that prevents us from retrieving a better signal from the acquisitions. The main hypothesis is that the source blurring induces a too important loss of coherence and the shot noise is too significant in that case. And they cannot be appropriately corrected for a good signal extraction.

As a conclusion, this new algorithm is very interesting because it uses an implicit scheme to retrieve the phase, making it a very fast and very sensitive algorithm with a pixel wise resolution. However, it appears that it cannot make miracles in cases where the source is too big, the set-up is not stable and the noise is too important.

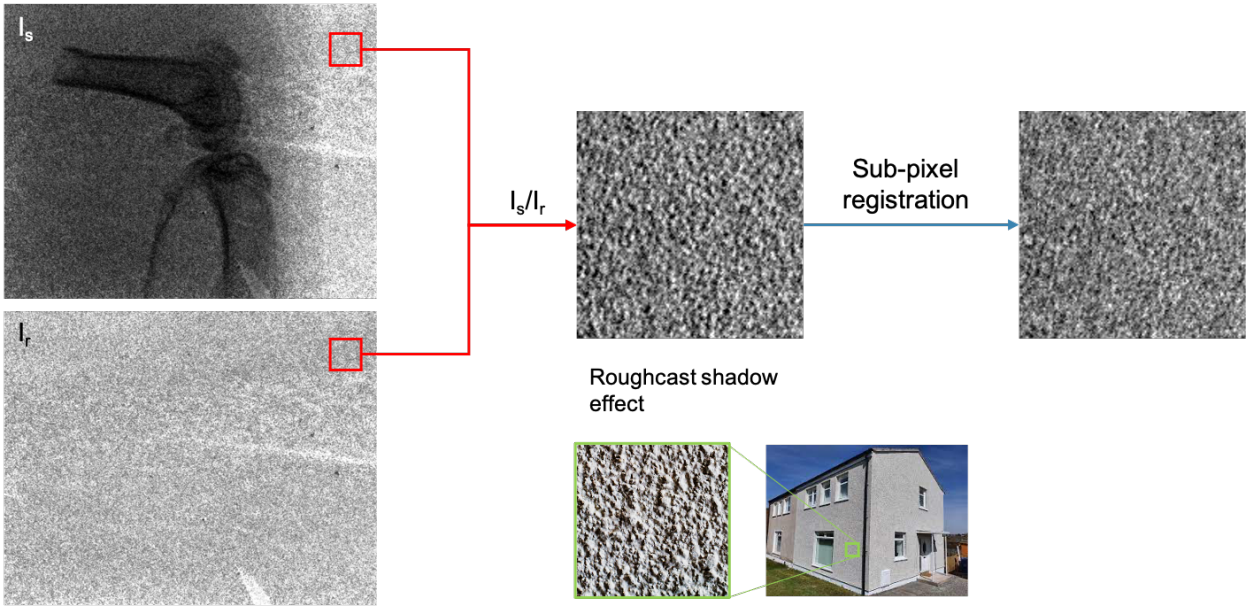

Figure 3.17: Process of comparison of the acquisition and correction of the roughcast shadow effect.

3.4 Comparison of algorithms

The work presented in this section was done in collaboration with Rafael Celestre, a beamline scientist at the ESRF.

Now that we have shown what is achievable with our new algorithm, we will compare it to the other algorithms that were introduced at the beginning of this chapter. We will have a look at various MoBI experiments:

1. A synchrotron medical imaging case (the ID17 mouse knee).
2. Two synchrotron quantitative experiment measurements (Beryllium lenses and nylon wire characterisation)
3. Two conventional source set-ups (the fly and the mouse knee on micro-CT)

3.4.1 Synchrotron biomedical case

The experiment used here is the one previously described as "Mouse knee - ID17" (exp. 3.1 p.95). All seven phase retrieval algorithms are compared: LCS, OF, UMPA, XST-XSVT, XSVT, WXSVT and SMOST. For the first six that give displacement maps (proportional to phase gradients) Frankot and Chellappa [130] integration algorithm was used to retrieve the phase as it is the one that gives images with the least low frequency artifact in this case.

Results obtained from 10 acquisitions are displayed in Figure 3.18. Due to Fourier integration or Fourier resolution the phase images obtained have offsets that make it impossible to compare their absolute values. Therefore the gray levels were adapted to each image and quantitative comparison of the phase is impossible. For the displacement maps, the same gray window was used for display.
The first observation is that, in those conditions, all the methods can give images with a contrast that allows to distinguish small details. However, the LCS, UMPA, XSVT and WXSVT appear to give the images with the lowest level of noise and higher sharpness. Compared to the other phase

gradient sensitive methods. On the phase image, the LCS appears to be the one capable to render straighter and sharper lines.
The OF gives very smooth images with no visible noise but a slight blur make some details difficult to see. This blur can be reduced by a low frequency filter in the Fourier domain but that leads to the appearance of an edge effect artifact. Also, because this method assumes a non absorbing sample, in this case where bones are highly absorbing, we can affirm that the signal retrieved here is at least partly composed of filtered absorption. Isolating only the phase signal of this sample is not possible with this algorithm.
The XST-XSVT method appears as the noisier. In this method, as in the UMPA, there is a trade-off between the resistance to noise from the acquisitions and the final resolution depending on the correlation window size. The two algorithms theoretically having similar way to solve the inverse problem (maximizing correlation or minimizing squared error on windows) the difference must be mainly due to the differences of implementation (one from our team and one from Zdora et al.'s team).
The SMOST phase image is the one showing the most details by far. However, it also shows some interference fringes and the image obtained is very similar to the one obtained in simple propagation. This is due to the nature of the retrieved signal that, assuming a single-material, combines information from the phase and attenuation. In addition, the similarity to the PBI formula raises an interrogation about the usefulness of the membrane in that case. Does it actually helps retrieving additional information or is it just perturbing the signal but not really used in the end? Finally, because the phase contribution to the signal here is mainly due to interference fringes (due to inherent assumptions), we can assume that in the case of less coherent beams, this algorithm can only give a signal that would correspond to a filtered attenuation.

Figure 3.19 presents similar images but from only four membrane positions of the data-set. For most of the algorithms, the observations are overall very similar to the previous case.
The OF and SMOST algorithms give results identical to the previous case deepening the doubt concerning the usefulness of the membrane in those cases and the nature of the retrieved signal.
For the LCS and UMPA, we observe a small loss of sensitivity and slightly less sharp edges which is to be expected with less information. The displacements are the most easily retrieved when the modulations are the most visible and have the highest gradients. With less membranes positions, there are some areas of the sample that might not overlap with sharp modulations making their displacement less efficiently tracked.
With only four membrane positions we can see that the XSVT and WXSVT fail to extract properly the displacements. This can be easily explained by the fact that those algorithms do not use windows of pixels to track displacements through cross-correlation but vectors of pixels from each pair of acquisitions. Vectors of only four values are too small to compute properly the cross correlation to retrieve the displacements.

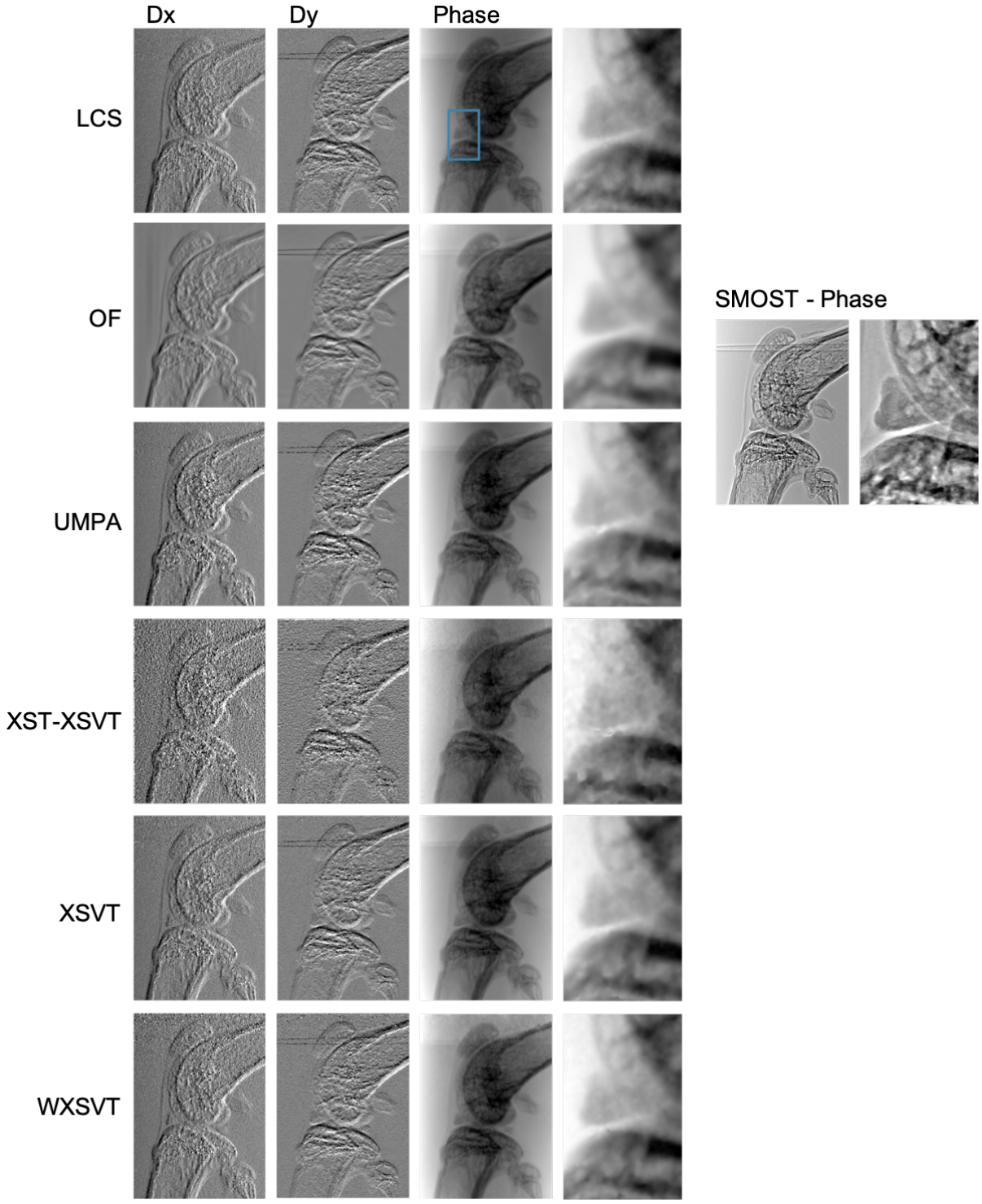

Figure 3.18: Displacement maps and phase images retrieved from acquisitions at 10 membrane positions with various phase retrieval algorithms.

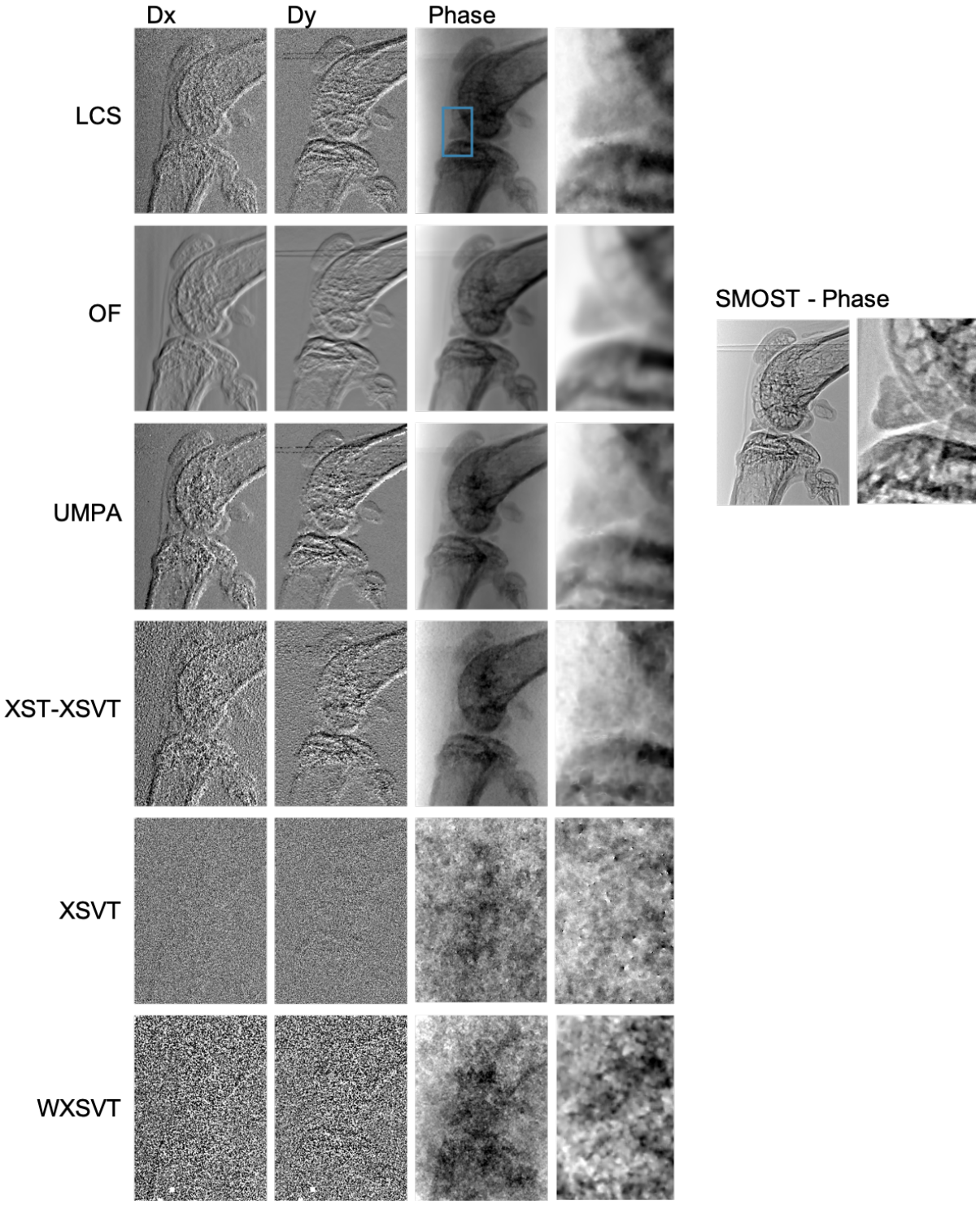

Figure 3.19: Displacement maps and phase images retrieved from acquisitions at 4 membrane positions with various phase retrieval algorithms.

3.4.2 Synchrotron quantitative measurements

We will now compare the algorithms in the case of quantitative measurements to characterise focusing lenses in a high resolution metrology experiment and a simple Nylon wire in an imaging set-up.

Experiment 3.5: Lens characterisation - BM05

- Distance source to membrane (z_0): 40.5 m
- Distance membrane to sample (z_1): 0.4 m
- Distance sample to detector (z_2): 80 cm (50 cm for the R50 lens)
- Source: Synchrotron bending magnet BM05 at 17 keV.
- Detector: PCO edge with magnifying optics giving a pixel size of 1.61 µm (0.64 µm for R50).
- Membrane: stack of sand paper.
- Sample: Lenses of varying curvature radii: 500 µm (R500), 4000 µm (R4000) and 50 µm (R50).
- Number of membrane positions acquired: 100 but 10 are selected randomly for phase retrieval.

The lenses studied in this experiment are focusing optics that need a precise characterisation in order to determine and correct their defects. A schematic of this kind of lens is displayed in Figure 3.20. These lenses aim at focusing the beam in a single spot in the sample to characterize it locally, or before the sample to create a secondary virtual source and a cone beam geometry. Lenses are not meant to attenuate the beam which is why they are made of very light almost non absorbing material, here Beryllium. In those experiments, the MoBI method is used to obtain a local information about the lenses. The detector is placed before the focal plane of the lenses. Because the rays going through the sample should all meet at the same position at some point through propagation, we expect the measured displacements to be a linear function in the plane perpendicular to propagation. Knowing that, we will here compare algorithms that allow to get displacement maps: LCS, UMPA, OF, XST-XSVT, XSVT and WXSVT that should give linear curve profiles.

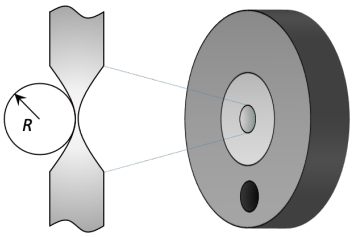

Figure 3.20: Schematic of an x-ray converging lens with its characteristic radius R.

The first results displayed in Figure 3.21 are for a 500 µm radius lens. The first observation here is that the OF is completely off track the other algorithms give images similar to each other. Horizontal profiles were extracted from those images, averaged over 40 lines and are plotted on the right. As previously mentioned we expect a linear profile. The reference methods for this type of studies are WXSVT and XSVT. Their profiles, in this case superimposed with the UMPA profile follow a linear curve. As previously observed, the OF is far from the expected values. The LCS and the XSVT algorithms are interesting as it appears that when the displacement to measure is between 1 and -1 pixels, they agree with the other algorithms but when the displacement gets bigger than 1 pixel they diverge. For the LCS this effect is inherent to the resolution method that works well under the pixel size but is not optimized for large displacements. Theoretically, it should still work as long as the modulations gradient is homogeneous over the displacement. Here the modulations are of about 5 pixels but with a wide standard deviation which can explain the loss of precision above one pixel. In theory, the XST-XSVT method is able to work with large displacement, the issue here comes from the implementation that was optimized for displacements smaller than the pixel leading it to diverge when the displacement is actually bigger. For quantitative comparison, the WXSVT method was taken as a reference and the NRMSE was used to compare the profiles from other methods to this one. It shows that the XSVT and UMPA methods give a difference lower than 1%. The LCS has a 6 % error, the

XST-XSVT a 19 % error and the OF error is even higher reaching 35 %. The computed errors are consistent with the previous observations.

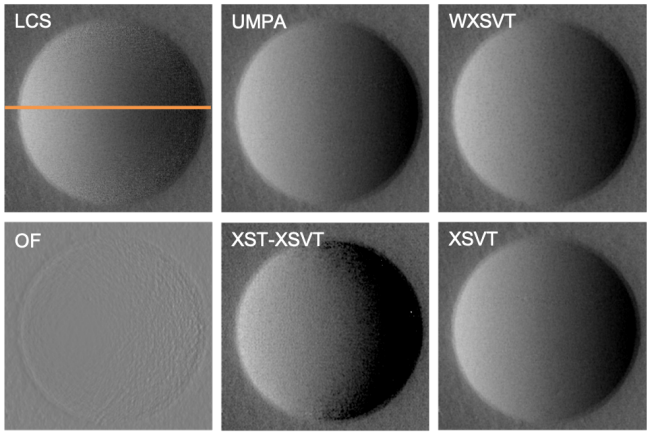

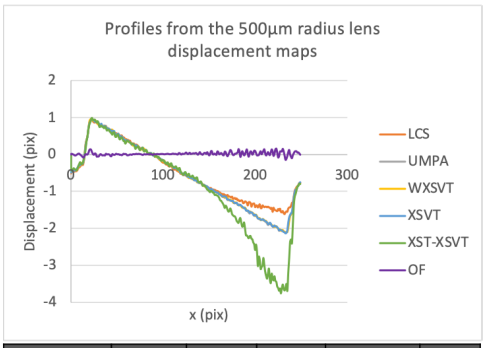

Algorithm	LCS	UMPA	XSVT	XST-XSVT	OF
NRMSE /WXSVT (%)	6	0.8	0.8	19	35

Figure 3.21: Displacement maps of a Beryllium lens with a characteristic radius of 500 µm. Displacements retrieved from acquisitions at 10 membrane positions with various phase retrieval algorithms used for metrology (XSVT and WXSVT) and imaging (LCS, OF, UMPA and XST-XSVT). The plots displays profiles taken in the middle of the lens. The table contains the NRMSE of the profiles obtained with all the algorithms compared to the wXSVT.

Figure 3.22 displays displacement images of a 50 µm radius lens (more converging than the previous one). Here the measured displacements are even bigger than for the previous lens. The observations made on the previous experiment are intensified in this case. UMPA, XSVT and WXSVT give linear results and are very similar to each other (NRMSE about 2 %). The LCS saturates completely above 2 pixels of displacements with an increasing amount of noise when increasing the displacement. The XST-XSVT appears to have a weird behaviour above 1 pixel. It also appears very noisy for small displacements. This is probably due to the algorithm parameter that allows to search for big displacements. Finally, the OF once again is completely lost and do not appear to detect any displacements.

The third experiment displays a 4000 µm radius lens in Figure 3.23. Here the lens is less convergent and the displacements are lower than the pixel size. In this case, the UMPA, XSVT and WXSVT are still very close but the LCS and XST-XSVT also agree with their profiles. The error of the LCS profile goes down to 1.5 % and the XST-XSVT to 2.4 %. This last algorithm however gives a quite noisy image as it can be observed on the profile. It appears to be more sensitive to set-up instabilities as the noise seem to have a granularity of size similar to the membrane modulations. In this case, the OF still gives a result that appear unrelated to the actual displacements. Those results raise the question of the ability of this algorithm to actually retrieve the phase and not simply filter attenuation (which is here absent).
A quantitative study was then conducted on the imaging set-up previously defined as "Nylon wire - ID17" (3.2 p.96). The same 6 algorithms were used to retrieve the displacement maps. Profiles averaged over 20 lines perpendicular to the wires were extracted from two wires: one with a diameter of 200 µm and one with a diameter of 140 µm. Results are displayed in Figure 3.24. In this experiment we observe that five algorithms out of six appear to be able to retrieve quantitative information. Once again, the OF is the one out of track. It appears to be able to

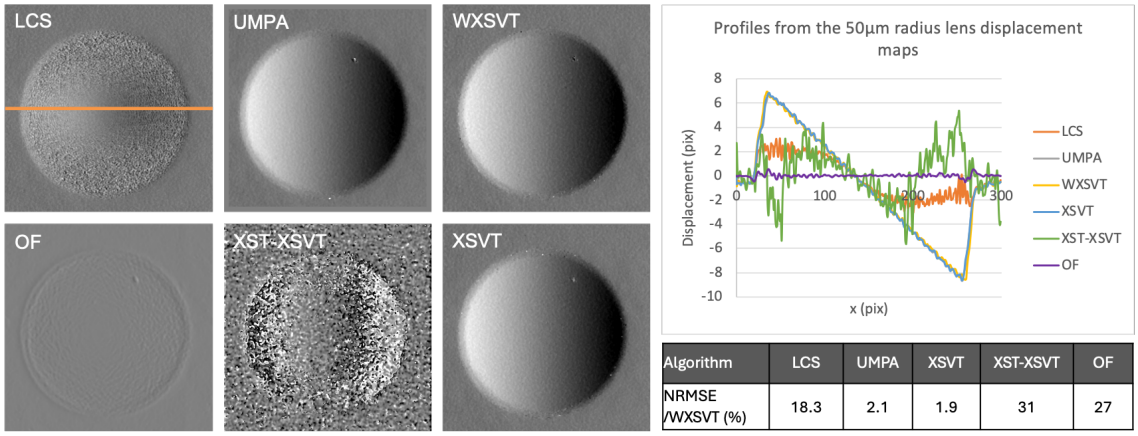

Algorithm	LCS	UMPA	XSVT	XST-XSVT	OF
NRMSE /WXSVT (%)	18.3	2.1	1.9	31	27

Figure 3.22: Displacement maps of a Beryllium lens with a characteristic radius of 50 µm. Displacements retrieved from acquisitions at 10 membrane positions with various phase retrieval algorithms used for metrology (XSVT and WXSVT) and imaging (LCS, OF, UMPA and XST-XSVT). The plots displays profiles taken in the middle of the lens. The table contains the NRMSE of the profiles obtained with all the algorithms compared to the wXSVT.

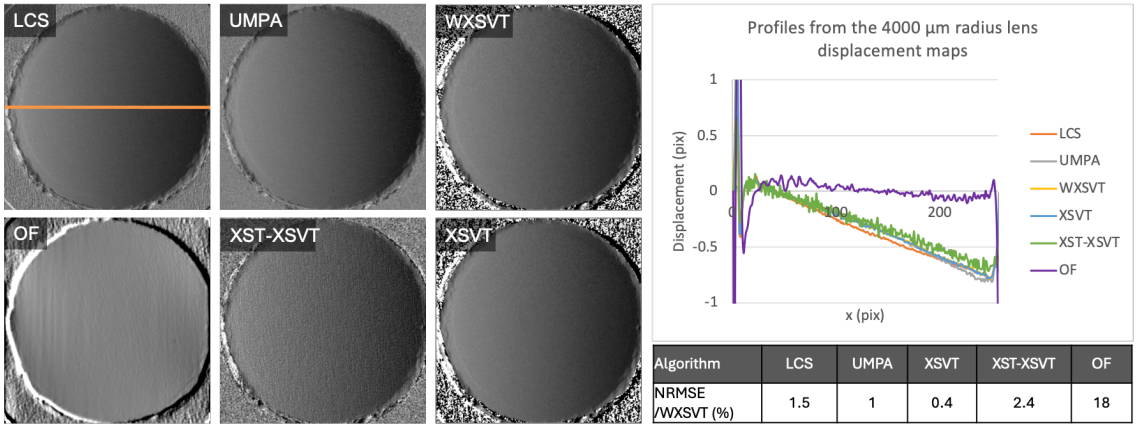

Algorithm	LCS	UMPA	XSVT	XST-XSVT	OF
NRMSE /WXSVT (%)	1.5	1	0.4	2.4	18

Figure 3.23: Displacement maps of a Beryllium lens with a characteristic radius of 4000 µm. Displacements retrieved from acquisitions at 10 membrane positions with various phase retrieval algorithms used for metrology (XSVT and WXSVT) and imaging (LCS, OF, UMPA and XST-XSVT). The plots displays profiles taken in the middle of the lens. The table contains the NRMSE of the profiles obtained with all the algorithms compared to the wXSVT.

retrieve a displacement-like information but this information being far from quantitative, we can assume that it is due to the weak but present attenuation of the nylon wires.
If we look at the NRMSE computed for each algorithm compared to the theoretical one, we can see that the UMPA gives the closest quantitative results with an error lower than 4 % for both wires. For the LCS, the WXSVT and the XST-XSVT the errors are between 4 and 6 %. These errors are possibly due to:

- The membrane random pattern that comprises areas with less visible modulations which induces the irregularities that are similarly visible in all the images at the wire edges.
- For the LCS: a small saturation effect when getting higher than 1 pixel of displacement.
- For the XST-XSVT: the diverging behaviour that was already observed with the lenses when reaching a displacement of 1 pixel.

Four main conclusions can be drawn from the above mentioned synchrotron experiments:

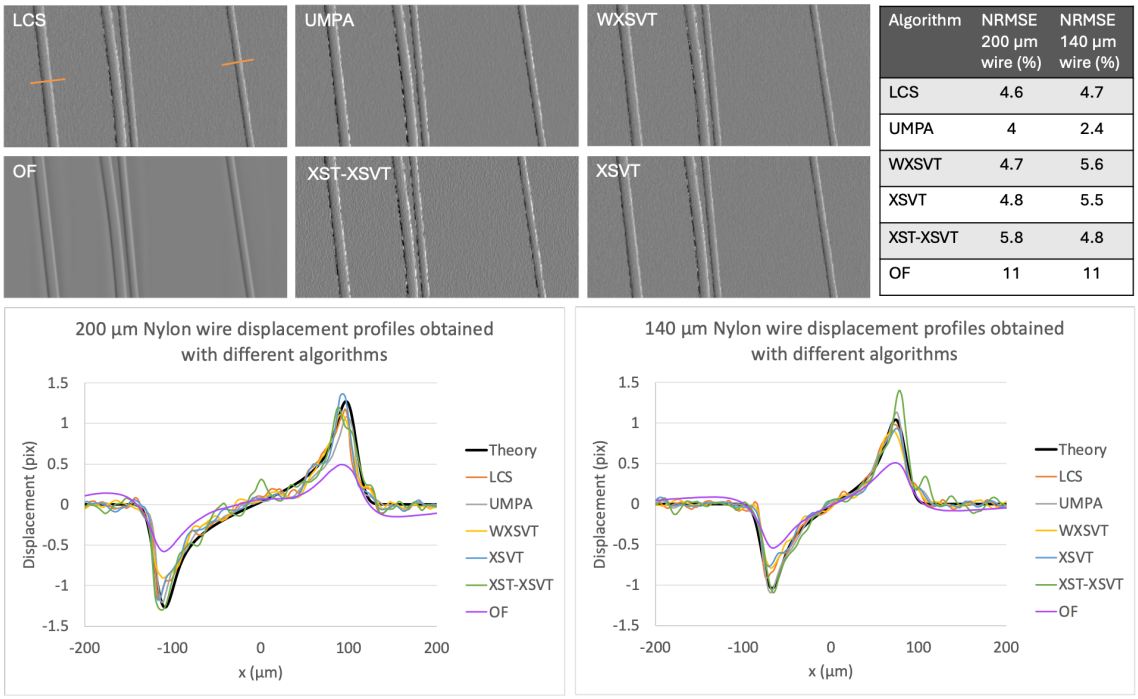

Algorithm	NRMSE 200 µm wire (%)	NRMSE 140 µm wire (%)
LCS	4.6	4.7
UMPA	4	2.4
WXSVT	4.7	5.6
XSVT	4.8	5.5
XST-XSVT	5.8	4.8
OF	11	11

Figure 3.24: Nylon wires displacement maps retrieved with different algorithms (LCS, UMPA, wXSVT, OF, XST-XSVT, XSVT). Plots of the wires profiles compared to theory. Table of the NRMSE calculated between the experimental profiles and the theoretical one.

1. LCS, UMPA, WXSVT, XSVT and XST-XSVT algorithms are capable of extracting quantitative displacements.
2. LCS and XST-XSVT are limited to small displacements smaller (< 1 pixel).
3. XSVT and WXSVT are designed for numerous membrane positions acquisition scheme and are not working with only a few positions.
4. OF and SMOST signals nature is difficult to identify and might not be phase. OF results are not quantitative, do not comprise membranes related artifacts as others do and it assumes non absorbing samples which will rarely be the case. SMOST formula is identical to single-material PBI, retrieves a signal from both attenuation and phase. Plus, SMOST results (which look like propagation images) do not seem to be influenced by the membrane and might not make use of it at all.

3.4.3 Conventional source imaging

In order to compare the algorithms in a low coherence laboratory case with a polychromatic source (x-ray tube), the "headless fly - Laboratory micro-CT" and "Mouse knee - Laboratory micro-CT" experiments data were used (exp. 3.3 p.98 and 3.4 p.105).

For the fly, the deconvolution was applied on the acquisitions before phase retrieval. For this comparison, 4, 10 and 16 membrane positions (N) were used. The obtained phase images are displayed in Figure 3.25. Because the noise structure vary a lot between the different algorithms and no efficient image quality metric could be found (without a tedious machine learning process), the quality assessment remains subjective and can be discussed. The results can be divided into three categories.

First, the LCS, UMPA and XST-XSVT appear to give equivalent results. The UMPA phase may appear slightly better with 4 positions but the LCS gives sharper, straighter lines at 16 positions.
Second, the OF gives identical slightly blurred result no matter the number of position. In this case the blur is balanced with an edge enhancement effect due to the Fourier low frequency filter. It appears to be the less noisy result however, as explained in the previous part, the nature of the signal retrieved here might be mainly due to filtered attenuation and not phase.
Third, the wXSVT and XSVT algorithms are definitely the noisiest results and they appear unable to extract phase information from only 4 membrane positions. Considering that they use a vector information over the number of positions and not window as the other explicit algorithms do, this is to be expected.

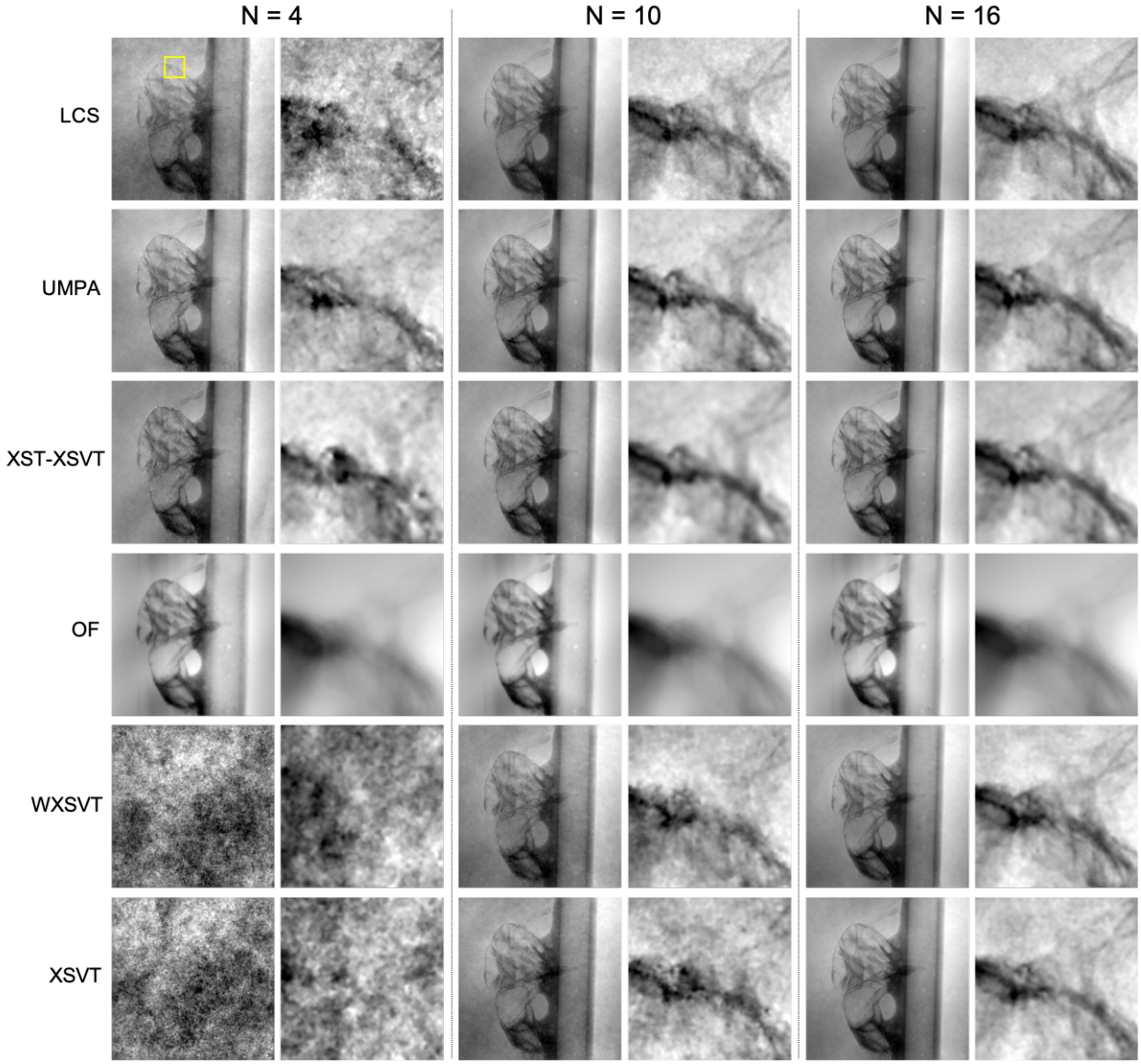

Figure 3.25: Phase images of a fly retrieved from a conventional laboratory set-up set of acquisitions with various available algorithms: LCS, UMPA, XST-XSVT, OF, wXSVT, XSVT from 4, 10 and 16 membrane positions.

Excluding the XSVT and wXSVT algorithms as they are least relevant in this configuration and the OF as it might not be retrieving phase, a

last comparison was done on the "Mouse knee - Laboratory micro-CT" experiment. The acquisitions were processed with sub-pixel registration and deconvolution before phase retrieval. In this case, as Figure 3.26 shows, all three algorithms appear to reach the limits of the achievable refraction signal extraction. One does not clearly outperform the others. Globally, under such conditions, UMPA, XST-XSVT and LCS give similar

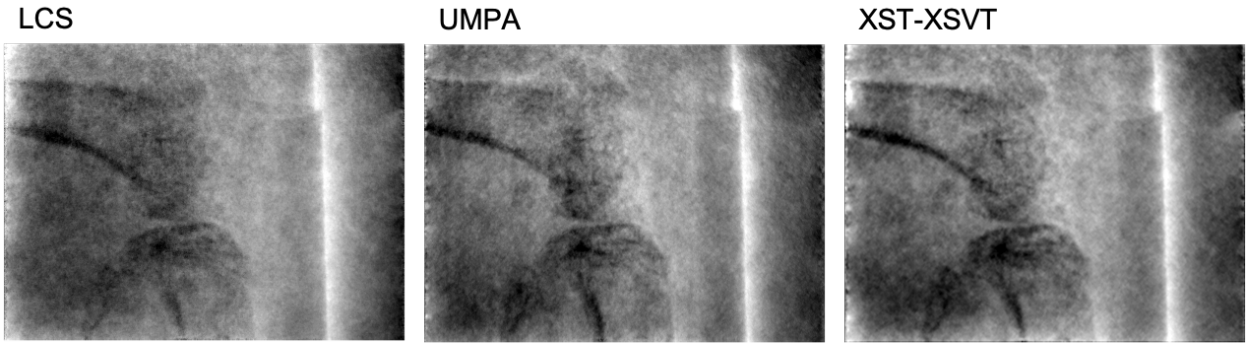

Figure 3.26: Phase images of a mouse knee retrieved from acquisition with a conventional laboratory set-up with three algorithms: LCS, UMPA and XST-XSVT.

results. The main difference that can be mentioned is the computational cost. Because the UMPA and XSVT compute error and correlation over windows of sizes $(2N_w + 1)^2$ that are displaced over distances $(2D_{max})^2$ on every pair of images N_p for every pixel of the images of dimensions $N_x \times N_y$ the total cost is $(2N_w+1)^2 \times (2D_{max})^2 \times N_p \times N_x \times N_y$ without even considering interpolation operations. The LCS however only computes a linear system on vectors of pixels from each acquisition at each membrane position leading to a cost of $N_p \times N_x \times N_y$. This explains why the LCS calculation is orders of magnitude faster than the UMPA or XST-XSVT.

3.4.4 Summary of the comparison of the algorithms

Table 3.1 summarizes a final comparison of the algorithms. The algorithms present different advantages and drawbacks. If searching for quantitative measures of high displacements (> 1 pixel) , the UMPA, XSVT and WXSVT are the best options. The WXSVT having a lower computational cost is probably the best option. For small displacements, the LCS and XST-XSVT also give quantitative results and the the LCS might be the fastest computation option based on the resolution method analysis.

For synchrotron high resolution imaging, LCS, UMPA, XSVT, XST-XSVT and WXSVT give similar results when a large number of membrane positions are acquired. With smaller numbers of points, XSVT and WXSVT are no longer good candidates.

For conventional micro-focus source imaging of complex samples, the LCS, UMPA and XST-XSVT give the best results and are similar to each other. In that case, for a fast computation, the LCS will be the best solution.

The OF and SMOST give interesting results when looking at complex samples but the nature of the extracted signal remains an issue. Further tests should be done to completely identify and characterize it. For example, a comparison between the signal retrieved with a membrane in

the sample and reference image and the same experiment without the membrane in the sample and reference images (then corresponding to propagation image and white) would give information on the usefulness of the membrane for the signal extraction of those algorithms. They might very well be just using interference fringes present at the edges of the sample and attenuation signal.

Algorithm	Quantitative measurement?	Computational cost	Sensitivity to small displacement
LCS	For displacements < 1 pixel	Low	++
UMPA	Yes	Very high	++
XST-XSVT	For displacements < 1 pixel (due to implementation)	Very high	++
OF	No	Very low	Lost in attenuation signal
SMOST	No due to Fourier frequency artefacts	Very low	Undetermined / unidentified nature of the signal
WXSVT	Yes	Medium	+ (With a lot of membrane positions)
XSVT	Yes	High	+ (With a lot of membrane positions)

Table 3.1: Summary of the characteristics of the various phase retrieval algorithms.

In clinical conditions, devices have very big pixels and a limited propagation distance, therefore, the sensitivity to small displacements will be one of the key factors. In addition, the computation would need to be fast and not require an additional costly computer. Finally, getting a quantitative measurement would be valuable and allow to differentiate and identify more easily the kinds of tissues. The LCS appear to be the candidate that best fit all those criteria.

3.4.5 Note on integration algorithms

As mentioned in the first section of this chapter, three algorithms are used for integrating displacement maps into phase images. One from Kottler et al. [132] that is used before tomographic reconstruction and was not used in the projection experiments presented in this chapter. The other two methods from Frankot and Chellappa [130] and Arnison et al. [131] are similar Fourier integration methods and, as any calculation in the Fourier space, when going back to real space some frequency artifact can appear. In the integration case especially artifacts appear due to the fact that the samples are often expanding out of the edges of the images and the boundary conditions are not respected. In order to reduce that effect, a mirror padding is applied on the displacement maps but most of the time a part of these artifacts remain. Interestingly, the two algorithms do not behave identically to each other and the prevalence of the artefacts depends on the experiment. Figure 3.27 shows example of integrated images from three experiments: the "Nylon wire - ID17" (exp. 3.2 p.96), the "Mouse knee - ID17" (exp. 3.1 p.95) and "The headless fly - Laboratory micro-CT" (3.3 p.98). The displacement images were computed with the LCS before integration.

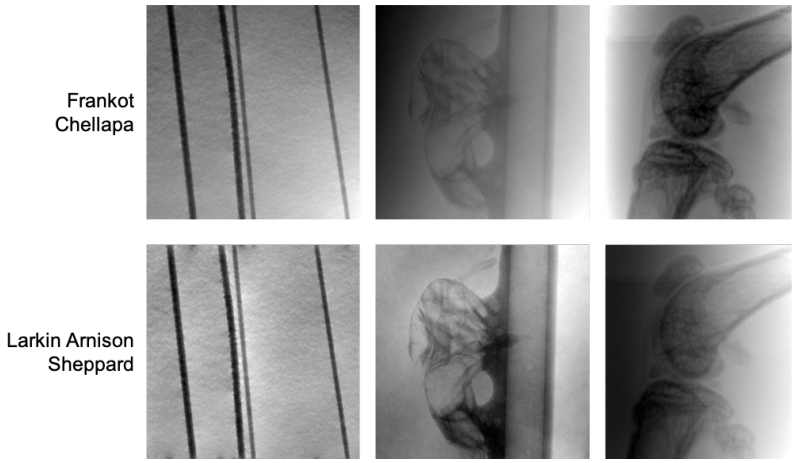

Figure 3.27: Phase integrated with two different algorithms: Frankot and Challapa's algorithm and Larkin Arnison Sheppard's algorithm. Initial refraction were retrieved with the LCS algorithms for the three samples acquired in different experiments.

3.5 Conclusion

This chapter focused on phase retrieval methods from MoBI acquisitions. Previous to this work, several algorithms had already been developed that could be categorized into two categories: explicit and implicit. The first used maximum correlation or error minimization to retrieve the displacement of the modulations due to refraction. While the second focused on solving the transport of intensity equation on every pixel to deduce those displacements. Explicit algorithms have the advantage of making no assumption on the sample or set-up however they are very computationally expensive. Implicit algorithms are several orders of magnitude faster but were based on very restrictive assumptions on the sample: non absorbing or composed of a single material.

In order to keep a fast calculation but to soften the hypothesis, we investigated new developments for phase retrieval. The first was based on the Fourier transform analysis of Fresnel interference patterns but it required acquiring several energies which is not often possible in our experiments. The second development was based on an adapted version of the transport of intensity equation with an additional term for the attenuation of the sample, assuming only a slowly varying displacement function. This algorithm especially designed for low coherence set-ups (even though it works as well on highly coherent set-ups) was called the Low Coherence System algorithm (LCS).

An extensive comparison of these algorithms on various experiments allowed to determine that the explicit algorithms along with the LCS are able to give quantitative results while other implicit algorithms do not. The LCS is a lot faster than the explicit algorithm however it is limited to displacements smaller than the pixel size. When considering very small displacements, the result depend a lot on the implementation of the algorithms. The LCS, UMPA and XST-XSVT were all designed to retrieve very small displacement and will work well on sub-pixel displacement while the XSVT and wXSVT ones are not correctly designed for that case. In clinical cases, where the imaging system will lead to very small displacements compared to the pixel size, the LCS will be the best option as it is fast and gives quantitative measurements that will allow to identify different tissues.

Résumé du Chapitre 3 en Français

Dans ce chapitre, nous nous intéressons aux méthodes numériques qui permettent d'extraire l'information de phase des acquisitions de référence et d'échantillon. Après avoir donné une vue d'ensemble des méthodes algorithmiques déjà existante, le travail que j'ai fait sur le développement de nouvelles méthodes est développé. Dans une dernière partie nous comparons tous ces algorithmes entre eux pour déterminer les forces et les faiblesses de chacun dans différentes conditions expérimentales.

Les premiers algorithmes inventés qui permettaient de récupérer la phase, nous les appelons "explicites" car ils cherchent a suivre de manière explicite les déplacements des modulations a travers des méthodes de corrélation croisée ou de minimisation d'erreur quadratique. Les seconds sont les algorithmes implicites qui sont basées sur la résolution d'une équation liée à la physique de l'expérience en chaque pixel. Cette équation de base est l'équation de transport d'intensité (ETI). La première version de la résolution implicite écrivait cette équation dans le cas d'un objet non absorbant, ce qui est très restrictif. La seconde supposait, elle, un objet constitué d'un unique matériau en plus d'autres hypothèses sur la variation de la phase.

Dans l'espoir de trouver une méthode avec moins d'hypothèse sur l'expérience, j'ai étudié d'autre méthodes. Pour la première, je me suis intéressée à la définition du motif d'interférence de Fresnel décrit par la fonction d'ambiguïté dans le plan de Fourier. En exprimant ainsi les images référence et échantillon on peut parvenir à deux résultats : un qui corrèle la ITE et un qui se rapproche de la fonction de transfert de contraste et qui peut être résolu en utilisant des acquisitions a plusieurs énergies. Acquérir plusieurs énergies n'étant pas facilement faisable sur des équipements classiques (besoin de détecteurs ou de sources spécifiques pour différentier les énergies), nous nous sommes concentrés sur les méthodes TIE.
En repartant de la première version de la TIE, un terme d'atténuation peut être ajouté et en faisant simplement l'hypothèse d'un échantillon dont la fonction de réfraction varie lentement, il est possible de simplifier grandement le problème. Le gradient de la réfraction correspondant au Laplacien de la phase, cela signifie que l'on néglige les franges d'interférence liées à la phase qui, en pratique, se retrouvent alors dans notre terme d'atténuation. On doit alors résoudre un simple système linéaire pour extraire les informations de l'atténuation et de la réfraction dans deux directions qui peuvent être intégrés en une image de phase. Cet algorithme a démontré sa capacité à récupérer une information quantitative sur deux expériences synchrotron et sa sensibilité aux faibles déplacements sur une expérience de laboratoire.

Dans une dernière partie, nous comparons toute une série d'algorithmes (pratiquement tous ceux existant dans la littérature) dans différentes conditions expérimentales et avec différents types d'échantillon. Nous observons que pour observer de grands déplacements de modulations par rapport à la taille des pixels, les algorithmes explicites donnent de meilleurs résultats. Dans le cas de faibles déplacements cependant, cela va dépendre grandement de leur implémentation et le LCS sera alors le plus rapide pour retrouver une information quantitative. Les autres algorithmes implicites donnent des résultats où de nombreux détails

apparaissent mais qui pourraient correspondre plus à de l'atténuation filtrée que réellement à de la phase. Le LCS semble égaler les performances des algorithmes explicit dans le cas de sources conventionnelles en un temps de calcul plusieurs ordres de grandeur plus faibles. Pour ces raisons, il serait l'algorithme de choix à utiliser en conditions cliniques.

Dark-field retrieval developments

4

4.1 Dark-field inverse problem algorithms 123
State of the art 123
Completing the LCS with a dark-field term 125
4.2 Directional dark-field 128
Theoretical developments and implementations 129
From tensors to ellipses . . 132
4.3 Applications to biological samples 137
Directional dark-field on a Mouse knee 137
Directional dark-field tomography of a tooth 138
In-vivo dark field radiography and tomography for the study of lung injuries 140
4.4 Dark-field on conventional laboratory sources 144
Directional dark-field with a low energy conventional source . . 144
High energy laboratory set-up146
4.5 Conclusion 148
Résumé du Chapitre 4 en Français 150

From modulations-based imaging acquisitions, in addition to the sample phase information, a second signal can be extracted: the dark-field. As mentioned in the first chapter, the dark-field corresponds to small angle scattering of the beam locally created by the presence of multiple micro-structures that induce multiple refraction of the beam at the interface between different materials. This signal is of special interest in medical imaging in order to study the lungs with their numerous alveoli that are too small to be seen directly on images but produce a strong dark-field signal thanks to the high number of interfaces between the lungs tissue and the air.

Figure 4.1 represents the influence of the dark-field on the reference pattern when introducing the sample. When taking a profile from the sample image and from the reference image we can see now the three contributions of the attenuation, the refraction and the scattering on this profile. Compared to the reference modulations, the sample profile gets lower in intensity with the attenuation of the sample, the modulations get shifted due to the refraction and finally, the modulations variations gets smaller due to the dark-field. Indeed, this scattering 'blurs' locally the reference pattern that gets less contrasted. It can therefore be defined as a local loss of visibility quantified by the standard deviation σ over a small window:

$$D_f = \frac{1}{T}\frac{\sigma_{Is}}{\sigma_{Ir}} \tag{4.1}$$

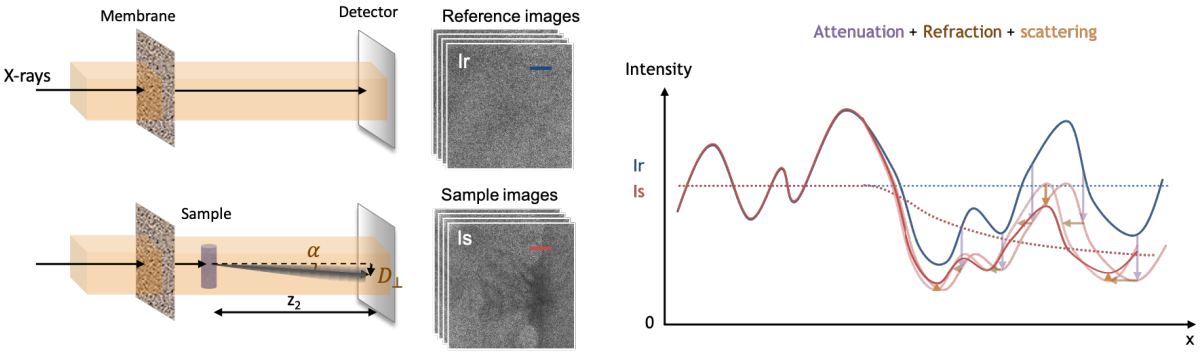

Figure 4.1: MoBI acquisition principle. A set of reference is taken in presence of the membrane at different positions (Ir) and a set is acquired with the sample in addition in the path of the beam (Is). The plot shows small profiles extracted from a sample and reference images. The profile of Is is lower due to attenuation, the membrane modulations are slightly shifted due to refraction and their amplitude decreases with dark-field.

In this chapter, we will first describe the already existing algorithms to retrieve the dark-field information. Then we will introduce new ones that allow to get a directional information about the micro-structures with some synchrotron phantoms experiments as a proof of concept. We will then show the interest of these contrasts on medically relevant

case studies and finally present some results obtained with laboratory set-ups.

Before starting, here are the mathematical and experimental notations used in this chapter.

Notations

Variables:

- n: complex refractive index
- δ: refractive index real part decay
- β: refractive index imaginary part
- μ: linear attenuation coefficient
- λ: wavelength
- $k = 2\pi/\lambda$: wavenumber
- $D_\perp = D_x, D_y$: intensity displacement in the detector plane related to refraction
- δ_x, δ_y: local displacements
- D_f: Dark-field
- $D_f^{(xx)}, D_f^{(xy)}, D_f^{(yy)}$: Directional dark-field tensors
- α: angle of refraction
- α_{df}: average opening angle of multiple refraction
- σ: standard deviation
- ϕ: phase
- z: spatial axis in the direction of propagation
- x, y : spatial coordinate perpendicular to propagation
- k_x, k_y: Fourier space coordinates (angular frequency)
- $\mathbf{f} = (f_x, f_y)$: Fourier space coordinates (frequency)
- $\{P\}$: set of membrane position
- z_0: distance between the source and the membrane
- z_1: distance between the membrane and the sample
- z_2: propagation distance between the sample and the detector
- I: intensity field
- I_r: Reference image of the optical elements without sample
- I_s: Sample image with the sample
- I_{obj}: intensity attenuation due to the object
- T: transmission of the object

Operators:

- ∇: gradient operator
- $Re\{\}$: Real part
- $\mathcal{F}$: Fourier transform
- $\mathcal{F}^{-1}$: inverse Fourier transform
- argmax_{param}: maximum argument when varying param
- argmin_{param}: minimum argument when varying param
- $\iint_{(x,y)} ..dxdy$: 2D surface integral
- $\sum_i$: sum of the following quantity for i in a set.
- log: natural logarithm
- e: exponential function

4.1 Dark-field inverse problem algorithms

In this section, we will introduce the three initial methods that allowed to retrieve the dark-field from MoBI experiments. Figure 4.2 summarizes the main algorithms that allow to retrieve the dark-field that were developed before my project. The XST-XSVT and UMPA were already introduced in the previous chapter as they were designed primarily to retrieve the phase but they can be completed to retrieve the dark-field signal. The MIST algorithm based on a new implicit scheme allows to retrieve also the phase but was especially designed for dark-field retrieval. After detailing how these algorithms allow to extract the dark-field signal, we will present the method that I used do complete the LCS algorithm with a dark-field component.

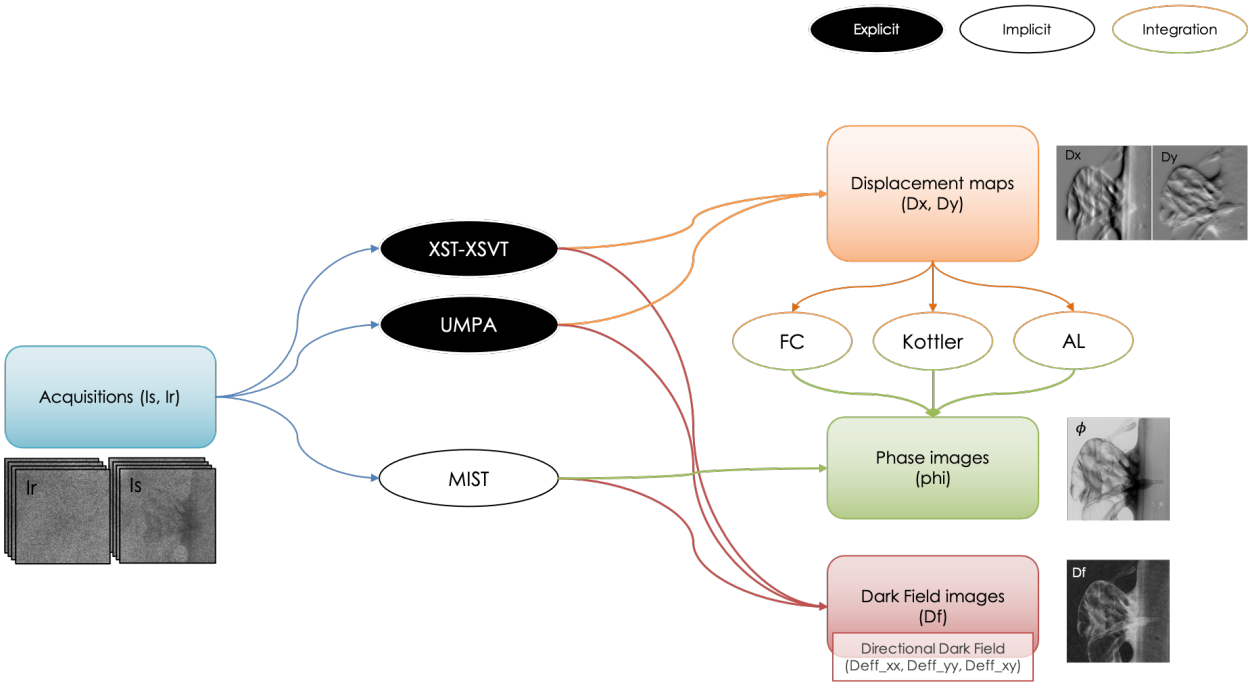

Figure 4.2: State of the art of the implicit and explicit phase retrieval algorithms and integration methods.

4.1.1 State of the art

For the explicit XST-XSVT algorithm, the dark-field can be easily computed using equation 4.1 on small local windows around each pixel [120]. Another way to do it is to complete the maximum correlation equation with the standard deviation of the sample and reference images of the considered patch $w(x_0, y_0)$. Then we use the computed correlation value for the dark-field [143]:

$$D_f(x_0, y_0) = 1 - \max_{\delta_x, \delta_y} \left[\sum_{p \in \{P\}} \frac{\iint_{x,y \in w(x_0,y_0)} I_s^{(p)}(x,y) I_r^{(p)}(x+\delta_x, y+\delta_y) dx dy}{\sigma^{(p)}_{Ir(w(x_0,y_0))} \sigma^{(p)}_{Is(w(x_0,y_0))}} \right] \tag{4.2}$$

For the UMPA, the dark-field coefficient was neglected in the previous chapter but the loss function to consider for each window $w(x_0, y_0)$ can

be written with an additional dark-field term D_f [117]:

$$\begin{aligned}\mathcal{L}(x_0, y_0; T, D_f, \delta_x, \delta_y) \\ = \sum_{p\in\{P\}} \iint_{x,y\in w(x_0,y_0)} \Big[T(x,y)[\hat{I_r} + D_f(I_r^{(p)}(x+\delta_x, y+\delta_y) - \hat{I_r})] \\ - I_s^{(p)}(x,y)\Big]^2 dxdy\end{aligned} \tag{4.3}$$

Where $\hat{I_r}$ is the average of all the pixels of the reference image over all the membrane positions. Then, as for the phase and transmission, the dark-field is retrieved by minimizing the loss function for each variable: $T, D_f, \delta_x, \delta_y$ for all the pixels (x_0, y_0):

$$D_\perp(x_0,y_0), T(x_0,y_0), D_f(x_0,y_0) = \underset{\delta_x,\delta_y,T,D_f}{\operatorname{argmin}} \mathcal{L}(x_0, y_0; T, D_f, \delta_x, \delta_y) \tag{4.4}$$

As for the phase, those algorithms are interesting because they do not make any assumption on the sample or the set-up but they are very computationally expensive.

Then again, very recently, an implicit scheme have been developed for dark-field retrieval. It is based on the Transport of Intensity Equation (TIE), as for the optical flow algorithm assuming a pure phase sample, but using the Fokker-Plank equation [144] to complete it with a diffusion term as described by Paganin and Morgan [145]:

$$I_r(x,y) - I_s(x,y) = \nabla_\perp[I_r(x,y)D_\perp(x,y)] - z_2\nabla_\perp^2[D_f(x,y)I_r(x,y)] \tag{4.5}$$

The first algorithm that was designed from that equation is the Multi-modal Intrinsic Speckle Tracking (MIST)[146]. In order to solve the inverse problem, eq. 4.5 is first developed to:

$$\begin{aligned}I_r(x,y) - I_s(x,y) =& I_r(x,y)\nabla_\perp[D_\perp(x,y)] \\ &+ \nabla_\perp[I_r(x,y)]D_\perp(x,y) \\ &- z_2 D_f(x,y)\nabla_\perp^2[I_r(x,y)] \\ &- z_2 I_r(x,y)\nabla_\perp^2[D_f(x,y)] \\ &- 2z_2\nabla_\perp[D_f(x,y)]\nabla_\perp[I_r(x,y)]\end{aligned} \tag{4.6}$$

In this MIST development, they assume that the displacements $D_\perp$ are very small and that the dark-field D_f is a slowly varying function allowing to neglect the second, fourth and fifth terms leading to:

$$I_r(x,y) - I_s(x,y) = I_r(x,y)\nabla_\perp[D_\perp(x,y)] - z_2 D_f(x,y)\nabla_\perp^2[I_r(x,y)] \tag{4.7}$$

$$I_r(x,y) - I_s(x,y) = \frac{z_2}{k} I_r(x,y)\nabla_\perp^2[\phi(x,y)] - z_2 D_f(x,y)\nabla_\perp^2[I_r(x,y)]$$

In the last line, the displacement field was replaced by the phase gradient as they are proportional. From there, there are two quantities to extract: the phase Laplacian and the dark-field signal. There are two ways to retrieve those variables. First, if we have two or more membrane positions, a linear least square method allows to solve the system (same methods

than for the LCS). The second way is to compute the analytical solution obtained by isolating the variables from a system with two membrane positions:

$$D_f(x,y) = \frac{1}{z_2} \frac{I_s^{(1)}(x,y) I_r^{(2)} - I_s^{(2)}(x,y) I_r^{(1)}}{I_r^{(2)} \nabla_\perp^2 I_r^{(1)}(x,y) - I_r^{(1)} \nabla_\perp^2 I_r^{(2)}(x,y)} \tag{4.8}$$

with (1), (2) the membrane positions. Then the phase Laplacian can be extracted from eq. 4.7 and integrated twice through Fourier space:

$$\phi(x,y) = \mathcal{F}^{-1} \left\{ -\frac{\mathcal{F}\left\{\nabla_\perp^2 \phi(x,y)\right\}}{k_x^2 + k_y^2} \right\} \tag{4.9}$$

This dark-field retrieval method, despite the very strong assumptions on the phase sample and small displacement was proven to give a dark-field image of higher contrast over noise ratio than the explicit methods especially when using a low number of images [146].

This MIST algorithm along with the complete versions of the XST-XSVT and UMPA are all implemented in the POPCORN python library that we developed.

4.1.2 Completing the LCS with a dark-field term

Inspired from eq. 4.5[145], the LCS algorithm introduced in the previous chapter could be completed with a diffusion term. Contrary to the MIST algorithm that assumes small displacements, we assume small variations of the displacement function that allow to simplify the term $\nabla_\perp^2[D_f(x,y) I_r(x,y)]$ by $D_f(x,y)\nabla_\perp^2[I_r(x,y)]$. The main difference is that, as already mentioned in the previous chapter, instead of considering that the displacements are small enough to neglect the term $D_\perp(x,y)\nabla_\perp[I_r(x,y)]$, we try to maximize the gradient of the reference image to be able to extract the displacement from this term. And we neglect instead the term with the gradient of the displacement which correspond to the phase Laplacian that creates interference fringes at the edge of the sample.
Then, as for the simple phase LCS version, we add the I_{obj} sink term to compensate for attenuation and that will comprise also those interference fringes in the most coherent cases. In the end we get the equation:

$$I_r(x,y) - \frac{I_s(x,y)}{I_{obj}(x,y)} = D_\perp(x,y)\nabla_\perp[I_r(x,y)] - z_2 D_f(x,y)\nabla_\perp^2[I_r(x,y)] \tag{4.10}$$

Once again here, in order to retrieve the attenuation, displacements and dark-field signal, we can simply solve a system with at least 4 membrane positions as we have now 4 variables:

$$\begin{cases} I_r^{(1)}(x,y) = \frac{I_s^{(1)}(x,y)}{I_{obj}(x,y)} + D_x(x,y)\frac{\partial I_r^{(1)}(x,y)}{\partial x} + D_y(x,y)\frac{\partial I_r^{(1)}(x,y)}{\partial y} - z_2 D_f(x,y)\nabla_\perp^2[I_r^{(1)}(x,y)] \\ I_r^{(2)}(x,y) = \frac{I_s^{(2)}(x,y)}{I_{obj}(x,y)} + D_x(x,y)\frac{\partial I_r^{(2)}(x,y)}{\partial x} + D_y(x,y)\frac{\partial I_r^{(2)}(x,y)}{\partial y} - z_2 D_f(x,y)\nabla_\perp^2[I_r^{(2)}(x,y)] \\ I_r^{(3)}(x,y) = \frac{I_s^{(3)}(x,y)}{I_{obj}(x,y)} + D_x(x,y)\frac{\partial I_r^{(3)}(x,y)}{\partial x} + D_y(x,y)\frac{\partial I_r^{(3)}(x,y)}{\partial y} - z_2 D_f(x,y)\nabla_\perp^2[I_r^{(3)}(x,y)] \\ I_r^{(4)}(x,y) = \frac{I_s^{(4)}(x,y)}{I_{obj}(x,y)} + D_x(x,y)\frac{\partial I_r^{(4)}(x,y)}{\partial x} + D_y(x,y)\frac{\partial I_r^{(4)}(x,y)}{\partial y} - z_2 D_f(x,y)\nabla_\perp^2[I_r^{(4)}(x,y)] \end{cases} \tag{4.11}$$

This algorithm was implemented along with the other ones in the Popcorn library.

The new LCS was tested on the synchrotron experiment that was used in [146] which experimental parameters are described below:

Experiment 4.1: Red currant - BM05

- Distance source to membrane (z_0): 55 m
- Distance membrane to sample (z_1): 0.5 m
- Distance sample to detector (z_2): 1 m
- Source: ESRF BM05 - 17 keV
- Detector: FReLoN e2V camera coupled with a scintillator. Pixel size of 5.8 µm.
- Membrane: Sandpaper stack
- Sample: Red currant.
- Number of membrane positions acquired: 25.

As for the phase, it is difficult to define a direct relationship between the spatial coherence length and the dark-field signal however, it can still be interesting to have an idea on the degree of coherence of the system. In this case, the spatial coherence length is about 40 µm which is about 7 times the pixel size.

Figure 4.3 shows the phase and dark-field images retrieved from the MIST and LCS algorithms. We can see that the phase and dark-field images appear to differ slightly between the two methods. This can be explained by the difference in the approximations and simplifications that were made. It appears that the MIST algorithm detects more signal at the sharp edges of the sample than the LCS. When comparing to the results obtained with the XSVT and UMPA shown on fig. 2 of [146], both algorithm detect more signal at the edges of the sample. This phenomenon is probably due to the approximations that are made in order to simplify the equation in the implicit schemes that are not necessary in the explicit ones (XSVT and UMPA). The main drawback of this experiment on a red currant is that it is difficult in that case to understand the source of the dark-field signal.

A new experiment was done more recently using a Haribo crocodile impaled with a wooden tooth pic as described below.

Experiment 4.2: Haribo Crocodile - ID17

- Distance source to membrane (z_0): 138 m
- Distance membrane to sample (z_1): 1.5 m

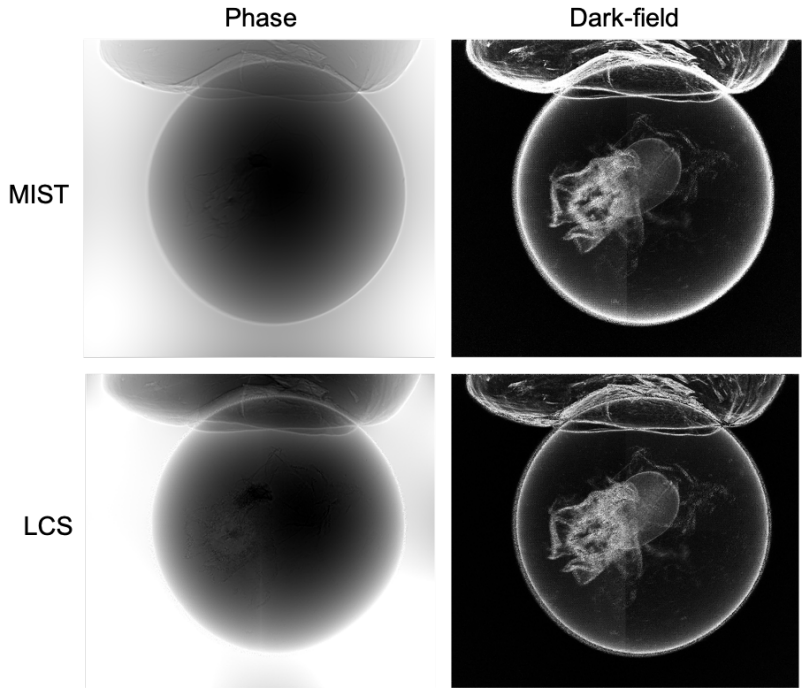

Figure 4.3: Phase and dark-field images of a red currant retrieved with the MIST and LCS algorithms.

- Distance sample to detector (z_2): 3.6 m
- Source: ID17 - 29 keV
- Detector: Photon counting Eiger from Dectris with pixels of 75 µm
- Membrane: Sandpaper stack
- Sample: Haribo crocodile impaled with a tooth pic (see Figure 4.4)
- Number of membrane positions acquired: 15

In this experiment, the spatial coherence length is 500 µm corresponding to about 7 times the pixel size.

This sample is more interesting because we know that dark-field signal is produced by numerous interfaces (as evidenced in [113]) and it happens that the white "foam" of the crocodile is full of those while the blue gel is not. The wooden stick which is a very fibrous sample also comprises a lot of interfaces. Figure 4.5 shows the dark-field signal obtained from this experiment using MIST and LCS algorithms. As expected, the algorithms are blind to the blue gel in the dark-field term but retrieve a lot of signal in the white foam and a little bit in the wooden stick. This allows to confirm that the signal retrieved with those algorithms is associated with the presence of numerous interfaces.

Figure 4.6 allows to better appreciate all the different signals that the LCS algorithm can extract from the MoBI experiment. The coloured image combines attenuation (Iobj), Dark-field (Df) and phase, into its RGB channels. It allows to better appreciate the different areas of the sample that produce different signals.

To conclude, we have upgraded the LCS to add a dark-field extraction in addition to displacement maps and attenuation retrieval and proven that it could retrieve those contrasts with a low level of noise in a highly

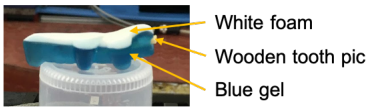

Figure 4.4: Haribo crocodile candy impaled with a wooden tooth pic.

Remark:
In these images, as well as in other figures later in the chapter, we can see a vertical black line. This is due to a dead area between two chips of the detector.

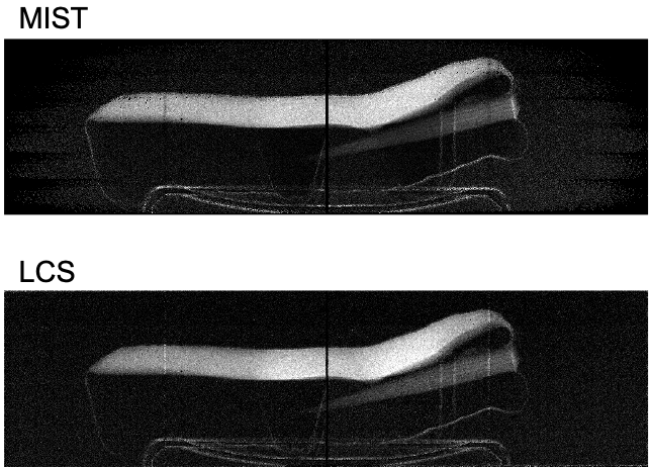

Figure 4.5: Dark-field signal of the Haribo crocodile retrieved with the MIST and LCS algorithms.

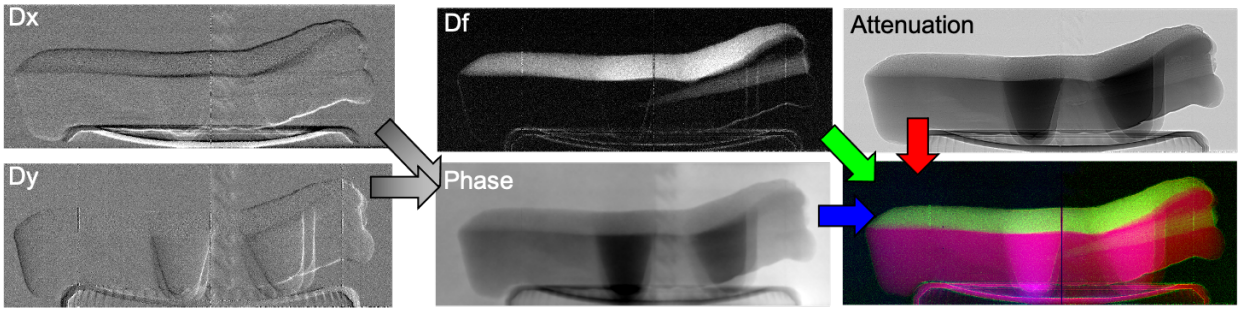

Figure 4.6: Various contrast images of the Haribo crocodile that can be retrieved with the LCS algorithm. Combined attenuation (Iobj), Dark-field (Df) and phase, into RGB channels of a coloured image.

coherent but low resolution case. There are now three main reasons why the LCS is a very powerful algorithm for MoBI:

- It allows to retrieve 4 signals at once: attenuation, refraction along the x axis, refraction along the y axis and dark-field
- It makes only small assumption on the sample assuming it produces slowly varying displacements and dark-field
- It is fast to compute as it is based on an implicit scheme and requires only to solve a linear system for each pixel that can be made massively parallel.

What if we could go even further and retrieve the direction of unresolved structures?

4.2 Directional dark-field

In the first chapter, we have introduced the dark-field as a blurring caused by multiple refraction through numerous particles. So far, we have considered isotropic particles and an isotropic blurring. But, in many cases, those micro-structures we observe through dark-field can be oriented (like fibers for example). Then the multiple refraction would be more important in the direction perpendicular to the fibers and the blurring would have a preferential direction. Figure 4.7 represents a beamlet that hits an oriented sample and gets anisotropically scattered. Instead of having a fading disk hitting the detector, we have a fading

ellipse. Investigating this scattering direction had already been done

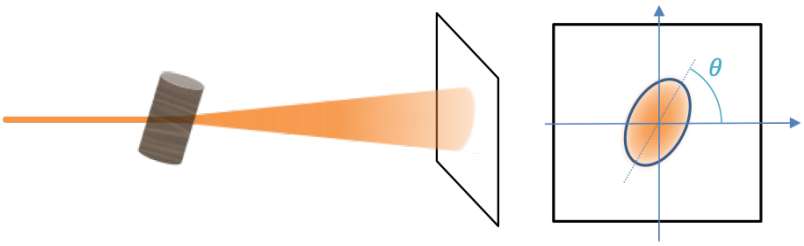

Figure 4.7: Schematic of the scattering cone emanating from a beamlet crossing the sample and hitting the detector as an ellipse shape with an orientation θ.

using gratings interferometry but, as the gratings are only 1D, the sample had to be rotated and the dark-field measure repeated in order to access the directional information [147–149]. The advantage of MoBI is that we can retrieve directly a 2D dark-field signal from the same acquisitions we have been working with since the beginning!

In this section, we will present the theoretical developments that were done with two implicit models, the proofs of concept and visualization optimization.

4.2.1 Theoretical developments and implementations

The directional dark-field developments presented in this section (particularly the MISTII developments) were done together with the Professors Pavlov, Kaye and Paganin from the University of Canterbury and the Monash university.

Considering *directional* dark-field requires to adapt the TIE - Fokker Planck equation 4.5 using a rank-two tensor to describe it [146]:

$$D_f(x,y) = \begin{bmatrix} D_f^{(xx)}(x,y) & D_f^{(xy)}(x,y) \\ D_f^{(xy)}(x,y) & D_f^{(yy)}(x,y) \end{bmatrix} \tag{4.12}$$

Then the eq. 4.5 becomes:

$$\begin{aligned} I_r(x,y) - I_s(x,y) = & \frac{z_2}{k}\nabla_\perp[I_r(x,y)\nabla_\perp\phi(x,y)] \\ & - z_2\frac{\partial^2}{\partial x^2}\left[D_f^{(xx)}(x,y)I_r(x,y)\right] \\ & - z_2\frac{\partial^2}{\partial y^2}\left[D_f^{(yy)}(x,y)I_r(x,y)\right] \\ & - z_2\frac{\partial^2}{\partial x\partial y}\left[D_f^{(xy)}(x,y)I_r(x,y)\right] \end{aligned} \tag{4.13}$$

From there, we developed three methods of resolutions following the schemes of the MIST and LCS algorithms [136, 150] .

[150]: Konstantin M Pavlov, David M Paganin, Kaye S Morgan, Heyang Thomas Li, Sebastien Berujon, Laurène Quénot, and Emmanuel Brun. 'Directional dark-field implicit x-ray speckle tracking using an anisotropic-diffusion Fokker-Planck equation'. In: *Physical Review A* 104.5 (2021)

[136]: Laurene Quenot, Helene Rougé-Labriet, Sylvain Bohic, Sébastien Berujon, and Emmanuel Brun. 'Implicit tracking approach for X-Ray Phase-Contrast Imaging with a random mask and a conventional system'. In: *Optica* (2021)

MISTII-a: case of a phase sample

In the first MIST-like development we use three quite restrictive hypothesis:

1. Non attenuating sample
2. Slow phase variations
3. Slow dark-field variations

in order to get:

$$\begin{aligned} I_r(x,y) - I_s(x,y) = &\frac{z_2}{k} I_r(x,y) \nabla_\perp^2 [\phi(x,y)] \\ &- z_2 D_f^{(xx)}(x,y) \frac{\partial^2}{\partial x^2} [I_r(x,y)] \\ &- z_2 D_f^{(yy)}(x,y) \frac{\partial^2}{\partial y^2} [I_r(x,y)] \\ &- z_2 D_f^{(xy)}(x,y) \frac{\partial^2}{\partial x \partial y} [I_r(x,y)] \end{aligned} \tag{4.14}$$

In this equation, we have four unknowns to retrieve so we will need at least four membrane positions. The main drawback of this method is that the phase sample hypothesis is a very restrictive one, especially when considering medical samples.

MISTII-b: case of a single material sample

In order to take into consideration more absorbing samples, a second version was developed. With a sink term compensating for the sample attenuation (I_{obj}) associated to the reference image eq. 4.13 can be completed:

$$\begin{aligned} I_r(x,y) I_{obj}(x,y) - I_s(x,y) = &\frac{z_2}{k} \nabla_\perp [I_r(x,y) I_{obj}(x,y) \nabla_\perp \phi(x,y)] \\ &- z_2 \frac{\partial^2}{\partial x^2} \left[D_f^{(xx)}(x,y) I_r(x,y) I_{obj}(x,y) \right] \\ &- z_2 \frac{\partial^2}{\partial y^2} \left[D_f^{(yy)}(x,y) I_r(x,y) I_{obj}(x,y) \right] \\ &- z_2 \frac{\partial^2}{\partial x \partial y} \left[D_f^{(xy)}(x,y) I_r(x,y) I_{obj}(x,y) \right] \end{aligned} \tag{4.15}$$

From there, we assume again that the phase and the dark-field are slowly varying. Considering the case of a single material sample, the phase and attenuation terms can be combined as they both depend on the sample thickness and the refractive index as described in [150]. In the end, the equation to solve can be written:

$$\begin{aligned} \frac{I_s(x,y)}{I_r(x,y)} = &\left(1 - \frac{\gamma z_2}{2k} \nabla_\perp^2\right) I_{obj}(x,y) \\ &+ z_2 D_f^{(xx)}(x,y) \left[I_{obj}(x,y) \frac{\frac{\partial^2}{\partial x^2} I_r(x,y)}{I_r(x,y)} + \frac{\partial^2}{\partial x^2} I_{obj}(x,y) \right] \\ &+ z_2 D_f^{(yy)}(x,y) \left[I_{obj}(x,y) \frac{\frac{\partial^2}{\partial y^2} I_r(x,y)}{I_r(x,y)} + \frac{\partial^2}{\partial y^2} I_{obj}(x,y) \right] \\ &+ z_2 D_f^{(xy)}(x,y) \left[I_{obj}(x,y) \frac{\frac{\partial^2}{\partial x \partial y} I_r(x,y)}{I_r(x,y)} + \frac{\partial^2}{\partial x \partial y} I_{obj}(x,y) \right] \end{aligned}$$

A linear system resolution once again allows to retrieve all the quantities.

LCS directional dark-field: completing the LCS with the dark-field tensors

Using that same theory, it is possible to add the dark-field tensor formalism to the LCS algorithm. Still neglecting the phase Laplacian (or considering its contribution incorporated into I_{obj}), eq. 4.13 becomes:

$$\begin{aligned} I_r(x,y) = \frac{I_s(x,y)}{I_{obj}(x,y)} + D_x(x,y)\frac{\partial}{\partial x}I_r(x,y) + D_y(x,y)\frac{\partial}{\partial y}I_r(x,y) \\ - z_2 D_f^{(xx)}(x,y)\frac{\partial^2}{\partial x^2}\left[I_r(x,y)\right] \\ - z_2 D_f^{(yy)}(x,y)\frac{\partial^2}{\partial y^2}\left[I_r(x,y)\right] \\ - z_2 D_f^{(xy)}(x,y)\frac{\partial^2}{\partial x \partial y}\left[I_r(x,y)\right] \end{aligned} \tag{4.16}$$

Here, the equation is solved using a system with at least six membrane positions as we have now six quantities to retrieve: I_{obj}, D_x, Dy, $D_f^{(xx)}$, $D_f^{(yy)}$, $D_f^{(xy)}$.

First directional dark-field results

Those 3 algorithms were tried on the "Red currant - BM05" experiment (exp. 4.1 p.126) and on the "Haribo Crocodile - ID17" experiment (exp. 4.2 p.126). For all three algorithms we can see that the retrieved information differ depending on the tensor components. On the $D_f^{(xx)}$ images, vertical structures appear, on the $D_f^{(yy)}$ we retrieve mainly the horizontal structures while on the $D_f^{(xy)}$ image, we retrieve the diagonal information which is not necessarily a positive value contrary to the first two component on the tensor. We observe that, on the phase sample version of the MIST development, the structures inside the berry are barely visible. This is probably due to the fact that the assumption of a non absorbing sample is not correct in this case at 17 keV.

Figure 4.9 presents now tensor images of the Haribo crocodile and its toothpick. As for the anisotropic versions of the algorithms we observe a lot of signal in the white foam of the crocodile and in the wood. The interesting thing that we observe here is that the toothpick which has very oriented structures has a much more important signal in the y direction than in the x direction and a small positive crossed term (indicated by the yellow arrows). This proves that the tensor components retrieved with those algorithms give real indications about the sample structures orientation.

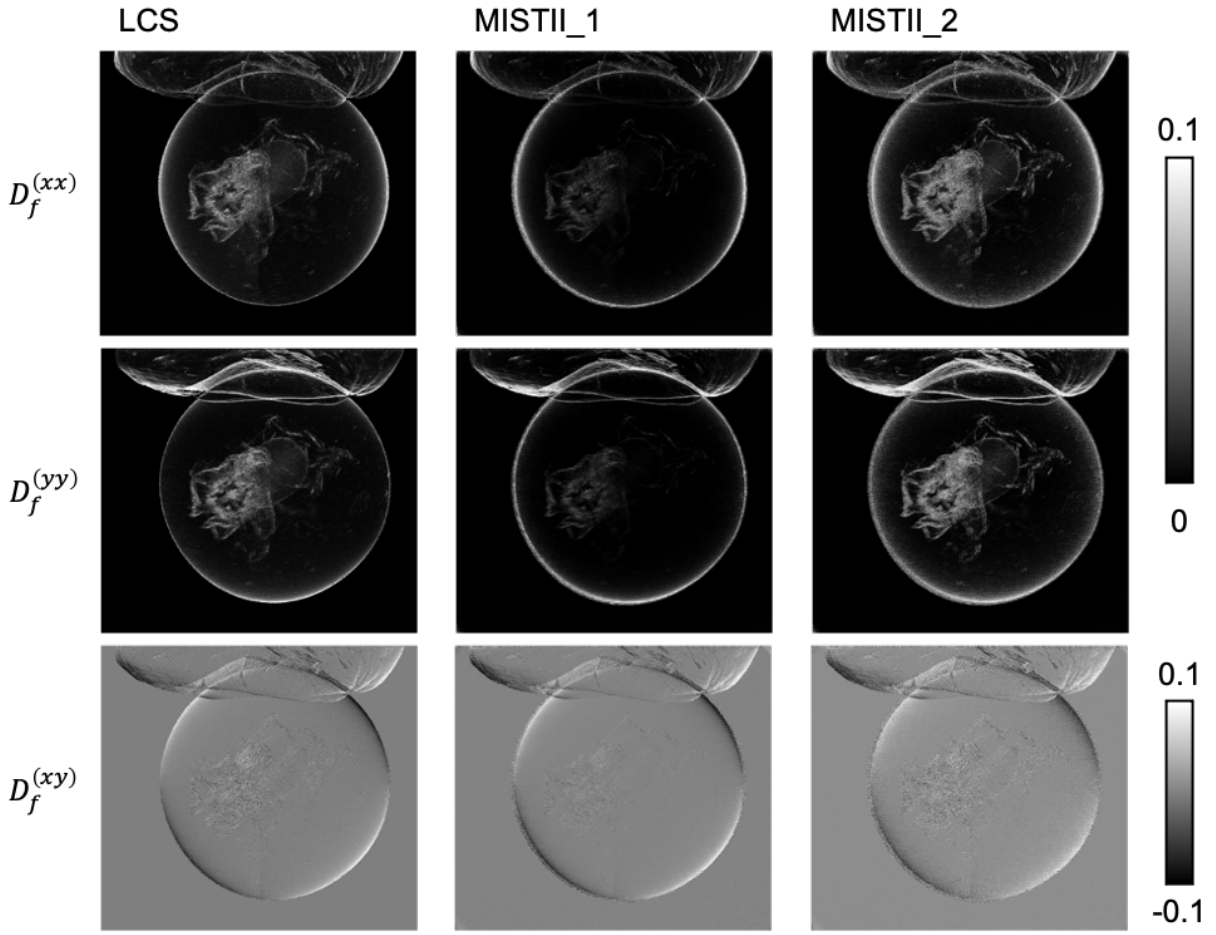

Figure 4.8: Red currant dark-field tensors retrieved with the LCS and MIST algorithms.

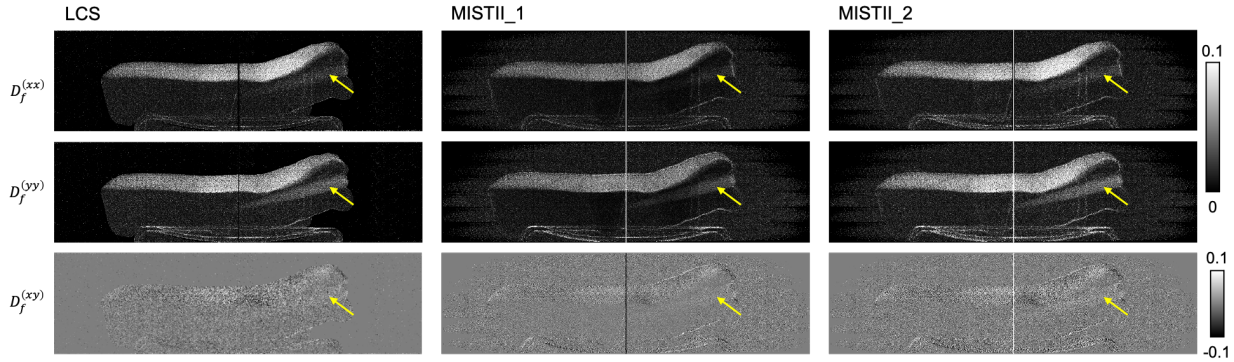

Figure 4.9: Haribo crocodile impaled with a wooden toothpick dark-field tensors retrieved with the LCS and MIST algorithms.

4.2.2 From tensors to ellipses

After showing that we were able to retrieve the tensors information, we have been wondering what would be the best way to represent the information in a single image. The first step would be to retrieve the orientation θ of the ellipses and their semi-major axis a and semi-minor axis b as they are represented in Figure 4.10.

For now, we have the parametric equation of the red rotated ellipse in

the x, y coordinates:

$$a_{11}x^2 + 2a_{12}xy + a_{22}y^2 + a_{33} = 0 \tag{4.17}$$

that we can associate to the dark-field tensors through:

$$\begin{cases} a_{11} = D_f^{(yy)}(x,y)D_f^{(xy)}(x,y) \\ a_{22} = D_f^{(xx)}(x,y)D_f^{(xy)}(x,y) \\ a_{12} = \frac{1}{2}D_f^{(xx)}(x,y)D_f^{(yy)}(x,y) \end{cases} \tag{4.18}$$

In order to find its semi-major and semi-minor axis, we need to find its rotation angle θ, then use it to compute the parametric equation in the (x',y') coordinates. In that space coordinates, the equation of the ellipse is simply:

$$\frac{x'^2}{a^2} + \frac{y'^2}{b^2} = c^{ste} \tag{4.19}$$

from which we can get directly the semi-major and semi-minor axis (a and b).

The first step is to change the coordinates (x,y) into (x',y') using:

$$\begin{cases} x = x'cos(\theta) - y'sin(\theta) \\ y = x'sin(\theta) + y'cos(\theta) \end{cases} \tag{4.20}$$

Then we re-write the parametric equation with those parameters leading to:

$$\frac{x'^2}{a^2} + \frac{y'^2}{b^2} + \frac{xy}{c^2} = c^{ste} \tag{4.21}$$

with:

$$\begin{cases} \frac{1}{a^2} = a_{11}cos^2(\theta) + a_{22}sin^2(\theta) + 2a_{12}cos(\theta)sin(\theta) \\ \frac{1}{b^2} = a_{11}sin^2(\theta) + a_{22}cos^2(\theta) - 2a_{12}cos(\theta)sin(\theta) \\ \frac{1}{c^2} = -2a_{11}cos(\theta)sin(\theta) + 2a_{22}cos(\theta)sin(\theta) + 2a_12[cos^2(\theta) - sin^2(\theta)] \end{cases} \tag{4.22}$$

We are searching for the orientation where the ellipse is not rotated which means the θ where $\frac{1}{c^2}$ is 0. This conditions gives us a relationship between θ and the initial parametric coefficients of the ellipse a_{11}, a_{22}, a_{12}:

$$\theta = \frac{1}{2}arctan\left(\frac{2 * a12}{a11 - a22}\right) \tag{4.23}$$

Using that value of θ we can now compute the values of our semi-major and semi-minor axis (a and b) from eqs. 4.22.

With those values, the eccentricity and the area of the ellipses can be easily deduced through the relations:

$$Eccentricity = \sqrt{1 - \frac{b^2}{a^2}} \tag{4.24}$$

$$Area = a.b.\pi \tag{4.25}$$

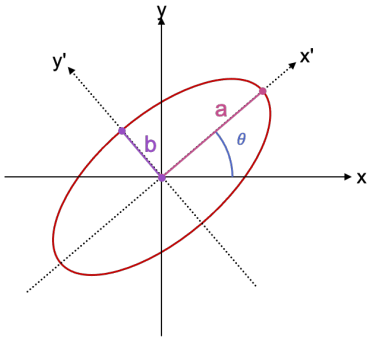

Figure 4.10: Schematic of a tilted ellipse and its defining quantities: angle of rotation θ, semi-major axis a and semi-minor axis b.

In the directional dark-field case, those quantities would have a lot of sense as the eccentricity would be related to how directional the diffusion cone is and by assimilation how directional the structures are. The area would give an information of the global spreading of the diffusion cone giving information about how strongly the beam was deviated.

Those quantities were computed for the Haribo Crocodile experiment 4.2 (p. 126) with the LCS algorithm and results are displayed in Figure 4.11. The first image is the simple quadratic norm of the tensors, the second and third are representations of the ellipse eccentricity and area. We can see that going through this ellipse calculations, the second and third images become a lot noisier than the tensor simple norm. This is mainly due to the fact that the noise of the original tensors induces some instabilities through the transformation into an ellipse. For starters, in some cases, the parametric equation obtained does not describe an ellipse. Indeed, for the equation to describe an ellipse we need $4a_{11}a_{22} - a_{12}^2 > 0$ and $a_{11}a_{22} > 0$. After discarding the pixels that do not respect these conditions, we still have some divisions in the computation of a, b and the eccentricity that diverge with very small denominators. Especially in the case of the eccentricity we can see that it increases the signal in the areas where the tensors signal is very small.

Quadratic norm:

$$QNorm = \sqrt{D_f^{(xx)^2} + D_f^{(yy)^2} + D_f^{(xy)^2}}$$

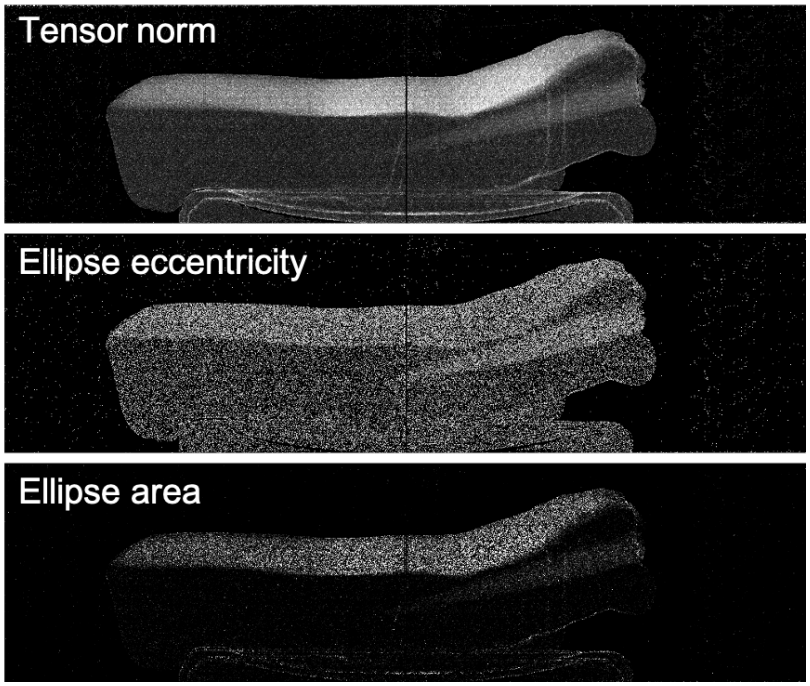

Figure 4.11: Haribo crocodile directional dark-field tensors norm computed from the LCS directional dark-field implementation. Area and eccentricity images computed from the tensors.

Probably, the most interesting information that we want to extract from those ellipses is their orientation. In order to represent it, we use a HSV colored image with the orientation as the hue, the area (or eccentricity) as the value and the saturation fixed at 1. Results obtained that way are displayed in Figure 4.12. We can visually distinguish more or less homogeneous colors in some areas but it remains very noisy.

In search of a more homogeneous result, a first attempt consisted in filtering the tensors components ($D_f(xx), D_f(xy), D_f(yy)$) before computing the ellipse components. Results using a median filter with a radius of 3 pixels are shown in Figure 4.13. This method disturbs greatly the

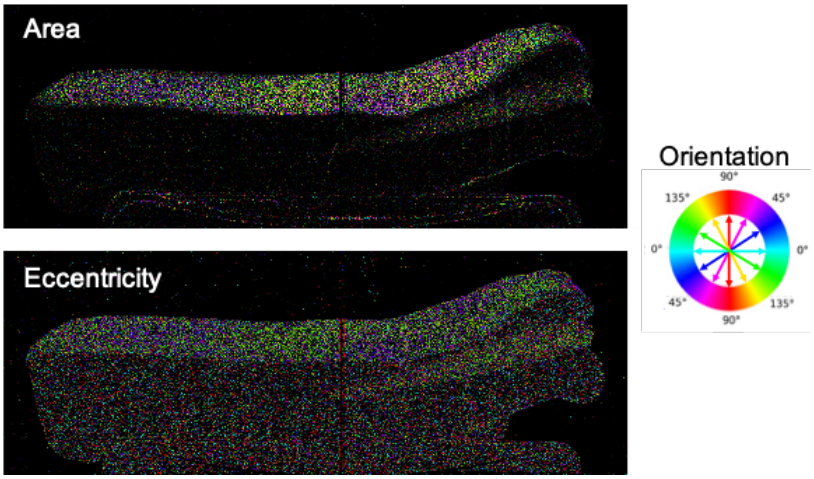

Figure 4.12: Haribo crocodile directional dark-field ellipses representation of the area and eccentricity with the computed orientation as the color hue.

computations of the area and eccentricity of the ellipse and the orientation despite it being more homogeneous. This is due to the fact that, all three tensors being computed through a system resolution for each pixel, their values are initially correlated. This correlation gets lost when the components are filtered independently.

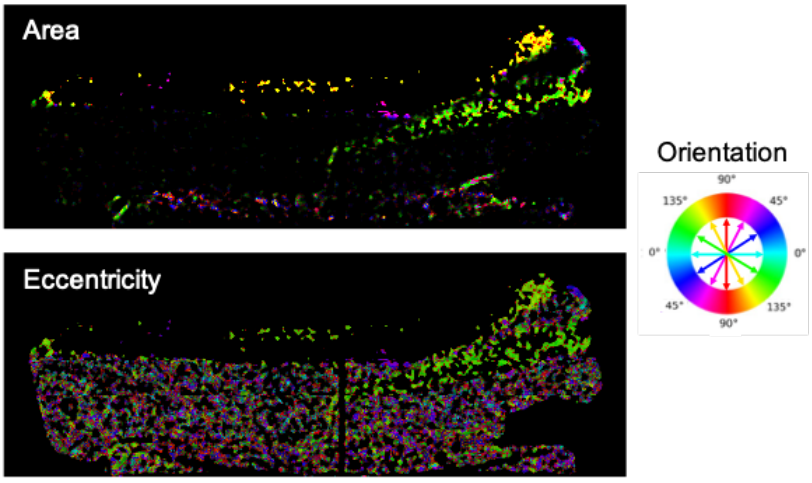

Figure 4.13: Haribo crocodile directional dark-field ellipses representation of the area and eccentricity with the computed orientation as the color hue obtained after filtering individually the tensors components with a median filter.

A second filtering attempt consisted in filtering directly the orientation. To do so, a 2D vector Gaussian filter was designed. Figure 4.14 presents the process on which this filter is based: for each pixel, a patch of the computed orientation matrix is extracted. It is multiplied by a Gaussian shaped patch of the same size in order to give more weight to the pixels close to the one considered. After that, all the vectors of the patch are summed and we get the orientation of the resulting vector for the pixel considered.

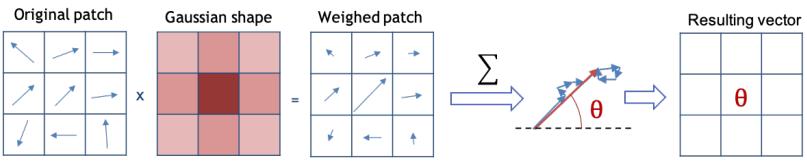

Figure 4.14: Pipeline for applying a Gaussian filter to an oriented vector.

Results of the colored area and eccentricity images after filtering the

orientation with this filter are shown in Figure 4.15. We can see that the retrieved orientation is more homogeneous than in the previous cases however some transitions between orientations still appear very sharp which makes no physical sense. This is associated to the question: what if in this area there is just no preferential direction?

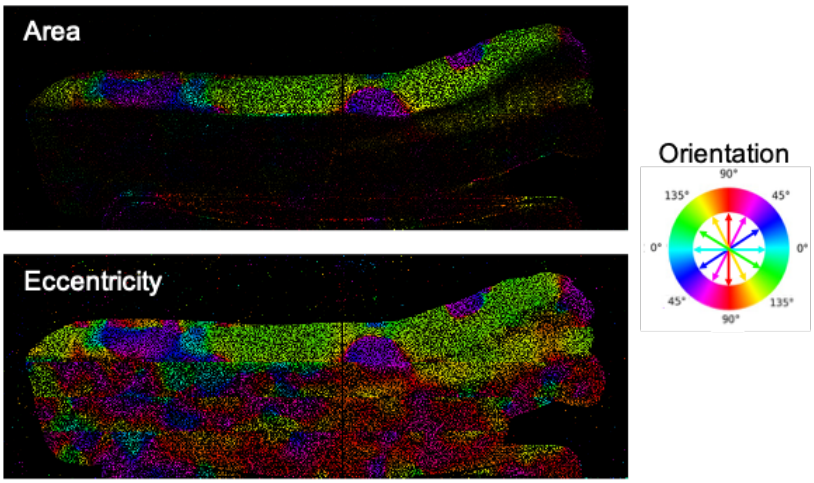

Figure 4.15: Haribo crocodile directional dark-field ellipses representation of the area and eccentricity with the computed orientation filtered with a Gaussian shaped kernel as the color hue.

In order to solve this issue, one last component was added to the coloured representation: the local orientation strength. Indeed, so far we only considered the orientation of the resulting filtered vector. We will now use the norm of this vector as the color saturation. Results are displayed in Figure 4.16. In those final images, the area or eccentricity correspond to the value, the orientation to the hue and the orientation strength to the saturation. This model allows to better see the regions where there is a strong orientation present in the sample.

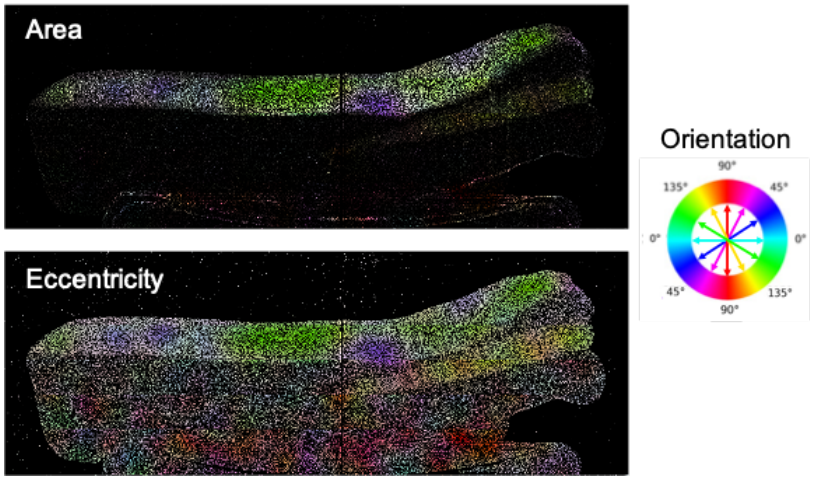

Figure 4.16: Haribo crocodile directional dark-field ellipses representation of the area and eccentricity with the computed orientation filtered with a Gaussian shaped kernel as the color hue and the local orientation strength as the saturation.

Now that we have filtered the orientation and obtained images of physical significance, we still wonder if it is the best representation of the sample dark-field. Figure 4.17 shows the image obtained when combining the tensor norm as the value, the filtered orientation as the hue and the local orientation strength as the saturation. This representation is definitely the less noisy and the one where it is easiest to visualize information. Until a better way to compute and filter the eccentricity and area of the ellipses is found, we will stick with this representation for the rest of the manuscript.

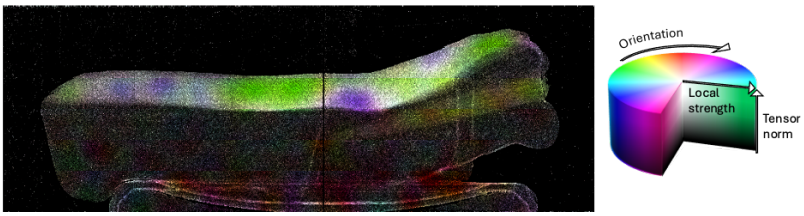

Figure 4.17: Haribo crocodile directional dark-field with the tensor norm as the value, the ellipse orientation filtered with a Gaussian shaped kernel as the color hue and the local orientation strength as the saturation.

4.3 Applications to biological samples

In the previous sections, we have shown all the contrast possibilities offered by MoBI and our newly developed algorithms. In this part, we will show examples of dark-field imaging on biological samples and the potential it may have for their study. The three cases that we will see are:

1. A mouse knee for osteo-articular studies
2. A human tooth for non-destructive volume structure study
3. *In-vivo* rat chest radiography and tomography for the study of lung diseases and injuries.

4.3.1 Directional dark-field on a Mouse knee

First, the algorithms were used on the "Mouse knee - id17" experiment (exp. 3.1 p.95) already mentioned in the third chapter.

Figure 4.18 shows the attenuation image obtained simply with the mouse knee in the beam and the one obtained with MoBI when extracting the dark-field using the LCS algorithm. As expected in a complex sample as this one, the dark-field is difficult to interpret with certainty. However, it has been shown that the dark-field could give information about the bones structure especially in osteoporosis cases [63].

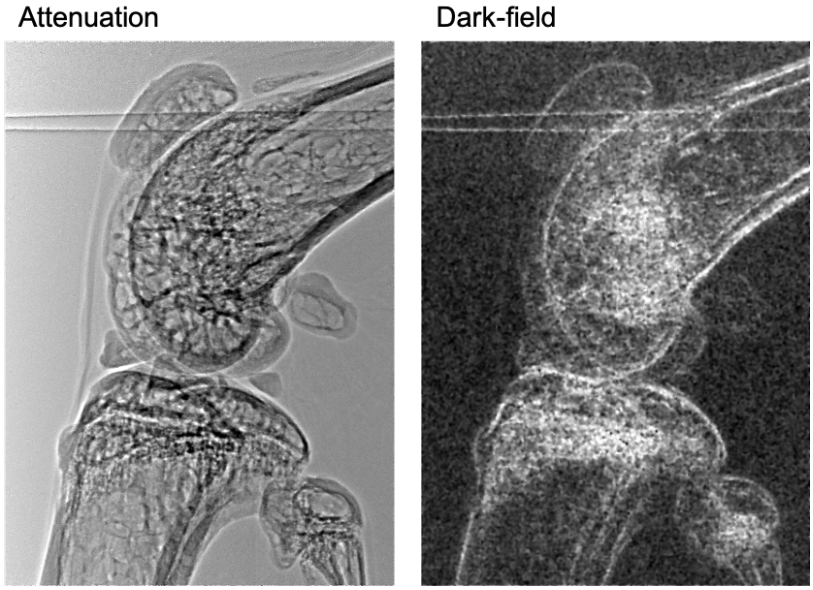

Figure 4.18: Attenuation and dark-field images a mouse knee.

Figure 4.19 presents the dark-field tensors and the coloured orientation representation of the scattered ellipses of the mouse knee. The retrieved

orientation appear very noisy and apart from some bone edges where it appears to detect some signal perpendicular to the bone, the colors appear without consistency and are difficult to interpret.

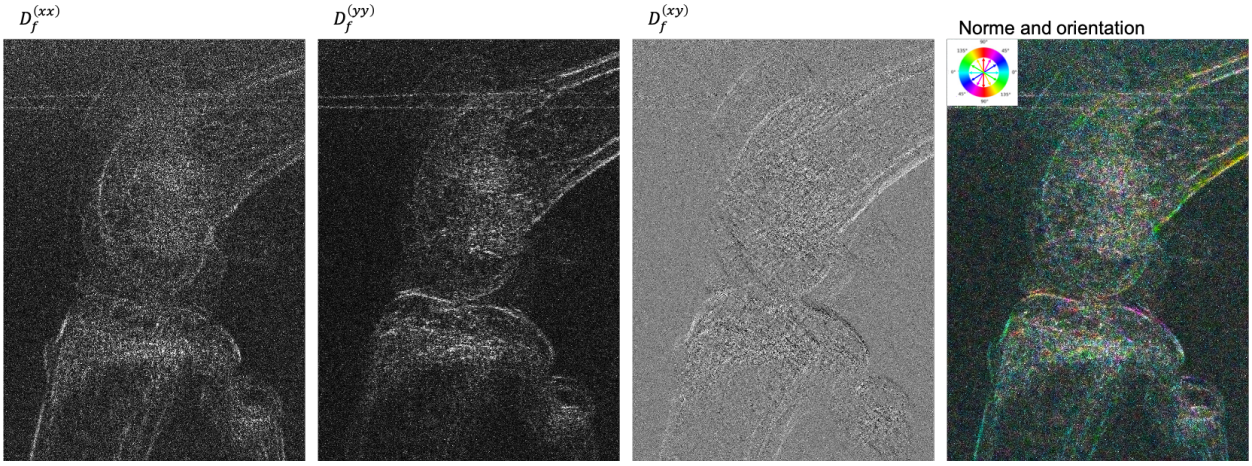

Figure 4.19: Mouse knee dark-field tensors and colored representation of the diffusion ellipse direction.

To conclude, it appears that MoBI allows to retrieve some dark-field signal in the joint but some more studies will be required to be able to understand better the source of this signal and interpret it.

4.3.2 Directional dark-field tomography of a tooth

The second sample that was studied is a human tooth. The experiment parameters used are the following:

Experiment 4.3: Human tooth - ID17

- Distance source to membrane (z_0): 138 m
- Distance membrane to sample (z_1): 1.5 m
- Distance sample to detector (z_2): 3.6 m
- Source: ID17 - 29 keV
- Detector: Photon counting Eiger from Dectris with pixels of 75 µm
- Membrane: Sandpaper stack
- Sample: human tooth (see Figure 4.4)
- Number of membrane positions acquired: 16
- Number of projections acquired: 901

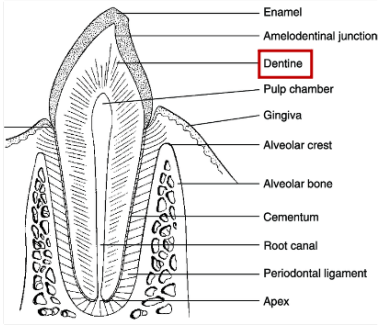

Figure 4.20: Schematic of a tooth with its principal structures.

The tooth is an interesting sample here because it has a component called dentin which has a very oriented tubular structure going from the pulp chamber toward the exterior or the enamel as shown on the scheme of Figure 4.20. Those tubular structures are about 7 µm in diameter and would therefore not be visible in images of 75 µm of resolution.

Before attempting tomography, we tried to do a simple radiography of the tooth with MoBI. Figure 4.21 presents a radiography, a simple dark-field image and a directional dark-field image of the tooth obtained with the LCS algorithm. First we can see on the attenuation image that the tubular structures of the dentine are not visible as expected because they are

smaller than the set-up resolution. What is interesting though is that the dark-field image shows a strong signal in the dentine area. And what is even more interesting is that we manage to retrieve a direction for those structures that correspond to the one that is expected. This first result demonstrate that oriented dark-field imaging can provide information about structures that are not even visible on the image.

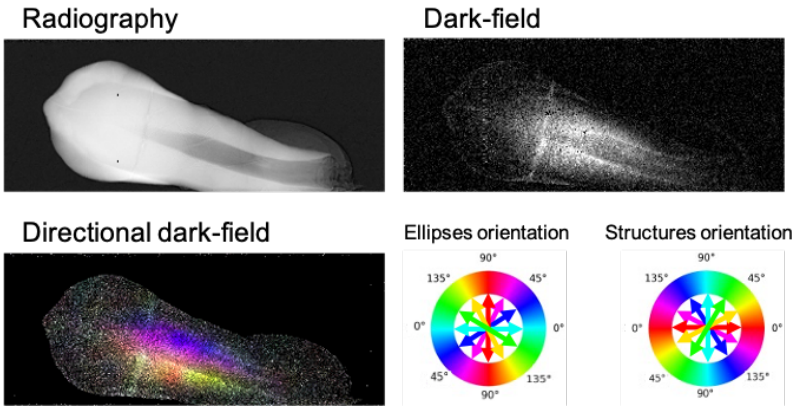

Figure 4.21: Attenuation, dark-field and directional dark-field images of a human tooth.

After such an encouraging result in simple projection imaging, we attempted to do a tomography of our tooth. Figure 4.22 shows projection images retrieved (10 out of the 901 computed) and the sinogram of a line of pixel taken at two third of the projections from the top. We can see that the retrieved dark-field gives very clear orientation signals as long as the tooth and most of its tubular structures are not oriented in the propagation direction. In the histogram it shows as the two noisiest areas. Reconstructing a 3D tensor field from those projections is far from being as straightforward as for a conventional tomography [151] and would require an expertise that we do not yet have.

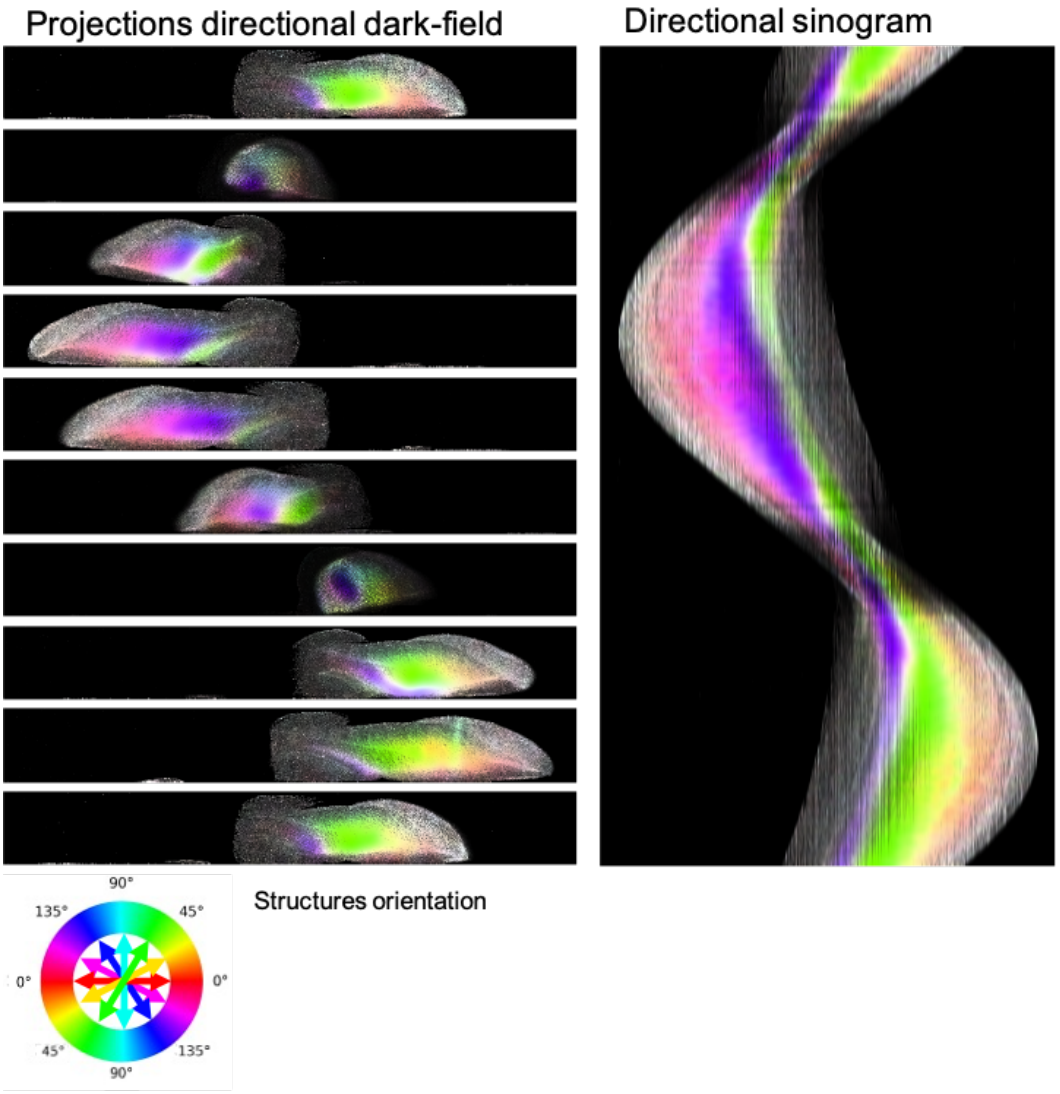

Figure 4.22: Human tooth directional dark-field tomography projection and their extracted sinogram. The hue corresponds to the fibers orientation (perpendicular to the diffusion ellipses orientation).

4.3.3 *In-vivo* dark field radiography and tomography for the study of lung injuries

As mentioned in the first chapter, dark-field imaging is especially interesting for the study of lung pathologies. In this section, we will present the first *in-vivo* dark-field tomography achieved using MoBI. We studied the effect of Ventilator Induced Lung Injury (VILI) on the dark-field signal. The experimental parameters are described below.

Experiment 4.4: Rat *in-vivo* - ID17

- Distance source to membrane (z_0): 138 m
- Distance membrane to sample (z_1): 1.5 m
- Distance sample to detector (z_2): 3.6 m
- Source: ID17 - 29 keV
- Detector: Photon counting Eiger from Dectris with pixels of 75

µm
- Membrane: Sandpaper stack
- Sample: rat (see Figure 4.4)
- Number of membrane positions acquired: 2x8 (in two apnea periods.)
- Number of projections acquired for tomography: 901
- Number of floors acquired for radiography: 11

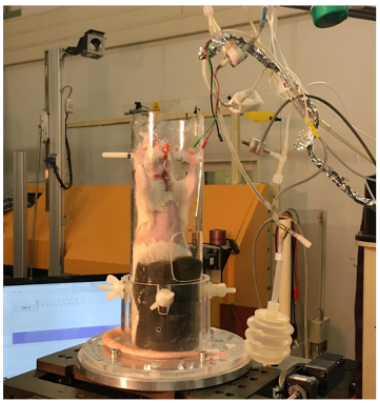

Figure 4.23: Rat installed in the tomography set-up with the ventilator.

Due to the reduced field of view available with the synchrotron beam (15 cm x 0.6 cm), acquisitions along a set of eleven floors was required to get the whole rat chest radiography. Figure 4.23 shows the set-up where the rat is installed with the ventilator. Having the rat ventilated allowed to provoke apnea during the acquisitions in order to avoid motion artifacts.

Let's first have a look to what can be obtained in simple projection. Figure 4.24 shows the radiography and dark-field images of the rat retrieved with the MIST algorithm before and after inducing VILI. The first observation is that the dark-field signal is indeed a great tool to observe the lung as it is the main element that produces signal (without considering the hair that was not properly shaved on the bottom left of the images). While in the radiography it is difficult to observe the lungs through the ribs, heart and other tissues signals, on the dark-field contrast, all those elements disappear and we only get the lungs signal. We can notice however that the ribs cause a little loss of signal. Comparing the healthy image to the VILI one it is clearly visible that there is a loss of signal in some areas. This is coherent with what we expect as the dark-field signal is proportional to the number of particles encountered. In the injured lung, the alveoli that were previously filled with air are now filled with fluid causing low to no refraction at the interface with the lung tissues. Here we can conclude that the dark-field image obtained with MoBI clearly allows to identify the injured areas of the rat lungs. Those result correlate with the ones obtained by Yaroshenko et al. using gratings interferometry.

Now, what about tomography? Figure 4.25 shows Dark-field and phase tomography of healthy and injured lungs of the rat. Here the phase tomography is very interesting as is allows to differentiate easily the lungs from the other tissues and with a very good resolution. The dark-field tomography, in a similar way to the simple projection image, allows to see the damaged areas of the lungs but the image appears quire blurred. The interest of these images is the possibility to quantify the loss of signal to estimate the amount of damaged alveoli.

Finally, we tried to retrieve a directional information about the collagen fibers present in the lung alveoli. Results are shown in Figure 4.26. No clear orientation could be detected. This is probably due to the fact that the areas containing those collagen fibers are too small compared to the system resolution. Even if we do not need to resolve the scattering structures to get information, we need them to be sufficiently concentrated to fill an area of pixel. In addition, the signal due to the collagen fibers is probably a lot weaker than the signal due to the lung/air interfaces.

To conclude on this part, using MoBI we are able to retrieve the dark-field signal in radiography and tomography on a living animal. The tomography would require a better resolution to be more competitive

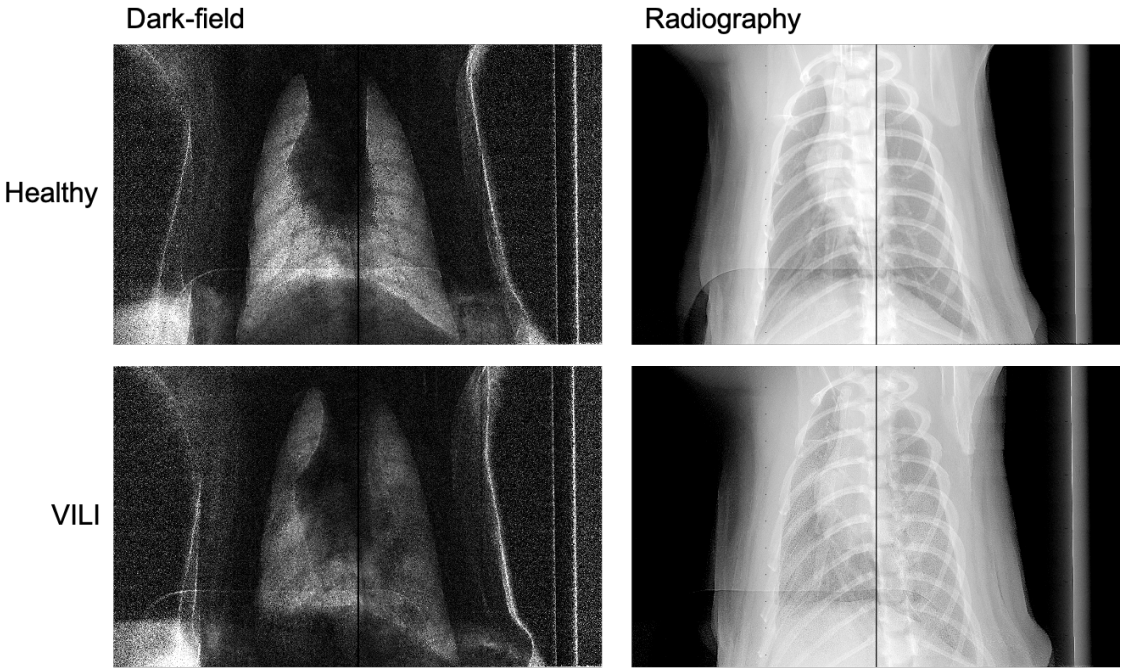

Figure 4.24: Rat chest dark-field image and radiography before and after Ventilator Induced Lung Injury (VILI).

with the phase signal, however, it has a good potential for quantitative studies of the lungs alveoli state. The directional information does not appear to show any interest in this specific case at this scale.

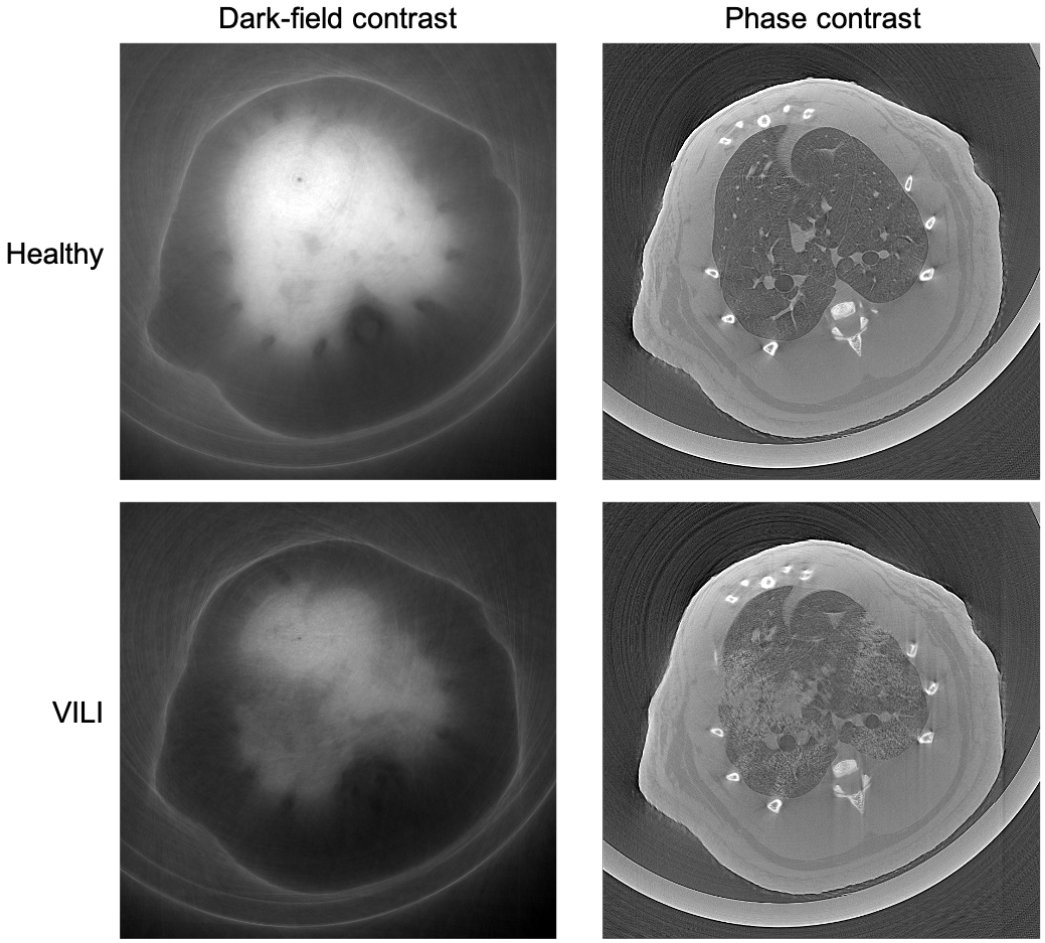

Figure 4.25: Rat chest dark-field and phase tomography slice before and after Ventilator Induced Lung Injury (VILI).

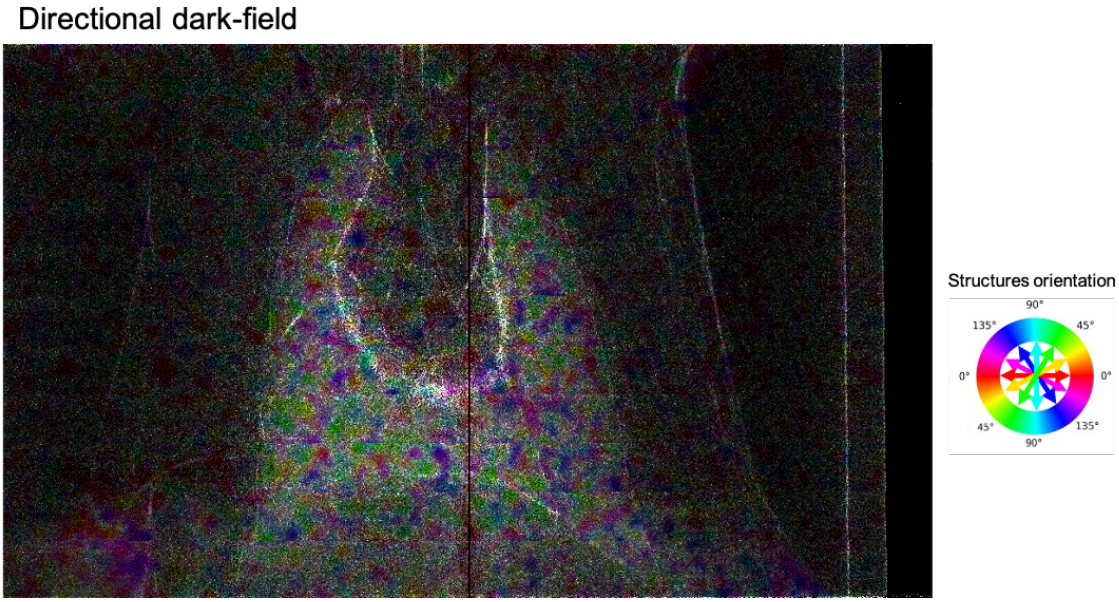

Figure 4.26: Directional dark-field projection of a rat chest retrieved with the MIST algorithm from 16 MoBI membrane positions.

4.4 Dark-field on conventional laboratory sources

Now that we have shown that it is possible to retrieve dark-field information on a living animal and to retrieve a directional information on a tooth, let's focus on the possibility to transfer the method to a clinical device. To do so, as for the phase retrieval, we started by studying its feasibility with a conventional laboratory source on a laboratory set-up.

Two experiments were attempted for dark-field retrieval with a conventional source: one at very low energy in vacuum with thin samples and another at higher energy with parameters closer to the clinics.

4.4.1 Directional dark-field with a low energy conventional source

The work presented in this section was done together with Clara Magnin, a Master 2 intern partly under my supervision.

This first experiment was performed in collaboration with XENOCS on an adapted SAXS/WAXS device: the XEUSS 3.0.

Definition: SAXS - WAXS

Small Angle X-ray Scattering (SAXS) and Wide Angle X-ray Scattering (WAXS) measurements consists in collimating a monochromatic x-ray beam in one point of the sample to observe the scattering pattern produced on a detector placed after the sample. The produced scattering pattern gives information on sample structures of a few for WAXS and of few hundreadths of nanometers for SAXS. More detail about the technique can be found in [152].

XENOCS company:
XENOCS is a company from Grenoble that produces SAXS and WAXS equipments for the characterization of materials at the nanoscale.

The parameters of this experiment are the following:

Experiment 4.5: Phantoms - XEUSS 3.0

- Set-up: XEUSS 3.0 adapted for MoBI
- Distance source to sample (z_0): 0.55 m
- Distance sample to membrane (z_1): 0.05 m
- Distance membrane to detector (z_2): 1.825 m
- Source: X-ray tube - Copper anode - 30 kVp - 8.6 keV average energy
- Detector: Photon counting Eiger from Dectris with pixels of 75 µm
- Membrane: Sandpaper stack
- Sample: Haribo flower candy and bundles of carbon fibers (see: Figure 4.27)
- Number of membrane positions acquired: 10

Figure 4.27: Samples used in the low energy laboratory set-up: a thin slice of a Haribo flower candy and bundles of carbon fibers.

The spatial coherence length of this set-up is about 1.32 µm for a resolution in the membrane plane of 20 µm. Those values are similar to the ones of the fly experiment used in the chapter 2.

The samples that are used with this set-up are described in Figure 4.27.

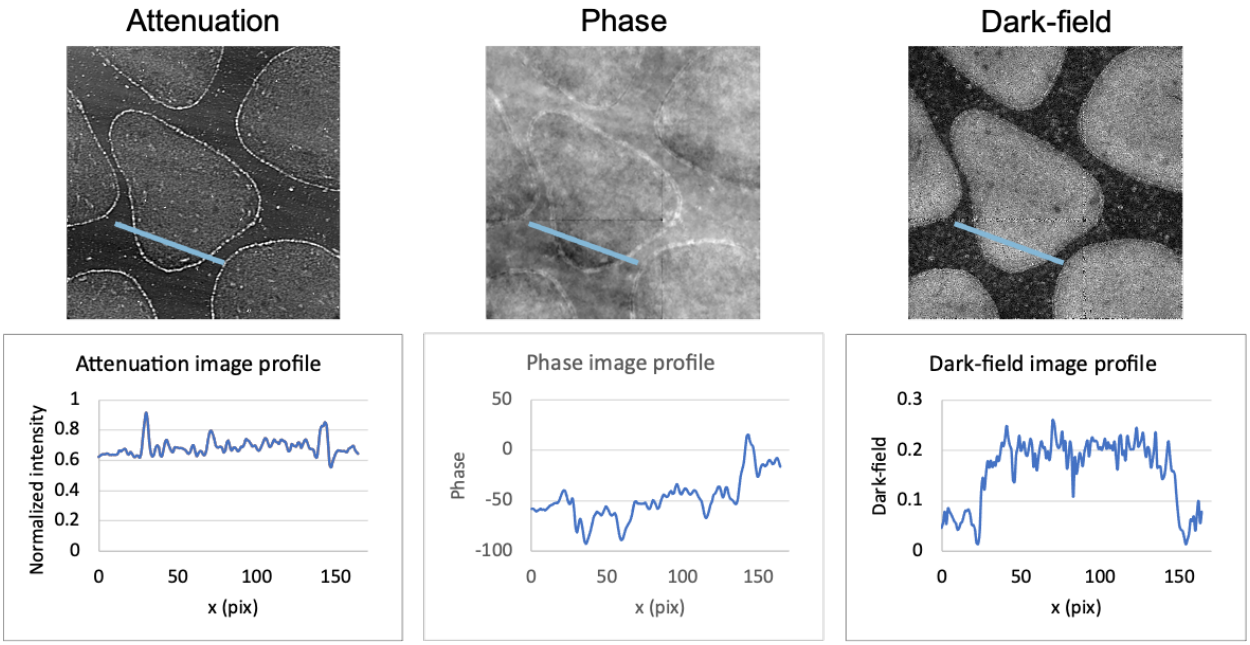

Figure 4.28: Attenuation, phase and dark-field images of the flower candy sample retrieved from 10 acquisitions with the LCS along with their extracted profiles along the blue line.

Figure 4.28 presents images of a thin slice of the flower candy that were obtained using MoBI with the LCS from 10 membrane positions. Profiles were extracted from each image along the light blue line. In the attenuation image we see a thin white line between the white and red parts of the sample. The white parts appear slightly lighter but the difference between the two materials is very small. The Contrast over Noise Ratio (CNR) between the two materials is 2.3 for the attenuation image. In the phase image we also see the outline of the white parts as thin light lines but the image appears very noisy and not at all homogeneous which makes the differentiation between the two materials impossible. The CNR value was not computed for the phase image because it is not meant for measuring low frequency noise and the value would vary widely depending on where the windows corresponding to the two materials were drawn. Finally, on the dark-field image, the difference between the white and red parts of the candy is striking. When looking at the profile it appears obvious that the red part produces almost no dark-field signal while the white part gives a strong signal. The CNR between those two parts is 3.6 which is significantly higher than for the attenuation. This result proves that we can retrieve a dark-field signal using this conventional source set-up and that this signal is not simply an artifact due to attenuation.

After having proven that we were able to retrieve a dark-field signal with this set-up, we went even further trying to retrieve a directional dark-field information. Figure 4.29 shows a directional dark-field image of bundles of carbon fibers with very oriented structures. On this image we can see two very distinctive colours (pink and yellow-green) corresponding to the two fibers orientation. As we can see, the colours remain quite homogeneous in the areas where the fibers are isolated and, unsurprisingly, appear to fluctuate between the two values in the area where they are superimposed.

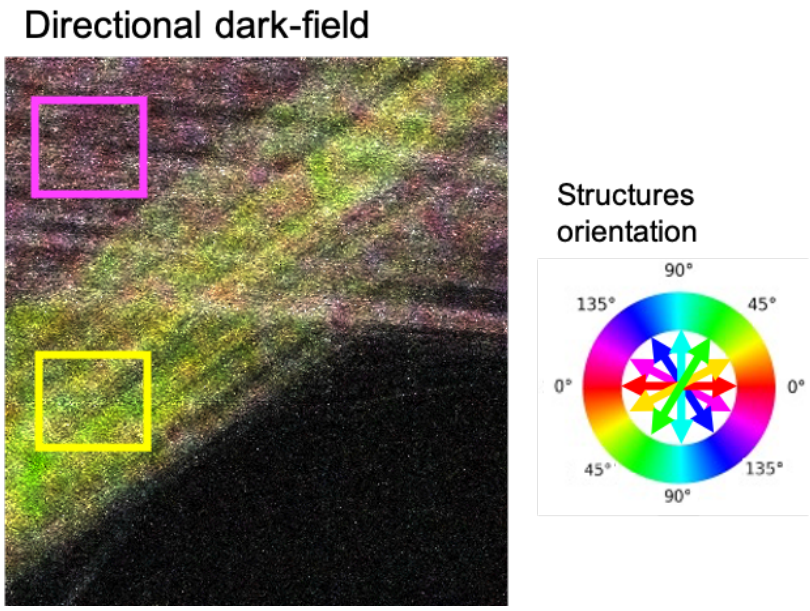

Figure 4.29: Directional dark-field image of carbon fibers retrieved with the LCS algorithm from a laboratory set-up MoBI experiment.

In order to assess the precision of the computed angles, the average angle values in the two rectangle were computed and compared to SAXS local measurements taken in those areas. The measurements are summarized in Table 4.1. As we can see the dark-field orientations computations are in very good agreement with the SAXS measurements. This proves that the orientation measurements are not only possible with MoBI but that they can be quantitative!

Table 4.1: SAXS and dark-field orientation measurements on the pink and yellow areas of the sample.

Method	Pink area	Yellow area
SAXS	175 º	33.9 º
Dark-field	171º ± 7º	34 ± 4º

In this part, we have shown that oriented dark-field measurements are possible without a synchrotron in these specific conditions of low energy and under vacuum. Unfortunately, those conditions are not compatible with clinical applications.

In the next (and last!) section we will show results of an attempt to get dark-field signal with a higher energy conventional laboratory set-up (not under vacuum).

4.4.2 High energy laboratory set-up

The work presented in this section was done in collaboration with Clarisse Fournier from the CEA Leti in Grenoble.

In this last study, the dark-field retrieval was attempted with MoBI with another laboratory set-up shared with us by the CEA Leti of Grenoble. On this set-up, the source produces energies compatible with clinical applications (from 40 to 100 kVp). We used again the Haribo crocodile sample as its white foam produced a strong signal on the ID17 beamline experiment. Experiment parameters are listed below:

Experiment 4.6: Haribo crocodile - Laboratory set-up

- Distance source to sample (z_0): 0.2 m
- Distance sample to membrane (z_1): 0.1 m
- Distance membrane to detector (z_2): 0.5 m
- Source: Nova micro-focus system 600 series - X-ray tube - Tungsten anode - 55 kVp - 20 µm spot size.

- Detector: Flat panel C7942CA from Hamamatsu with CsI scintillator and a pixel size of 50 µm
- Membrane: Tungsten grains of 250 µm maximum size deposited on PMMA plates with double sided tape.
- Sample: Haribo crocodile candy impaled with a toothpick.
- Number of membrane positions acquired: 10

In these conditions, the spatial coherence length is 0.62 µm for a resolution in the sample plane of 12.5 µm.

Figure 4.30 shows the attenuation, phase and dark-field images that were retrieved from this experiment. We can see here that the attenuation image is comparable to the one that was obtained with the synchrotron. However, the phase and dark-field images are far from what we expect. The "phase signal" displayed here is negative which means that it is not actually "phase" but probably an effect of attenuation. This phenomenon was already observed with the mouse knee sample on a conventional laboratory set-up in the previous chapter due to the source blurring. The dark-field signal does not correspond to multiple scattering through small particles either as it does not appear in the foam (contrary to the ID17 experiment) but seems stronger in the most attenuating parts of the sample. This dark-field signal is probably a beam hardening artifact due to attenuation in the sample instead of a meaningful information representative of the sample structure.

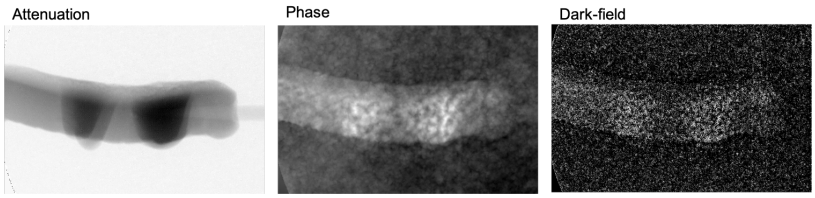

Figure 4.30: Attenuation, phase and dark-field images of a crocodile Haribo retrieved from a laboratory set-up experiment at clinical compatible energy.

In this case, the impossibility to retrieve the signals of interest is probably due to three things:

1. The low bit depth of the detector. This detector was probably not optimal for this experiment as it had a very limited bit depth (meaning that we could not integrate over a long exposure time) that gave very noisy images. In order to overcome this issue, series of ten identical images were acquired and averaged but this did not solve the problem.
2. The source size creates a big blurring and very low spatial resolution. The spot size is 20 µm wide which creates a projected blurring spot of 33 µm for the membrane and 60 µm for the sample. Deconvolution of the acquisition was attempted to reduce this effect but little to no improvement was observed in this case.
3. The wide energy bandwidth of the source. This might induce a lot of beam hardening effects in the sample. We could have tried filtering the low energies as we showed using simulations that this could help reduce beam-hardening artifacts. However, the number of photons detected was already very low and filtering the source would have further reduced this number.

These three issues combined did not allow to retrieve the information of interest from this experiment. It appears that the blurring due to

the detector PSF and source spot size combined with the noisy images retrieved from the detector degrade the acquisitions too much for it to be used to extract phase and dark-field signals.

In order to improve this experiment, several elements could be investigated and changed. We could try with a photon counting detector, use a more focused and powerful source with a low energy filter (to improve temporal coherence) or try to improve the configuration in order to have a sharper membrane image.

4.5 Conclusion

In this chapter we have investigated the possibilities to retrieve a dark-field signal giving information about the micro-structures of the sample using MoBI. The LCS that had already proven to be a fast and sensitive way to extract the phase signal was completed to retrieve the dark-field signal. Going even further, the dark-field signal could be considered to have a preferential scattering direction due to oriented micro-structures in the sample. In order to retrieve this information, we completed the MIST and LCS algorithm to extract a tensor dark-field information that could be represented as coloration in the images.

The performance of these algorithms were tested on synchrotron experiments of medical interest and tried on laboratory set-ups. It appears that the dark-field signal can be efficiently retrieved in radiography and tomography *in-vivo* and allows to assess the extend of the alveoli damages that appear upon ventilator induced lung injury. For the directional information, it proved to be able to give information about the dentin tubular structures orientation of human tooth that are ten times smaller than the system resolution. Dark-field retrieval using MoBI was finally proven to be retrievable on phantoms using a low energy adapted SAXS set-up but was not yet achieved at higher energies on biological samples.

Three main results can be outlined for the transfer of dark-field with MoBI on clinical devices. We have demonstrated that:

- Dark-field can be retrieved with a low resolution detector: 75 µm photon counting detectors used on ID17 experiments and the adapted XEUSS set-up.
- Dark-field can be retrieved from a low spatial coherence set-up: the spatial coherence length of the XEUSS set-up is only 1.32 µm which is more than ten times smaller than the system resolution.
- it is possible to perform *in-vivo* dark-field radiography and tomography: imaging of living rats with and without VILI were performed on ID17.

In-vivo dark-field tomography with low resolution and low spatial coherence systems had already been achieved with Grating Interferometry [153]. However, to the best of our knowledge, dark-field imaging using MoBI was confined to high resolution and high spatial coherence set-ups [113, 154, 155].

The results obtained in this PhD should eventually allow, with the proper means, to combine low resolution, low coherence and *in-vivo* dark-field tomography using MoBI.

Theoretically, the retrieved dark-field signal can give quantitative information about the number of particles encountered by the beam during its journey through the sample. The extraction of quantitative measurements from dark-field signal was already investigated in the case of Grating Interferometry [156] or with modulations from explicit methods [113] but not yet using implicit algorithms.

To conclude on this chapter and the previous one, along with the simulation software, the main work that was accomplished in this PhD was the design of new, fast and sensitive phase and dark-field retrieval algorithms. Along with already existing ones, those algorithms were implemented all together in the POPCORN software as it is summarized in Figure 4.31. Those numerical phase and dark-field extraction methods have various limitations, are efficient in different cases and are more or less computationally efficient. For the time being, the LCS remains the more advantageous one as it can retrieve all kinds of contrasts at once: attenuation, refraction, dark-field and directional dark-field. It is also one of the less computationally expensive and has a very good signal sensitivity even for very weak refraction or weak blurring due to scattering.

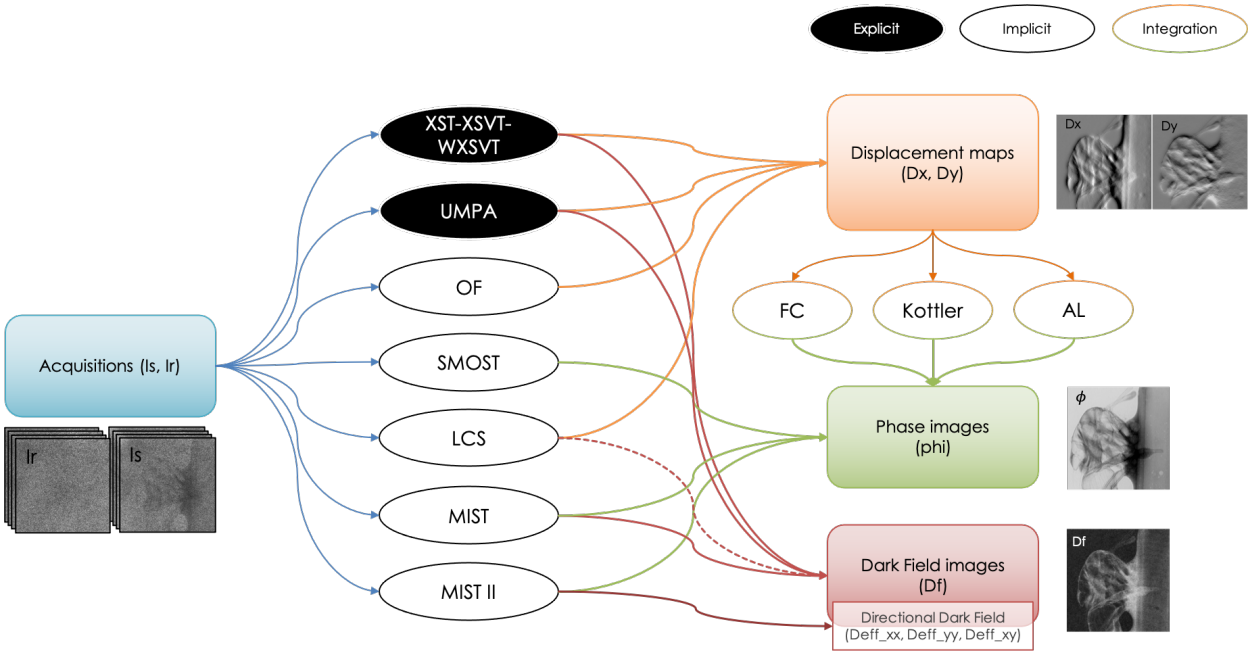

Figure 4.31: Summary of all the phase gradient, phase, dark-field and integration algorithms that are implemented into the POPCORN software.

Résumé du Chapitre 4 en Français

Ce dernier chapitre s'intéresse à l'extraction du signal du champ sombre (dark-field) associé à la présence de micro-structures dans l'échantillon. Après une vue d'ensemble des méthodes déjà existante, la version complétée du LCS permettant d'extraire le signal de diffusion est introduite. Nous présentons ensuite la possibilité d'extraire une information directionnelle liée à la présence de structures orientées dans l'échantillon. Une mise en pratique de l'utilisation de ces algorithmes est ensuite faite sur des échantillons biologiques montrant leur potentiel intérêt. Enfin nous exposons les premiers tests et preuves de conceptes réalisés avec des appareils de laboratoire.

Parmi les algorithmes déjà existant permettant d'extraire le dark-field des acquisitions, il existe des versions complétées des méthodes explicites, ajoutant un terme de dark-field aux équations d'erreur quadratique de corrélation croisée comparant images référence et échantillon. Une méthode implicite a également été imaginée, utilisant l'équation de Fokker-Planck pour compléter l'ETI. Cet algorithme comporte encore une hypothèse très contraignante puis qu'il considère un objet non absorbant.

Dans le but de s'affranchir de cette hypothèse, nous avons combiné la méthode utilisée dans le LCS avec l'équation de Fokker-Planck pour obtenir un algorithme moins restrictif sur l'expérience et qui aurait un coût algorithmique plus faible que les méthodes explicites. Cette nouvelle version du LCS complétée avec un terme de dark-field a fait ses preuves sur une expérience synchrotron et permet donc maintenant d'obtenir à la fois l'atténuation la réfraction dans les 2 directions perpendiculaires à la propagation et le dark-field.

Dans un second temps, nous nous sommes intéressés à la possibilité de récupérer une information de diffusion directionnelle. En effet, si un échantillon contient des microstructures fibreuses orientées, la diffusion produite sera plus importante dans la direction perpendiculaire à ces structures. Les algorithmes implicites ont donc été complétés avec une écriture tensorielle du dark-field plutôt que scalaire. Cette écriture tensorielle nécessite de rajouter des inconnues à notre équation et donc d'acquérir plus de positions de membranes pour récupérer toutes les informations intéressantes. Une fois les composantes du tenseur du dark-field récupérées, il est possible d'associer la direction des fibres à une nuance de couleur pour une visualisation directe de l'orientation sur l'image.

Ces algorithmes ont été appliqués sur trois cas médicaux : une patte de souris, une dent humaine et un thorax de rat vivant. Dans le cas de la patte de souris, il est difficile de déterminer si le dark-field est bien présent mais son signal est difficile à interpréter. Dans le cas de la dent en revanche, le dark-field orienté semble très intéressant puisqu'il permet de retrouver l'orientation des tubes de dentine composant la dent alors que ces structures sont dix fois plus petites que la taille des pixels donc complètement invisible sur les images de phase ou d'atténuation. Enfin nous avons étudié le cas d'images de poumons en projections et en tomographie. Nous avons pu montrer que l'image de dark-field permet

de très bien visualiser les dommages provoqués aux poumons liés à des lésions induites par un respirateur.

Pour finir, nous avons tenté d'extraire l'information de dark-field en utilisant des acquisitions provenant d'appareils de laboratoire. Dans un premier cas, nous avons utilisé un appareil à très basse énergie. Nous avons alors pu montrer qu'il est possible d'obtenir un contraste en dark-field dans des éléments peu distinguables en atténuation ou en phase et qu'il était même possible de récupérer une information quantitative concernant la direction de fibres. Le second cas avec un appareil de laboratoire à été réalisé à plus haute énergie mais cette expérience a été peu concluante pour diverse raisons expérimentales. Il a été impossible d'obtenir des acquisitions de qualité suffisante pour extraire une information de dark-field.

General Conclusion

The goal of this work was to develop and optimize a phase contrast imaging technique, Modulations-Based Imaging, for a transfer from the synchrotron to clinical devices. This objective requires first to adapt the set-up and numerical tools (phase and dark-field retrieval) to low coherence and low resolution systems. For the set-up optimization, I worked on the creation of a simulation program. And, regarding the numerical tools, I developed a new, fast and quantitative phase retrieval algorithm and worked on new dark-field retrieval methods for low coherence systems.

Modulations-based imaging simulations

Prior to my thesis, there were very few tools allowing a fast simulation of a MoBI experiment and it was not possible to find one that allowed the flexibility required to optimize various parameters of the experiment that we were interested in. Therefore, I decided to implement my own simulation tool, taking into account a very broad range of possible experimental parameters. This tool was implemented with two physical approaches: one based on a ray-tracing model and a second based on a Fresnel propagator. These two approaches were validated through comparison with real experiments: one synchrotron experiment and one experiment on a laboratory set-up with a conventional source. They were also compared to a GATE simulation that is the gold standard of particle physics interaction simulations based on a Monte Carlo approach.

This developed tool allowed us to optimize the dose required during an experiment and to study the influence of the source temporal coherence on the retrieved images quality. These are key parameters in clinical conditions.

Phase retrieval

There are two families of phase retrieval algorithms: explicit and implicit algorithms. While the explicit ones have the impairment of being very time consuming, the implicit ones were based on very restrictive hypothesis which, when not perfectly met, induced strong artifacts on the retrieved phase images which were not quantitative. In search for the best of both worlds, I investigated two approaches.

The first one, based on the description of intensity in reciprocal space allowed to unite the physics of this model with the Transport of Intensity Equation (TIE). This formalism also lead to a Contrast Transfer Function equation for phase retrieval that could theoretically be solved using multi-energy measurements.

The second phase retrieval approach I worked on is a variation of other implicit algorithms based on the TIE modified to relax the restrictive

approximations and optimized for low coherence experiments: the Low Coherence System algorithm (LCS). This algorithm was validated on Synchrotron experiments as well as laboratory set-ups with low coherence and low resolution.

Regarding phase retrieval, an extended study was conducted on the comparison of seven different algorithms in various experimental cases. It allowed to show that the LCS, despite being limited to the detection of displacement smaller than the pixel size, combines the advantages of being fast, provide quantitative results and have a good sensitivity to small displacements. These qualities will be essential in a clinical case.

Dark field imaging

Implicit and explicit approaches already allowed to retrieve the dark-field prior to my PhD. Inspired from the implicit theory for dark-field, I was able to complete the LCS algorithm allowing to retrieve the dark-field with conventional laboratory systems as we were able to experimentally prove on a commercial device.

We also worked on a complementary theory for the dark-field in the case of a directional diffusion and were able to retrieve an information indicating the orientation of micro-structures in the sample. This theory was also validated on a synchrotron experiment and on an experiment with a conventional source.

We were able to show the feasibility and interest of phase and dark-field imaging on medical examples. Amongst these, we were able to get dark-field radiographies and tomographies of *in-vivo* rats chests. It even allowed to show the possibility of using MoBI dark-field contrast for the study of ventilator induced lung injuries.

To conclude, my work allowed to evidence the potential and feasibility of transferring phase contrast and dark-field imaging to conventional sources using MoBI. Associated with the newly theorized and implemented phase and dark-field retrieval algorithms, the developed simulation tool will allow to optimize acquisition parameters to various low coherence systems. However, the journey is far from over and there is still work to be done in order to create a clinical compatible system that would combine phase and dark-field imaging of a patient in tomography.

Scientific communications

Articles:

1. Peer reviewed article: Hélène Rougé-Labriet, Sebastien Berujon, Hervé Mathieu, Sylvain Bohic, Barbara Fayard, Jean-Noel Ravey, Yohann Robert, Philippe Gaudin, and Emmanuel Brun. 'X-ray Phase Contrast osteo-articular imaging: a pilot study on cadaveric human hands'. In: *Scientific reports* 10.1 (2020)
2. Conference proceeding: Laurène Quénot, Ludovic Broche, Clément Tavakoli, Sylvain Bohic, and Emmanuel Brun. 'Towards x-ray phase contrast tomography in clinical conditions: simulation and phase retrieval development'. In: *Medical Imaging 2021: Physics of Medical Imaging*. Vol. 11595. International Society for Optics and Photonics. 2021
3. Peer reviewed article as 1st author: Laurene Quenot, Emmanuel Brun, Jean Michel Létang, and Max Langer. 'Evaluation of simulators for x-ray speckle-based phase contrast imaging'. In: *Physics in Medicine & Biology* (2021)
4. Peer reviewed article as 1st author: Laurene Quenot, Helene Rougé-Labriet, Sylvain Bohic, Sébastien Berujon, and Emmanuel Brun. 'Implicit tracking approach for X-Ray Phase-Contrast Imaging with a random mask and a conventional system'. In: *Optica* (2021)
5. Peer reviewed article: Konstantin M Pavlov, David M Paganin, Kaye S Morgan, Heyang Thomas Li, Sebastien Berujon, Laurène Quénot, and Emmanuel Brun. 'Directional dark-field implicit x-ray speckle tracking using an anisotropic-diffusion Fokker-Planck equation'. In: *Physical Review A* 104.5 (2021)

Conferences:

1. XNPIG 2019 - Presentation: Comparison of Speckle Based imaging phase retrieval algorithms for optimizing transfer to conventional sources, L. Quenot, H. Rougé-Labriet, D. M. Paganin, S. Bohic, B. Fayard, S. Berujon, E. Brun
2. SPIE medical imaging 2021 - Poster and proceeding article: Towards x-ray phase contrast tomography in clinical conditions: simulation and phase retrieval development, Quénot, L., Broche, L., Tavakoli, C., Bohic, S., Brun, E.
3. ICTMS 2022 - Presentation: Modulation-Based dark-field tomography for micro-structures orientation studies. Quenot L., Bravin A., Bohic S., Bayat S., Brun E.

Other communications:

- Hercules school, poster presentation (march 2020)
- Deep imaging school, poster presentation (April 2021)

Bibliography

Here are the references in citation order.

[1] Sebastien Berujon, Hongchang Wang, and Kawal Sawhney. 'X-ray multimodal imaging using a random-phase object'. In: *Physical Review A* 86.6 (2012), p. 063813 (cited on pages 6, 37, 83).

[2] Kaye S Morgan, David M Paganin, and Karen KW Siu. 'X-ray phase imaging with a paper analyzer'. In: *Applied Physics Letters* 100.12 (2012), p. 124102 (cited on pages 6, 37, 83).

[3] Wilhelm Conrad Röntgen. 'On a new kind of rays'. In: *Science* 3.59 (1896), pp. 227–231 (cited on pages 7, 19).

[4] Allan Macleod Cormack. 'Representation of a function by its line integrals, with some radiological applications'. In: *Journal of applied physics* 34.9 (1963), pp. 2722–2727 (cited on page 7).

[5] Amy Berrington de Gonzalez and Sarah Darby. 'Risk of cancer from diagnostic X-rays: estimates for the UK and 14 other countries'. In: *The lancet* 363.9406 (2004), pp. 345–351 (cited on page 7).

[6] Frits Zernike. 'Phase contrast, a new method for the microscopic observation of transparent objects'. In: *Physica* 9.7 (1942), pp. 686–698 (cited on page 9).

[7] Alberto Bravin, Paola Coan, and Pekka Suortti. 'X-ray phase-contrast imaging: from pre-clinical applications towards clinics'. In: *Physics in Medicine & Biology* 58.58 (2013), R1–R35. DOI: 10.1088/0031-9155/58/1/R1 (cited on pages 9, 32).

[8] Franz Pfeiffer, Martin Bech, Oliver Bunk, Philipp Kraft, Eric F Eikenberry, Ch Brönnimann, Christian Grünzweig, and Christian David. 'Hard-X-ray dark-field imaging using a grating interferometer'. In: *Nature materials* 7.2 (2008), pp. 134–137 (cited on page 9).

[9] Kaye S Morgan and David M Paganin. 'Applying the fokker–planck equation to grating-based x-ray phase and dark-field imaging'. In: *Scientific reports* 9.1 (2019), pp. 1–14 (cited on page 9).

[10] Yunzhe Zhao, Emmanuel Brun, Paola Coan, Zhifeng Huang, Aniko Sztrókay, Paul Claude Diemoz, Susanne Liebhardt, Alberto Mittone, Sergei Gasilov, Jianwei Miao, et al. 'High-resolution, low-dose phase contrast X-ray tomography for 3D diagnosis of human breast cancers'. In: *Proceedings of the National Academy of Sciences* 109.45 (2012), pp. 18290–18294. DOI: 10.1073/pnas.1204460109 (cited on pages 9, 33).

[11] Hélène Rougé-Labriet, Sebastien Berujon, Hervé Mathieu, Sylvain Bohic, Barbara Fayard, Jean-Noel Ravey, Yohann Robert, Philippe Gaudin, and Emmanuel Brun. 'X-ray Phase Contrast osteo-articular imaging: a pilot study on cadaveric human hands'. In: *Scientific reports* 10.1 (2020), pp. 1–8. DOI: https://doi.org/10.1038/s41598-020-58168-3 (cited on pages 9–11, 155).

[12] RB Lipton, TJ Schwedt, BW Friedman, et al. 'GBD 2015 Disease and Injury Incidence and Prevalence Collaborators. Global, regional, and national incidence, prevalence, and years lived with disability for 310 diseases and injuries, 1990-2015: a systematic analysis for the Global Burden of Disease Study 2015. Lancet. 2017 Jan 5; 388 (10053): 1545–602. doi:. PMID: 27733282.[PubMed: 27733282][Cross Ref]'. In: (2016) (cited on page 9).

[13] Sandra H Van Oostrom, H Susan J Picavet, Simone R De Bruin, Irina Stirbu, Joke C Korevaar, Francois G Schellevis, and Caroline A Baan. 'Multimorbidity of chronic diseases and health care utilization in general practice'. In: *BMC family practice* 15.1 (2014), pp. 1–9 (cited on page 9).

[14] Annie Horng, Emmanuel Brun, Alberto Mittone, Sergei Gasilov, Loriane Weber, Tobias Geith, Silvia Adam-Neumair, Sigrid D Auweter, Alberto Bravin, Maximilian F Reiser, et al. 'Cartilage and soft tissue imaging using X-rays: propagation-based phase-contrast computed tomography of the human knee in comparison with clinical imaging techniques and histology'. In: *Investigative radiology* 49.9 (2014), pp. 627–634. DOI: 10.1097/RLI.0000000000000063 (cited on page 10).

[15] Tobias Geith, Emmanuel Brun, Alberto Mittone, Sergei Gasilov, Loriane Weber, Silvia Adam-neumair, Alberto Bravin, Maximilian Reiser, Paola Coan, Annie Horng, et al. 'Degenerative Cartilage and Subchondral Bony Lesions in a Preserved Cadaveric Knee'. In: (2018) (cited on page 10).

[16] Fulvia Arfelli, M Assante, V Bonvicini, A Bravin, Giovanni Cantatore, Edoardo Castelli, L Dalla Palma, M Di Michiel, Renata Longo, A Olivo, et al. 'Low-dose phase contrast x-ray medical imaging'. In: *Physics in Medicine & Biology* 43.10 (1998), p. 2845 (cited on page 10).

[17] CJ Kotre and IP Birch. 'Phase contrast enhancement of x-ray mammography: a design study'. In: *Physics in Medicine & Biology* 44.11 (1999), p. 2853 (cited on page 10).

[18] Noel T Brewer, Talya Salz, and Sarah E Lillie. 'Systematic review: the long-term effects of false-positive mammograms'. In: *Annals of internal medicine* 146.7 (2007), pp. 502–510 (cited on page 10).

[19] Karen K Lindfors, John M Boone, Thomas R Nelson, Kai Yang, Alexander LC Kwan, and DeWitt F Miller. 'Dedicated breast CT: initial clinical experience'. In: *Radiology* 246.3 (2008), pp. 725–733 (cited on page 10).

[20] Hiroto Hatabu and Bruno Madore. *Dark-field chest X-ray imaging: an evolving technique in the century-old history of chest X-ray imaging*. 2021 (cited on page 11).

[21] Eddy Fan, Daniel Brodie, and Arthur S Slutsky. 'Acute respiratory distress syndrome: advances in diagnosis and treatment'. In: *Jama* 319.7 (2018), pp. 698–710 (cited on page 11).

[22] Kai Scherer, Andre Yaroshenko, Deniz Ali Bölükbas, Lukas B Gromann, Katharina Hellbach, Felix G Meinel, Margarita Braunagel, Jens von Berg, Oliver Eickelberg, Maximilian F Reiser, et al. 'X-ray dark-field radiography-in-vivo diagnosis of lung cancer in mice'. In: *Scientific reports* 7.1 (2017), pp. 1–9 (cited on page 11).

[23] Katharina Hellbach, Felix G Meinel, Thomas M Conlon, Konstantin Willer, Andre Yaroshenko, Astrid Velroyen, Margarita Braunagel, Sigrid Auweter, Maximilian F Reiser, Oliver Eickelberg, et al. 'X-ray dark-field imaging to depict acute lung inflammation in mice'. In: *Scientific Reports* 8.1 (2018), pp. 1–9 (cited on page 11).

[24] Andre Yaroshenko, Tina Pritzke, Markus Koschlig, Nona Kamgari, Konstantin Willer, Lukas Gromann, Sigrid Auweter, Katharina Hellbach, Maximilian Reiser, Oliver Eickelberg, et al. 'Visualization of neonatal lung injury associated with mechanical ventilation using x-ray dark-field radiography'. In: *Scientific reports* 6.1 (2016), pp. 1–8 (cited on pages 11, 141).

[25] Konstantin Willer, Alexander A Fingerle, Wolfgang Noichl, Fabio De Marco, Manuela Frank, Theresa Urban, Rafael Schick, Alex Gustschin, Bernhard Gleich, Julia Herzen, et al. 'X-ray dark-field chest imaging for detection and quantification of emphysema in patients with chronic obstructive pulmonary disease: a diagnostic accuracy study'. In: *The Lancet Digital Health* 3.11 (2021), e733–e744 (cited on pages 11, 34).

[26] Inna O'Hea. 'The development of phase-contrast imaging techniques toward implementation in clinical mammography'. In: (2015) (cited on page 14).

[27] Yi Wang. 'Intuitive dimensional analyses of the energy and atomic number dependences of the cross sections for radiation interaction with matter'. In: *Journal of X-ray Science and Technology* 15.3 (2007), pp. 169–175 (cited on pages 13, 14).

[28] William Thomlinson, Hélène Elleaume, L Porra, and P Suortti. 'K-edge subtraction synchrotron X-ray imaging in bio-medical research'. In: *Physica Medica* 49 (2018), pp. 58–76 (cited on page 16).

[29] Leonard Mandel and Emil Wolf. *Optical coherence and quantum optics*. Cambridge university press, 1995 (cited on pages 16, 17).

[30] Franz Pfeiffer, Timm Weitkamp, Oliver Bunk, and Christian David. 'Phase retrieval and differential phase-contrast imaging with low-brilliance X-ray sources'. In: *Nature physics* 2.4 (2006), pp. 258–261 (cited on pages 17, 34).

[31] Jens Als-Nielsen and Des McMorrow. *Elements of modern X-ray physics*. John Wiley & Sons, 2011 (cited on page 17).

[32] Keith A Nugent. 'Coherent methods in the X-ray sciences'. In: *Advances in Physics* 59.1 (2010), pp. 1–99 (cited on page 17).

[33] Dominika Kalasov, Tom Zikmund, Ladislav Pna, Yoshihiro Takeda, Martin Horvth, Kazuhiko Omote, and Jozef Kaiser. 'Characterization of a laboratory-based X-ray computed nanotomography system for propagation-based method of phase contrast imaging'. In: *IEEE Transactions on Instrumentation and Measurement* 69.4 (2019), pp. 1170–1178 (cited on page 17).

[34] Oscar Hemberg, M Otendal, and HM Hertz. 'Liquid-metal-jet anode electron-impact x-ray source'. In: *Applied Physics Letters* 83.7 (2003), pp. 1483–1485 (cited on page 18).

[35] Paul Alle, Emmanuel Wenger, S Dahaoui, Dominik Schaniel, and Claude Lecomte. 'Comparison of CCD, CMOS and hybrid pixel x-ray detectors: detection principle and data quality'. In: *Physica Scripta* 91.6 (2016), p. 063001 (cited on page 20).

[36] Richard Garnett. 'A comprehensive review of dual-energy and multi-spectral computed tomography'. In: *Clinical Imaging* 67 (2020), pp. 160–169 (cited on page 23).

[37] Wolfram Stiller. 'Basics of iterative reconstruction methods in computed tomography: a vendor-independent overview'. In: *European journal of radiology* 109 (2018), pp. 147–154 (cited on page 25).

[38] Robert von Nardroff. 'Refraction of x-rays by small particles'. In: *Physical Review* 28.2 (1926), p. 240 (cited on page 29).

[39] David Paganin, Sheridan C Mayo, Tim E Gureyev, Peter R Miller, and Steve W Wilkins. 'Simultaneous phase and amplitude extraction from a single defocused image of a homogeneous object'. In: *Journal of microscopy* 206.1 (2002), pp. 33–40 (cited on pages 31, 87).

[40] Chao Zuo, Jiaji Li, Jiasong Sun, Yao Fan, Jialin Zhang, Linpeng Lu, Runnan Zhang, Bowen Wang, Lei Huang, and Qian Chen. 'Transport of intensity equation: a tutorial'. In: *Optics and Lasers in Engineering* 135 (2020), p. 106187 (cited on pages 31, 85).

[41] Jean Pierre Guigay, Max Langer, Renaud Boistel, and Peter Cloetens. 'Mixed transfer function and transport of intensity approach for phase retrieval in the Fresnel region'. In: *Optics letters* 32.12 (2007), pp. 1617–1619 (cited on pages 31, 89, 92).

[42] Mareike Töpperwien, Franziska van der Meer, Christine Stadelmann, and Tim Salditt. 'Three-dimensional virtual histology of human cerebellum by X-ray phase-contrast tomography'. In: *Proceedings of the National Academy of Sciences* 115.27 (2018), pp. 6940–6945 (cited on page 32).

[43] Ulf Lundström, Daniel H Larsson, Anna Burvall, Per AC Takman, L Scott, H Brismar, and Hans M Hertz. 'X-ray phase contrast for CO2 microangiography'. In: *Physics in Medicine & Biology* 57.9 (2012), p. 2603 (cited on page 32).

[44] Alessandro Variola. 'The THOMX project'. In: *2nd International Particle Accelerator Conference (IPAC'11)*. Joint Accelerator Conferences Website. 2011, pp. 1903–1905 (cited on page 32).

[45] TE Gureyev, DM Paganin, B Arhatari, ST Taba, S Lewis, PC Brennan, and HM Quiney. 'Dark-field signal extraction in propagation-based phase-contrast imaging'. In: *Physics in Medicine & Biology* 65.21 (2020), p. 215029 (cited on page 32).

[46] Thomas A Leatham, David M Paganin, and Kaye S Morgan. 'X-ray dark-field and phase retrieval without optics, via the Fokker-Planck equation'. In: *arXiv preprint arXiv:2112.10999* (2021) (cited on page 32).

[47] Miles N Wernick, Oliver Wirjadi, Dean Chapman, Zhong Zhong, Nikolas P Galatsanos, Yongyi Yang, Jovan G Brankov, Oral Oltulu, Mark A Anastasio, and Carol Muehleman. 'Multiple-image radiography'. In: *Physics in Medicine & Biology* 48.23 (2003), p. 3875 (cited on page 32).

[48] Luigi Rigon, Fulvia Arfelli, and Ralf-Hendrik Menk. 'Three-image diffraction enhanced imaging algorithm to extract absorption, refraction, and ultrasmall-angle scattering'. In: *Applied Physics Letters* 90.11 (2007), p. 114102 (cited on page 32).

[49] PC Diemoz, A Bravin, and P Coan. 'Theoretical comparison of three X-ray phase-contrast imaging techniques: propagation-based imaging, analyzer-based imaging and grating interferometry'. In: *Optics express* 20.3 (2012), pp. 2789–2805 (cited on page 33).

[50] Wei Zhou, Keivan Majidi, and Jovan G Brankov. 'Analyzer-based phase-contrast imaging system using a micro focus x-ray source'. In: *Review of Scientific Instruments* 85.8 (2014), p. 085114 (cited on page 33).

[51] Vasco Ronchi. 'Forty years of history of a grating interferometer'. In: *Applied optics* 3.4 (1964), pp. 437–451 (cited on page 33).

[52] Irene Zanette, Christian David, Simon Rutishauser, and Timm Weitkamp. '2D grating simulation for X-ray phase-contrast and dark-field imaging with a Talbot interferometer'. In: *AIP Conference Proceedings*. Vol. 1221. 1. American Institute of Physics. 2010, pp. 73–79 (cited on page 34).

[53] Florian T Gassert, Theresa Urban, Manuela Frank, Konstantin Willer, Wolfgang Noichl, Philipp Buchberger, Rafael Schick, Thomas Koehler, Jens von Berg, Alexander A Fingerle, et al. 'X-ray dark-field chest imaging: qualitative and quantitative results in healthy humans'. In: *Radiology* (2021), p. 210963 (cited on page 34).

[54] Manuel Viermetz, Nikolai Gustschin, Clemens Schmid, Jakob Haeusele, Maximilian von Teuffenbach, Pascal Meyer, Frank Bergner, Tobias Lasser, Roland Proksa, Thomas Koehler, et al. 'Dark-field computed tomography reaches the human scale'. In: *Proceedings of the National Academy of Sciences* 119.8 (2022), e2118799119 (cited on page 34).

[55] Thomas Köhler, Klaus Jürgen Engel, and Ewald Roessl. 'Noise properties of grating-based x-ray phase contrast computed tomography'. In: *Medical physics* 38.S1 (2011), S106–S116 (cited on page 35).

[56] A Olivo, Fulvia Arfelli, Giovanni Cantatore, Renata Longo, RH Menk, S Pani, M Prest, P Poropat, Luigi Rigon, G Tromba, et al. 'An innovative digital imaging set-up allowing a low-dose approach to phase contrast applications in the medical field'. In: *Medical physics* 28.8 (2001), pp. 1610–1619 (cited on page 35).

[57] Alessandro Olivo and Robert Speller. 'A coded-aperture technique allowing x-ray phase contrast imaging with conventional sources'. In: *Applied Physics Letters* 91.7 (2007), p. 074106 (cited on page 35).

[58] PC Diemoz, CK Hagen, M Endrizzi, and Alessandro Olivo. 'Sensitivity of laboratory based implementations of edge illumination x-ray phase-contrast imaging'. In: *Applied Physics Letters* 103.24 (2013), p. 244104 (cited on page 35).

[59] Charlotte K Hagen, Marco Endrizzi, Rebecca Towns, Jeffrey A Meganck, and Alessandro Olivo. 'A preliminary investigation into the use of edge illumination X-ray phase contrast micro-CT for preclinical imaging'. In: *Molecular imaging and biology* 22.3 (2020), pp. 539–548 (cited on page 35).

[60] Gibril K Kallon, Michal Wesolowski, Fabio A Vittoria, Marco Endrizzi, Dario Basta, Thomas P Millard, Paul C Diemoz, and Alessandro Olivo. 'A laboratory based edge-illumination x-ray phase-contrast imaging setup with two-directional sensitivity'. In: *Applied Physics Letters* 107.20 (2015), p. 204105 (cited on page 36).

[61] Han Wen, Eric E Bennett, Monica M Hegedus, and Stefanie C Carroll. 'Spatial harmonic imaging of x-ray scattering—initial results'. In: *IEEE transactions on medical imaging* 27.8 (2008), pp. 997–1002 (cited on pages 36, 37).

[62] Harold H Wen, Eric E Bennett, Rael Kopace, Ashley F Stein, and Vinay Pai. 'Single-shot x-ray differential phase-contrast and diffraction imaging using two-dimensional transmission gratings'. In: *Optics letters* 35.12 (2010), pp. 1932–1934 (cited on pages 36, 37).

[63] Han Wen, Eric E Bennett, Monica M Hegedus, and Stanislas Rapacchi. 'Fourier X-ray scattering radiography yields bone structural information'. In: *Radiology* 251.3 (2009), pp. 910–918 (cited on pages 37, 137).

[64] Eric E Bennett, Rael Kopace, Ashley F Stein, and Han Wen. 'A grating-based single-shot x-ray phase contrast and diffraction method for in vivo imaging'. In: *Medical physics* 37.11 (2010), pp. 6047–6054 (cited on page 37).

[65] Weiyuan Sun, Carolyn A MacDonald, and Jonathan C Petruccelli. 'Propagation-based and mesh-based x-ray quantitative phase imaging with conventional sources'. In: *Computational Imaging IV*. Vol. 10990. International Society for Optics and Photonics. 2019, 109900U (cited on page 37).

[66] Congxiao He, Weiyuan Sun, CA MacDonald, and Jonathan C Petruccelli. 'The application of harmonic techniques to enhance resolution in mesh-based x-ray phase imaging'. In: *Journal of Applied Physics* 125.23 (2019), p. 233101 (cited on page 37).

[67] Hélène Rougé Labriet, Sébastien Berujon, and Emmanuel Brun. 'Dispositif d'imagerie par rayons x et procede d'imagerie associe'. BNT226114PC00. 2021 (cited on pages 39, 55).

[68] Michał J Cieślak, Kelum AA Gamage, and Robert Glover. 'Coded-aperture imaging systems: Past, present and future development–A review'. In: *Radiation Measurements* 92 (2016), pp. 59–71 (cited on page 39).

[69] Ombeline de La Rochefoucauld, Samuel Bucourt, Daniele Cocco, Guillaume Dovillaire, Fabrice Harms, Mourad Idir, Dietmar Korn, Xavier Levecq, Martin Piponnier, Rakchanok Rungsawang, et al. 'Hartmann wavefront sensor in the EUV and hard X-ray range for source metrology and beamline optimization (Conference Presentation)'. In: *Relativistic Plasma Waves and Particle Beams as Coherent and Incoherent Radiation Sources III*. Vol. 11036. SPIE. 2019, 110360P (cited on page 39).

[70] Ginevra Begani Provinciali. 'X-ray phase imaging based on Hartmann Wavefront Sensor for applications on the study of neurodegenerative diseases'. PhD thesis. Institut Polytechnique de Paris, 2022 (cited on page 39).

[71] F Cerrina. 'Ray tracing of recent VUV monochromator designs'. In: *Application, Theory, and Fabrication of Periodic Structures, DiffractionGratings, and Moire Phenomena II*. Vol. 503. SPIE. 1984, pp. 68–77 (cited on page 46).

[72] Manuel Sanchez del Rio, Niccolo Canestrari, Fan Jiang, and Franco Cerrina. 'SHADOW3: a new version of the synchrotron X-ray optics modelling package'. In: *Journal of Synchrotron Radiation* 18.5 (2011), pp. 708–716 (cited on page 46).

[73] Manuel Sanchez del Rio and Luca Rebuffi. 'OASYS: A software for beamline simulations and synchrotron virtual experiments'. In: *AIP Conference Proceedings*. Vol. 2054. 1. AIP Publishing LLC. 2019, p. 060081 (cited on page 46).

[74] Oleg Chubar and P Elleaume. 'Accurate and efficient computation of synchrotron radiation in the near field region'. In: *proc. of the EPAC98 Conference*. Vol. 1177. 1998 (cited on page 47).

[75] Sea Agostinelli, John Allison, K al Amako, John Apostolakis, H Araujo, Pedro Arce, Makoto Asai, D Axen, Swagato Banerjee, GJNI Barrand, et al. 'GEANT4—a simulation toolkit'. In: *Nuclear instruments and methods in physics research section A: Accelerators, Spectrometers, Detectors and Associated Equipment* 506.3 (2003), pp. 250–303 (cited on page 47).

[76] Sébastien Jan, G Santin, D Strul, Steven Staelens, K Assié, D Autret, S Avner, R Barbier, M Bardies, PM Bloomfield, et al. 'GATE: a simulation toolkit for PET and SPECT'. In: *Physics in Medicine & Biology* 49.19 (2004), p. 4543 (cited on page 47).

[77] Silvia Cipiccia, Fabio A Vittoria, Maria Weikum, Alessandro Olivo, and Dino A Jaroszynski. 'Inclusion of coherence in Monte Carlo models for simulation of x-ray phase contrast imaging'. In: *Optics express* 22.19 (2014), pp. 23480–23488 (cited on pages 47, 48).

[78] Max Langer, Zhenjie Cen, Simon Rit, and Jean M Létang. 'Towards Monte Carlo simulation of X-ray phase contrast using GATE'. In: *Optics express* 28.10 (2020), pp. 14522–14535 (cited on page 47).

[79] J Bahrdt, U Flechsig, S Gerhardt, and I Schneider. 'PHASE: a universal software package for the propagation of time-dependent coherent light pulses along grazing incidence optics'. In: *Advances in Computational Methods for X-Ray Optics II*. Vol. 8141. International Society for Optics and Photonics. 2011, 81410E (cited on page 47).

[80] Erik Bergbäck Knudsen, Andrea Prodi, Jana Baltser, Maria Thomsen, Peter Kjær Willendrup, Manuel Sanchez del Rio, Claudio Ferrero, Emmanuel Farhi, Kristoffer Haldrup, Anette Vickery, et al. 'McXtrace: a Monte Carlo software package for simulating X-ray optics, beamlines and experiments'. In: *Journal of Applied Crystallography* 46.3 (2013), pp. 679–696 (cited on page 47).

[81] Tomáš Faragó, Petr Mikulık, Alexey Ershov, Matthias Vogelgesang, Daniel Hänschke, and Tilo Baumbach. 'syris: a flexible and efficient framework for X-ray imaging experiments simulation'. In: *Journal of Synchrotron Radiation* 24.6 (2017), pp. 1283–1295 (cited on page 47).

[82] Silvia Peter, Peter Modregger, Michael K Fix, Werner Volken, Daniel Frei, Peter Manser, and Marco Stampanoni. 'Combining Monte Carlo methods with coherent wave optics for the simulation of phase-sensitive X-ray imaging'. In: *Journal of synchrotron radiation* 21.3 (2014), pp. 613–622 (cited on page 48).

[83] Jonathan Sanctorum, Jan De Beenhouwer, and Jan Sijbers. 'X-ray phase contrast simulation for grating-based interferometry using GATE'. In: *Optics Express* 28.22 (2020), pp. 33390–33412 (cited on page 48).

[84] A Prodi, E Knudsen, P Willendrup, S Schmitt, C Ferrero, Robert Feidenhans, and Kim Lefmann. 'A Monte Carlo approach for simulating the propagation of partially coherent x-ray beams'. In: *Advances in Computational Methods for X-Ray Optics II*. Vol. 8141. International Society for Optics and Photonics. 2011, p. 814108 (cited on page 48).

[85] P Bartl, J Durst, W Haas, T Michel, A Ritter, T Weber, and G Anton. 'Simulation of X-ray phase-contrast imaging using grating-interferometry'. In: *2009 IEEE Nuclear Science Symposium Conference Record (NSS/MIC)*. IEEE. 2009, pp. 3577–3580 (cited on page 48).

[86] Stefan Tessarini, Michael Karl Fix, Peter Manser, Werner Volken, Daniel Frei, Lorenzo Mercolli, and Marco Stampanoni. 'Semi-classical Monte Carlo algorithm for the simulation of X-ray grating interferometry'. In: *Scientific reports* 12.1 (2022), pp. 1–14 (cited on page 48).

[87] TP Millard, M Endrizzi, PC Diemoz, CK Hagen, and A Olivo. 'Monte Carlo model of a polychromatic laboratory based edge illumination x-ray phase contrast system'. In: *Review of Scientific Instruments* 85.5 (2014), p. 053702 (cited on page 48).

[88] Laila Hassan, Uttam Pyakurel, Weiyuan Sun, Carolyn A MacDonald, and Jonathan C Petruccelli. 'Development of simulations for a mesh-based x-ray phase imaging system'. In: *Computational Imaging V*. Vol. 11396. International Society for Optics and Photonics. 2020, 113960E (cited on page 48).

[89] Ginevra Begani Provinciali, Alessia Cedola, Ombeline de La Rochefoucauld, and Philippe Zeitoun. 'Modelling of phase contrast imaging with x-ray wavefront sensor and partial coherence beams'. In: *Sensors* 20.22 (2020), p. 6469 (cited on page 48).

[90] Marie-Christine Zdora, Pierre Thibault, Franz Pfeiffer, and Irene Zanette. 'Simulations of x-ray speckle-based dark-field and phase-contrast imaging with a polychromatic beam'. In: *Journal of Applied Physics* 118.11 (2015), p. 113105 (cited on page 48).

[91] Sebastian Meyer, Serena Z Shi, Nadav Shapira, Andrew DA Maidment, and Peter B Noël. 'Quantitative analysis of speckle-based X-ray dark-field imaging using numerical wave-optics simulations'. In: *Scientific Reports* 11.1 (2021), pp. 1–9 (cited on page 48).

[92] Somayeh Saghamanesh and Robert Zboray. 'Virtual speckle-based X-ray phase-contrast and dark-field imaging with digital phantoms'. In: *Optics Express* 29.25 (2021), pp. 41703–41718 (cited on pages 48, 51).

[93] Robert G Waggener, Louis B Levy, Lee F Rogers, and Peter Zanca. 'Measured X-ray spectra from 25 to 110 kVp for a typical diagnostic unit'. In: *Radiology* 105.1 (1972), pp. 169–175 (cited on page 48).

[94] MR Ay, M Shahriari, S Sarkar, M Adib, and H Zaidi. 'Monte Carlo simulation of x-ray spectra in diagnostic radiology and mammography using MCNP4C'. In: *Physics in Medicine & Biology* 49.21 (2004), p. 4897 (cited on page 48).

[95] Magdalena Bazalova and Frank Verhaegen. 'Monte Carlo simulation of a computed tomography x-ray tube'. In: *Physics in Medicine & Biology* 52.19 (2007), p. 5945 (cited on page 48).

[96] DWO Rogers, B Walters, Iwan Kawrakow, et al. 'BEAMnrc users manual'. In: *Nrc Report Pirs* 509 (2009), p. 12 (cited on page 48).

[97] Andrew M Hernandez and John M Boone. 'Tungsten anode spectral model using interpolating cubic splines: unfiltered x-ray spectra from 20 kV to 640 kV'. In: *Medical physics* 41.4 (2014), p. 042101 (cited on page 49).

[98] Jacob Punnoose, J Xu, Alejandro Sisniega, W Zbijewski, and JH Siewerdsen. 'spektr 3.0—A computational tool for x-ray spectrum modeling and analysis'. In: *Medical physics* 43.8Part1 (2016), pp. 4711–4717 (cited on page 49).

[99] R Birch and M Marshall. 'Computation of bremsstrahlung x-ray spectra and comparison with spectra measured with a Ge (Li) detector'. In: *Physics in Medicine & Biology* 24.3 (1979), p. 505 (cited on page 49).

[100] R Birth. 'Catalogue of spectral data for diagnostic x-rays'. In: *Hospital Physicists' Assocoation* (1979) (cited on page 49).

[101] K Cranley, BJ Gilmore, GWA Fogarty, and L Desponds. 'IPEM Report 78: Catalogue of diagnostic x-ray spectra and other data'. In: *York: The Institute of Physics and Engineering in Medicine* (1997) (cited on page 49).

[102] Gavin Poludniowski, Guillaume Landry, François Deblois, PM Evans, and Frank Verhaegen. 'SpekCalc: a program to calculate photon spectra from tungsten anode x-ray tubes'. In: *Physics in Medicine & Biology* 54.19 (2009), N433 (cited on page 49).

[103] Robert Bujila, Artur Omar, and Gavin Poludniowski. 'A validation of SpekPy: A software toolkit for modelling X-ray tube spectra'. In: *Physica Medica* 75 (2020), pp. 44–54 (cited on page 49).

[104] S Brennan and PL Cowan. 'A suite of programs for calculating x-ray absorption, reflection, and diffraction performance for a variety of materials at arbitrary wavelengths'. In: *Review of scientific instruments* 63.1 (1992), pp. 850–853 (cited on page 49).

[105] Christopher T Chantler. 'Theoretical form factor, attenuation, and scattering tabulation for Z= 1–92 from E= 1–10 eV to E= 0.4–1.0 MeV'. In: *Journal of Physical and Chemical Reference Data* 24.1 (1995), pp. 71–643 (cited on page 49).

[106] Christopher T Chantler, Karen J Olsen, Robert A Dragoset, A R Kishore, Svetlana A Kotochigova, D S Zucker, et al. 'X-ray form factor, attenuation and scattering tables (version 2.0)'. In: (2003) (cited on pages 49, 50).

[107] Tom Schoonjans, Antonio Brunetti, Bruno Golosio, Manuel Sanchez del Rio, Vicente Armando Solé, Claudio Ferrero, and Laszlo Vincze. 'The xraylib library for X-ray–matter interactions. Recent developments'. In: *Spectrochimica Acta Part B: Atomic Spectroscopy* 66.11-12 (2011), pp. 776–784 (cited on page 49).

[108] WT Elam, BD Ravel, and JR Sieber. 'A new atomic database for X-ray spectroscopic calculations'. In: *Radiation Physics and Chemistry* 63.2 (2002), pp. 121–128 (cited on page 49).

[109] Lynn Kissel. 'RTAB: the Rayleigh scattering database'. In: *Radiation Physics and Chemistry* 59.2 (2000), pp. 185–200 (cited on page 49).

[110] David Paganin et al. *Coherent X-ray optics*. 6. Oxford University Press on Demand, 2006 (cited on pages 50–52).

[111] Kaye Susannah Morgan, Karen Kit Wan Siu, and DM Paganin. 'The projection approximation and edge contrast for x-ray propagation-based phase contrast imaging of a cylindrical edge'. In: *Optics Express* 18.10 (2010), pp. 9865–9878 (cited on page 51).

[112] Elisabeth R Shanblatt, Yongjin Sung, Rajiv Gupta, Brandon J Nelson, Shuai Leng, William S Graves, and Cynthia H McCollough. 'Forward model for propagation-based x-ray phase contrast imaging in parallel-and cone-beam geometry'. In: *Optics Express* 27.4 (2019), pp. 4504–4521 (cited on page 51).

[113] Ying Ying How and Kaye S Morgan. 'Quantifying the x-ray dark-field signal in single-grid imaging'. In: *Optics Express* 30.7 (2022), pp. 10899–10918 (cited on pages 54, 127, 148, 149).

[114] Emmanuel Brun, Jerome Vicente, Frederic Topin, and Rene Occelli. 'iMorph: A 3D morphological tool to fully analyze all kind of cellular materials (in Cellmet'08'. In: *Dresden, Germany* (2008) (cited on page 57).

[115] Ilian Häggmark, Kian Shaker, and Hans M Hertz. 'In Silico Phase-Contrast X-Ray Imaging of Anthropomorphic Voxel-Based Phantoms'. In: *IEEE Transactions on Medical Imaging* 40.2 (2020), pp. 539–548 (cited on page 59).

[116] Laurene Quenot, Emmanuel Brun, Jean Michel Létang, and Max Langer. 'Evaluation of simulators for x-ray speckle-based phase contrast imaging'. In: *Physics in Medicine & Biology* (2021) (cited on pages 65, 155).

[117] Marie-Christine Zdora, Pierre Thibault, Tunhe Zhou, Frieder J Koch, Jenny Romell, Simone Sala, Arndt Last, Christoph Rau, and Irene Zanette. 'X-ray phase-contrast imaging and metrology through unified modulated pattern analysis'. In: *Physical review letters* 118.20 (2017), p. 203903 (cited on pages 66, 85, 108, 124).

[118] Kaye S Morgan, David M Paganin, and Karen KW Siu. 'Quantitative single-exposure x-ray phase contrast imaging using a single attenuation grid'. In: *Optics express* 19.20 (2011), pp. 19781–19789 (cited on page 83).

[119] Sebastien Berujon and Eric Ziegler. 'Near-field speckle-scanning-based x-ray tomography'. In: *Physical Review A* 95.6 (2017), p. 063822 (cited on page 84).

[120] Sebastien Berujon and Eric Ziegler. 'Near-field speckle-scanning-based x-ray imaging'. In: *Physical Review A* 92.1 (2015), p. 013837 (cited on pages 84, 123).

[121] Sebastien Berujon and Eric Ziegler. 'X-ray multimodal tomography using speckle-vector tracking'. In: *Physical Review Applied* 5.4 (2016), p. 044014 (cited on page 84).

[122] Sebastien Berujon, Ruxandra Cojocaru, Pierre Piault, Rafael Celestre, Thomas Roth, Raymond Barrett, and Eric Ziegler. 'X-ray optics and beam characterization using random modulation: Theory'. In: *Journal of Synchrotron Radiation* 27.2 (2020), pp. 284–292 (cited on page 84).

[123] Sebastien Berujon, Ruxandra Cojocaru, Pierre Piault, Rafael Celestre, Thomas Roth, Raymond Barrett, and Eric Ziegler. 'X-ray optics and beam characterization using random modulation: experiments'. In: *Journal of Synchrotron Radiation* 27.2 (2020), pp. 293–304 (cited on page 84).

[124] Zhi Qiao, Xianbo Shi, Rafael Celestre, and Lahsen Assoufid. 'Wavelet-transform-based speckle vector tracking method for X-ray phase imaging'. In: *Optics Express* 28.22 (2020), pp. 33053–33067 (cited on page 84).

[125] Marie-Christine Zdora. 'State of the art of X-ray speckle-based phase-contrast and dark-field imaging'. In: *Journal of Imaging* 4.5 (2018), p. 60 (cited on page 85).

[126] Michael Reed Teague. 'Deterministic phase retrieval: a Green's function solution'. In: *JOSA* 73.11 (1983), pp. 1434–1441 (cited on page 85).

[127] David M Paganin, Hélène Labriet, Emmanuel Brun, and Sebastien Berujon. 'Single-image geometric-flow x-ray speckle tracking'. In: *Physical Review A* 98.5 (2018), p. 053813. DOI: 10.1103/PhysRevA.98.053813 (cited on pages 85, 90).

[128] Helene Rouge-Labriet, Laurene Quenot, Sylvain Bohic, Barbara Fayard, David M Paganin, Emmanuel Brun, and Sebastien Berujon. 'Comparison of X-ray speckle-based imaging deflection retrieval algorithms for the optimization of radiation dose'. In: *Physics in Medicine & Biology* 66.6 (2021), p. 065005 (cited on page 86).

[129] Konstantin M Pavlov, David M Paganin, Sebastien Berujon, Hélène Rougé-Labriet, Emmanuel Brun, et al. 'Single-shot x-ray speckle-based imaging of a single-material object'. In: *Physical Review Applied* 13.5 (2020), p. 054023 (cited on page 87).

[130] Robert T. Frankot and Rama Chellappa. 'A method for enforcing integrability in shape from shading algorithms'. In: *IEEE Transactions on pattern analysis and machine intelligence* 10.4 (1988), pp. 439–451 (cited on pages 87, 107, 117).

[131] Matthew R Arnison, Kieran G Larkin, Colin JR Sheppard, Nicholas I Smith, and Carol J Cogswell. 'Linear phase imaging using differential interference contrast microscopy'. In: *Journal of microscopy* 214.1 (2004), pp. 7–12 (cited on pages 88, 117).

[132] C Kottler, C David, F Pfeiffer, and O Bunk. 'A two-directional approach for grating based differential phase contrast imaging using hard x-rays'. In: *Optics express* 15.3 (2007), pp. 1175–1181 (cited on pages 88, 117).

[133] P Guigay. 'Fourier-transform analysis of Fresnel diffraction patterns and in-line holograms'. In: *Optik* 49 (1977), pp. 121–125 (cited on page 89).

[134] S Zabler, P Cloetens, J-P Guigay, J Baruchel, and M Schlenker. 'Optimization of phase contrast imaging using hard x rays'. In: *Review of Scientific Instruments* 76.7 (2005), p. 073705 (cited on page 92).

[135] Max Langer, Peter Cloetens, and Françoise Peyrin. 'Regularization of phase retrieval with phase-attenuation duality prior for 3-D holotomography'. In: *IEEE Transactions on Image Processing* 19.9 (2010), pp. 2428–2436 (cited on page 93).

[136] Laurene Quenot, Helene Rougé-Labriet, Sylvain Bohic, Sébastien Berujon, and Emmanuel Brun. 'Implicit tracking approach for X-Ray Phase-Contrast Imaging with a random mask and a conventional system'. In: *Optica* (2021) (cited on pages 95, 129, 155).

[137] Laurène Quénot, Ludovic Broche, Clément Tavakoli, Sylvain Bohic, and Emmanuel Brun. 'Towards x-ray phase contrast tomography in clinical conditions: simulation and phase retrieval development'. In: *Medical Imaging 2021: Physics of Medical Imaging*. Vol. 11595. International Society for Optics and Photonics. 2021, p. 115954M (cited on pages 95, 155).

[138] Daniel Vavrik and Jan Jakubek. 'Radiogram enhancement and linearization using the beam hardening correction method'. In: *Nuclear Instruments and Methods in Physics Research Section A: Accelerators, Spectrometers, Detectors and Associated Equipment* 607.1 (2009), pp. 212–214 (cited on page 99).

[139] Uttam Pyakurel, Weiyuan Sun, Pikting Cheung, Desirée D'Moore, Xiaoyun Zhang, Carolyn A MacDonald, and Jonathan C Petruccelli. 'Phase and dark-field imaging with mesh-based structured illumination and polycapillary optics'. In: *Medical Physics* 48.11 (2021), pp. 6642–6657 (cited on page 99).

[140] François Orieux, Jean-François Giovannelli, and Thomas Rodet. 'Bayesian estimation of regularization and point spread function parameters for Wiener–Hunt deconvolution'. In: *JOSA A* 27.7 (2010), pp. 1593–1607 (cited on page 99).

[141] Qiong Xu, Hengyong Yu, Xuanqin Mou, Lei Zhang, Jiang Hsieh, and Ge Wang. 'Low-dose X-ray CT reconstruction via dictionary learning'. In: *IEEE transactions on medical imaging* 31.9 (2012), pp. 1682–1697 (cited on page 102).

[142] Alessandro Mirone, Emmanuel Brun, and Paola Coan. 'A dictionary learning approach with overlap for the low dose computed tomography reconstruction and its vectorial application to differential phase tomography'. In: *PloS one* 9.12 (2014). DOI: https://doi.org/10.1371/journal.pone.0114325 (cited on page 102).

[143] Hongchang Wang, Sebastien Berujon, Julia Herzen, Robert Atwood, David Laundy, Alexander Hipp, and Kawal Sawhney. 'X-ray phase contrast tomography by tracking near field speckle'. In: *Scientific reports* 5.1 (2015), pp. 1–6 (cited on page 123).

[144] Hannes Risken. 'Fokker-planck equation'. In: *The Fokker-Planck Equation*. Springer, 1996, pp. 63–95 (cited on page 124).

[145] David M Paganin and Kaye S Morgan. 'X-ray Fokker–Planck equation for paraxial imaging'. In: *Scientific reports* 9.1 (2019), pp. 1–18 (cited on pages 124, 125).

[146] Konstantin M Pavlov, David M Paganin, Heyang Thomas Li, Sebastien Berujon, Hélène Rougé-Labriet, and Emmanuel Brun. 'X-ray multi-modal intrinsic-speckle-tracking'. In: *Journal of Optics* 22.12 (2020), p. 125604 (cited on pages 124–126, 129).

[147] Wataru Yashiro, Sébastien Harasse, Katsuyuki Kawabata, Hiroaki Kuwabara, Takashi Yamazaki, and Atsushi Momose. 'Distribution of unresolvable anisotropic microstructures revealed in visibility-contrast images using x-ray Talbot interferometry'. In: *Physical Review B* 84.9 (2011), p. 094106 (cited on page 129).

[148] Torben Haugaard Jensen, Martin Bech, Irene Zanette, Timm Weitkamp, Christian David, Hans Deyhle, Simon Rutishauser, Elena Reznikova, Jürgen Mohr, Robert Feidenhans, et al. 'Directional x-ray dark-field imaging of strongly ordered systems'. In: *Physical Review B* 82.21 (2010), p. 214103 (cited on page 129).

[149] Florian Schaff, Martin Bech, Paul Zaslansky, Christoph Jud, Marianne Liebi, Manuel Guizar-Sicairos, and Franz Pfeiffer. 'Six-dimensional real and reciprocal space small-angle X-ray scattering tomography'. In: *Nature* 527.7578 (2015), pp. 353–356 (cited on page 129).

[150] Konstantin M Pavlov, David M Paganin, Kaye S Morgan, Heyang Thomas Li, Sebastien Berujon, Laurène Quénot, and Emmanuel Brun. 'Directional dark-field implicit x-ray speckle tracking using an anisotropic-diffusion Fokker-Planck equation'. In: *Physical Review A* 104.5 (2021), p. 053505 (cited on pages 129, 130, 155).

[151] Jonas Graetz. 'Simulation study towards quantitative X-ray and neutron tensor tomography regarding the validity of linear approximations of dark-field anisotropy'. In: *Scientific Reports* 11.1 (2021), pp. 1–11 (cited on page 139).

[152] Cy M Jeffries, Jan Ilavsky, Anne Martel, Stephan Hinrichs, Andreas Meyer, Jan Skov Pedersen, Anna V Sokolova, and Dmitri I Svergun. 'Small-angle X-ray and neutron scattering'. In: *Nature Reviews Methods Primers* 1.1 (2021), pp. 1–39 (cited on page 144).

[153] Rico Burkhardt, Thomas Gora, Alexander A Fingerle, Andreas P Sauter, Felix Meurer, Florian T Gassert, Sophie Dobiasch, Daniela Schilling, Annette Feuchtinger, Axel K Walch, et al. 'In-vivo X-ray dark-field computed tomography for the detection of radiation-induced lung damage in mice'. In: *Physics and Imaging in Radiation Oncology* 20 (2021), pp. 11–16 (cited on page 148).

[154] I Zanette, Tunhe Zhou, Anna Burvall, Ulf Lundström, Daniel H Larsson, M Zdora, P Thibault, Franz Pfeiffer, and Hans M Hertz. 'Speckle-based x-ray phase-contrast and dark-field imaging with a laboratory source'. In: *Physical review letters* 112.25 (2014), p. 253903 (cited on page 148).

[155] SJ Alloo, DM Paganin, KS Morgan, MJ Kitchen, AW Stevenson, SC Mayo, HT Li, B Kennedy, A Maksimenko, J Bowden, et al. 'Speckle-based x-ray dark-field tomography of an attenuating object'. In: *Developments in X-Ray Tomography XIII*. Vol. 11840. SPIE. 2021, pp. 78–90 (cited on page 148).

[156] Jonas Graetz, Andreas Balles, Randolf Hanke, and Simon Zabler. 'Review and experimental verification of X-ray dark-field signal interpretations with respect to quantitative isotropic and anisotropic dark-field computed tomography'. In: *Physics in Medicine & Biology* 65.23 (2020), p. 235017 (cited on page 149).

List of Figures

1.1 Ratio δ/β for some human tissues at clinical x-ray energies. . . . 10
1.2 Images of a human wrist: a) MRI, b) synchrotron phase contrast tomography, d) conventional tomography. c) displays the visibility of numerous structures rated by radiologists for the different modalities. Results from Rougé-Labriet et al. [11]. . . . 11
1.3 Schematic of radiations wavelength and energy associated to technological applications. (From https://www.embibe.com/exams/x-rays/) . . . 13
1.4 Interactions of x-rays with matter, schematic. (Figure adapted from O'Hea [26]). . . . 14
1.5 Interactions predominance depending on material atomic number and photons energy. . . . 14
1.6 Photography of the scientists from General Electric synchrotron around the vacuum chamber in 1947 (photo courtesy of NSLS, Brookhaven). . . . 15
1.7 Synchrotron source and its different parts. (Adapted from https://www.esrf.fr/) . . . 16
1.8 ID17 beamline x-ray available spectrum in comparison to a conventional x-ray tube spectrum 110 kVp. From [28]. . . . 16
1.9 X-ray tube schematic. . . . 17
1.10 X-ray tube spectrum and schematic of the involved physical interactions. . . . 18
1.12 Example of old radiograph films. . . . 19
1.11 Examples of recent x-ray sources and projects. . . . 19
1.13 X-ray direct vs indirect detector. . . . 20
1.14 Schematic of photons as rain being collected into pixels 'buckets'. . . . 21
1.15 Poisson distribution and shot noise. . . . 21
1.16 Representation of a parallel beam and a cone beam (adapted from https://serc.carleton.edu/18399) 22
1.17 Two types of clinical devices: a simple radiography machine (2D imaging) and a CT scan with a rotational gantry (3D imaging). (Images from https://en.wikipedia.org/wiki/X-ray_machine and Garnett [36]) . . . 23
1.18 Process from DNA damage to cancer. (image from https://serc.carleton.edu/) . . . 24
1.19 Influence of spot size on the projected image. (from https://www.axt.com.au/) . . . 24
1.20 Outline of tomographic global process. (Image from Stiller [37]). . . . 25
1.21 Outline of tomographic reconstruction process through slice-projection theorem and back-projection. (Figure from Department of Physics Munich School of Bioengineering Technical University of Munich X-ray Computed Tomography Advanced Lab Course No. 79) . . . 26
1.22 Tomography k-space representation. . . . 26
1.23 Filters used in filtered back-projection tomography. . . . 26
1.24 Physical phenomenon associated to different types of contrasts. . . . 28
1.25 Schematic of the refraction of a ray at the interface between two media. . . . 29
1.26 Propagation-based imaging set-up. . . . 30
1.27 Holography imaging set-up . . . 32
1.28 Analyzer-based imaging set-up . . . 33
1.29 Grating interferometer imaging set-up . . . 33
1.30 Talbot carpet pattern created by phase gratings. . . . 34
1.31 Edge illumination imaging set-up . . . 35
1.32 Mesh based imaging set-up . . . 36
1.33 Mesh-Based imaging phase retrieval principle. Simulated sample image with a phantom and a grid. The Fourier transofrm of this image contains the fourier transform of the sample convoluted to a Dirac comb. The harmonics contain various pieces of information about the sample. . . . 37
1.34 Modulations-based imaging set-up . . . 38
1.35 MoBI principle outline . . . 38

2.1 Fresnel scaling theorem as illustrated in Paganin et al. [110]. . . . 52
2.2 Beamlets redistribution due to refraction after propagation. . . . 53

2.3 Beamlets redistribution due to dark-field blurring after propagation. 54
2.4 2D and 1D Gaussian shapes representations. 54
2.5 Outline of realistic image degradation for simulations: source blurring, pixel size down sampling to detector pixel size, detector PSF blurring and additional shot noise. 55
2.6 Three membranes observed with an optical microscope: one simple sandpaper sheet and two metal powder homemade membranes. 56
2.7 Granulometry pipeline with FIJI: threshold segmentation completed by a watershed and particles characterization. 56
2.8 Outline of the process to simulate the membrane with blender 57
2.9 Membrane segmentation with IMorph 58
2.10 Implemented phantoms geometry. 59
2.11 Illustration of numerical sampling of a sphere sample compared to the analytical truth. 59
2.12 Nylon wire propagation profile with decreasing sampling size dx (i.e. increasing oversampling factor compared to the detector) in the Fresnel model. 60
2.13 Nylon wire propagation profile with decreasing sampling size dx (i.e. increasing oversampling compared to the detector) in the Ray-tracing model. 60
2.14 Schematic of spectrum sampling with energy bins of 2 keV and 10 keV. Nylon wire propagated profiles with different spectrum energy sampling dE. 61
2.15 Summary of all the flexible parameters to define in the simulation. 63
2.16 xml files used for input parameters of the simulation program. 64
2.17 Example output of the simulations: sample and reference images set, propagation image, white field and a text file with a summary of the experiment and algorithm details. 65
2.18 Monochromatic nylon wire sample, reference and propagation images. The images are from a real experiment and 3 simulations: the two models previously introduced (RT and Fresnel) and a Monte Carlo approach from the GATE software. The Dx and Dy retrieved displacement maps were obtained with the UMPA algorithm. 66
2.19 Profiles extracted from lines perpendicular to the nylon wire from the propagation images (a) and from the displacement images Dy (b). 67
2.20 Reference images simulations with and without taking into account the detector PSF. 67
2.21 Propagation sample and reference images from polychromatic simulations and an experiment. Extracted profiles from the propagation images. 69
2.22 Profiles of the simulated nylon wire compared to the experiment when taking into account various elements of the chain. Profiles with only the sample and no other elements (None), then, adding the efficiency of the scintillator (1 element), adding the detector protective plate (2 elements), adding the air volume (3 elements) and finally adding the source beam exiting window (4 elements). The second graph shows the normalized spectrums from the intensity detected in the white image at each energy with and without the detector plate. 69
2.23 Dark-field simulation compared to the experiment. Glass beads cone geometry. Retrieved dark-field from the simulations. Retrieved dark-field from the experiment. Plot of the dark-field extracted profiles. 71
2.24 Schematic of the source projected shape in the detector plane with respect to the sample (orange) and to the membrane (red). 71
2.25 Schematic of the sample geometric deformation to take into account in the case of a cone beam geometry and a thick sample. 71
2.26 Refraction and phase images of a simple phantom retrieved from simulated images. Simulations comprised a constant total number of photons on the set of acquisition simulated but with an increasing number of membrane positions (75 000 photons per pixel in average = 0.1 mGy). 73
2.27 Refraction and phase images of a simple phantom retrieved from simulated images. Simulations comprised a constant total number of photons on the set of acquisition simulated but with an increasing number of membrane positions (750 000 photons per pixel in average = 1 mGy). 74
2.28 Evolution of the standard deviation of the noise in the background of the displacement maps with an increasing number of membrane positions as presented on the two previous figures. 74

2.29 Displacement maps and integrated phase of a nylon wire from a synchrotron monochromatic experiment. Two acquisition schemes were followed one with 5 membrane positions, the other with 10 membrane positions but with the same total exposition time. . . . 75
2.30 Evolution of the noise in displacement maps when increasing the number of photons per pixel per acquisition with 10 membrane positions. . . . 75
2.31 Displacement maps of a bone sphere from simulation with an increasing aluminum filter thickness behind the source. Plot of the standard deviation of an area inside the sample (illustrated by the blue square on the last image) from the different images. . . . 76
2.32 a) Normalized spectrums reaching the detector in the white field with increasing thickness of the aluminum filter. b) Fraction of the initial emitted flux reaching the detector with increasing thickness of the aluminum filter. c) Mean energy and standard deviation and transversal coherence length of the beam. . . . 77

3.1 MoBI acquisition principle. A set of reference images is taken in presence of the membrane at different positions (Ir) and a set is acquired with the sample inserted in the path of the beam (Is). The plot shows small profiles extracted from a sample and reference images. The profile of Is is lower due to attenuation and the membrane modulations are slightly shifted due to refraction. . . 81
3.2 State of the art of the implicit and explicit phase retrieval algorithms and integration methods. . . 83
3.3 Examples of denominator function from association of acquisitions with various energies to illustrate periodic 0-crossing removal. . . . 92
3.4 Mouse knee sample schematic and the main skeletal elements that will be visible on x-rays: patella, femur, tibia and fibula. . . . 95
3.5 Mouse knee attenuation image I_{obj} and displacement maps (D_x, D_y) retrieved with the LCS along with the phase image integrated with the FC method. . . . 96
3.6 Nylon wires sample. . . . 97
3.7 Nylon wire displacement map perpendicular to the wires orientation and their extracted profiles compared to theoretical profiles. . . . 97
3.8 Headless fly radiograph and its structures. . . . 99
3.9 First phase gradient images of the fly retrieved with the LCS from acquisition with a conventional laboratory set-up. . . . 99
3.10 Sample images acquisitions after deconvolution by an unsupervised Wiener algorithms with an increasing full width half max (FWHM) Gaussian shaped kernel. . . . 100
3.11 Evolution of the displacement maps and phase images retrieved with the LCS after de-blurring of the acquisitions with an increasing FWHM of the gaussian shaped deconvolution kernel. . . . 101
3.12 CNR measure on the phase images with increasing FWHM of the deconvolution shape. . . . 102
3.13 Evolution of the level of noise in refraction images with increasing membrane positions. . . . 102
3.14 Displacement map and phase images without filters, with a median filter on the refraction image and after de-noising the refraction image with a dictionary learning method. . . . 103
3.15 Evolution of the refraction and phase images retrieved from acquisitions with an increasing pixels size obtained through binning of the initial acquisitions. . . . 104
3.16 Displacement map and integrated phase retrieved from raw acquisitions (first raw) from acquisitions after deconvolution (middle raw) and from acquisitions after registration and deconvolution (bottom raw). . . . 106
3.17 Process of comparison of the acquisition and correction of the roughcast shadow effect. . . . 107
3.18 Displacement maps and phase images retrieved from acquisitions at 10 membrane positions with various phase retrieval algorithms. . . . 109
3.19 Displacement maps and phase images retrieved from acquisitions at 4 membrane positions with various phase retrieval algorithms. . . . 110
3.20 Schematic of an x-ray converging lens with its characteristic radius R. . . . 111
3.21 Displacement maps of a Beryllium lens with a characteristic radius of 500 µm. Displacements retrieved from acquisitions at 10 membrane positions with various phase retrieval algorithms used for metrology (XSVT and WXSVT) and imaging (LCS, OF, UMPA and XST-XSVT). The plots displays profiles taken in the middle of the lens. The table contains the NRMSE of the profiles obtained with all the algorithms compared to the wXSVT. . . . 112

3.22 Displacement maps of a Beryllium lens with a characteristic radius of 50 µm. Displacements retrieved from acquisitions at 10 membrane positions with various phase retrieval algorithms used for metrology (XSVT and WXSVT) and imaging (LCS, OF, UMPA and XST-XSVT). The plots displays profiles taken in the middle of the lens. The table contains the NRMSE of the profiles obtained with all the algorithms compared to the wXSVT. 113
3.23 Displacement maps of a Beryllium lens with a characteristic radius of 4000 µm. Displacements retrieved from acquisitions at 10 membrane positions with various phase retrieval algorithms used for metrology (XSVT and WXSVT) and imaging (LCS, OF, UMPA and XST-XSVT). The plots displays profiles taken in the middle of the lens. The table contains the NRMSE of the profiles obtained with all the algorithms compared to the wXSVT. 113
3.24 Nylon wires displacement maps retrieved with different algorithms (LCS, UMPA, wXSVT, OF, XST-XSVT, XSVT). Plots of the wires profiles compared to theory. Table of the NRMSE calculated between the experimental profiles and the theoretical one. 114
3.25 Phase images of a fly retrieved from a conventional laboratory set-up set of acquisitions with various available algorithms: LCS, UMPA, XST-XSVT, OF, wXSVT, XSVT from 4, 10 and 16 membrane positions. 115
3.26 Phase images of a mouse knee retrieved from acquisition with a conventional laboratory set-up with three algorithms: LCS, UMPA and XST-XSVT. 116
3.27 Phase integrated with two different algorithms: Frankot and Challapa's algorithm and Larkin Arnison Sheppard's algorithm. Initial refraction were retrieved with the LCS algorithms for the three samples acquired in different experiments. 118

4.1 MoBI acquisition principle. A set of reference is taken in presence of the membrane at different positions (Ir) and a set is acquired with the sample in addition in the path of the beam (Is). The plot shows small profiles extracted from a sample and reference images. The profile of Is is lower due to attenuation, the membrane modulations are slightly shifted due to refraction and their amplitude decreases with dark-field. 121
4.2 State of the art of the implicit and explicit phase retrieval algorithms and integration methods. . . 123
4.3 Phase and dark-field images of a red currant retrieved with the MIST and LCS algorithms. 127
4.4 Haribo crocodile candy impaled with a wooden tooth pic. 127
4.5 Dark-field signal of the Haribo crocodile retrieved with the MIST and LCS algorithms. 128
4.6 Various contrast images of the Haribo crocodile that can be retrieved with the LCS algorithm. Combined attenuation (Iobj), Dark-field (Df) and phase, into RGB channels of a coloured image. . 128
4.7 Schematic of the scattering cone emanating from a beamlet crossing the sample and hitting the detector as an ellipse shape with an orientation θ. 129
4.8 Red currant dark-field tensors retrieved with the LCS and MIST algorithms. 132
4.9 Haribo crocodile impaled with a wooden toothpick dark-field tensors retrieved with the LCS and MIST algorithms. 132
4.10 Schematic of a tilted ellipse and its defining quantities: angle of rotation θ, semi-major axis a and semi-minor axis b. 133
4.11 Haribo crocodile directional dark-field tensors norm computed from the LCS directional dark-field implementation. Area and eccentricity images computed from the tensors. 134
4.12 Haribo crocodile directional dark-field ellipses representation of the area and eccentricity with the computed orientation as the color hue. 135
4.13 Haribo crocodile directional dark-field ellipses representation of the area and eccentricity with the computed orientation as the color hue obtained after filtering individually the tensors components with a median filter. 135
4.14 Pipeline for applying a Gaussian filter to an oriented vector. 135
4.15 Haribo crocodile directional dark-field ellipses representation of the area and eccentricity with the computed orientation filtered with a Gaussian shaped kernel as the color hue. 136
4.16 Haribo crocodile directional dark-field ellipses representation of the area and eccentricity with the computed orientation filtered with a Gaussian shaped kernel as the color hue and the local orientation strength as the saturation. 136

4.17 Haribo crocodile directional dark-field with the tensor norm as the value, the ellipse orientation filtered with a Gaussian shaped kernel as the color hue and the local orientation strength as the saturation. . . . 137
4.18 Attenuation and dark-field images a mouse knee. . . . 137
4.20 Schematic of a tooth with its principal structures. . . . 138
4.19 Mouse knee dark-field tensors and colored representation of the diffusion ellipse direction. . . . 138
4.21 Attenuation, dark-field and directional dark-field images of a human tooth. . . . 139
4.22 Human tooth directional dark-field tomography projection and their extracted sinogram. The hue corresponds to the fibers orientation (perpendicular to the diffusion ellipses orientation). . . . 140
4.23 Rat installed in the tomography set-up with the ventilator. . . . 141
4.24 Rat chest dark-field image and radiography before and after Ventilator Induced Lung Injury (VILI). 142
4.25 Rat chest dark-field and phase tomography slice before and after Ventilator Induced Lung Injury (VILI). . . . 143
4.26 Directional dark-field projection of a rat chest retrieved with the MIST algorithm from 16 MoBI membrane positions. . . . 143
4.27 Samples used in the low energy laboratory set-up: a thin slice of a Haribo flower candy and bundles of carbon fibers. . . . 144
4.28 Attenuation, phase and dark-field images of the flower candy sample retrieved from 10 acquisitions with the LCS along with their extracted profiles along the blue line. . . . 145
4.29 Directional dark-field image of carbon fibers retrieved with the LCS algorithm from a laboratory set-up MoBI experiment. . . . 146
4.30 Attenuation, phase and dark-field images of a crocodile Haribo retrieved from a laboratory set-up experiment at clinical compatible energy. . . . 147
4.31 Summary of all the phase gradient, phase, dark-field and integration algorithms that are implemented into the POPCORN software. . . . 149

List of Tables

1.1 Interactions cross sections [27] . . . 14
1.2 Summary of different features of the PCI techniques . . . 40

2.1 Summary of the number of photons per pixel per position in each acquisition depending on the number of membrane positions. . . . 72
2.2 PARESIS software final appraisal compared to initial specifications. . . . 78

3.1 Summary of the characteristics of the various phase retrieval algorithms. . . . 117

4.1 SAXS and dark-field orientation measurements on the pink and yellow areas of the sample. . . . 146

Summary

English

X-ray phase contrast and dark-field imaging were proven to have a great potential for medical diagnosis of various pathologies thanks to the new contrasts they can provide compared to conventional radiography. Contrary to the attenuation that is directly visible on a radiography as the “shadow” of the sample, the phase and dark-field signals need special set-ups for them to be retrieved. Phase contrast imaging techniques were first invented using super-powerful x-ray sources: synchrotrons. However, those sources are not compatible with clinical routines. Therefore, new techniques were invented: Grating interferometry, Edge illumination or Modulations-based imaging.
The present work reports advances toward the transfer of a synchrotron technique called speckle-based imaging to set-ups with conventional sources, renaming the method Modulation-Based Imaging (MoBI) due to the disappearance of the ’speckle’ phenomenon with those set-ups. This method consists in placing a randomly structured membrane in the path of the beam in order to create a reference pattern and then analyze the pattern modifications upon introduction of the sample in the path of the beam. The difficulty is that the modifications of the pattern gets less visible when working with a conventional source and a low-resolution detector such as the ones used in clinical devices. The work presented in this manuscript includes the creation and validation of a simulation tool for set-up optimization along with new signals extraction algorithms adapted to less coherent cases. Results on synchrotron experiments as well as on conventional sources set-ups are presented. The numerical tools developed here should allow, with some more optimization work and means, the creation of a clinical compatible device.

Français

Il a été prouvé que l’imagerie à rayons X par contraste de phase et en champ sombre ont un grand potentiel pour le diagnostic médical de diverses pathologies grâce aux nouveaux contrastes qu’ils fournissent par rapport à la radiographie conventionnelle. Contrairement à l’atténuation qui est directement visible sur une radiographie sous la forme de "l’ombre" de l’échantillon, les signaux de phase et de champ sombre nécessitent des dispositifs spéciaux pour être récupérés. Les techniques d’imagerie par contraste de phase ont d’abord été inventées en utilisant des sources de rayons X superpuissantes : les synchrotrons. Cependant, ces sources ne sont pas compatibles avec les routines cliniques. De nouvelles techniques ont donc été inventées : l’interférométrie par réseaux, l’illumination de bord ou l’imagerie basée sur les modulations.
Ce travail présente des avancées concernant le transfert d’une technique synchrotron appelée imagerie par tavelures (’speckle-based imaging’ en anglais) vers des installations à sources conventionnelles. La méthode est alors renommée imagerie par modulations en raison de la disparition du phénomène de ’speckle’ avec la perte de cohérence de ces installations. Cette méthode consiste à placer une membrane structurée de manière aléatoire dans la trajectoire du faisceau afin de créer un motif de référence, puis, d’analyser les modifications du motif lors de l’insertion de l’échantillon dans la trajectoire du faisceau. La difficulté est que les modifications du motif sont moins visibles lorsque l’on travaille avec une source conventionnelle à faible cohérence et un détecteur à faible résolution tel que ceux utilisés dans les appareils cliniques. Le travail présenté dans ce manuscrit comprend la création et la validation d’un outil de simulation pour l’optimisation du set-up ainsi que de nouveaux algorithmes d’extraction de signaux adaptés aux cas moins cohérents. Des résultats sur des expériences de synchrotron ainsi que sur des dispositifs à sources conventionnelles sont présentés. Les outils numériques développés ici devraient permettre, avec un travail d’optimisation complémentaire et de moyens matériels, la création d’un dispositif compatible avec la clinique.